Collège de doctorat en Électricité, Électronique et Informatique

École Doctorale en Sciences Technologie Santé EDSTS - (ED n° 585)

Faculty of Applied Sciences

DOCTORAL THESIS

SUBMITTED IN PARTIAL FULFILMENT OF THE REQUIREMENTS FOR THE DEGREE OF

DOCTOR OF PHILOSOPHY (PH.D.)

IN

ELECTRICAL ENGINEERING

PRESENTED BY

KAOUTAR HAZIM

ENTITLED

High-frequency analysis methods of inter-turn stresses in the windings of electrical machines

The jury composition:

President	**Professor Philippe Vanderbemden**	University of Liège
Reviewers	**Professor Noureddine Takorabet**	University of Lorraine
	Professor Ruth Vasquez Sabariego	University of Leuven
Examiners	**Ph.D. Sabrina Ayat**	SAFRAN Electrical & Power
	Professor Stéphane Duchesne	University of Artois
	Professor Yvonnick Le Menach	University of Lille
Supervisors	**Professor Christophe Geuzaine**	University of Liège
	Professor Guillaume Parent	University of Artois

ACE

Laboratoire Systèmes Electrotechniques et Environnement

Colophon

This PhD manuscript, titled “High-frequency analysis methods of inter-turn stresses in the windings of electrical machines”, was written and compiled by Kaoutar HAZIM. It represents the culmination of 3 years and 8 months of research and study conducted at the University of Liège and University of Artois.

The manuscript was typeset using LaTeX, a high-quality document preparation system.

The manuscript was printed and sent to the members of the jury. It is preferable for future reference, to be shared electronically, promoting both environmental sustainability and accessibility.

Special thanks are extended to the members of the jury, my supervisors, my family and friends who have contributed in every way shape or form to the successful completion of this work through their guidance, support, and collaboration.

This research thesis was conducted at:

Applied and Computational Electromagnetics
University of Liège
Montefiore Institute (Building B28, Parking P32)

Sart Tilman Campus, Quartier Polytech 1
Allée de la découverte 10
B-4000 Liège, Belgium

Phone: +32 4 366 37 30
Fax : +32 4 366 29 50

ACE

Laboratoire Systèmes Electrotechniques et Environnement
Université d'Artois

Faculté des Sciences Appliquées
Technoparc Futura – 62400 Béthune

Phone: +33 3 21 63 72 35 or +33 6 32 43 51 78
Fax : +33 3 21 63 72 11

Author Contact Information:

Kaoutar HAZIM

ACE - Applied and Computational Electromagnetics,
Dept. of Electrical Engineering and Computer Science,
Université de Liège

Montefiore Institute B28,
Quartier Polytech 1,
Allée de la Découverte 10,
4000 Liège, Belgium

Email: kaoutar.hazim@doct.uliege.be or khazim@uliege.be

Funding:

This research work was co-financed by the European Union with the financial support of European Regional Development Fund (ERDF), the French State, the French Region of Hauts-de-France as well as the University of Liège.

Computational resources have been provided by the Consortium des Équipements de Calcul Intensif (CÉCI), funded by the Fonds de la Recherche Scientifique de Belgique (F.R.S.-FNRS) under Grant No. 2.5020.11

ᕀ ᓄᔨᐱᓇᓄᕀᕀ ᑕᓄᐞᒪᕀᕀᑐᕀᑕ

"وَيَجهَدُ الناسُ في الدُنيا مُنافَسَةً
وَلَيسَ لِلناسِ شَيءٌ غَيرَ ما رُزِقوا"

أبي العتاهية

"ما في المقامِ لذي عقلٍ وذي أدب
مِنْ رَاحَة فَدعِ الأَوْطَانَ واغْتَرِبِ

سافر تجد عوضاً عمَّن تفارقهُ
وَانْصِبْ فَإنَّ لَذِيذَ الْعَيْشِ فِي النَّصَبِ

إني رأيتُ وقوفَ الماء يفسدهُ
إِنْ سَال طَابَ وَإِنْ لَمْ يَجْرِ لَمْ يَطِبِ

والأسدُ لولا فراقُ الأرض ما افترست
والسَّهمُ لولا فراقُ القوسِ لم يصب

و الشمس لو وقفت في الفلكِ دائمة
لَمَلَّهَا النَّاسُ مِنْ عُجْمٍ وَمِنَ عَرَبِ

و البدر لولا أفول منه ما نظرت
إليه في كل حين عين مرتقب

والتِّبْرَ كالتُّرْبَ مُلْقَى في أَمَاكِنِه
والعودُ في أرضه نوعًا من الحطب

فإن تغرَّب هذا عزَّ مطلبهُ
وإِنْ تَغَرَّبَ ذَاكَ عَزَّ كالذَّهَبِ"

الإمام الشافعي

People struggle in this world with competition
people have nothing that what they are provided with.

Abu Al-Atahiya

There is no rest in residence for a person of culture and intellect,
so travel and leave where you're residing

Travel, you will find a replacement for what you have left
and strive, the sweetness of life is in striving

I've seen that water stagnates if still
becomes pure if it runs, but not if it does not flow

If the lion does not leave his den he cannot hunt
and the arrow will not strike without leaving its bow

If the sun stood still in its heavenly course
then people, Arab and non-Arab, it would bore

Gold dust is as the earth where commonly found
and in its land, oud is but another wood in store

If one travels, he becomes sought out
If one travels, he is honoured like gold.

Ash-Shafi'i

ACKNOWLEDGEMENTS

I would like to seize this opportunity to express my gratitude to the individuals who have played a significant role in my personal, professional, and intellectual growth within the ACE and LSEE laboratories, as well as those I have met outside the labs.

To my thesis advisors, Pr. Christophe Geuzaine and Pr. Guillaume Parent, I am truly immensely grateful for the invaluable insights and guidance offered to me on both personal and professional levels throughout my journey. Your unwavering dedication and feedback have been instrumental in shaping the direction and quality of my work.

I extend my sincere thanks to the members of my jury for accepting to review and examine my manuscript: Pr. Philippe Vanderbemden, Pr. Noureddine Takorabet, Pr. Ruth Vasquez Sabariego, Dr. Sabrina Ayat, Pr. Stéphane Duchesne and Pr. Yvonnick Le Menach.

Special gratitude goes to both François Henrotte and Fabrice Frébel. You really have been exceptional sources of strength, always willing to lend an ear and provide insightful advice whenever I felt the need to discuss the inconveniences that I was facing. Thank you.

I am indebted to Dr. Arnaud Videt not only for recommending me for this Ph.D. opportunity but also for the training he provided me with during my masters. My gratitude also extends to Dr. Bilel Zaidi who tremendously contributed to the training as well. That training really served as a solid foundation for the successful start of my doctoral journey.

I am appreciative and grateful to my colleagues at both the ACE[1] and LSEE[2] laboratories for their collaboration, encouragement, stimulating discussions and good food. I would like to acknowledge the contributions of Aicha Laidoudi[2], Anthony Royer[1], Boris Martin[1], Florent Purnode[1], Giovana Pereira dos Santos Lima[2], Hugues Fabrice Zango[2], Ismail Badia[1], Jonathan Velasco[1], Jean Arban[1], Julien Dular[1], Matteo Cicuttin[1], Nicolas Davister[1], Philippe Marchner[1], Pierre Beerten[1], Ronan Corin[2], Sara Jammoul[2], Tarek Ameid[2], Théo Mathurin[2] and Xavier Adriaens[1].

I was also fortunate enough to meet great people outside the workplace whether in Béthune or Liège; some I had ping-pong matches with, others I enjoyed rock-climbing and bouldering with, while others were always present whenever I needed someone to listen, provide advice

or even do me favours. For this I specifically thank: Alix Bixhain, Florentin Salomez, Hajar Hakkoum, Jihad Srour, Karol Cascavita, Nicolas Legrand and Thibault Fontaine.

Lastly, I would like to express my deepest gratitude to my precious family: my father Lahsen Hazim, my mother Fatima Chraa, my sister Khaoula Hazim, my brother Ilyas Abdessamad Hazim and my grandmother Fadma Jamil. Not to forget my aunts and uncles especially Khadija Chraa, Zahra Chraa, Ayad Chraa and Mehdi Chraa and both my cousins Amina Benaceur and Oussama Benaceur. Their continuous love, support, and understanding have been my constant source of strength.

To all those mentioned, please accept my heartfelt appreciation for your encouragement throughout this challenging and rewarding journey.

Liège, September 2023.

Kaoutar Hazim.

RÉSUMÉ

Cette thèse de doctorat se concentre sur la modélisation des contraintes électriques imposées par la nouvelle génération de dispositifs à semi-conducteurs sur les enroulements des machines électriques. Nous utilisons un modèle de circuit préalablement développé dont les paramètres ont été calculés à une seule fréquence, et nous l'améliorons en configurant correctement les différentes techniques d'identification des paramètres en termes de précision, de complexité de calcul et de dépendance en fréquence. Par le biais d'investigations expérimentales, nous explorons le comportement dépendant de la fréquence du couplage capacitif et justifions son omission dans le modèle. Les éléments dépendant de la fréquence sont initialement incorporés dans le domaine fréquentiel. La méthode proposée est automatique et ne nécessite pas l'utilisation de *vector fitting*. La précision du modèle en domaine fréquentiel est validée sur différents cas test en comparant les impédances calculées avec leurs valeurs mesurées respectives. Ensuite, le modèle fréquentiel est utilisé pour calculer la matrice d'admittance nodale, en se concentrant uniquement sur les nœuds d'intérêt pour un calcul simple des tensions nodales. Ces tensions sont ensuite transformées en domaine temporel à l'aide d'une transformée de Fourier rapide inverse. Pour évaluer la précision et la complexité du calcul, nous comparons nos résultats avec une implémentation équivalente utilisant la méthode du *vector fitting*. L'implémentation de la transformée de Fourier rapide inverse est automatique, deux fois plus rapide qu'une implémentation du *vector fitting* et prédit avec précision les surtensions en domaine temporel. Cependant, elle présente des oscillations parasites qui sont considérablement réduites par l'implémentation équivalente utilisant la méthode du *vector fitting*. Les tensions nodales calculées en domaine temporel sont utilisées pour déduire les tensions inter-spires, démontrant une bonne concordance avec les mesures. La méthode proposée peut être utilisée en entrée pour les différentes méthodes numériques employées dans la prédiction de la défaillance prématurée des enroulements des machines électriques.

Mots-clé: *bobinages des machines électriques, méthodes des éléments finis (MEF), paramètres dépendents de la fréquence, simulation dans le domaine fréquentiel, simulation dans le domaine temporel, matrice d'admittance nodale.*

ABSTRACT

This Ph.D. thesis focuses on modelling the electrical constraints imposed by the new generation of semiconductor devices on electrical machine windings. We make use of a previously developed circuit model the parameters of which were computed at a single frequency and improve it by properly configuring the different parameter identification techniques in terms of accuracy, computational complexity, and frequency dependency. Through experimental investigation, we explore the frequency-dependent behaviour of capacitive coupling and provide justification for its neglect in the model. The frequency-dependent elements are initially incorporated in the frequency domain. Our proposed method is automatic and does not require the use of any fitting technique. The accuracy of the frequency domain model is validated against various test cases by comparing the computed impedances with their respective measured values. Subsequently, the frequency model is employed to compute the nodal admittance matrix, focusing only on the nodes of interest for a straightforward computation of the nodal voltages. These voltages are then transformed into the time domain using an inverse fast Fourier transform. To evaluate the accuracy and computational complexity, we compare our results with an equivalent vector fitting implementation. The inverse fast Fourier transform implementation is automatic, twice as fast as a vector fitting implementation and accurately predicts time domain over-voltages. However, it exhibits spurious oscillations, which are substantially reduced by the equivalent fitting implementation. The computed time domain nodal voltages are used to deduce the inter-turn voltages, demonstrating good agreement with time domain measurements. The proposed method can be used as input to the various numerical methods employed in predicting premature failure of electrical machine windings.

Keywords: *windings of electrical machines, finite element method (FEM), frequency-dependent parameters, frequency domain simulation, time domain simulation, nodal admittance matrix.*

Contents

LIST OF ACRONYMS

2D	Two-Dimensional
3D	Three-Dimensional
BEM	Boundary Element Method
CO_2	Carbon Dioxide
EIS	Electrical Insulation System
EMI	Electromagnetic Interference
FDM	Finite Difference Method
FDTD	Finite Difference Time Domain
FEM	Finite Element Method
FRA	Frequency Response Analysis
FRVF	Frequency Response Vector Fitting
FVM	Finite Volume Method
Ga	Gallium
GaN	Gallium Nitride
GHG	Greenhouse Gas
GND	The ground
GSE	Generalized Steinmetz Equation
IET	Infinite Electromagnetic Transformation
IFFT	Inverse Fast Fourrier Transform
IFT	Inverse Fourrier Transform
LPM	Lumped Parameter Model
LSM	Loss Surface Model

MBPE	Model-Based Parameter Estimation
MNA	Modified Nodal Analysis
MoM	Method of Moments
MSE	Modified Steinmetz Equation
NA	Nodal Analysis
NSE	Natural Steinmetz Extension
PAI	Polyamide-Imide
PD	Partial Discharges
PDIV	Partial Discharge Inception Voltage
PE	Polyethylene
PEI	Polyester-Imide
PWM	Pulse Width Modulation
SiC	Silicon Carbide
TLM	Transmission Line Model
VF	Vector Fitting

LIST OF SYMBOLS

C_{G_i}	Turn to ground capacitance
$C_{t_{ij}}$	Turn to turn capacitance
C	Capacitance
I_i	The excitation current imposed on the i^{th} conductor
I_j	The excitation current imposed on the j^{th} conductor
L_{PVC}	The PVC length
L_{s_i}	The self inductance of the i^{th} turn
M_{ij}	The mutual inductance between the i^{th} and j^{th} turns
P_J	The Joule losses
P_ε	The power dissipation in dielectric materials
R_{ext}	The external radius of the infinite electromagnetic transformation
R_{int}	The internal radius of the infinite electromagnetic transformation
R_{G_i}	Turn to ground resistance
R_{p_i}	The iron losses resistance
R_{s_i}	The self resistance of the i^{th} turn
$R_{t_{ij}}$	Turn to turn resistance
R_{ij}	The mutual resistance between the i^{th} turn and the j^{th} turn
R	Resistance
T_{sw}	The switching period
V_{DC}	The DC input voltage
V_D	The voltage across the diode
V_{t_1}	The voltage of the first turn

V_i	The excitation voltage imposed on the i^{th} conductor
V_j	The excitation voltage imposed on the j^{th} conductor
W_{e}	The stored electic energy
W_{m}	The stored magnetic energy
α	The duty cycle
δ	The skin depth
ℓ_{insul}	The insulation thickness
$\mathbf{C}$	Capacitance matrix
$\mathbf{L}$	Inductance matrix
$\mathbf{R}_{\varepsilon}$	The dielectric losses resistance matrix
$\mathbf{R}$	Resistance matrix
$\mathbf{a}$	The magnetic vector potential
$\mathbf{b_{sat}}$	The magnetic induction at saturation
$\mathbf{b}$	The magnetic induction
curl	The curl operator
$\mathbf{d}$	The electric induction
$\mathbf{e}$	The electric field
grad	The gradient operator
$\mathbf{h_{sat}}$	The magnetic field once saturation is reached
$\mathbf{h}$	The magnetic field
$\mathbf{j_r}$	The reaction current density
$\mathbf{j_s}$	The source current density
$\mathbf{j}$	The current density
$\mathbf{n}$	The outward vector to the boundary
div	The divergence operator
k	The mutual inductive coupling coefficient
m	The number of frequency samples
μ_0	The vacuum permeability
μ_{r}	The relative magnetic permeability
μ	The magnetic permeability
ω	The angular frequency
$\overline{C}_{\text{pp}}$	The capacitance of a parallel plate capacitor
$\overline{Q}_j$	The complex electric charge on the j^{th} conductor
$\overline{Q}$	The complex electric charge
$\overline{U}_i$	The voltage difference across the i^{th} turn
$\overline{U}_j$	The voltage differenceacross the j^{th} turn
$\overline{Y}_{\text{C}_{\text{pp}}}$	The impedance of a parallel plate capacitor
$\overline{Y}_{ii}$	The diagonal elements of the nodal admittance matrix
$\overline{Y}_{ij}$	The off-diagonal elements of the nodal admittance matrix
$\overline{Z}_{\text{s}_i}$	The self impedance of the i^{th} turn
$\overline{Z}_{m_{ij}}$	The mutual impedance coupling the i^{th} and the i^{th} turns
$\overline{\mathbf{Y}}$	The nodal admittance matrix
$\overline{\mu}$	The complex permeability
$\bar{\varepsilon}_{\text{PEI}}$	The complex permittivity of polyester-imide

$\overline{\varepsilon}_{\mathrm{PE}}$	The relative complex permittivity of polyethylene
$\overline{\varepsilon}_{\mathrm{PVC}}$	The relative complex permittivity of PVC
$\overline{\varepsilon}_{\mathrm{r}}$	The relative complex permittivity
$\overline{y}_{ii}$	The admittance between the i^{th} turn and the ground
$\overline{y}_{ij}$	The admittance between the i^{th} and the j^{th} turns
ϕ	The magnetic flux
ρ	The electric resistivity
σ_{copper}	The electric conductivity of copper
σ	The electric conductivity
$\varepsilon_{\mathrm{r}}''$	The imaginary part of $\overline{\varepsilon}_r$
$\varepsilon_{\mathrm{r}}'$	The real part of $\overline{\varepsilon}_{\mathrm{r}}$
ε_0	The vacuum permittivity
$\varepsilon_{\mathrm{inf}}$	The relative permittivity at optical frequencies
ε_{s}	The relative static permittivity (at $f = 0Hz$)
ε	The dielectric permittivity
d_{c}	The conductor diameter
e_{PVC}	The PVC thickness
e_{it}	The inter-turn spacing
e_{lam}	The lamination thickness
f_{res}	The resonance frequency
f_{r}	The relaxation frequency
f_{sw}	The switching frequency
f	The frequency
h_{ext}	The external height of PVC
h_{int}	The internal height of PVC
j	The square root of -1
l_{PVC}	The PVC width
n_{ℓ_1}	The number of turns of the first layer
n_{ℓ_2}	The number of turns of the second layer
n_{ℓ_3}	The number of turns of the third layer
n_{ℓ_4}	The number of turns of the fourth layer
n_{p}	The number of poles
n	The number of turns
r_{PVC}	The external radius of the PVC
r_{air}	The airgap between the winding and the symmetry axis
r_{c}	The conductor radius
t_{f}	The fall time
t_{r}	The rise time
v	The electric scalar potential

LIST OF FIGURES

LIST OF TABLES

GENERAL INTRODUCTION

Context and motivation

The European Green Deal, released by the European Union at the end of 2019, addresses the environmental and climate challenges faced by the European Union and its citizens [1]. Among these challenges, the continuously rising levels of Greenhouse Gas (GHG) emissions warming our planet is of particular concern [2], [3], to which the transportation sector alone—that includes cars, trucks, air planes, trains and ships—is responsible for 25 % and is continuing to grow due to its dependence on fossil fuels as its energy source [4]. Burning of the fossil fuels is a significant source of these GHG emissions, particularly Carbon Dioxide (CO_2) emissions [5], hence the urgency to reduce these emissions up to 90 % by the end of 2050.

The GHG emissions reduction demands the implementation of a cleaner transportation system which explains the ongoing measures taken to ensure a smooth and urgent transition from oil-based to electrical-based transportation [6]. While the recent technological breakthroughs that aim at fostering electrified transportation industry are commendable, the emission reduction objectives remain far from being achieved. Nevertheless, there is extensive support for the potential of achieving CO_2 neutrality in the foreseeable future [4], [5]. As a matter of fact, using internal combustion engines to power vehicles is far less advantageous when compared to electric motor drives efficiency-wise. The former can convert up to 30 % of the primary energy, whilst the later can reach up to 90 % efficiency. Furthermore, electric motors open up opportunities to utilize renewable energy sources, such as solar, wind and hydro, that are carbon free [2]. Accordingly, the shift towards electrified transportation and the increasing demand for electric propulsion necessitate a new era of automotive electrical actuation.

In consequence, power electronics has become a necessity. It facilitates the control over different electrical quantities allowing thus for high efficiencies, which justifies its wide spread in both domestic and industrial environments. Subsequently, and as a means to meet the power demand surge and a higher efficiency, both the supply voltage[1] and the switching frequency

[1] An eventual increase of the current could be considered as well, except that the conductors will be very heavy, which is to be avoided when willing to increase the power density.

f_{sw} are further increased [7], [8], respectively. The increase of f_{sw}, particularly made possible with the new generation of the semiconductor devices, offers advantages such as smaller component size, improved control and higher power density which are favourable in embedded systems. This is not free of shortcomings. The increase of the f_{sw} might be of significant harm to the nearby equipments because of the generated conducted and radiated Electromagnetic Interference (EMI). The generated conducted EMI can be mitigated if a properly designed filter is inserted between the power supply and the converter [9]. This is part of the electromagnetic compatibility study which is investigated in various research works (refer to [9]–[12]). The second inconvenience is the impact the increase of f_{sw} and the accompanying fast transient voltages have on the Electrical Insulation System (EIS) of the supplied electrical machine; recognized by the scientific community as one of the primary failure reasons of electrical machines [13]–[16]. The imposed high electrical constraints on the electrical machine windings induce the generation of high electric fields between the winding turns. Once these inter-turn electric fields exceed the Partial Discharge Inception Voltage (PDIV), the possibility of Partial Discharges (PD) occurrence increases. Although considered low energetic phenomena, the repetitive occurrences of these PD lead to the breakage of the polymeric bonds of the insulation, accelerating thus its ageing and resulting in premature conductor short-circuits [17]. Considering this, any insulation failure—primarily caused by the imposed electrical stresses [18]—can swiftly result in a sudden malfunction of the electrical machine [19], [20] reducing thus its lifespan.

The EIS of electrical machine windings plays a crucial role since it ensures the galvanic separation between the different conductive components of the electrical machines windings. The EIS is made of three insulation groups as portrayed in Fig. 1, where (a) is the insulation between the conductors of different phases (1), (b) is the insulation between each conductor and the The ground (GND) (2), and (c) is the insulation between turns (3), henceforth referred to as inter-turn insulation.

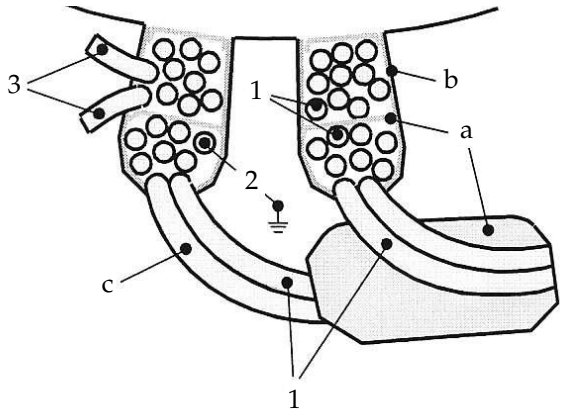

FIGURE 1: The Electrical Insulation System of rotating electrical machines (according to the standard IEC/TS 60034-18-41).

The insulation between the different phases of the winding is characterized by a significant thickness and a tensile strength. It hence ought to be able to withstand high temperatures by quickly dissipating the generated Joule losses heating within the winding. The insulation between each conductor of the winding and the GND is subject to high mechanical and electrical stresses which justifies its larger thickness compared to the other insulation types of the EIS. The last type of insulation, the inter-turn insulation which is usually a thin layer of enamel made of an organic chemical composition, is particularly the most susceptible to electrical

stresses, especially for random wound windings [17], [21], where there is a probability that electrically distant turns may be geometrically adjacent. In addition, the inter-turn faults are considered to be the most serious of winding faults [22], [23].

Correspondingly, numerous attempts have been made to quantitatively evaluate the risk of PD in electrical windings [24]–[26], most of which rely on Paschen's law as a PD risk criterion. It is an efficient and an easy to implement technique that enables the evaluation of the PD occurrence probability by comparing the electric field between the considered conductors to the chosen PD risk criterion [27]. It has been demonstrated in [28] that this can be implemented using finite element computations provided that the voltage difference between the conductors is known. Appropriately, the prediction of the electrical field stresses occurring within the electrical machine windings requires first, the prediction of the inter-turn voltage distribution, then, the calculation of the PD occurrence probability. Hence, the need of well parametrized models of the electrical machines windings.

Dissertation goals

In this work, we focus on the impact of the switching frequency increase on the EIS of electrical machine windings, in particular the inter-turn insulation. As a matter of fact, the harmonically rich input voltage imposed on the windings ends up exciting the different parasitic elements of the studied energy conversion system, therefore generating a non-linear distribution of the voltage across the turns of the winding. Depending on the switching frequency as well as the rise time, the voltage amplitude can reach up to triple the value of the input voltage V_{DC}. The higher the potential difference between turns, the higher the electrical stress and the more prone PD are to occur [28]–[30]. Accordingly, the objective of this research work is to develop a model that predicts the inter-turn voltage distribution within the turns of the electrical winding. This will serve as an input to the various numerical efforts [24], [31] dedicated to calculate the PD occurrence probability, *e.g.* using Paschen's law [28], [32], [33].

Previous research work [34] has introduced a phenomenological elementary Lumped Parameter Model (LPM) defined per turn, modelling the different electromagnetic phenomena that take place within the windings. Its main limitation lies in its parametrization: while some parameters were evaluated analytically, at one frequency, others were evaluated numerically or deduced from experimental measurements. This hinders the usage of the model as a predictive tool. Even though Toudji in [17] improved the model parametrization by proposing a method enabling the computations of its parameter values numerically, inter-turn dielectric losses as well as the proximity effects were not properly taken into account. Additionally, the model parameters were also estimated at the first resonance frequency only, neglecting therefore their frequency dependent behaviour.

Our aim is to propose a predictive diagnostic tool that enables an accurate estimation of the inter-turn voltage distribution by accounting for the different frequency dependencies of the previously proposed LPM in both frequency domain and time domain. While developing the model, different constraints are to be dealt with, like for example the computational complexity of the proposed numerical tool which ought to have a reasonable value without inducing any loss of accuracy given the size of electrical machines. Consequently, the adopted research methodology to address the faced challenges and reach the fixed goal is as follows:

- use an electrical winding model that is as computationally light as possible, while still accurate enough to capture the phenomena of interest;

- study the frequency dependent behaviour of the capacitive coupling, previously neglected;

- propose a Finite Element Method (FEM) model that will allow the prediction of the parameters of the winding model by inspection over the frequency range of interest;

- propose a method to account for the various frequency behaviours in frequency domain simulations;

- validate the frequency domain model by confronting the output of the model to the experimental measurement data of representative case studies;

- propose a method to include this frequency dependency in time domain to compute the voltage distribution;

- validate the time domain model by comparing the computations with the measurements.

In order to achieve this, we re-implemented the methodology proposed in [17] and used it as benchmark to evaluate the benefits of the model proposed in this work.

Thesis outline

This work is divided into three chapters.

The **first chapter** is a state of the art that introduces the different electrical winding models found in the literature. Accordingly, the previously developed models alongside their parametrization are presented, compared and their limitations elaborated. Then follows the description of the different techniques that account for the frequency dependent behaviour of the winding of electrical machines in both frequency and time domain simulations.

The **second chapter** details the chosen frequency domain model of electrical machine windings by first presenting the different identification techniques that can be used to compute the values of the parameters by inspection. The frequency dependent behaviour of the used dielectrics is investigated experimentally. Then, a verification and a comparison of the different identification techniques according to both their computational complexity and accuracy is performed and the choice of one over another is justified. Subsequently, the developed frequency domain elementary cell of the winding where the various frequency dependencies are included is presented. Finally comes the experimental validation of the model performed on various windings with and without a magnetic core.

The **third chapter** addresses the time domain modelling of the electrical windings. It starts by investigating the usage of equivalent circuits per turn and highlights the encountered difficulties when accounting for the different mutual couplings in time domain simulations. After that, the usage of the frequency domain nodal analysis to compute the nodal admittance matrix is justified and its computation by inspection described. Then, a new technique to reduce the proposed model of the winding to the nodes of interest is presented and the computation of the nodal voltages using IFFT is described. The experimental investigation is performed and the results are confronted to those deduced for an equivalent VF implementation. Finally, a comparison with the computed results when adopting the previous developed model [17] is presented to justify the purpose of this research work.

Publications and International Conferences

The main contributions of this thesis have been showcased in the subsequent peer-reviewed journals and international conferences:

Publication in Peer-Reviewed International Journals

- "2D Electrostatic Modelling of Twisted Pairs" in the International Journal for Computation and Mathematics in Electrical and Electronic Engineering (COMPEL), volume 41, pages 48–63, 2022.

International Conferences

- Poster presentation at the International Conference Compumag 2023. Title: A Circuit Model Accounting for the frequency dependent Behaviour of Electrical Machine Windings. The conference took place in Japan from May 22nd to May 26th, 2023.

- Poster presentation at the International Conference Compumag 2021. Title: Frequency Dependent Behaviour of the Lumped Parameter Model of the Windings of Electrical Machines in Transient Simulations. The conference was held online from January 16th to January 20th, 2022.

- Oral presentation at the 12th International Symposium on Electric and Magnetic Fields (EMF 2021). Title: A frequency dependent Behaviour of the Lumped Parameter Model of the Windings of Electrical Machines in Transient Simulations. The symposium was held online from July 6th to July 8th, 2021.

CHAPTER

1

STATE OF THE ART

Contents

1.1 Introduction

Power electronics has become essential in a wide variety of electrical devices. It has revolutionized both the generation and consumption of electrical power, and continues to expand its domain of applications, in particular with respect to electric vehicles and future electric planes [35], [36]. For these applications, in order to achieve the highest efficiency with the smallest size (and mass) at an acceptable cost [37], a primary focus of recent developments has been on increasing the switching frequency, which will lead to an increase of the power density. This has been made possible by the introduction, during the last decade, of new generations of wide-gap semiconductor devices [38], in particular Silicon Carbide (SiC) and Gallium Nitride (GaN) [39]–[41]. The effect of this high frequency power electronics revolution has been particularly significant in the design and operation of electric motor control through variable speed drives [12], [42].

In this thesis, we focus on the effect of the increase of the switching frequency of motor drives on the actual electric machines, specifically on their windings. Indeed, this frequency increase comes with its inconveniences. First, the very fast commutations of the switching devices result in an increased pollution of the electromagnetic environment by generating electromagnetic interferences both conducted and radiated [9], [43]. Second, the switching frequency increase (with the accompanying decrease in voltage rise and fall times) imposes higher electrical constraints on the EIS of the windings of electrical machines, more specifically the inter-turn insulation. In this study we will target the latter, and consider the representative energy conversion system depicted in Fig. 1.1, where V_{t_1} refers to the voltage imposed on the electrical machine. The chosen notation for this voltage is justified in the ensuing chapter.

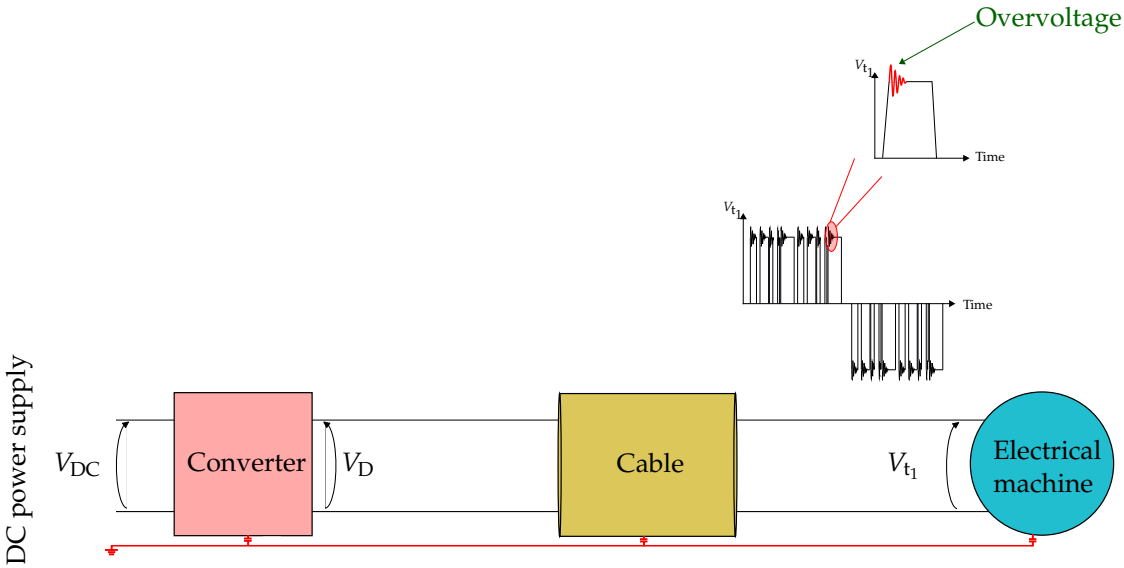

FIGURE 1.1: The considered energy conversion system.

The considered energy conversion system consists of a DC power feeding a static converter composed of controlled switches made of diodes and transistors that switch states (On-Off) according to the switching frequency. The switching of these elements generates a chopped voltage supplying the electrical machine through a cable. A typical elementary cell of a converter resembles the one seen in Fig. 1.2, where V_{DC} refers to the voltage supply and V_D the voltage across the diode supplying the cable.

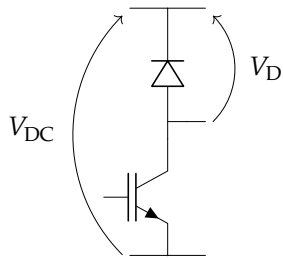

FIGURE 1.2: A typical elementary cell of a transistor based static converter.

The converter is connected to the electrical machine through a cable of a given length that depends on the desired design flexibility and motor drive modularity. In effect, the cables linking the converter to the machine combined with the parasitic components of the windings can lead to voltage surges at the terminals of the machine [44]; this is because the high frequency chopped input voltage V_D excites the parasitic elements of both the winding and the cable. The steeper the input voltage is (small rise time t_r), the higher the voltage surge across the winding. When a steep-fronted voltage propagates within the cable, wave reflection phenomena and impedance mismatch take place at its extremities [7], [45]–[48]. With the impedance of the machine being superior to that of the cable, a reflection occurs on the machine side with a coefficient close to 1. On the converter side, on the other hand, an electrical wave reflection of a coefficient close to -1 takes place [12], [49]. This is depicted in Fig. 1.1. Hence, the longer the cable alongside the different parasitic elements of the windings, the sharper the electrical constraints are, which causes a non-uniform voltage distribution within the winding turns [47], [50], [51]. Moreover, some configurations may be programmed to impose two sufficiently close switchings, that the occurring reflection phenomena are combined and result in an even larger over-voltage at the extremities of the electrical machine [12], [52].

These imposed electrical constraints remain concentrated at the first turns of the winding most of the time and if they exceed the PDIV, the possibility of having PD increases. The occurrence of the latter may result in an inter-turn local fault, implying higher thermal stresses that the electrical machine has to withstand [53]. This accelerates the ageing of the EIS of the machine connected as a load, especially during the switching transitions [54]. Moreover, the expansion of the local fault can eventually lead to the premature breakdown of the machine [55]. For this reason the reliability of the electrical machine depends primarily on its EIS [56], [57].

Taking everything into account, the PD as well as the velocity of the resulting EIS ageing rely mainly on the inter-turn voltage characteristics, insulation design and temperature. Hence, in order to develop a predictive tool that enables the prediction of the PD whereabouts, the inter-turn voltage distribution has to be computed before/during the design phase of the electrical machine. In order to achieve the latter, a model of the winding has to be developed.

At first thought, the usage of a brute-force model of the entire electrical machine might seem tempting: a full 3D geometrical definition of the machine (a number of turns wound on a magnetic core) followed by the numerical resolution of the full-wave Maxwell's equations. However, the usage of the brute-force model is hindered by the enormous computational resources required (CPU time and memory), no matter the chosen numerical method (FEM, Finite Difference Method (FDM), Method of Moments (MoM), ...). In addition, while we are interested in the frequency response of the windings from DC to high frequencies, stable broadband models are hard to achieve [58]–[61]. Lighter models of the windings are thus clearly needed [62]–[64]. A possible simplification can be performed to alleviate the time expenses by adopting the corresponding 2D electromagnetic field models, by accounting for the connections between the

2D model of winding turns via electrical circuits consisting of inductances, resistances, capacitances, current and voltage sources [65]–[68]. Therefore, the voltage drops and the currents in the turns are considered unknowns of the system, and are added to the set of field equations [69]. However the computational cost of solving the field coupled equations remains very high which prevents such an approach to be implemented when opting to develop an electrical winding design tool.

As a means to overcome the aforementioned limitations, circuit models were introduced [17], [34], [55], [70], [71]. Not only are they fast compared to the previously mentioned numerical methods, but they also offer a close technical understanding of the modelled system, in our case, electrical machine windings. There are two commonly used circuit models to emulate electrical machine windings: TLM and LPM [72]–[74].

The first circuit model TLM, also referred as transmission line matrix [75], was developed in 1971 by Johns and Beurle [76] to model electromagnetic waves propagating through space and time. This model uses equivalent circuit elements, *i.e.* inductances, resistances and capacitances connected in parallel and in series configurations to represent the distributed effects of transmission lines [77]. In the case of a bundle of conductors, as in the winding of electrical machines, the conductors in the slots are replaced by equivalent wires [78], [79] so as to consider the distributed nature of the turns. Thus, a difficulty is faced in extracting the inter-turn voltages because the TLM describes the electromagnetic phenomena occurring on a distributed cell level instead of a turn. Another difficulty is faced when the conductors are rearranged [17], [34] since this rearrangement affects the impedance as well as the propagation characteristics of the transmission line. This model is thereupon forsaken given our interest in the inter-turn voltage distribution. For an elaborate discussion on this model, it is helpful to refer to [17], [34], [77].

The second circuit model LPM, models the winding using discrete electrical elements and grants its modelling on a turn level. For this thesis, our attention is directed toward a LPM presented in previous research works initially developed by Mihaila [55], where the model parameters were calculated analytically. This was later on improved by Toudji [17], where the values of the parameters were computed numerically. Our objective is to further improve the resulting LPM by accounting for the frequency dependency of its electrical parameters in both frequency domain and time domain, for an accurate prediction of the inter-turn voltage distributions in a larger frequency spectrum.

This chapter is organised as follows: the first section 1.2 presents an insight on the LPM of electrical machine windings, the different approaches in which it can be used, the adopted topology as well as the previously adopted parametrization techniques of its elements [34], [55]. Next, we mention the enhancements provided by Toudji [17] in section 1.2.2, followed by the limitations of its parametrization. Then, the different frequency behaviours of the electrical parameters defining the adopted circuit topology are presented and elaborated on in section 1.3. Following this, the different methods suggested in the literature accounting for the frequency dependency of these electrical parameters are outlined in section 1.4. These methods can be grouped in two categories: numerical methods and circuit methods. Willing to conserve the circuit character of the adopted model, we focus on the different circuit models that allow accounting for the frequency dependency of the parameters. These electrical networks are deduced after applying fitting techniques. Accordingly, three different fitting methods are presented and compared in section 1.4.3.

1.2 Lumped Parameters Model of electrical machine windings

In order to accurately predict the inter-turn voltage distribution within the windings of electrical machines, a proper model of its winding is needed. This work focuses on improving the previously proposed LPM of electrical machine windings, extensively used in the literature [34], [37], [80]–[83], that enables a straightforward access to the inter-turn voltage distribution. But first, a reminder of its structure as well as an insight on the different approaches in which it can be used are provided.

The LPM provides a discrete association of lumped resistances, inductances and capacitances either representing the studied system as a whole or as an association of its portions each emulated with a RLC circuit. When choosing to implement the latter, a quasi-linear voltage is required across each association of the LPM representing a portion of the studied system. Therefore, the length of the longest element represented by each portion should be shorter than the smallest wavelength of the frequency range of interest [81].

In light of this, the LPM can be configured under two approaches: either a systemic approach [71], [84], [85] or a phenomenological approach [17], [34] as seen in Fig. 1.3.

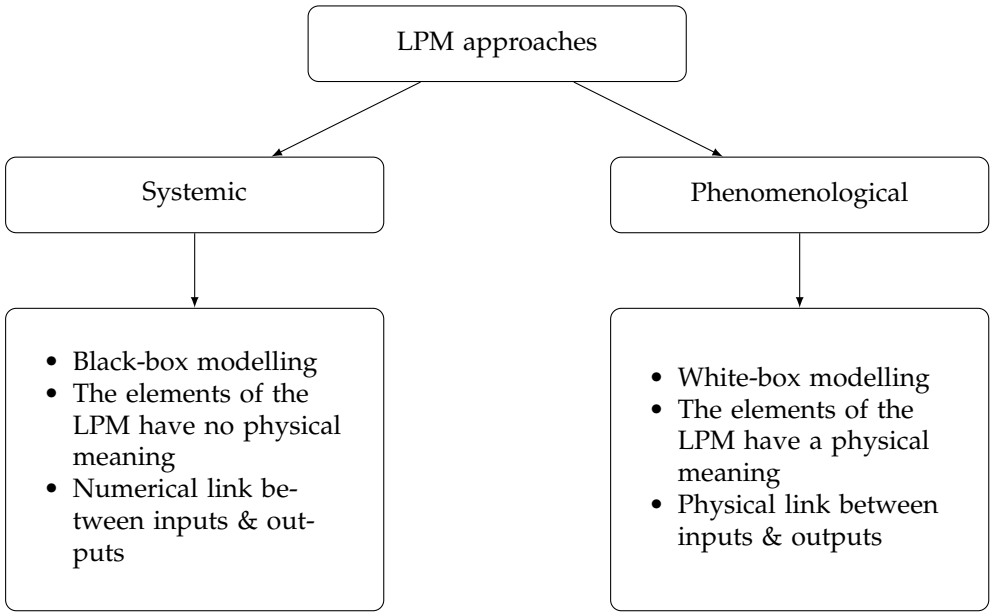

FIGURE 1.3: The two approaches that can be adopted when using a lumped parameter model.

The systemic approach describes the behaviour of the system as if it were a "black-box" [46], [86], [87], and so the internal structure is unknown to the user (or is of no interest to them). This approach is mainly used when the physical processes of the studied system are poorly understood or are very complex, and can be very useful since it provides an accurate prediction of the behaviour of the system. In this case, the values of the lumped parameters are determined through a fitting technique by forcing the electrical components association to reproduce the frequency behaviour of the studied system. Accordingly, the input and output of the system are linked through mathematical expressions and thus the deduced electrical parameters of the LPM have no direct physical interpretation. This approach was used by Gustavsen [86] where

he modelled a two-winding power transformer. First, the frequency response of the transformer was measured on a wide frequency range extending from 50 Hz to 1 MHz, that was later on represented using a LPM configuration reproducing the same frequency behaviour. However, although the accuracy of the proposed model was verified through experimental validation, the internal behaviour per turn cannot be extracted. Similarly, in [88], the author presented a broadband equivalent circuit model of synchronous machines, by first measuring its impedance on the frequency range of interest; then, its response is modelled with different RLC circuits where each one is computed based on a resonance point. The different RLC circuits are eventually cascaded. Likewise, Idir [89] measured the wideband impedance characteristics of synchronous machine, then used empirical and asymptotic formulae to deduce the equivalent LPM model from 10 kHz to 30 MHz. With this in mind, using this approach does not allow for an investigation of the winding on a turn level, and is therefore cast aside.

Conversely, the phenomenological approach takes into account the occurring physical phenomena within the system, whether resistive, inductive or capacitive, by modelling them using either a resistor, an inductor or a capacitor, respectively. Also referred to as "white-box" modelling, this approach is typically used when the underlying occurring phenomena governing the studied system are well understood. This allows to link the inputs and outputs of the studied system in a physical way rather than with purely mathematical relations that allow no formal links to the underlying physical phenomena. Thus, a physical understanding and interpretation of the outputs can be achieved [17]. This approach makes it possible to study the outputs of the model while also having the ability to trace back to the influencing inputs. For instance, Moreau [81] used the elementary electrical cell presented in Fig. 1.4 to model self effect of a transformer winding. The element R_{s_i} stands for the ohmic losses generated by both the self-skin effect in the electrical mesh and the induced current loops in the remaining electrical meshes of the model. The element L_{s_i}, on the other hand, models the electromotive force generated by the current flowing through the electrical mesh. The coupling to the GND is taken into account using the elements R_{G_i} and C_{G_i} placed in parallel. This chosen model for the capacitive coupling is further elaborated on in section 1.3.4.

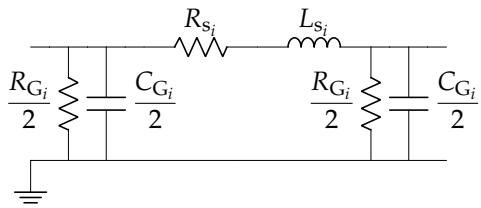

FIGURE 1.4: A lumped parameter model of the self effect of a transformer elementary cell used in [81].

The mutual effect between the different electrical meshes describing the winding is modelled using the elementary cell seen in Fig. 1.5, where the elements R_{ij} and M_{ij} model the resistive and mutual inductive couplings between the electrical meshes, respectively. As a matter of fact, the term R_{ij} models the eddy currents loop that develop in the different conductive materials. The capacitive coupling between the electrical meshes is taken into account with $C_{t_{ij}}$ in parallel with $R_{t_{ij}}$.

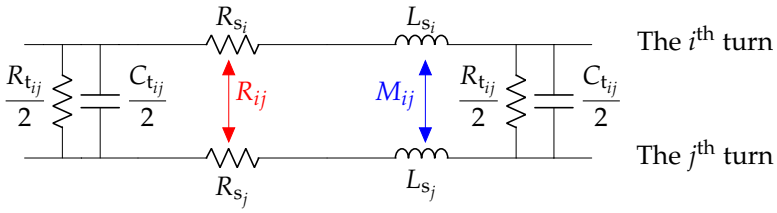

FIGURE 1.5: A lumped parameter model of the mutual effect between the i^{th} and j^{th} elementary cells of the transformer used in [81].

In [90], Mirafzal proposed a standard T-equivalent phase level circuit to model a three phase induction motor. The chosen circuit model is an extension of the IEEE Standard 112 low-frequency circuit model [91]. The model reproduces the frequency behaviour of the motor over a wide frequency range (from 10 Hz to 10 MHz). Perisse in [71], proposed a model of an induction machine discretized on a turn level, where each turn was modelled using the LPM circuit represented in Fig. 1.6, where only the mutual inductive coupling between adjacent turns was taken into account. The capacitive coupling between turns was accounted for using a capacitance $C_{t_{ij}}$ in parallel with a resistance $R_{t_{ij}}$ and was only accounted for adjacent turns as well.

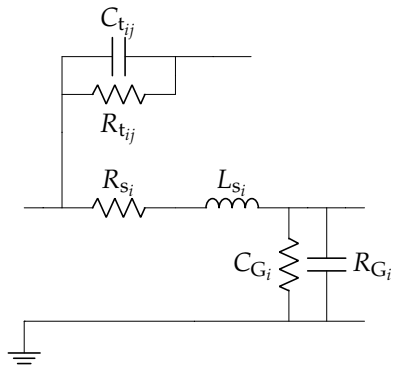

FIGURE 1.6: The lumped parameter model used by Perisse [71] to model an induction machine.

Mihaila followed the same approach [34], and modelled each turn of the machine using the LPM seen in Fig. 1.7. Unlike Perisse [71], the mutual inductive coupling M_{ij} between all turns (not only adjacent ones) was taken into account. The resistance R_{s_i} describes the Joule losses that occur in each turn. The electromotive force generated by the magnetic flux that crosses each turn is taken into account by the inductance L_{s_i} placed in parallel with the resistance R_{p_i} that accounts for the occurring iron losses when a magnetic material is inserted. The capacitive coupling of the turn with the magnetic material (considered the GND) is modelled with C_{G_i} in parallel R_{G_i} and to the other turns with $C_{t_{ij}}$ in parallel with $R_{t_{ij}}$. Here, the capacitance represents the stored electrostatic energy, whereas the parallel resistance models the dielectric losses. This will be elaborated in section 1.3.4. Henceforth, the input node to the i^{th} turn is refereed to as "t_i".

Using the LPM in the phenomenological approach proposed by Mihaila allows for a discrete modelling of one turn at a time, hence an easier computation of the inter-turn voltages and it is therefore chosen as the basis model for this research work. Subsequently, the adopted topology

will be further elaborated through a test case in section 1.2.1. Moreover, properly setting up the parameters of the chosen circuit model is of equal importance, as it strongly affects the accuracy level of the computed inter-turn voltage distribution. There are three methods to assign values to its electrical parameters: either determine their values numerically, deduce them from measurements, or compute them using numerical techniques. The pros and cons of each one of the parametrization techniques are further elaborated in section 1.2.2.

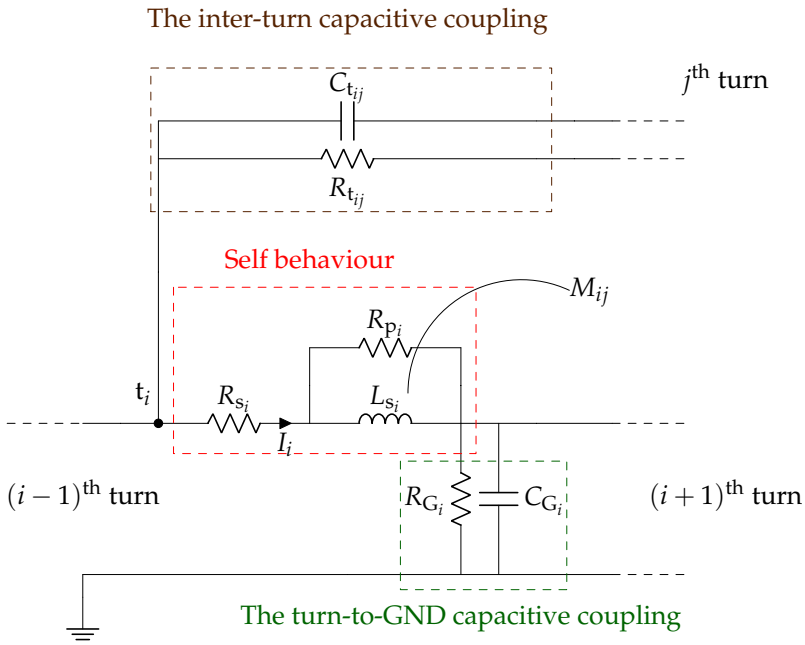

FIGURE 1.7: A lumped parameter model of a winding turn of the studied electrical machine [17].

1.2.1 The adopted topology of the winding of electrical machines

As previously stated, the proposed phenomenological LPM by Mihaila [34] is chosen to be our basis model. It allows to emulate the different electromagnetic phenomena on a turn level while maintaining the different couplings (both capacitive and inductive) between turns. Hence, it provides a straightforward access to the inter-turn voltage distribution within the windings. The model of the entire winding of the studied electrical machine can be deduced by reproducing the elementary cell (see Fig 1.7) of a turn as many times as the number of turns and by respecting the arrangement of the winding.

An example of a three turns winding sample arrangement wounded on a magnetic tooth is presented in Fig. 1.8; it has the corresponding LPM depicted in Fig. 1.9. Each labelled node (t_1, t_2, and t_3) refers to the entry point of a turn (first, second and third, respectively) from which the voltages are computed using the chosen circuit simulator. The mutual inductive coupling, although not represented for readability purposes, was also taken into account. Taking as an example the second turn, its inductive coupling with the remaining turns is accounted for using the following mutual inductances M_{ij}: M_{21} and M_{23}, where the subscript "i" refers to the turn in question (the second), whereas "j" refers to the remaining turns.

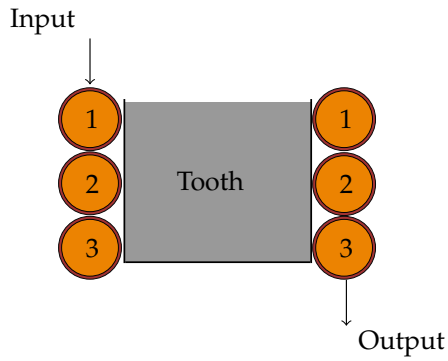

FIGURE 1.8: An example of a three turns winding arrangement placed on a magnetic tooth.

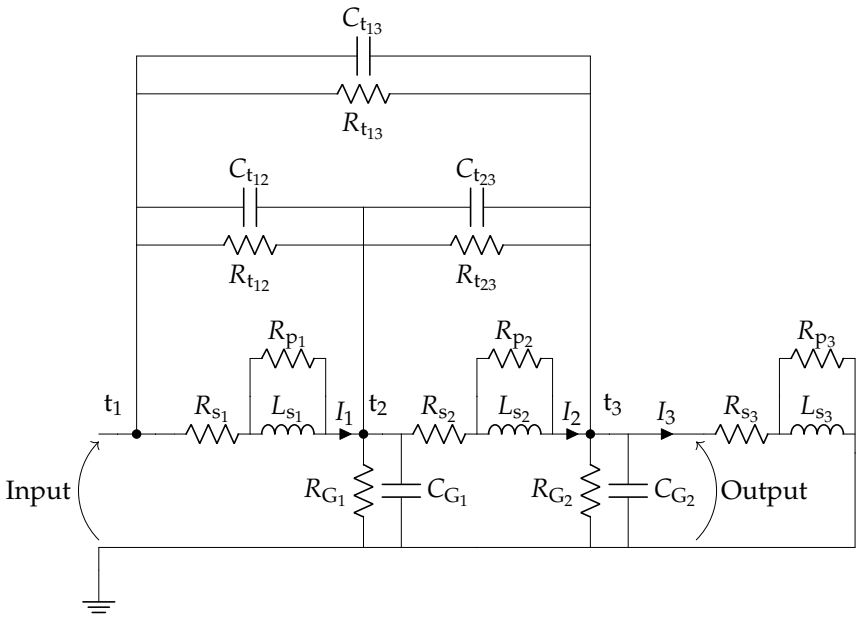

FIGURE 1.9: The corresponding lumped parameter model of the three turns winding seen in Fig. 1.8.

Although Mihaila has only taken into account the capacitive coupling between adjacent turns, for this small case study, we have represented all couplings. In the case of the absence of the magnetic core, the three turns winding model becomes the circuit seen in Fig. 1.10.

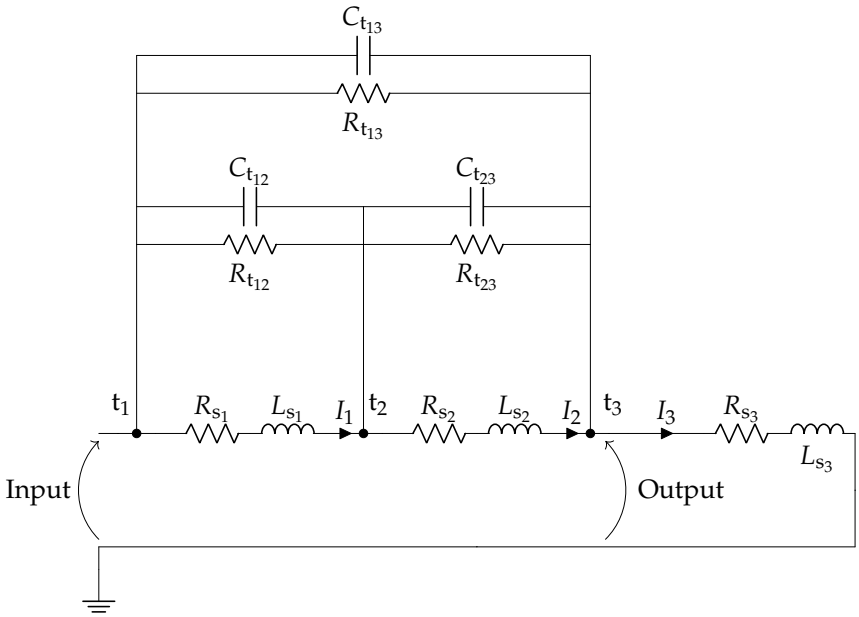

FIGURE 1.10: The corresponding lumped parameter model of the three turns winding seen in Fig. 1.8 when no magnetic core is inserted.

For an accurate prediction of the inter-turn voltage distribution, a precise computation of the values of the electrical parameters defining the chosen model is necessary. In the next section, we will study the different parametrization techniques and compare those previously proposed for the adopted LPM [17], [55].

1.2.2 Parametrization of the adopted topology

An accurate modelling of the electrical machine windings depends on the values given to its electrical model parameters: R_{s_i}, L_{s_i}, M_{ij}, $C_{t_{ij}}$, C_{G_i}, $R_{t_{ij}}$, R_{G_i}, and, R_{p_i}. These electrical parameters could either be determined analytically [55], [92], [93], deduced from measurements [94]–[96], or, computed using numerical methods [17], [97] as described in Fig. 1.11.

Although useful when solving engineering problems, the analytical parameter determination technique relies on mathematical models based on a number of assumptions that may not be valid or accurate enough to be fully representative of the studied system. This eventually reduces its range of validity because of the large number of the required presuppositions. Moreover, it is most of the time defined for a given geometry, having therefore a lack of generality.

On the other hand, deducing the values of the electrical parameters from measurements may result in a reduced accuracy due to the fact that the performed measurements can be affected by numerous factors such as the noise, instrument resolution and measurements errors, among others. Additionally, since the objective of this work is to predict the inter-turn voltage distribution before (or during) the design phase of the machine, this method is cast aside.

On the contrary, using numerical methods to determine by inspection the values of the electrical parameters defining the model, allows for a prediction of their values even for complex geometries. There is a variety of numerical methods that can be used to study electromagnetic problems: FEM, FDM, MoM, Boundary Element Method (BEM) and Finite Volume Method (FVM) [98]–[100], the choice of the appropriate numerical method to use depends on the complexity of the studied problem, the required accuracy, programming ease and simulation time amongst others. The comparison of these numerical methods is detailed in [98], [101], [102].

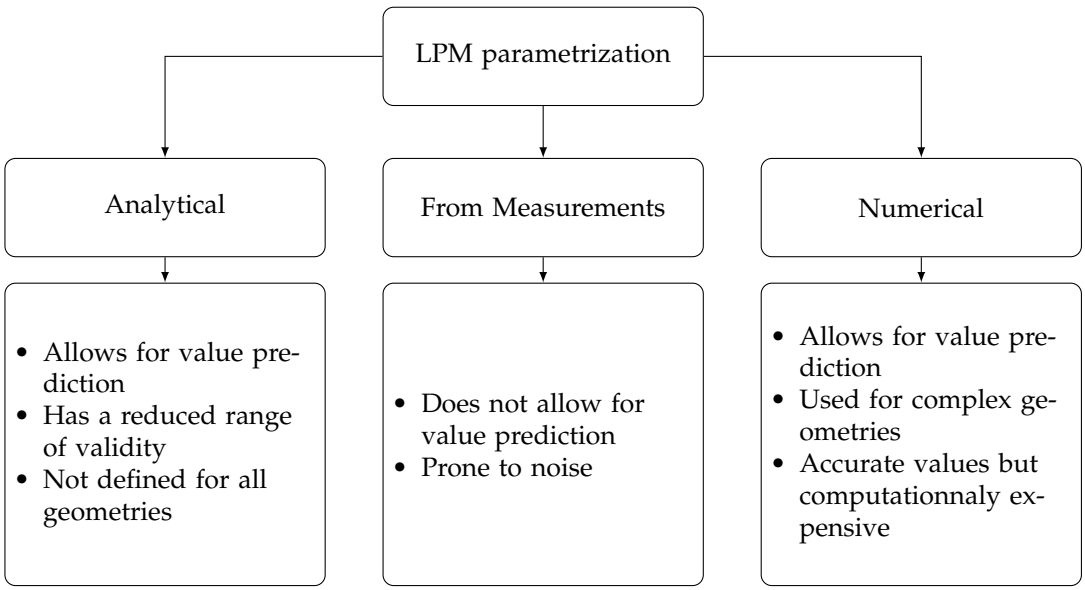

FIGURE 1.11: The lumped parameter model parametrization techniques.

Evaluating the strengths and weaknesses of each parameter determination method discussed herein, numerical methods are far ahead of its competitors, in particular FEM because it allows for taking into account all the occurring phenomena with no simplifying hypotheses whatsoever [17]. In addition, it also takes into consideration the studied geometry of the conductors and most importantly, permits the establishment of a predictive model.

Now that the basis circuit model to build from has been chosen and the context appropriate parametrization technique selected, a comparison of the parametrization technique proposed by Mihaila [55] and the parametrization improvements made by Toudji [17] is performed.

Mihaila [55] neglected proximity effect, thus the series turn resistance, in his work, only modelled skin effects whose value was computed analytically at 20 MHz using the following expression:

$$R = \frac{\rho l}{\pi \left(r^2 - (r-\delta)^2\right)}, \tag{1.1}$$

with r, ρ, l, μ, σ being the radius of the conductor, the electric resistivity of the used conductive material (in $\Omega\,\mathrm{m}$), the length of the wire (in m), the magnetic permeability (in $\mathrm{H\,m^{-1}}$) and, the electric conductivity of the used material (in $\mathrm{S\,m^{-1}}$), respectively. Here, δ is the skin depth mathematically defined as follows,

$$\delta = \frac{1}{\sqrt{\pi \mu \sigma f}}, \tag{1.2}$$

and represents the depth at which the current density has decreased up to 37 % of its value. The skin depth value decreases with the increase of the frequency f (in Hz) implying thus an increase of the values of the resistance R and is sketched in Fig. 1.12.

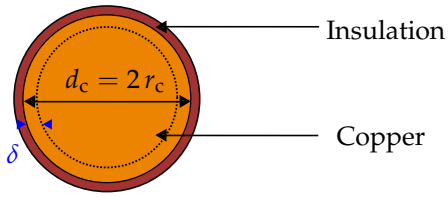

FIGURE 1.12: The geometrical definition of the skin depth.

Concerning the capacitive couplings, only those of adjacent turns were taken into account and their values were considered constant for all turns, even though they vary according to frequency, the position of the turn as well as to the geometry of the slot. This simplifying hypothesis was justified by the fact that their variation is negligible given the similar geometry of the turns. The same approach has been adopted for the capacitive coupling to the GND: only that of the turns located close to the slots was considered. Both capacitive couplings, inter-turns and turn to GND were computed using FEM at DC. However, the resistors modelling the dielectric losses, R_{G_i} and $R_{t_{ij}}$, were measured at 20 MHz.

The self inductances, on the other hand, were also computed at 20 MHz using FEM, whereas the mutual inductances were computed analytically as follows:

$$M_{ij} = k\sqrt{L_{s_i} L_{s_j}}, \tag{1.3}$$

where k, L_{s_i} and L_{s_j} are the mutual coupling coefficient (its value does not exceed 1 and depends on the spacing between turns) and the self inductances of the i^{th} turn and the j^{th} turn, respectively. The value of the coupling coefficient k was considered constant and equal to 0.9. Its value was computed by averaging a set of values obtained experimentally.

Given the different simplifying hypotheses performed by Mihaila during the parametrization process of the model, Toudji in [17] stepped in to improve the model by providing a more accurate technique of computing the values of its parameters. He used FEM to compute L_{s_i} and M_{ij} by taking into account the flux penetration, R_{s_i} by taking into account both skin effect at the resonance frequency of the machine f_{res} using a magneto-dynamic FEM simulation. The different capacitive couplings were accounted for no matter the adjacency or not of the turns and were not given the same value. The capacitances $C_{t_{ij}}$ and, C_{G_i} were computed in an electrostatic FEM simulation, whereas the values of the resistances R_{G_i} and $R_{t_{ij}}$ were fixed to 800 kΩ and 40 kΩ, respectively.

Since this is a predictive study, Toudji in [17] estimated the resonance frequency of the machine f_{res} by computing the parameters of the model at 50 Hz, automatically generating the netlist [1] corresponding to the arrangement of the studied machine, running it in the frequency domain and extracting its value. It has been highlighted that only one iteration is enough for an accurate prediction of f_{res}. The parameters are then recomputed at f_{res} and the new netlist automatically generated and simulated in transient analysis, enabling the extraction of the inter-turn voltage distribution. This is summarized in Fig. 1.13.

[1] A file describing the connectivity of a given electronic circuit.

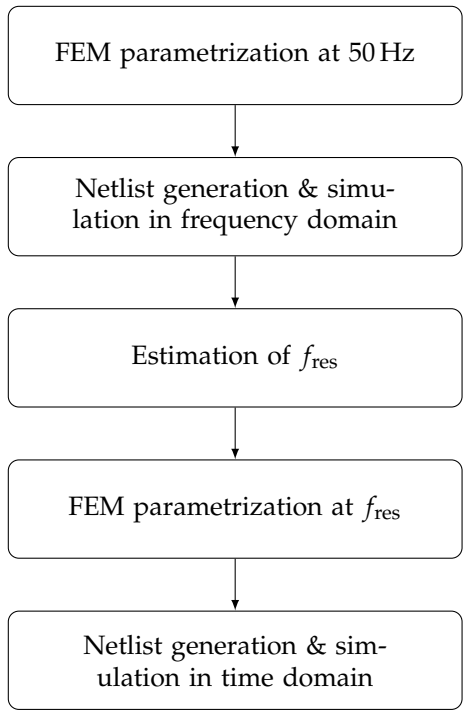

FIGURE 1.13: Flowchart of the model parametrization technique proposed by Toudji in [17].

In [17], it has been shown that only one iteration was sufficient to estimate the values of f_{res}. Also, it is worth mentioning that for the frequency domain validation of the model in [17], the low frequency netlist generated during the first iteration was the one chosen, whereas in time domain the second netlist whose parameters are computed at f_{res} is selected.

The two previously proposed model parametrization techniques are summarized in Tab. 1.1.

TABLE 1.1: Comparison of the lumped parameter model parametrization methods proposed by previous research works [17], [34].

Electrical parameter	Mihaila parametrization [34]	Toudji parametrization [17]
R_{s_i}	Analytically (1.1) at 20 MHz	FEM at 50 Hz and f_{res}
L_{s_i}	FEM at 20 MHz	FEM at 50 Hz and f_{res}
M_{ij}	Analytically (1.3)	FEM at 50 Hz and f_{res}
C_{G_i} & $C_{t_{ij}}$	FEM	FEM at DC
R_{G_i} & $R_{t_{ij}}$	Measurements at 20 MHz	Fixed values: 800 kΩ & 40 kΩ

The comparison of the two model parametrization approaches (*i.e.* the one followed by Mihaila and that followed by Toudji) on a case study (a 56 turns electrical winding) is presented in

Fig. 1.14. An improvement is noticed for the latter where we notice that the shift has been improved as well as the maximum voltage attained.

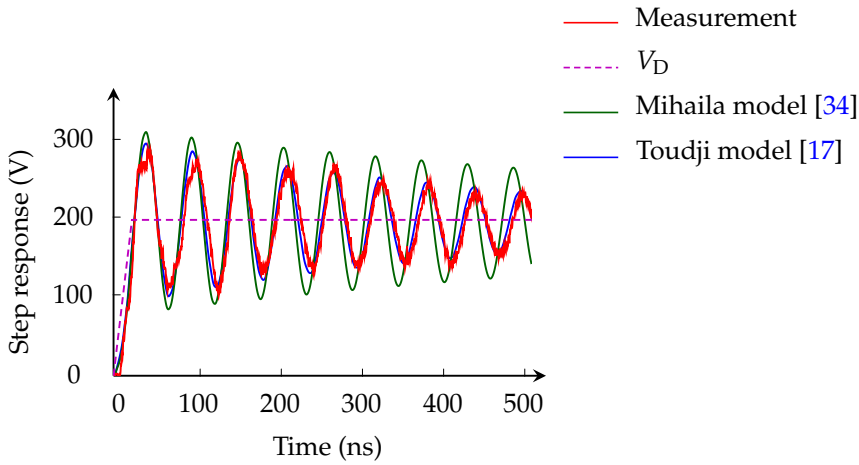

FIGURE 1.14: Comparison of the measured and simulated input voltages of a 56 turn winding electrical machine. *Data extracted from* [17].

Thus, a better prediction of the whereabouts of the PD depends on an accurate determination of the values of the model parameters. Besides, the shift noticed between the measurements and the computed input voltage is due to the frequency dependent behaviour of these parameters that was not accounted for. The limitation of the parametrization technique proposed by Toudji [17] is expanded upon in the coming section.

1.2.3 Limitation of the previous model

Previous research works have determined the values of the parameters at a given frequency, regardless of their frequency dependent behaviour. This was done because the simulation was run in time domain (a transient analysis), so a value had to be assigned, and that at the resonance frequency f_{res} proved to give the most precise results [17]. Had it been a sinusoidal input voltage, a computation of the parameters values at the frequency of the input signal would have been enough to accurately predict the inter-turn voltage distribution. Nonetheless, for this research work the electrical machine is subject to a Pulse Width Modulation (PWM) input voltage as depicted in Fig. 1.1. Given the non-instantaneous nature of the real-life commutations, the chopped input voltage is defined as a trapezoidal waveform in time domain as seen in Fig. 1.15.

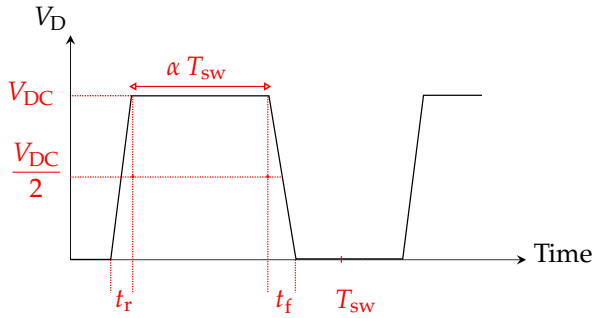

FIGURE 1.15: Parametrization of the trapezoidal waveform of the imposed input voltage.

The parameters t_r, t_f, f_{sw}, T_{sw}, α and, V_{DC} are the rise & the fall times of the voltage across the transistor, the switching frequency, the switching period of the transistor, the duty cycle and, the DC input voltage, respectively.

The spectrum of the trapezoidal waveform is depicted in Fig. 1.16 where t_f=t_r, and expands from DC (not mentioned in the figure because of the logarithmic scale) to high frequencies.

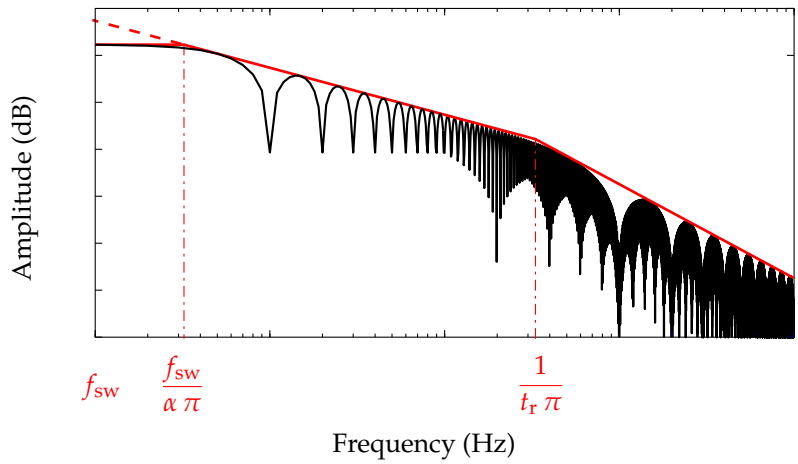

FIGURE 1.16: The spectrum of the input voltage seen in Fig. 1.15 for when t_f=t_r.

From a frequency value of $\frac{f_{sw}}{\pi\ \alpha}$ up to a frequency value of $\frac{1}{\pi\ t_r}$ the spectrum follows a -20 dB per decade slope; then it changes to a -40 dB per decade slope.

Given the harmonically rich input voltage, the response of the windings to each and every one of the harmonics has to be considered for an accurate modelling. This work aims at improving the already existing model so as to enable the prediction, with a better precision, of the inter-turn voltage distribution within the winding of electrical machines to eventually, better locate the possible whereabouts of PD during the design process of the machine.

To put things into perspective, the diagnostic tool to be improved ought to take into account the frequency dependent behaviour of the different resistive, capacitive and, inductive couplings occurring within the winding since the input voltage (as seen in Fig. 1.15) has a wide range spectrum as is depicted in Fig. 1.16. That is, the response of the studied system, in this case the

input cable and the electrical machine, to each harmonic of the spectrum of the input voltage has to be considered in frequency domain and accounted for in time domain.

With this in mind, the following section will exhibit the different frequency behaviours of the considered electrical parameters defining the adopted phenomenological LPM.

1.3 Frequency dependent behaviour of the model parameters

To take into account the frequency dependent behaviour of the parameters of the model, we need to first elaborate on the behaviour of each one of them. This section will discuss the evolution of the electrical parameters of the adopted model according to frequency, starting from the ohmic losses resistance to the inductances, both self and mutual, to the dielectric losses and finally, the iron losses.

1.3.1 The ohmic losses resistance

In a DC circuit and for a given temperature, the current is uniformly distributed on the cross-sectional area of the conductors. Yet, for alternating currents the current is no longer uniformly distributed in the surface of the conductors. This is due to the occurring skin and proximity effects [103], [104].

The former, *i.e.* skin effect, takes place because the applied AC magnetic field induces, within the conductor, an opposing electric field, which ends up confining the current distribution on the "skin" of the conductor at what is called skin depth. The analytic expression of the latter was presented in (1.2). Therefore, a frequency increase results in an increase of the effective resistance of the conductor, which eventually leads to a significant power loss for high frequency applications. The frequency dependent behaviour of the skin effect has been computed analytically using (1.1) by Mihaila and is plotted in Fig. 1.17, where a difference is noticed between the computation and the measured resistance. This is due to proximity effect.

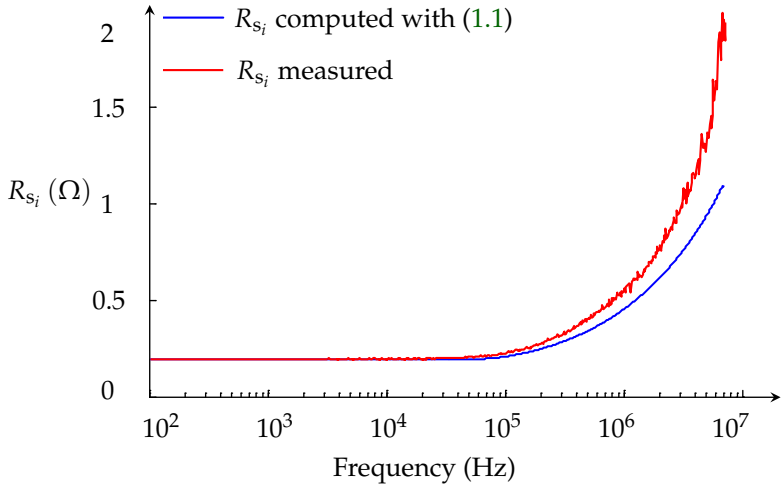

FIGURE 1.17: The frequency dependent behaviour of the ohmic losses resistance of a four turns winding. *Data extracted from [34].*

Proximity effect, is the second phenomenon that takes place when working with alternating currents. It refers to the impact a magnetic field of one conductor has on the neighbouring

conductors by inducing an opposing electric field on them. This implies an uneven current distribution within the conductors, further increasing the effective resistances of the studied system, and more power loss. Thus, proximity effect is also to be taken into account when working with alternating currents. This is illustrated in Fig. 1.17, where we notice a difference at high-frequencies between the values of the resistance computed using (1.1) and the measurements of a four turns winding [34].

It is worth mentioning that not appropriately accounting for ohmic losses underestimates the propagation delay as it has been elaborated in [105], which further highlights the objective of this research work.

1.3.2 The self and mutual inductances

The self inductance represents the magnetic flux energy created when a current flows through the inductor (or turn) in question. For this work, the magnetic behaviour of each turn is accounted for separately as depicted in Fig. 1.9.

When the winding of the electrical machine is placed on a magnetic core, used to canalize the magnetic flux ϕ, the value of the inductance is significantly impacted [106]. For power frequencies, the value of the inductance is notably high because of the good flux channelling the magnetic material guarantees, the inductance L_{s_i} being proportional to the circulating magnetic flux ϕ. However, for very high frequencies, no flux penetrates the magnetic circuit because of the increase of the losses and thus the magnetic circuit no longer contributes to the value of the inductance [80], [107]. The magnetic core, *i.e.* steel laminations, starts to behave as a flux barrier, hence, most of the produced flux is only leakage flux. Inductance measurements have been carried out by Toudji [17] as presented in Fig. 1.18, where a difference in values is seen for when the inductor is placed on a magnetic material and when it is not.

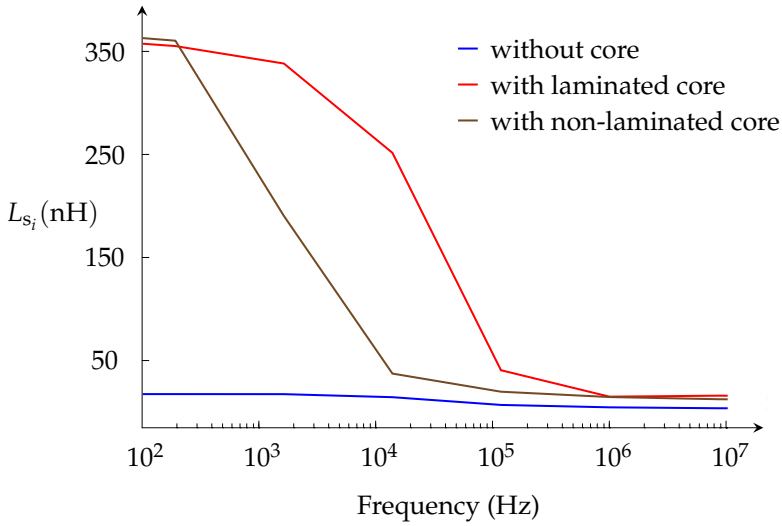

FIGURE 1.18: A comparison of the frequency dependent behaviour of the self inductance of the first turn of a six turns winding when placed on a magnetic material, laminated or not, and when no magnetic material is inserted. *Data extracted from* [17].

For a non-laminated core, the impact of eddy currents, which are the prevalent source of losses [108], is noticeable when comparing the values of the inductances measured with a non-laminated and a laminated core. The latter helps in reducing eddy currents.

Concerning the mutual inductance, it describes the magnetic influence a circuit has on a neighbouring ones. For this work, it refers to the magnetic impact each turn has on the remaining turns of the winding of the electrical machine. A variation in the current of a turn induces a voltage in the neighbouring turns. The value of the mutual inductance also varies with frequency. Toudji also measured the mutual inductance between the first and third turns for a sample winding. Its variation according to frequency is plotted in Fig. 1.19 and follows that of the self inductance.

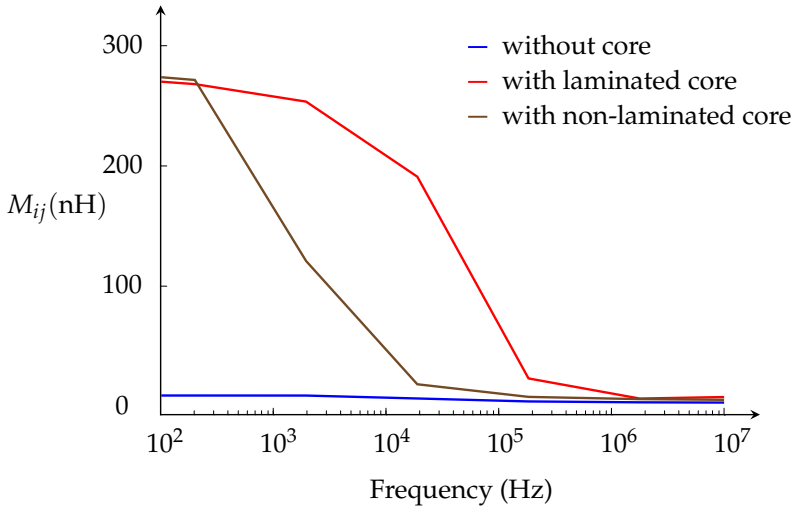

FIGURE 1.19: A comparison of the frequency dependent behaviour of the mutual inductance between the first and third turn of a six turns machine when placed on a magnetic material, laminated or not, and when no magnetic material is inserted. *Data extracted from [17]*

1.3.3 The iron losses resistance

Iron losses, also referred to as core losses, are from a physical perspective based on ohmic heating [109] since relaxation losses, which are due to the spin, are negligible below the MHz range. When an external magnetic field $\mathbf{h}$ is applied on a magnetic material, the magnetization changes which in turn creates heating. Once the applied magnetic field $\mathbf{h}$ equates a value of $\mathbf{h_{sat}}$, the saturation is reached, and thus no matter how much we further increase $\mathbf{h}$, the magnetic induction $\mathbf{b_{sat}}$ remains intact. This is depicted in the ($\mathbf{b}$,$\mathbf{h}$) curve presented in Fig. 1.20.

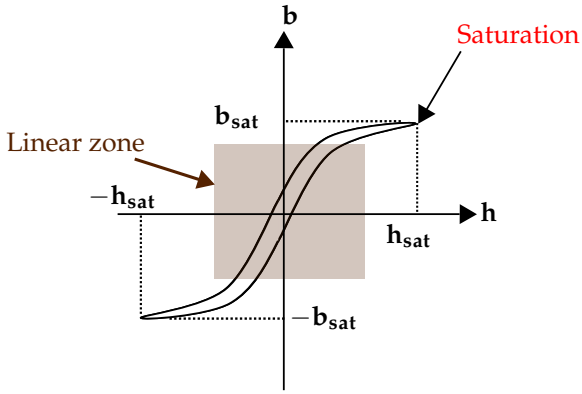

FIGURE 1.20: Example of the (**b**,**h**) curve.

This change in the magnetization causes hysteresis and eddy currents losses which can be emulated with different models of different levels of accuracies and can be grouped in two categories: Steinmetz equations (Modified Steinmetz Equation (MSE), Generalized Steinmetz Equation (GSE) and Natural Steinmetz Extension (NSE)) and mathematical hysteresis models (Loss Surface Model (LSM), viscosity-based magneto-dynamic model, energy-based vector hysteresis model or friction like hysteresis model).

It should be mentioned that the classical Steinmetz equation is only correct for sinusoidal flux densities. It also presents the inconvenience of its frequency dependent coefficients. Thus, a difficulty emerges in finding the most suitable set of coefficients for a frequency range modelling of the iron losses, hence the different modifications (MSE, GSE and NSE) developed in order to extend its validity for non-sinusoidal waveforms as well. For a comprehensive analysis of these models, it is helpful to refer to [110].

The different Steinmetz equations certainly offer a fast and simple prediction of the iron losses where their coefficients could be either specified by the manufacturer or computed by curve fitting the data of the manufacturer. Nevertheless, they present the inconvenience of having frequency dependent coefficients which reduces their accuracy.

The hysteresis loss models, on the other hand, need a more profound knowledge of the used material, either through prior measurements or from already available data. Moreover, they present a difficulty when willing to integrate them in FEM software unlike the Steinmetz equations, which can easily be integrated in the latter. To take into account the iron losses, Mihaila used a resistance R_{p_i} placed in parallel with the self inductance L_{s_i}.

1.3.4 The dielectric losses parameters

Dielectric materials, in real applications, are not perfect, hence the presence of dielectric losses [111]. This justifies the emergence of a resistive behaviour ($R_{\mathrm{t}_{ij}}$ and R_{G_i} seen in Fig. 1.7) within a capacitive one. The electric properties of dielectric materials are described in terms of their dielectric permittivity [97], which has paved the way to introduce the definition of the complex dielectric permittivity [112] as in:

$$\bar{\varepsilon}_{\mathrm{r}} = \varepsilon'_{\mathrm{r}} - j\varepsilon''_{\mathrm{r}}, \tag{1.4}$$

where $\bar{\varepsilon}_{\mathrm{r}}$, $\varepsilon'_{\mathrm{r}}$, and, $\varepsilon''_{\mathrm{r}}$ refer to the complex relative permittivity, the real part of $\bar{\varepsilon}_{\mathrm{r}}$ representing the stored electric energy, and, the imaginary part of $\bar{\varepsilon}_{\mathrm{r}}$ representing the occurring dielectric losses, respectively [17], [113].

In electrical machines, the dielectric materials used as an insulation to the turns, lead to the emergence of capacitive couplings within it because of the presence of the copper, *i.e.* a conductive material as seen in Fig. 1.21a. The classical arrangement of the EIS used in electrical machines is Polyester-Imide (PEI) with Polyamide-Imide (PAI) on top.

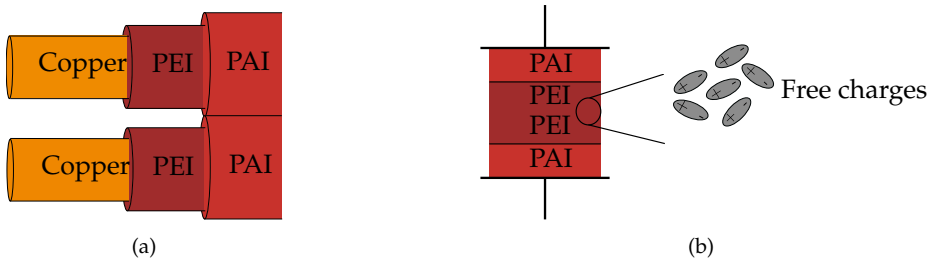

FIGURE 1.21: (a) A figure portraying the turn-to-turn capacitive coupling occurring within the winding of the electrical machine. (b) A parallel plate capacitor modelling of the inter-turn capacitive coupling.

As an illustration, a parallel plate capacitor is used as in Fig. 1.21b.

Considering the complex dielectric permittivity, its capacitance becomes (when using the parallel plate capacitor approximation for illustration):

$$\overline{C}_{\text{pp}} = \frac{\varepsilon_0 \overline{\varepsilon}_{\text{r}} S}{e} = \frac{\varepsilon_0 \left(\varepsilon'_{\text{r}} - j\varepsilon''_{\text{r}}\right) S}{e}, \tag{1.5}$$

where S is the surface of the conductive plate and e the thickness of the insulation. Therefore, its admittance writes:

$$\overline{Y}_{\text{C}_{\text{pp}}} = j\overline{C}_{\text{pp}}\omega. \tag{1.6}$$

Equation (1.6) is what we model in our work with $R//C$ for both the turn-to-turn and turn-to-ground capacitive coupling as seen in Fig. 1.7. The equivalent admittance of the defined model is equal to the impedance $\overline{Y}_{\text{C}_{\text{pp}}}$. This allows to write the following:

$$\begin{aligned} \overline{Y}_{\text{C}_{\text{pp}}} =& j\overline{C}_{\text{pp}}\omega \\ =& \frac{j\varepsilon_0 \left(\varepsilon'_{\text{r}} - j\varepsilon''_{\text{r}}\right) S\omega}{e} \\ =& \frac{1}{R} + jC\omega. \end{aligned} \tag{1.7}$$

By identification, we get the following expressions of both R and C:

$$\begin{cases} R = \dfrac{e}{S\varepsilon_0\varepsilon''_{\text{r}}\omega} \\ C = \dfrac{S\varepsilon_0\varepsilon'_{\text{r}}}{e}. \end{cases} \tag{1.8}$$

This shows the link between the real and imaginary parts of the complex permittivity, and the capacitive coupling. The higher the real part of $\overline{\varepsilon}_{\text{r}}$ the higher the value of the capacitance. Whereas the more dielectric losses, the lesser the resistive coupling there is between turns.

Once the EIS is subject to an external electric field, molecular events occur. The latter are caused by the movement of charges and dipole orientation referred to as the inducted polarization[2] [114] discovered by Michael Faraday in 1837. The dipole density rises with different polarization mechanisms thoroughly detailed in [115]. However, when the frequency of the applied external electric field increases, the polarization faces a difficulty in following its variation, increasing therefore the dielectric losses that is followed by a decrease in the stored electric energy. As a matter of fact, the loss factor reaches its peak at what is called the relaxation frequency f_r, and could be modelled with a Debye model [116], [117]. The latter will be viewed in section. 1.4.3.

An example of the frequency dependent behaviour of the real and imaginary parts of the complex dielectric permittivity $\bar{\varepsilon}_r$ using a Debye model is portrayed in Fig. 1.22. The values we chose for this example are: a relaxation frequency of $f_r = 0.4\,\mathrm{MHz}$, a static permittivity of $\varepsilon_s = 4\,\varepsilon_0\,\mathrm{F\,m^{-1}}$ and a relative dielectric permittivity at optical frequencies of $\varepsilon_{inf} = 1.1\varepsilon_0\,\mathrm{F\,m^{-1}}$.

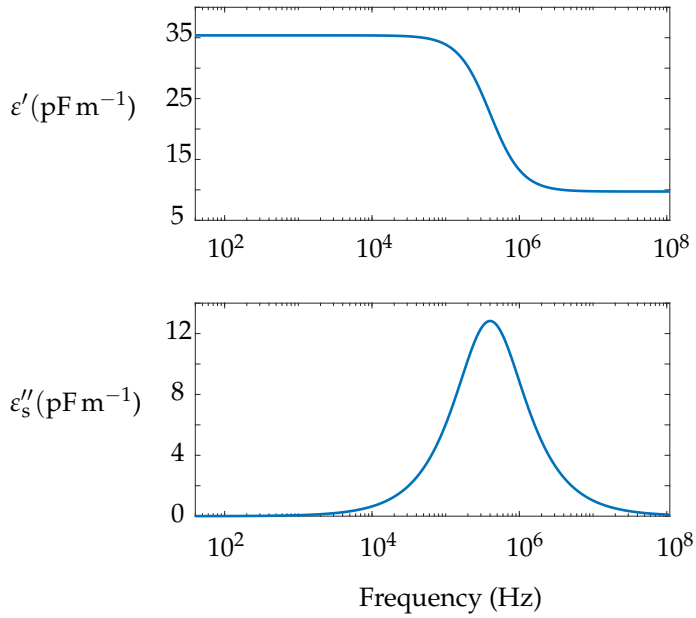

FIGURE 1.22: An example of the frequency dependent behaviour of the complex dielectric permittivity.

Moreover, the electric properties of the dielectric materials also vary according to the temperature [113], and could be modelled using Arrhenius model. For this study, it is the frequency dependent behaviour of the dielectric properties of both PEI and PAI that are of interest. In [118], Loubeau experimentally studied the variation of ε'_r and ε''_r of PEI according to frequency and temperature. Whereas Diaham studied that of PAI in [113] which both seemed to follow the Debye model variation.

In order to investigate the frequency behaviour of the capacitive coupling, a dielectric permittivity measurement technique was studied, performed and presented in the next chapter.

[2]It defines the capacity of the poles to move when an external electric field is applied

With the different frequency dependencies now in mind, justifying the purpose of this research work, we present the different techniques elaborated in the literature that account for them in both frequency domain and time domain.

1.4 Accounting for the frequency dependent behaviour

The aim of this research is to take into account the frequency dependent behaviour of the parameters of the model (see Fig 1.7) in both frequency and time domain simulations for a better prediction of the inter-turn voltage distribution within the winding of the to-be-designed electrical machine. This will eventually allow a better prediction of the possible whereabouts of the PD, to mitigate the possibility of them prematurely damaging the winding of the machine. In fact, the electrical machine responds differently for each harmonic of the input voltage, *i.e.* for each harmonic, the system (the power cable and the machine) has a different value of the impedance because of the frequency dependency of the parameters of the adopted phenomenological LPM.

The first straightforward idea that comes to mind when willing to take into account the frequency dependencies of these different parameters is to compute the values of model electrical elements at different frequencies, then apply an Inverse Fourrier Transform (IFT). This will yield the different time domain functions $R(t)$, $L(t)$ and $C(t)$. However, the convolution is time consuming with quadratic runtime cost [119], and is very much CPU demanding because of the many time steps the simulation requires [120]. Different research works have dealt with the matter using several approaches: they either apply numerical methods, in this instance recursive convolution on functions with known/existing IFT and the Finite Difference Time Domain (FDTD) technique, or passive electrical networks that reproduce the same electrical behaviour as the system under study (LPM used in the systemic approach).

These techniques are discussed in the ensuing sections.

1.4.1 Numerical methods

Convolution methods are time consuming, which makes them computationally prohibitive. In [121], an analytical method equivalent to convolution is presented. The author observed that most step responses considered are approximated by either an exponential function or a sum thereof, enabling thus a recursive convolution as a much more efficient implementation. That is, if the convolution integral $s(t)$ is of an exponential form at time step t, its value can be easily and directly deduced from its value at the previous time step $s(t - \Delta t)$. In [122], a model of a high frequency transformer that accounts for the occurring high frequency phenomena was presented. FEM was used to compute the values of the resistances by taking into account skin and proximity effects as well as core losses. The scatter plot are later on approximated in frequency domain with a set of functions of known/existing IFT. Then convolution integrals are applied. The numerical results were compared with the measurements, and a good agreement has been achieved. In [123], the same approach as the previously mentioned one has been followed, aiming to improve it by including the frequency dependent behaviour of the inductance as well in the model. The dielectric losses were not considered. The deduced time

domain expressions are the following:

$$\begin{cases} l(t) = d_L \cdot \delta(t) + \sum_{k=1}^{n_\mathrm{p}} a_{L,k} e^{-b_{L,k} \cdot |t|}, \\ r(t) = d_R \cdot \delta(t) + \sum_{k=1}^{n_\mathrm{p}} a_{L,k} \delta(t) - \dfrac{a_{R,k} \cdot b_{R,k}}{2} e^{-b_{R,k} \cdot |t|}, \end{cases} \tag{1.9}$$

where δ(t), $l(t)$, $r(t)$, n_p, $a_{L,k}$, $b_{L,k}$, $a_{R,k}$, $b_{R,k}$, d_L and, d_R are the Dirac impulse, the inductance per second, the resistance per second, the number of fitting parameters a and b with the corresponding subscript linking them to the fitted functions $L(f)$ and $R(f)$ respectively. The computation of the convolution integrals when applying the IFT was performed using trapezoidal integration rule—which proved to be faster than Runge-Kutta—for a better efficiency, combined with a Backward Euler rule, to eliminate possible numerical oscillations due to the sudden variation in the state of the non-linear element of the circuit. The method proved to be very efficient since it only takes $O(n)$ operations compared to the conventional convolution which is of $O(n^2)$ operation [107]. Nevertheless, numerically evaluating convolution integrals may require very high computational effort and lead to numerical stability problems.

In reference [124], a different method was applied to take into account the frequency dependent behaviour of the TLM parameters: the FDTD method. The method consists in discretizing Maxwell's equations in both time domain and frequency domain. Also, boundary conditions are imposed because of the discretization of the computational domain. The capacitive coupling was assumed frequency-independent for this study, whereas the frequency dependent behaviour of the series impedance was taken into account using the VF algorithm, which will be elaborated in the subsequent section. The author rewrites the telegraph equations [125] in Laplace domain expressed as follows:

$$\begin{cases} \dfrac{\partial \mathbf{I}(x,s)}{\partial x} + \mathbf{Y}(s)\,\mathbf{V}(x,s) = 0, \\ \dfrac{\partial \mathbf{V}(x,s)}{\partial x} + \mathbf{Z}(s)\,\mathbf{I}(x,s) = 0, \end{cases} \tag{1.10}$$

where $\mathbf{V}(x,s)$, $\mathbf{I}(x,s)$, $\mathbf{Y}$, $\mathbf{Z}$ are the vector of the line voltages, the vector of line currents, the matrix representing the shunt admittance and the matrix representing the series impedance, respectively. The latter matrices are defined as follows:

$$\begin{cases} \mathbf{Y}(s) = \mathbf{G} + s\,\mathbf{C}, \\ \mathbf{Z}(s) = \mathbf{R} + s\,\mathbf{L} + \mathbf{Z}'(s). \end{cases} \tag{1.11}$$

In (1.11), $\mathbf{G}$ and $\mathbf{C}$ are the frequency-independent conductance and capacitance defined per-unit-length. Whereas $\mathbf{Z}'(s)$ refers to the frequency dependent behaviour of the series impedance $\mathbf{Z}$ and is deduced using a VF algorithm. The same applies for the values of $\mathbf{R}$ and $\mathbf{L}$.

Then, the system (1.10) is rewritten in time domain to eventually become (1.12):

$$\begin{cases} \dfrac{\partial I(x,t)}{\partial x} + C\dfrac{\partial V(x,t)}{\partial t} + GV(x,t) = 0, \\ \dfrac{\partial V(x,t)}{\partial x} + L\dfrac{\partial I(x,t)}{\partial t} + RI(x,t) + Z'(t) * I(x,t) = 0, \\ \mathbf{Z}'(s) = \displaystyle\sum_{i=1}^{n_\mathrm{p}} \frac{c_i}{s - a_i}, \end{cases} \tag{1.12}$$

where n_p refers to the number of poles a_i used when applying the VF algorithm, with their corresponding residues c_i.

The originality resides in the fact that the convolution to be computed was modified to ease the computations; instead of computing the convolution product as is, the authors chose to compute the convolution of this frequency domain expression:

$$\mathbf{Z}'(s)\,\mathbf{I}(x,s) = \frac{\mathbf{Z}'(s)}{s}\,.s\,\mathbf{I}(x,s). \tag{1.13}$$

Combining both FDTD and recursive convolution integral, which is made possible by the exponential approximation, helps to compute the convolution effectively by only storing the last three previous values of the current. The deduced two-port model is presented in Fig 1.23.

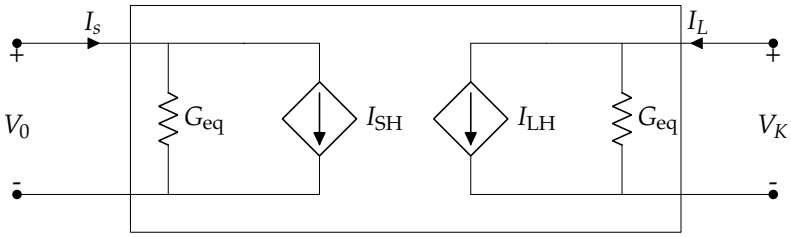

FIGURE 1.23: The model used for the studied transmission line in EMTP in [124].

The FDTD is called by the circuit simulator at each time step to update the values of the currents and voltages.

Although, recursive convolution and FDTD present better alternatives to IFT they have their limitations. Recursive convolution is sensitive to the round-off errors which can still eventually lead to numerical instability. This may result in inaccuracy or even divergence of the results. The FDTD, on the other hand, is the best suited for low frequency simulations [126].

In the next section, the different circuit models applied to account for the frequency dependency of the model parameters in both frequency and time domains are touched upon.

1.4.2 Frequency dependent network equivalent

Another technique that is not as computationally costly[3] [127] as the previously presented numerical solutions, is the use of electrical equivalent circuits [120]. For instance, in [128], which also studies a transformer, an equivalent circuit that takes into account the high frequency phenomena and that could be used in any circuit simulator was presented. As an initial point, homogenization is used by replacing each layer of the wires by an equivalent conductive plate

[3]Depends on the order of the network.

whose impedance depends on the properties of the material: complex permeability $\overline{\mu}$ and permittivity $\overline{\varepsilon}_{\mathrm{r}}$. The impedance is later on fitted with a transfer function of the following expression:

$$r_{\mathrm{s_{DC}}} + j\,\omega\, l_{\mathrm{s_{DC}}} \prod_{i=1}^{K} \frac{1 + j\frac{f}{f_{\mathrm{c_{2i}}}}}{1 + j\frac{f}{f_{\mathrm{c_{2i-1}}}}}, \tag{1.14}$$

where K, $r_{\mathrm{s_{DC}}}$ and $l_{\mathrm{s_{DC}}}$ are the cell number, the DC resistance, and the DC inductance, respectively, whereas $f_{c_{2i}}$ is one of the cut-off frequencies, which are to be positioned accurately for good results. For a first cut-off frequency $f_{\mathrm{c_{2i-1}}}$, and when the modulus of the fitting function starts deviating and exceeds the already defined error margin, a new cut-off frequency is introduced $f_{\mathrm{c_{2i}}}$ to recover the deviation. Once the error starts increasing again, another pair of cut-off frequencies is introduced in the expression (1.14) and so on until the entire studied frequency range is covered. Then, an equivalent lumped parameter model of the form presented in Fig. 1.24—a Foster circuit—is associated to the fitting function where the inductane $L_{\mathrm{s_{HF}}}$ takes into consideration the stored energy in the air.

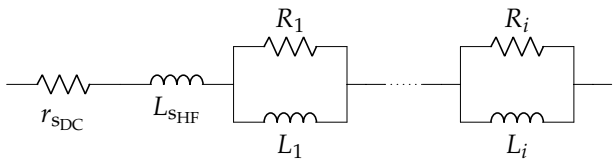

FIGURE 1.24: The equivalent lumped parameter model reproducing the same frequency dependent behaviour of the studied transformer used in [128].

The different expressions of the inductances L_i and resistances R_i are deduced as follows:

$$\begin{cases} L_i = l_{\mathrm{s_{DC}}} \left(1 - \dfrac{f_{c_{2i-1}}}{f_{c_{2i}}}\right) \displaystyle\prod_{n=1, n\neq i}^{K} \left(\dfrac{1 - \frac{f_{c_{2i-1}}}{f_{c_{2n}}}}{1 - \frac{f_{c_{2i-1}}}{f_{c_{2n-1}}}}\right), \\ R_i = \dfrac{L_i}{2\pi f_{c_i}}. \end{cases} \tag{1.15}$$

Several topologies are possible, but the chosen one allows the most direct identification of the used electrical parameters.

In reference [129], a multi-conductor TLM has been modelled using a closed-form model. The latter helped overcome the frequency/time simulation usually encountered and which is to be overcome as well for our research work. Starting from the telegraph system of equations (1.10), which describes the electrical behaviour of transmission lines, the authors chose to study the system in the Laplace domain and use the exponential functions that are approximated using rational closed-form Padé polynomial functions, which are linked with several recursive expressions and whose coefficient are known already and were computed analytically. As a matter of fact, the Padé function can be represented by a combination of sub-circuits formed in pole-zero poles enabling the representation of the multi-conductor transmission line as a set of sub-circuits as seen in Fig. 1.25.

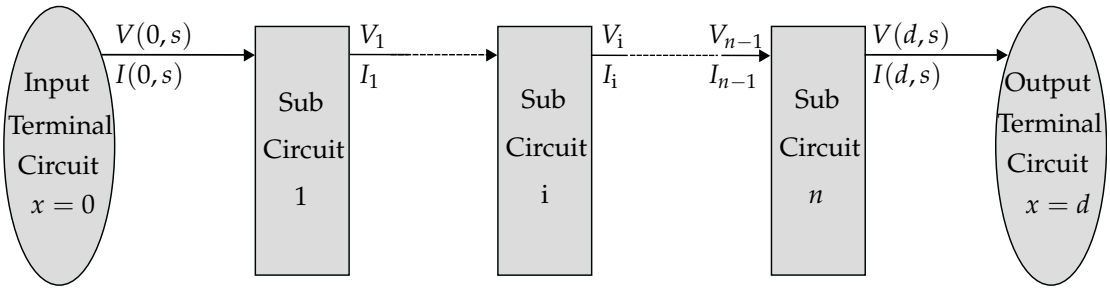

FIGURE 1.25: The representation of the studied TLM by the subsections of Padé model.

As a matter of fact, rational functions are widely used to approximate the behaviour of each parameter according to frequency, which are later on easily incorporated given the rational form of the model. In [130] the frequency dependent functions were fitted by rational functions and then expanded to fractions:

$$Z(s) = k_0 + \frac{k_1}{s + p_1} + \frac{k_2}{s + p_2} + \cdots + \frac{k_n}{s + p_n}. \tag{1.16}$$

Those partial fractions could easily be converted to equivalent RC components as in Fig. 1.26.

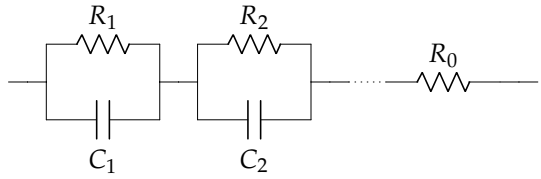

FIGURE 1.26: The equivalent electrical circuit reproducing the same frequency behaviour as the studied system used in [130].

The values of the electrical parameters are computed as follows:

$$\begin{cases} R_0 = k_0, \\ R_i = \dfrac{k_i}{p_i}, \\ C_i = \dfrac{1}{k_i}. \end{cases} \tag{1.17}$$

This method works well for smooth functions but not so well for functions with several peaks in their frequency responses [131]. To overcome this, another fitting technique (VF) may be used where the fractions could be translated to a set of time domain passive circuits. The conversion of the function into electrical circuit is elaborated hereinafter [132], where each branch is given as a rational function of the following expression:

$$y(s) = \sum_{m=1}^{n_p} \frac{c_m}{s - a_m} + d + se, \tag{1.18}$$

with c_m and a_m being the residue and its corresponding pole, in the order given, and d and e are real numbers [133]. The fitting order is referred to as n_{p}. This expression can be converted to the electrical network seen in Fig. 1.27.

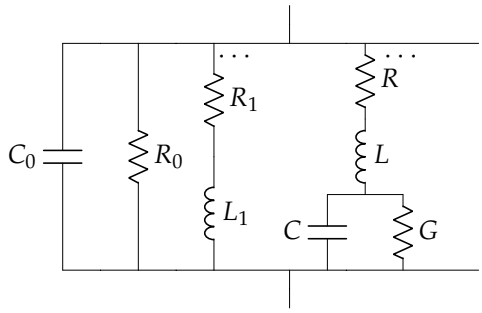

FIGURE 1.27: The corresponding vector fitting electrical network.

The values of the generated vector fitting electrical elements are deduced from the fitting parameters and are computed as follows:

$$\begin{cases} C_0 = e, \\ R_0 = \dfrac{1}{d}, \end{cases} \tag{1.19}$$

and the real poles could be represented by an $R_1 L_1$ branch of the following values:

$$\begin{cases} R_1 = -\dfrac{a}{c_m}, \\ L_1 = \dfrac{1}{c_m}. \end{cases} \tag{1.20}$$

For each complex conjugate pole defined by a real part a'_m and an imaginary part a''_m and its corresponding residue with c'_m and c''_m being its real and imaginary parts, respectively, expressed as:

$$\frac{c'_m + j\,c''_m}{s - (a'_m + j\,a''_m)} + \frac{c'_m - j\,c''_m}{s - (a'_m - j\,a''_m)} \tag{1.21}$$

they could be represented by an RLCG branch, where their values are to be computed using expressions (1.22):

$$\begin{cases} L = \dfrac{1}{2\,c'_m}, \\ R = (-2\,a'_m + 2(c'_m\,a'_m + c''_m\,a''_m)L)L, \\ \dfrac{1}{C} = (a'^2_m + a''^2_m + 2(c'_m\,a'_m + c''_m\,a''_m)R)L, \\ G = -2(c'_m\,a'_m + c''_m\,a''_m)C\,L. \end{cases} \tag{1.22}$$

To account for skin and proximity effects as well as dielectric losses, Weens [134] used ladder circuits. He modelled the frequency dependent behaviour of shielded and un-shielded cables using the RL and RC ladder circuits depicted in Fig. 1.28 and Fig. 1.29, to take into account skin and proximity effects and dielectric losses, respectively.

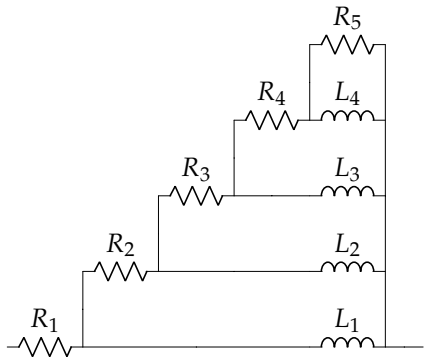

FIGURE 1.28: The used ladder circuit that takes into account ohmic losses (skin and proximity effects) in [134].

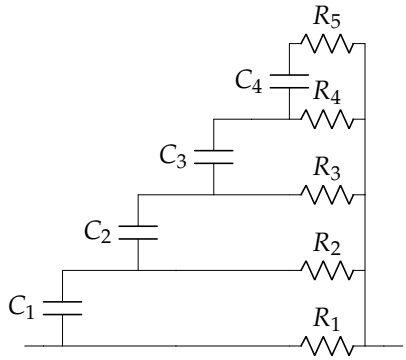

FIGURE 1.29: The used ladder circuit that takes into account dielectric losses in [134].

These ladder-type networks were initially developed by Chaves [135] for a limited range of frequencies, which were in due course improved to take into account skin effect in the frequency range of interest [136]. The more branches, the more accurate the model is, and since an infinite number of branches is not practical, a number of branches is to be set depending on the desired accuracy [136]. Although an optimal number of branches is preferable, a very high number of branches might lead to negatively valued inductances and resistances. The values of the parameters of the ladder were determined by Weens in [134] using a mathematical solver tool. They could also be computed using a trial and error procedure which is not practical [137]. The difficulty in computing the values of the parameters (R_i,L_i) is observed in [138] but was not solved. In [136] a method easy to implement that estimates the values of these parameters using a "sequential circuit order reduction" was presented.

Magdun in [139] also used the RL ladder circuit depicted in Fig. 1.28 modelling the frequency behaviour of each turn, which was eventually simulated in time domain and the inter-turn voltage distribution deduced and compared to the measurements. Similarly in [74], a method that allows the synthesis of an RL Cauer ladder network of the structure seen in Fig. 1.28, so as to homogenize multi-turns windings in FEM calculations in time domain has been proposed. The synthesis of the ladder parameters was performed by the simple Euclidean algorithm for polynomial division.

In [140], the frequency dependent behaviour of the parameters of medium voltage power cables has been taken into account using an equivalent passive electrical circuit deduced from the VF presented in Fig. 1.30.

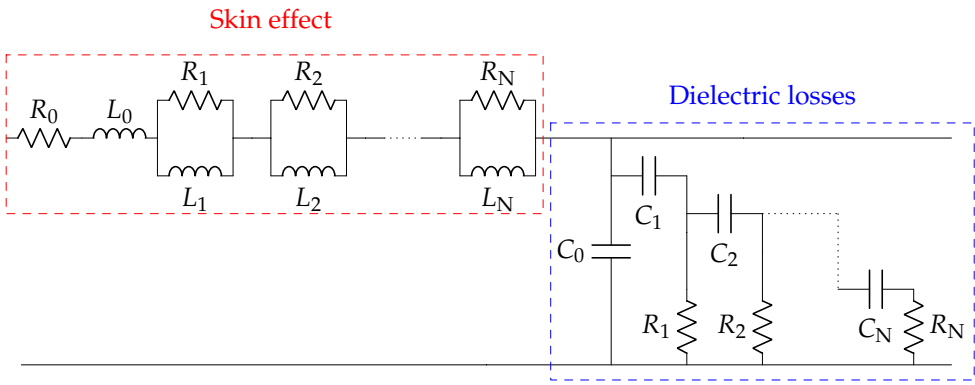

FIGURE 1.30: The equivalent lumped parameter model that takes into account skin effects and dielectric losses used in [140].

Accounting for skin effects in circular cross sectional conductors in [141] was also done using a compact equivalent circuit model, a four ladder circuit, of the form depicted in Fig. 1.28, enabling to cover the entire frequency range (from DC to $1/\pi t_r$). The model is based on an improvement of the model presented by Yen [142] because the proposed method failed to accurately represent skin effect in high frequencies. The DC resistance of the ladder is forced to be equal to the DC resistance of the conductor, and the constraints on the values of the resistances are taken to be:

$$\begin{cases} R_1 = \alpha_R \cdot R_{DC} \\ \dfrac{R_i}{R_{i+1}} = R_R,\ i = 1,\ 2,\ 3, \end{cases} \tag{1.23}$$

with R_R being a constant to be determined by solving the following cubic polynomial:

$$R_R{}^3 + R_R{}^2 + R_R + (1 - \alpha_R) = 0. \tag{1.24}$$

It was found that for a maximum frequency of interest f_{max}, the value of α_R ought to be chosen so as to satisfy:

$$\alpha_R = 0.53 \cdot \frac{r_c}{\delta_{max}}, \tag{1.25}$$

with r_c and δ_{max} being the wire radius and the skin depth computed at f_{max} (see equation (1.2)), respectively. The same approach was applied for the values of the inductances L_i, where it was found that $\alpha_L = 0.315\,\alpha_R$ should be used for the computation of the value of the different inductances, where:

$$\begin{cases} L_1 = \dfrac{L_{lf}}{\alpha_L}, \\ \dfrac{L_i}{L_{i+1}} = L_L,\ i = 1,\ 2, \end{cases} \tag{1.26}$$

where L_{lf} is the internal low frequency value of the inductance. Equation (1.26) leads to the following expression, that permits the computation of the value of L_L once the value of R_R

determined:

$$\frac{1}{{L_L}^2}+\left(1+\frac{1}{R_R}\right)^2\frac{1}{L_L}+\left(\frac{1}{{R_R}^2}+\frac{1}{R_R}+1\right)^2-\alpha_L\left(\left(1+\frac{1}{R_R}\right)\left(\frac{1}{{R_R}^2}+1\right)\right)^2=0. \tag{1.27}$$

However, since this model computes the values of the elements of the circuit by using of semi-empirical formulae, its accuracy is not guaranteed for arbitrary shaped conductors [143].

Ruiz-Sarrió in [13] also resorted to fitting techniques to account for the frequency behaviour of electrical machine windings to predict its common-mode and differential-mode behaviours. The fitting functions are of the following form:

$$\begin{cases} R(f)=p_1\,f^{p_2}+p_3, \\ \omega L(f)=p_4\,f^{p_5}+p_6, \end{cases} \tag{1.28}$$

where the p_1, p_2, p_3, p_4, p_5, p_6 parameters are chosen to build the function over the specified frequency interval. The choice of the fitting function was performed based on a trade-off between simplicity, method compliance and accuracy. The proposed electrical circuit that is only available for frequency domain simulations for an n-turns winding is presented in Fig. 1.31.

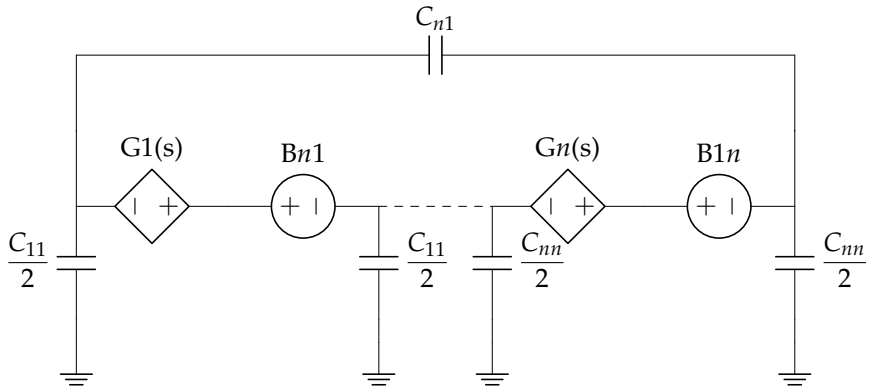

FIGURE 1.31: The SPICE equivalent circuit emulating the frequency behaviour of each turn through Laplace transfer functions.

The voltage controlled current sources are used to link the current and voltage of the turn through a transfer function G1(s). The behavioural voltage sources B1n and Bn1, on the other hand, are used to account for the mutual coupling between turns. The frequency domain results of this model for the common-mode and differential-mode are presented in Fig. 1.32 and Fig. 1.33, respectively, where the model and measurements agree well up to 1 MHz.

Nevertheless, for an equivalent circuit to be deduced, fitting techniques are applied. The usage of the latter allows the expression of the resulting scatter plot in an analytical form. This will enable the deduction of the electrical passive network that reproduces the same frequency behaviour as elaborated in this section. Although already briefly mentioned in this section, the most used fitting techniques are elaborated on and compared in the following section.

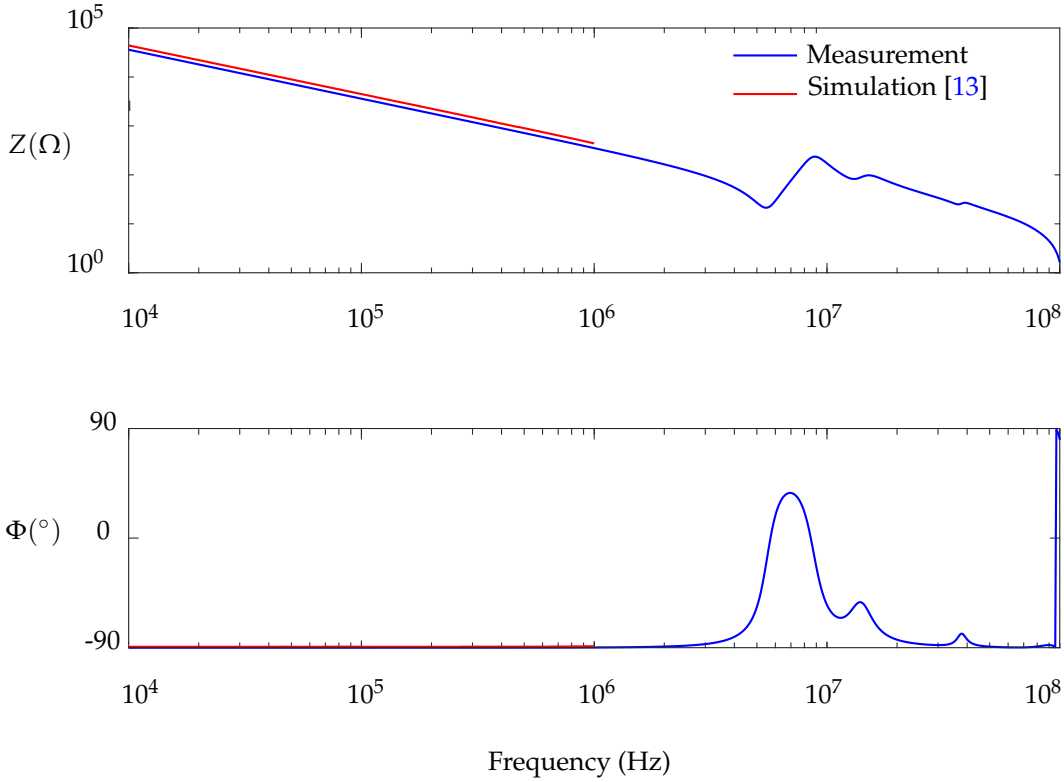

FIGURE 1.32: The prediction of the frequency common-mode behaviour of the model proposed by Ruiz-Sarrió. *Data extracted from* [13].

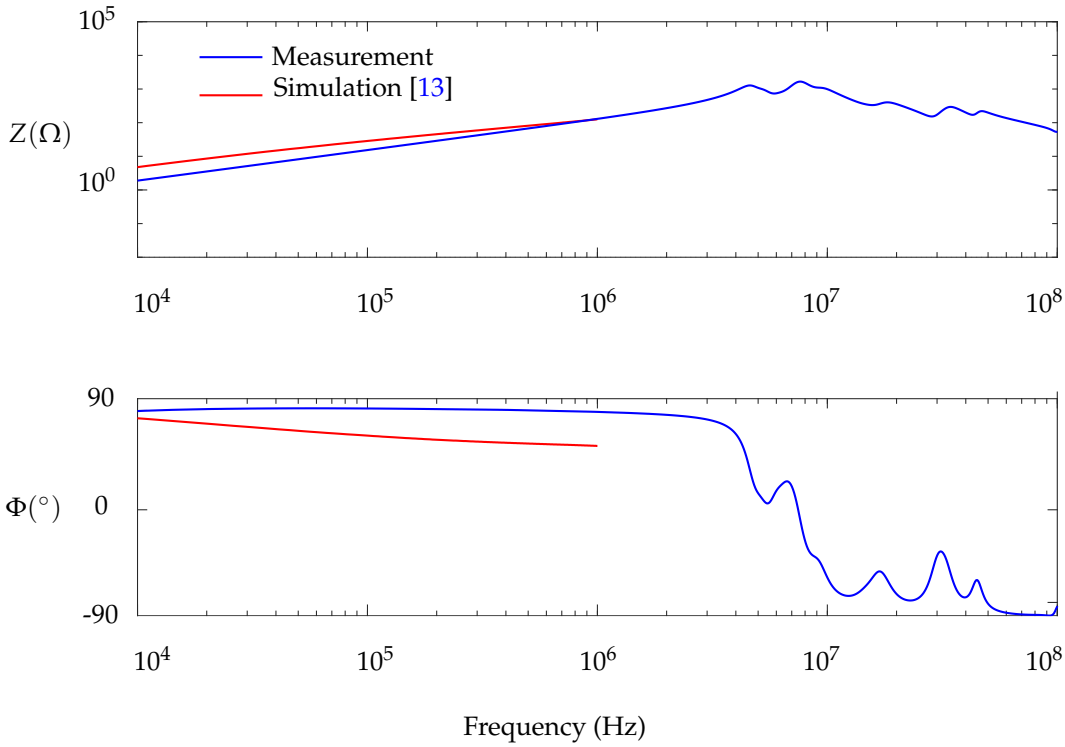

FIGURE 1.33: The prediction of the frequency differential-mode behaviour of the model proposed by Ruiz-Sarrió. *Data extracted from* [13].

1.4.3 Fitting techniques

Let $H'(\omega)$ be the rational approximation of the frequency dependent function to be fitted $H(\omega)$. Several techniques can be used to compute $H'(\omega)$ that has the following form:

$$H'(\omega) = \frac{N_0 + N_1(j\omega) + N_2(j\omega)^2 + \cdots + N_n(j\omega)^n}{D_0 + D_1(j\omega) + D_2(j\omega)^2 + \cdots + D_d(j\omega)^d}. \tag{1.29}$$

with $N(\omega)$ and $D(\omega)$ being polynomials in $j\omega$ of order n and d, respectively.

This section brings about the three main fitting techniques when performing time domain analysis of problems with frequency dependent parameters: Model-Based Parameter Estimation (MBPE), Debye type fitting, and VF—briefly mentioned previously—.

1.4.3.1 Model-based parameter estimation (MBPE) technique

Regarding the first fitting technique, MBPE, it was at first applied to the analysis of electromagnetic problems [120] and was later on extended to transmission lines [144], then to the computation of the GND impedance [145]. This fitting technique is an extension of Prony's approach [127].

The first step of the fitting algorithm is to set D_d to 1, then few assumptions are made: the poles p_i are assumed to be either conjugated pairs or real, the coefficients to be estimated, *i.e.* N_i and D_j, are assumed real valued, and $H'(\omega)$ is assumed strictly proper (that is $n \leq d$). If the high frequency value of the to-be-fitted function is not null and is of value H'_{HF}, then the fitting is applied to $\left(H'(\omega) - H'_{\mathrm{HF}}\right)$. A point-matching algorithm is then performed so as to compute the values of the unknown coefficients. Just like its name might have already implied, for each value of the function to be fitted on the frequency range of interest, the value of $H'(\omega)$ is forced to be equal to that of the function to be fitted, the equation $H(\omega_i) = H'(\omega_i)$ is therefore solved, and the values of the coefficients deduced. Nonetheless, this technique has its limitations. For very high values of the angular frequency ω, computer overflow errors may occur. For functions $H(\omega)$ with several resonance peaks, ill-conditioning problems are faced. The function can then be approximated by parts on several sub-domains. Also, poles of $H'(\omega)$ are not necessarily the poles of $H(\omega)$, particularly. This technique is only suitable for the approximation of smooth functions and the computations of their IFT. Also, and in order to circumvent the ill-conditioning, the power series $\left(1, \omega_i, \omega_i^2, \cdots\right)$ could be replaced by a Chebyshev polynomial which are well suited to approximate very high order. Then the equivalent of the power series $\left(1, \omega_i, \omega_i^2, \cdots\right)$ could be computed using Clenshaw's recurrence formula which is a recursive technique that enables the evaluation of a linear combination of Chebychev polynomials [127], [146].

1.4.3.2 Debye fitting technique

The second fitting technique is the Debye fitting technique [116], previously briefly mentioned. In effect, this fitting procedure was introduced by Debye in order to describe the physical behaviour of the different dispersive media. It is typically used for functions with smooth frequency behaviour where the fitting function is of the following expression:

$$H'(\omega) = H'_{\mathrm{HF}} + \sum_{i=1}^{n_{\mathrm{P}}} \frac{K_i}{1 + j\omega Q_i}, \tag{1.30}$$

with n_p, K_i and Q_i being the order of approximation and two real positive values, with the first describing the absorption peak and the second, the $(2\,\pi\,Q_i)$ the relaxation frequency f_r, respectively. Their expressions are the following:

$$\begin{cases} K_i = -\dfrac{c_i}{a_i}, \\ Q_i = -\dfrac{1}{a_i}. \end{cases} \tag{1.31}$$

where a_i and c_i are the i^{th} pole and its corresponding residue.

Because this model only admits real poles, the Kramers-Kronig relation is satisfied. The latter is a relation that connects the real and imaginary parts of a complex analytic function. Moreover, the model could be easily incorporated in time domain algorithms; no convolution needed whatsoever, just a set of first order differential schemes [120], [147], [148]. Also, a circuit representation could be easily deduced [120]. The critical aspect for this model is the proper choice of the approximation order as well as the set of the starting poles.

1.4.3.3 Vector-Fitting (VF) technique

The third technique is the VF technique, that was developed by Gustavsen and Semlyen [132]. This technique can help overcome the limitations of the previously elaborated techniques. The fitting function is written as in the following expression:

$$H'(\omega) = H_{\text{HF}} + \sum_{i=1}^{n_p} \frac{c_i}{j\omega - a_i}, \tag{1.32}$$

with c_i and a_i being the i^{th} residue and its corresponding pole, in the order given. The poles are either real values, complex conjugated pairs or a combination of both. The VF algorithm does the following: after specifying a set of starting poles by the user c_{0i}, an unknown function $\sigma(\omega)$ is introduced and approximated with the following rational expression [149]:

$$\sigma'(\omega) = 1 + \sum_{1}^{n_p} \frac{c_{\sigma i}}{j\,\omega - a_{0i}}, \tag{1.33}$$

so that the fitting model of $G(\omega) = \sigma(\omega)\,H(\omega)$ is

$$G'(\omega) = H_{\text{HF}} + \sum_{1}^{n_p} \frac{c_i}{j\omega - a_{0i}}. \tag{1.34}$$

Then, the parameters of the fitting function are computed using the m sampled values of $H(\omega)$ functions and solving the following linear system of equations:

$$G'(\omega_k) = \sigma'(\omega_k)\,H(\omega_k), \tag{1.35}$$

for the unknowns c_i, $c_{\sigma i}$ and H_{HF} with $k = 1, 2, \cdots \text{m}$, by applying iterative least-squares technique. Thus, the fitting function $H'(\omega)$ is expressed as follows:

$$H'(\omega) = \frac{G'(\omega)}{\sigma'(\omega)}. \tag{1.36}$$

The error is computed and the procedure is reiterated by a new set of starting poles. Experimental analysis has proven that for smooth functions $H(\omega)$, good accuracy is obtained by using linearly spaced real valued starting poles. The critical aspect of the VF technique resides in the choice of the starting poles a_{i0}. For non-smooth functions, on the other hand, complex ones are to be used [132],[127]. In the case of a nodal admittance matrix of a network, VF could be used also, where all coefficient of the matrix are represented by the same set of poles as described here [150]. Ill-conditioning is avoided by assuming that the real parts of the initial set of poles are a hundred times smaller that the corresponding imaginary parts [132]. The main advantage of this fitting procedure is that the computed poles and residues represent the function $H(\omega)$ over the whole frequency range. The usage of equivalent electrical circuits deduced from the fitting of the frequency dependent behaviour of the parameter could however result in negative values of the components, *i.e.* a network with non-physical electrical properties, implying thus a generation of active power instead of its absorption [127], [151] for whatever set of applied currents and voltages. This does not impede the running of the frequency simulation in the chosen simulator; unlike for time domain simulations. Moreover, the usage of stable poles (negative-valued real parts) is not sufficient to guarantee the stability of the system. The loss of the stability of the system may cause unwanted spurious oscillations. Several research works have proposed the enforcement of the passivity by applying the positive-definite criterion [127], [151], [152]. In [151], a correction to the admittance matrix is introduced by enforcing the positive-definite criterion. The performed correction does not induce large errors with respect to the fitting and is based on the linearization and constrained minimization by quadratic programming. The positive-definite criterion proved to give good results with respect to the stability of the simulation. However, for a very broad frequency range, enforcing the positive-definite criterion may result in very high computational time. It is for that reason that Neumayer in [127] proposed a standard minimal-order realization deduced from a co-prime factorization. The imposed criterion is the Kalman–Yakubovich–Popov criterion, which is a lemma that establishes an equivalence between the conditions on the state-space representation matrices, the conditions in frequency domain for the system to be positive real, and the input-output relationship of the system in time domain.

1.5 Conclusion

In this chapter, the adopted circuit model for the electrical machine winding proposed in previous work [34] was presented, as well as its topology and its different parametrization methods. The pros and cons of each parametrization technique were studied and the selection of FEM justified: it allows for a physical modelling of the occurring phenomena within the winding, regardless of its geometry. The previously proposed model parametrization procedures by both Mihaila [34] and Toudji [17] were compared and their limitations highlighted. The frequency dependent behaviour of the different parameters was presented, followed by several techniques discussed in the literature that allow for taking it into account the frequency dependency in both frequency domain and time domain that were presented and compared. The choice of using equivalent passive networks seemed more convenient than others, given the interest in the local voltages. The three different fitting techniques enabling the deduction of the passive electrical network were introduced, where it was shown that the VF overcomes the limitations of the other two.

CHAPTER

2

FREQUENCY DOMAIN MODELLING

Contents

2.1 Introduction

After presenting and comparing the different available tools that enable the computation of the LPM elements as well as the inclusion of their frequency dependent behaviour in both frequency domain and time domain in the previous chapter, we will now use the appropriate tools context-wise to improve the adopted phenomenological LPM [34]. Before extracting the inter-turn voltage distribution in the time domain, we will first incorporate the frequency dependent behaviour in the frequency domain. This will permit the confrontation of the chosen parametrization technique, as well as the proposed method to include the frequency behaviour, with the experimental measurements of the frequency domain response of the winding. This will eventually allow a frequency domain validation of the new proposed elementary circuit. Then comes the use of this frequency dependent model as a layout for the time domain investigation and eventually the computation of the inter-turn voltage distribution, which is left for the subsequent chapter. In pursuit of this aim, an accurate parametrization of the model with the different frequency dependencies included is necessary, as illustrated in Fig. 2.1. Notice the introduction of the mutual resistance R_{ij} that was not accounted for previously, where "t_i" refers to the i^{th} turn and "m" refers to the number of frequency samples.

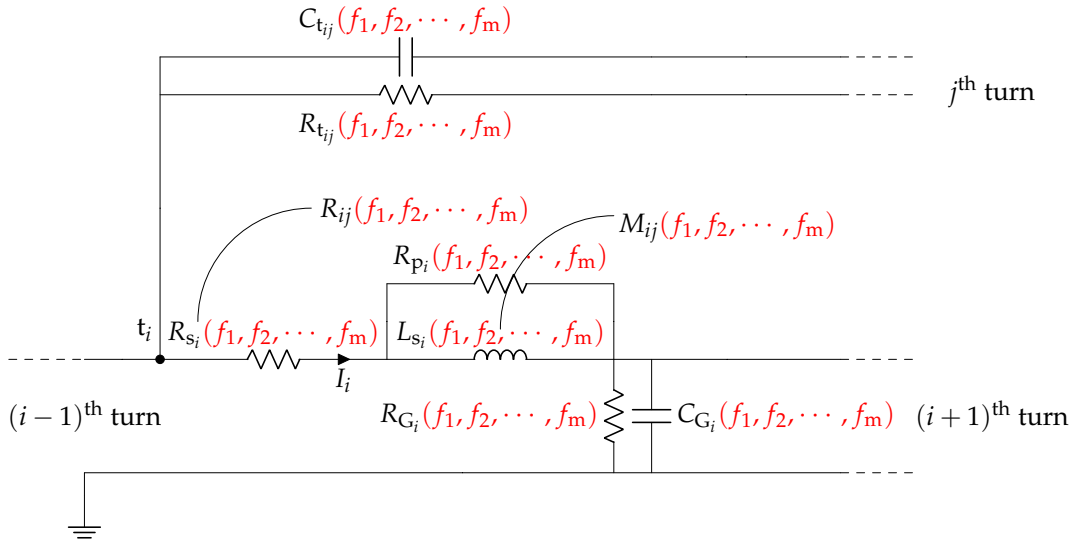

FIGURE 2.1: The elementary cell we are aiming to achieve.

Hence and as discussed in section 1.2.2, we use numerical methods, since they enable the prediction of the model parameters values, they can be used for complex geometries and they guarantee a good accuracy when implemented correctly, in particular FEM. Accordingly, an immediate solution to ensure that the accuracy of the modelled occurring electromagnetic phenomena in frequency domain is not compromised, would be to fully define and characterize the winding with its corresponding 3D geometry. Nevertheless, not only is this solution computationally expensive, but it does not allow for a distributed model of the winding to be deduced. Indeed, when implementing a full 3D frequency domain investigation of the studied geometry, the latter is studied as a whole and not distributed on a turn level, which presents a difficulty in numerically computing the values of the LPM elements. Thus, in view of the lumped nature of the adopted circuit model, and given our interest in modelling the winding of electrical machines on a turn level for an eventual computation of the inter-turn voltage distribution, this solution is discarded.

Instead, we prefer to study judiciously chosen 2D slices of the to-be-designed winding. While this entails some inaccuracies, since not only the full complexity of the geometries may not be captured but the applied constraints may not always represent accurately the actual boundary conditions; there are exceptions: planar [153], [154], axisymmetric [155]–[159] and helicoidal problems [144]–[146] are exceptions to the aforementioned limitations of using only the 2D cross-section of the studied 3D problems.

When studying a planar problem, and when its corresponding electrical and magnetic properties are invariant in the third dimension, the studied 3D geometry can be reduced to its 2D cross-section. An example of a planar geometry is seen Fig. 2.2.

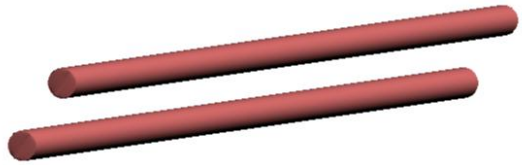

FIGURE 2.2: An example of a planar geometry.

In problems that are axisymmetric, the system being studied has a symmetry of rotation around an axis. This means that the characteristics of the system do not change as we move around it, but only in the directions of the axis and the radius. As a result, creating a 2D cross-section of the 3D axisymmetric geometry does not result in an inaccurate model, when correctly configured. To put it simply, the properties of the studied system remain the same in the circumferential direction, while they vary only in the axial and radial directions. An example is illustrated in Fig. 2.3.

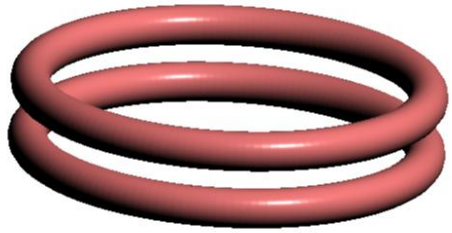

FIGURE 2.3: An example of an axisymmetric geometry.

For helicoidal problems, on the other hand, the 3D problem is reformulated in helicoidal coordinates [160] instead of Cartesian coordinates. This leads to a corresponding 2D field modelling with an adapted metric easily implemented in FEM codes. Hence, the resulting 2D slice representation maintains the same level of accuracy as the 3D problem. This has been studied and confirmed in the following research work [161] in an electrostatic field modelling. An example of a helicoidal geometry is depicted in Fig. 2.4.

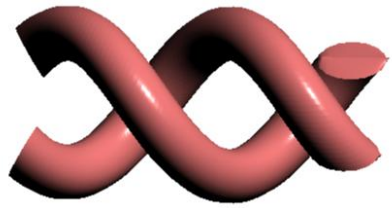

FIGURE 2.4: An example of a helicoidal geometry.

In the case of electrical machines, the turns as well as the magnetic core ought to satisfy one of the aforementioned geometrical exceptions for the electrical machine to be studied in only 2D. Accordingly, in the case of the electrical windings, the turns are usually stacked close to one another that the helicoidal structure of the whole winding can be considered axisymmetric. For illustration, two winding examples are depicted in Fig. 2.5, where the first geometry presented in Fig. 2.5a can only be studied in a helicoidal geometrical approximation, whereas the winding in Fig. 2.5b, although helicoidal as well, can be considered axisymmetric given the small inter-turn spacing between its turns. As for the geometry of the magnetic core, it is most of the time exempted from these geometrical exceptions. This highlights the importance of using an adequately configured 3D model that takes into account its aforecited inconveniences.

(a)

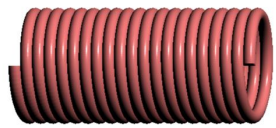

(b)

FIGURE 2.5: An example of two windings with a (a) large (b) small inter-turn spacing.

In order to intrinsically capture 3D effects (*e.g.* a complex shaped core with corners) while keeping the advantages of slices defined on a turn level, the studied geometry could be decomposed and redefined as 3D "slices" linked with different virtual connections. This could be an interesting workaround to investigate on non-2D-reducible geometries.

In this thesis, and as a mean to mitigate the possibility of introducing geometrical inaccuracies, we focus on the 2D reducible geometries, in particular axisymmetric problems, for simplicity purposes, even though the proposed frequency domain model is available for all geometries.

After defining the 2D geometry of the studied winding by configuring its constituting turns and respecting their arrangement, their electrical properties (copper radius r_c, insulation thickness ℓ_{insul}, inter-turn spacing e_{it}, etc), the geometry of the inserted magnetic core, if there is any, and defining its corresponding magnetic properties, a choice of a suitable electromagnetic field model has to be made. The chosen electromagnetic field model will allow the computation of the physical quantities (*i.e.* magnetic field, electric field, current density, etc) in frequency domain modelling the occurring phenomena within the winding. The values of the model parameters are deduced from these computed quantities given the adopted phenomenological approach. This is summarized in Fig. 2.6. The values of the LPM parameters are computed over the frequency range of interest so as to account for their frequency dependency.

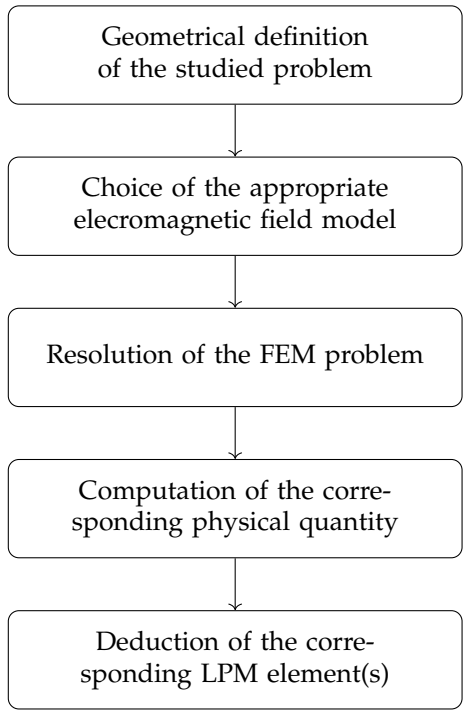

FIGURE 2.6: The functional workflow of the proposed tool.

As mentioned in the previous chapter, section 1.4.2, frequency dependent network equivalents are the most used technique to include these frequency dependencies in both frequency domain and time domain. In this chapter, we will mention some of the difficulties faced when willing to account for the frequency dependent behaviour of the electrical parameters, especially the different mutual couplings between the turns using these equivalent networks. The adopted LPM will be improved so that the frequency behaviour of its parameters is properly accounted for in the frequency domain over the frequency range of interest. The novelty of the resulting approach lies in the fact that the proposed new elementary cell does not require the use of fitting techniques, resulting in the developed frequency domain tool being fully automatic, and not calling for the intervention of the user to properly set up the fitting parameters.

The chapter is organized as follows. We start by introducing the different electromagnetic field models that allow for the modelling of the occurring electromagnetic phenomena within the windings in section 2.2. Then, we present the different identification techniques of the

parameters of the previously elaborated model seen in Fig. 1.7 in section 2.3. Next, an investigation of the frequency behaviour of the permittivity through measurements is performed in paragraph 2.3.3.3, and the choice of using an electrostatic model is justified. Following this, in section 2.4, a comparison of the different identification techniques on a winding sample is carried on. A choice of a specific identification technique over another is made based on its accuracy and the required number of computations. Subsequently, we propose a method to take into account the frequency dependent behaviour of these parameters, including the mutual inductive coupling, and the new elementary cell of the winding is presented in section 2.5. The proposed frequency domain model does not call for any fitting technique whatsoever, making the proposed frequency domain model automatic and not user-dependent. Finally, the proposed frequency domain model is experimentally validated on different test cases without and with a magnetic core in section 2.6. As previously stated concerning the choice of the test cases, and in the aim of proposing a light model that does not introduce geometrical inaccuracies we focus on 2D reducible geometries, in particular axisymmetric problems. An investigation of a test case with a geometry non-reducible to its 2D slice is performed in section 2.6.6, where the geometrical impact is quantified. Moreover, it is relevant to mention that this chapter focuses solely on accurately computing and accounting for the frequency behaviour of the winding model described on a turn level in the frequency domain. In view of this, the experimental validation is conducted by comparing the frequency domain measurements of the studied winding response with the simulated winding response.

2.2 Electromagnetic field modelling

To develop an accurate model that accounts for the electromagnetic phenomena occurring within the windings of electrical machines, it is essential to have a good understanding of the existing electromagnetic models. To describe these phenomena, Maxwell's equations are used, which are a set of partial differential equations that link magnetic and electric phenomena. These equations serve as a physical basis for understanding the different electromagnetic phenomena within electrical machines and guide the development of a comprehensive model that accurately emulates them.

To solve the Maxwell's equations, FEM is used. For each phenomenon, an electromagnetic field model is applied, and the corresponding field values are deduced.

Maxwell equations write:

$$\mathbf{curl}\,\mathbf{h} = \mathbf{j} + \frac{\partial \mathbf{d}}{\partial t}, \tag{2.1}$$

$$\mathbf{curl}\,\mathbf{e} = -\frac{\partial \mathbf{b}}{\partial t}, \tag{2.2}$$

$$\mathrm{div}\,\mathbf{b} = 0, \tag{2.3}$$

$$\mathrm{div}\,\mathbf{d} = \rho, \tag{2.4}$$

where $\mathbf{h}$ is the magnetic field (in $\mathrm{A\,m^{-1}}$), $\mathbf{j}$ is the current density (in $\mathrm{A\,m^{-2}}$), $\mathbf{d}$ is the electric induction (in $\mathrm{C\,m^{-2}}$), $\mathbf{e}$ is the electric field (in $\mathrm{V\,m^{-1}}$), $\mathbf{b}$ is the magnetic induction (in T) and ρ is the volume density of charges (in $\mathrm{C\,m^{-3}}$).

Maxwell's equations entail a coupling between the electric and magnetic quantities as seen in equations (2.1) and (2.2). Also, the second term in (2.1) ($\partial\mathbf{d}/\partial t$) refers to the displacements currents that are most of the time neglected in electrotechnics [17]. Nonetheless, behavioural laws,

either magnetic or electric, are necessary for a complete characterization of the electromagnetic phenomena.

Considering the magnetic behaviour and depending on the type of the magnetic material, a behavioural law is defined[1]. There are three types of magnetic materials: diamagnetic, paramagnetic, and ferromagnetic materials. For the first two, *i.e.* diamagnetic and paramagnetic materials, assuming them linear and isotropic, the behavioural law can be written as

$$\mathbf{b} = \mu\,\mathbf{h}, \tag{2.5}$$

with μ the constant magnetic permeability (in $\mathrm{H\,m^{-1}}$) that is close to the vacuum permeability $\mu \approx \mu_0$ with $\mu_0 = 4\,\pi\,10^{-7}\,\mathrm{H\,m^{-1}}$.

For the ferromagnetic materials, on the other hand, hysteresis and/or saturation phenomena ought be considered and μ can no longer be considered constant (neither scalar in case of anisotropy).

Concerning the electrical behavioural laws, they write:

$$\mathbf{j} = \sigma\,\mathbf{e}, \tag{2.6}$$

$$\mathbf{d} = \varepsilon\,\mathbf{e}. \tag{2.7}$$

The first electrical behavioural law (2.6) is referred to as Ohm's law and relates the current density $\mathbf{j}$ to the electric field $\mathbf{e}$, whilst the second (2.7) relates the electric induction $\mathbf{d}$ to the electric field $\mathbf{e}$. Here, ε is the dielectric permittivity (in $\mathrm{F\,m^{-1}}$) and σ is the electric conductivity (in $\Omega^{-1}\,\mathrm{m^{-1}}$).

For this work, the smallest wavelength of interest ($\lambda \approx 3\,\mathrm{m}$ for $f_\mathrm{m} = 110\,\mathrm{MHz}$ in the air) is much larger than the overall size of the windings (few cm). And even if the length of the wounded wires reaches the same order of magnitude as λ, they are made of very good conductive materials, where conduction currents largely dominate displacement currents. Consequently, we choose to decouple the electrical and magnetic phenomena by considering, on the one hand, an electrostatic model in insulators and air to model capacitive effects and a magneto-dynamic model in both the air and the conductors so as to capture inductive and resistive effects.

It is worth mentioning that for each model several formulations could be developed. In this work, we will consider the usual potential formulations in terms of the scalar electric and magnetic potentials which do not in any way compromise the accuracy of the computations. For details about alternative formulations, see [162], [163].

2.2.1 Electrostatic field model

Starting with the electrostatic field model, where the considered phenomena do not vary according to time t. The system of equations studied becomes:

[1]The overall form of the law is the same, only the behaviour of the material, linear or not, having a remanent magnetization or not, that changes, modifying thus the expression of the permeability and adding or not the remanent magnetization, respectively.

$$\mathbf{curl}\,\mathbf{h} = \mathbf{j}, \tag{2.8}$$
$$\mathbf{curl}\,\mathbf{e} = 0, \tag{2.9}$$
$$\mathrm{div}\,\mathbf{b} = 0, \tag{2.10}$$
$$\mathrm{div}\,\mathbf{d} = \rho. \tag{2.11}$$

In this model, we focus on equations (2.9) and (2.11), which study systems that are defined by a given charge distribution.

Since $\mathbf{curl}\,(\mathbf{grad}\,\cdot) = 0$, equation (2.9) implies the existence of a scalar potential v satisfying the following equation:

$$\mathbf{e} = -\mathbf{grad}\,v, \tag{2.12}$$

which when inserted in (2.11) gives the electrostatic formulation:

$$\mathrm{div}\,(-\varepsilon\,\mathbf{grad}\,v) = 0. \tag{2.13}$$

We will see in paragraph 2.3.3.3 that using the electrostatic formulation (2.13) is sufficient to achieve an accurate model.

2.2.2 Magneto-dynamic field model

As its name might have already implied to the reader, the magneto-dynamic field model investigates the electromagnetic phenomena occurring in a dynamic state, where the effects of displacement currents $\partial\mathbf{d}/\partial t$ are neglected. The system to be solved is thus the following:

$$\mathbf{curl}\,\mathbf{h} = \mathbf{j}, \tag{2.14}$$
$$\mathbf{curl}\,\mathbf{e} = -\frac{\partial \mathbf{b}}{\partial t}, \tag{2.15}$$
$$\mathrm{div}\,\mathbf{b} = 0. \tag{2.16}$$

The current density can be decomposed to two terms $\mathbf{j_s}$ and $\mathbf{j_r}$ such that:

$$\mathbf{j} = \mathbf{j_s} + \mathbf{j_r}, \tag{2.17}$$

with $\mathbf{j_s}$ and $\mathbf{j_r}$ being the source (imposed) current density and the reaction (induced) current density, respectively. Equation (2.14) becomes:

$$\begin{aligned} \mathbf{curl}\,\mathbf{h} &= \mathbf{j_s} + \mathbf{j_r}, \\ &= \mathbf{j_s} + \sigma\,\mathbf{e}. \end{aligned} \tag{2.18}$$

Since $\mathrm{div}\,(\mathbf{curl}\,\cdot) = 0$, there exists a magnetic vector potential $\mathbf{a}$ satisfying the following expression:

$$\mathbf{b} = \mathbf{curl}\,\mathbf{a}, \tag{2.19}$$

therefore, (2.15) rewrites:

$$\mathbf{curl}\left(\mathbf{e} + \frac{\partial \mathbf{a}}{\partial t}\right) = 0. \tag{2.20}$$

which implies the existence of a scalar potential v satisfying:

$$\mathbf{e} = -\mathbf{grad}\, v - \frac{\partial \mathbf{a}}{\partial t}. \tag{2.21}$$

Inserting (2.21) in (2.18) and using the magnetic behaviour law, we get:

$$\mathbf{curl}\left(\mu^{-1}\,\mathbf{curl}\,\mathbf{a}\right) + \sigma\left(\mathbf{grad}\, v + \frac{\partial \mathbf{a}}{\partial t}\right) = \mathbf{j_s}. \tag{2.22}$$

such that (2.19) and (2.21) hold, *i.e.* $\mathbf{b} = \mathbf{curl}\,\mathbf{a}$ and $\mathbf{e} = -\mathbf{grad}\, v - \frac{\partial \mathbf{a}}{\partial t}$.

The different models presented above enable the calculation of the parameters of the adopted LPM through the computed corresponding electromagnetic fields (electric fields or magnetic fields, respectively). Since there are three types of phenomena (resistive, inductive, and capacitive) and given the prevalent phenomenon a choice of the model is made. Hence, for the computation of the values of the resistances and inductances, the distribution of both the current density $\mathbf{j}$ and the magnetic flux ϕ are needed for the determination of their values. Consequently, a magneto-dynamic formulation is solved.

Concerning the computation of the values of the different capacitances of the model, the values of the scalar potential as well as the static charges between the two studied turns are required. If the frequency dependent behaviour of the used insulation is not taken into account, as it will be justified, an electrostatic computation is used. This is summarized in Tab. 2.1.

TABLE 2.1: The chosen formulation for the determination of the value of each model parameter.

Parameter	Phenomenon	Formulation
Resistance	Skin and proximity effects	Magneto-dynamic (2.22)
Inductance	Induced currents and voltages	Magneto-dynamic (2.22)
Capacitance	Distribution of the electric charges	Electrostatic (2.13)

After elaborating on the different electromagnetic models that will enable the computations of the electrical parameters values on the frequency range of interest, we will discuss in the subsequent section the different parameter identification techniques of the adopted LPM.

2.3 Identification of the winding parameters

The section addresses the different identification techniques of each electrical parameter of the model parameters that is performed in the frequency domain. The values of these parameters are identified by inspection using the appropriate electromagnetic field model (refer to section 2.2) solved with FEM after defining the geometry of the test cases and applying the suitable set of boundary conditions in harmonic regime.

As a matter of fact, in open boundary problems [164], [165] (*i.e.* unbounded domains), as is the case of electrical machine windings, the electromagnetic fields propagate outwardly indefinitely, which raises the question on how to properly configure the boundary conditions that

ought to be defined at infinity. An intuitive approach would be to truncate the domain of study. Although easy to implement, it is heavily dependent on the size at which the domain is truncated: the bigger the domain of study the more accurate the model is. This can quickly become a computational burden. To overcome this shortcoming, different transformation methods were developed, in particular Infinite Electromagnetic Transformation (IET) [166], that allow the modelling of infinite domains by means of finite elements in a shell defined sub-domain. This technique permits as a close of a representation of the studied electromagnetic system as possible and is used for this research work.

In this following sections we will present the different resistance, inductance and capacitance identification techniques, respectively.

2.3.1 The Ohmic losses resistance

As it has been presented in section 1.3.1, the ohmic losses resistance increases with frequency due to skin and proximity effects which were demonstrated to have an impact on the propagation delay [143]. This emphasizes on the necessity to:

- correctly take into account both skin and proximity effects for an accurate computation of the Joule losses resistances;
- account for the frequency dependent behaviour of these Joule losses resistances.

The ohmic losses resistance is computed in a magneto-dynamic approximation to account for its frequency dependency. Thus, in order to solve the formulation (2.22) using FEM and deduce the values of the ohmic losses resistances by inspection, an appropriate choice of the excitation is fundamental.

As elaborated in the previous chapter, specifically in section 1.3.1, the skin effect refers to the current distribution in the excited conductor, whereas proximity effect refers to the impact of the current traversing one turn over the current distribution in the other turns. As an illustration of the latter and in order to elaborate even further on section 1.3.1, two case studies of the same axisymmetric geometrical definition—hence only half of the 2D cross-section is studied—are presented hereafter: a three turns winding versus a one turn winding investigated in a magneto-dynamic field model.

For both test cases only one turn is set to a chosen value $I_i = 1\,\text{A}$ as an excitation source. The results are presented for two frequency samples, low frequency and high frequency, 40 Hz and 1 MHz, and are shown in Fig. 2.7 and Fig. 2.8.

At low frequency (Fig. 2.7a and Fig. 2.7b), the current is evenly distributed on the surface of the conductor set to $I_i = 1\,\text{A}$ for both test cases. However, when increasing the frequency, the current distribution is no longer similar even though the excitation is maintained the same. For the one turn winding, the current density is evenly distributed on the "skin" of the conductor at 1 MHz as depicted in Fig. 2.8a. This is skin effect. Nevertheless, for the three turns winding as seen in Fig. 2.8b, not only the skin effect is noticed but the impact the excited turn has on the adjacent conductive materials is observed as well. This is proximity effect.

The currents captured at the surface of the conductors set to $I_j = 0\,\text{A}$ are called induced currents and give rise to power dissipation on those conductors are well. These induced currents in the nearby conductors are due to the fact that the studied conductors are in close juxtaposition. The magnetic field generated by the excited turn has its lines impinged upon the neighbouring conductors, changing hence the current distribution on those turns. Additionally, these induced currents tend to be higher on the side of the excited conductor (first conductor in this case). However, in real life applications, the current flows through the conductors of the winding simultaneously. We therefore have proximity effect of every conductor on the remaining

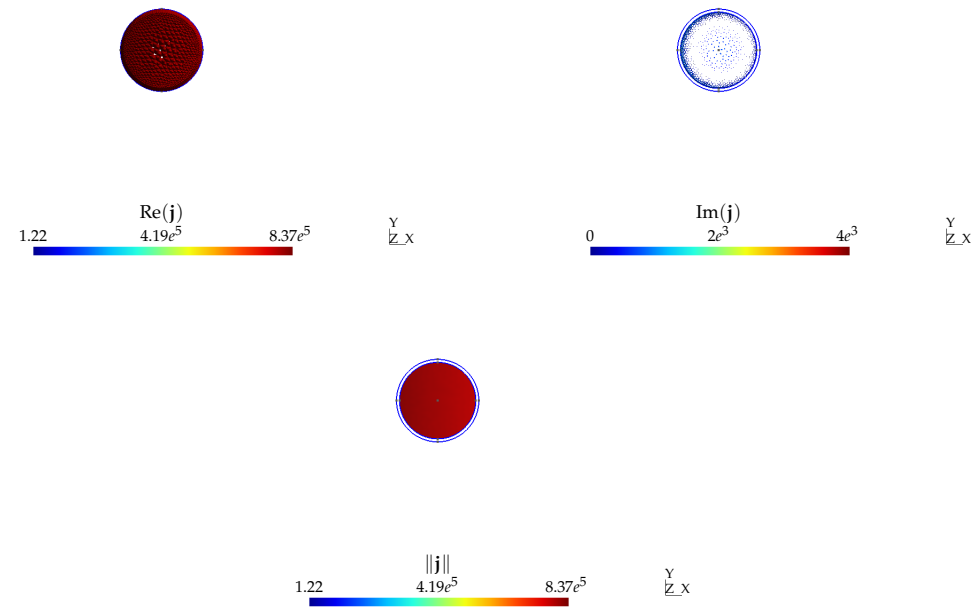

(a)

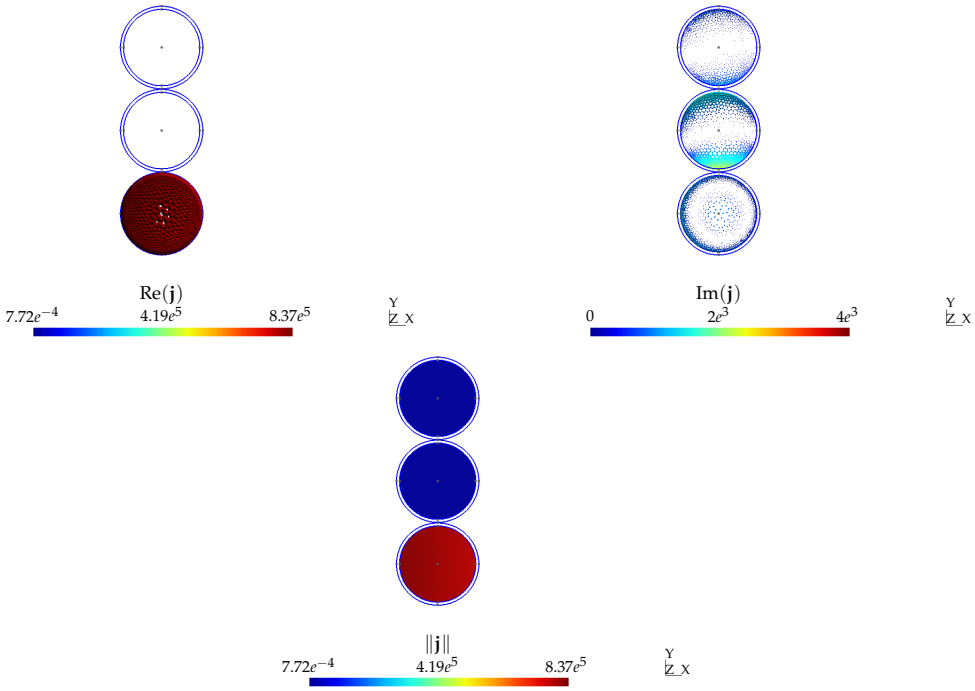

(b)

FIGURE 2.7: (a) The current density for a one turn winding at 40 Hz. (b) The current density for a three turns winding at 40 Hz when exciting the first turn (*conductor at the bottom*).

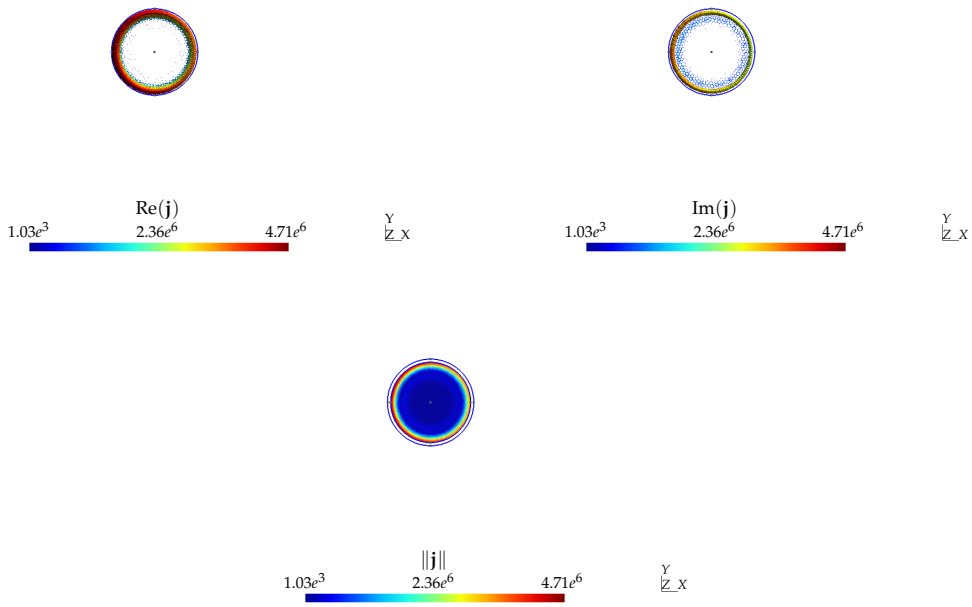

(a)

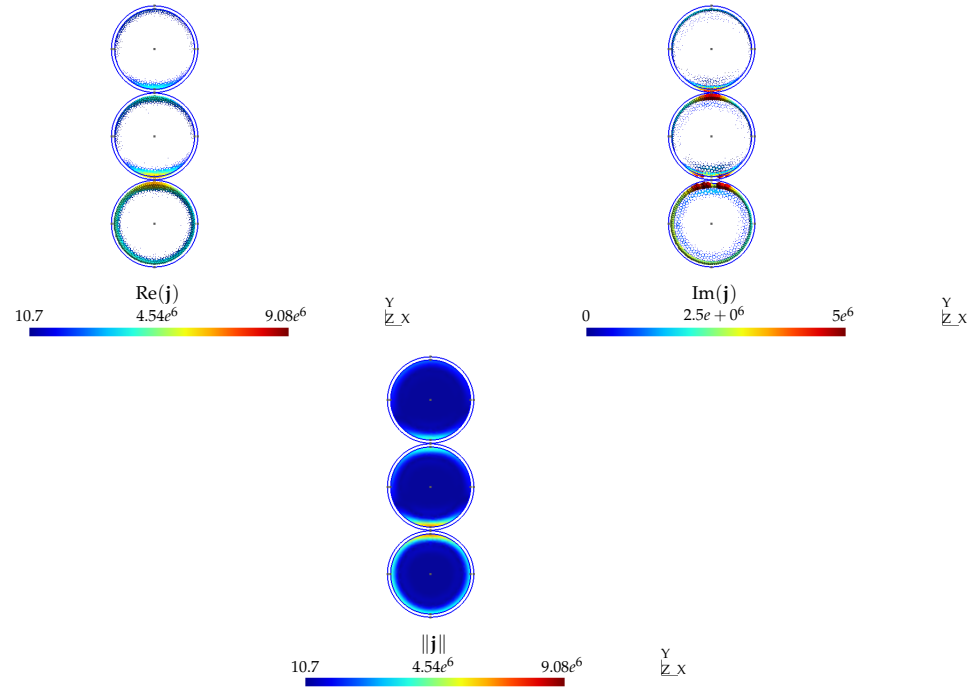

(b)

FIGURE 2.8: (a) The current density for a one turn winding at 1 MHz. (b) The current density for a three turns winding at 1 MHz when exciting the first turn (*conductor at the bottom*).

others as well as skin effect. To capture the overall impact of all conductors on each other, we set the three turns to $I_i = 1\,\text{A}$ for 40 Hz and 1 MHz. The current distribution is depicted in Fig. 2.9.

Here, not only do we capture the skin effect of each conductor but the different proximity effects conductors have on each other. Nonetheless, it is difficult to extract the values of the resistance of each conductor alone when all conductors are set to $I_i = 1\,\text{A}$ because the currents of the system matrix—three turns winding for this case—are all non-null. This complicates the identification by inspection.

To demonstrate, we describe the structure of the three turns winding using its impedance matrix $[\overline{\mathbf{Z}}]$:

$$[\overline{\mathbf{U}}] = [\overline{\mathbf{Z}}] \cdot [\overline{\mathbf{I}}]\,, \tag{2.23}$$

which, when written in matrix form, yields:

$$\begin{pmatrix} \overline{U}_1 \\ \overline{U}_2 \\ \overline{U}_3 \end{pmatrix} = \begin{pmatrix} \overline{Z}_{11} & \overline{Z}_{12} & \overline{Z}_{13} \\ \overline{Z}_{21} & \overline{Z}_{22} & \overline{Z}_{23} \\ \overline{Z}_{31} & \overline{Z}_{32} & \overline{Z}_{33} \end{pmatrix} \cdot \begin{pmatrix} \overline{I}_1 \\ \overline{I}_2 \\ \overline{I}_3 \end{pmatrix}, \tag{2.24}$$

where $\overline{U}_1$, $\overline{U}_2$ and $\overline{U}_3$ are the potential differences at the extremities of each conductor, whereas $\overline{I}_1$, $\overline{I}_2$ and $\overline{I}_3$ are the corresponding currents, respectively.

Exciting the three conductors simultaneously with real valued currents $I_i = 1\,\text{A}$ currents ($I_1 = I_2 = I_3 = 1\,\text{A}$) leads to the following set of equations:

$$\begin{cases} \overline{U}_1 = \overline{Z}_{11} \cdot 1\,\text{A} + \overline{Z}_{12} \cdot 1\,\text{A} + \overline{Z}_{13} \cdot 1\,\text{A}, \\ \overline{U}_2 = \overline{Z}_{21} \cdot 1\,\text{A} + \overline{Z}_{22} \cdot 1\,\text{A} + \overline{Z}_{23} \cdot 1\,\text{A}, \\ \overline{U}_3 = \overline{Z}_{31} \cdot 1\,\text{A} + \overline{Z}_{32} \cdot 1\,\text{A} + \overline{Z}_{33} \cdot 1\,\text{A}. \end{cases} \tag{2.25}$$

Supposing that the impedance matrix of the sample winding is symmetrical, which is often the case, we end up with six variables (*i.e.* $\overline{Z}_{11}$, $\overline{Z}_{22}$, $\overline{Z}_{33}$, $\overline{Z}_{12}$, $\overline{Z}_{13}$ and $\overline{Z}_{23}$) linked with only three equations, which makes an under-determined system of equations.

As a workaround, and in order to properly account for the general induced currents, we make use of the mutual resistances R_{ij} [167]–[170] that model the voltage drop in the j^{th} turn induced by the i^{th} turn. These mutual resistances refer to the resistance increase in the j^{th} turn due the presence of the nearby i^{th} turn, and model the distortion of both magnetic and electric fields. These resistances were not accounted for in previous research works [17], [34].

Considering only the resistive behaviour of the turns, the resistive couplings are exhibited in Fig. 2.10 for illustration.

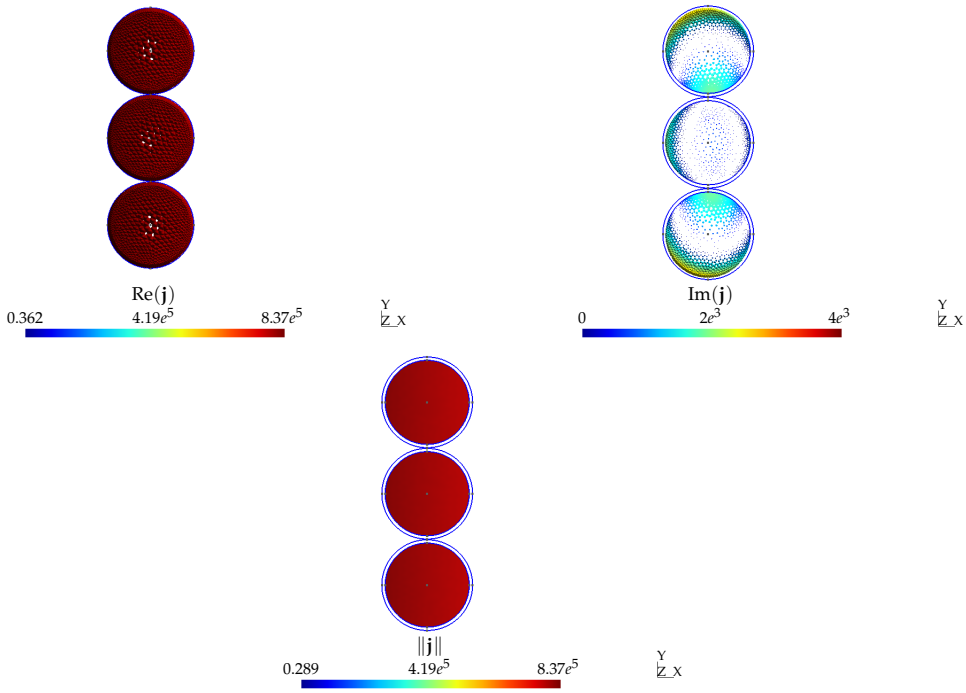

(a)

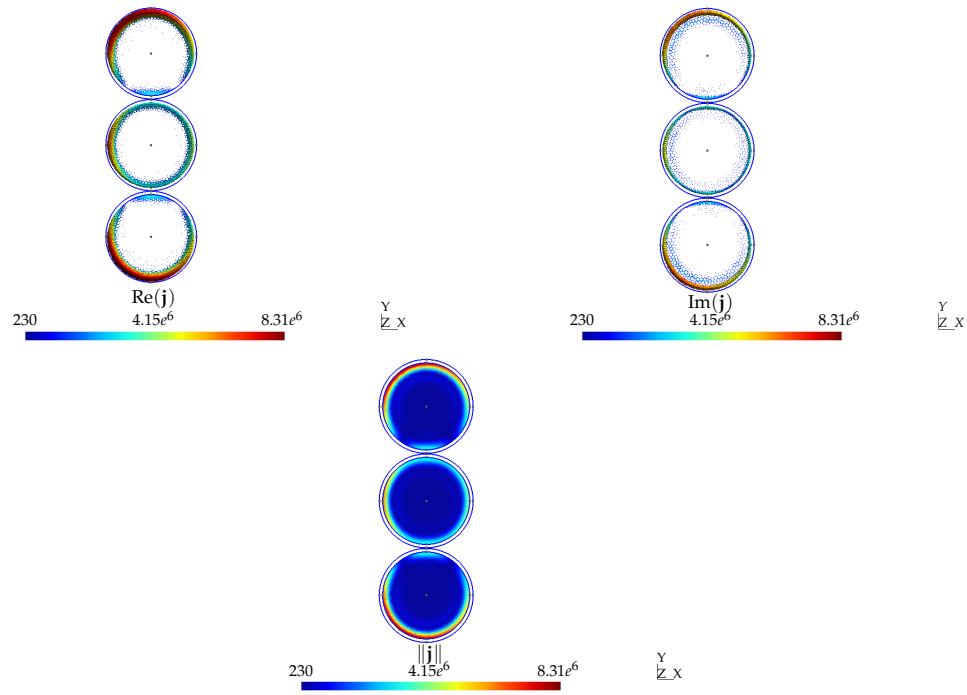

(b)

FIGURE 2.9: (a) The current density and distribution for the three turns winding at 40 Hz when all conductors are set to $I_i = 1$ A. (b) The current density and distribution for the three turns winding at 1 MHz when all conductors are set to $I_i = 1$ A.

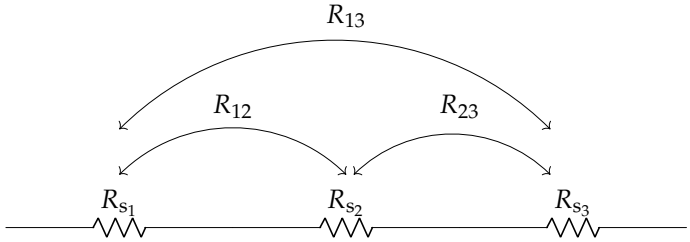

FIGURE 2.10: Illustration of the resistive coupling between turns.

To summarize, the ohmic losses within the turns of a given winding comprise the skin and proximity effects power dissipation. As a means to take them both into account and to properly model each turn alone, we deduce the self and mutual resistances of the studied winding by inspection using FEM by solving the magneto-dynamic formulation (2.22).

The ohmic losses resistance value can be computed in two ways:

- deduce the resistances from the computed Joule losses P_J;
- deduce the resistances from the computed impedance of the turn.

These two techniques are elaborated in the ensuing paragraphs.

2.3.1.1 From the Joule losses

The value of the resistance, whether self or mutual (R_{s_i} or R_{ij}, respectively) can be deduced from the Joule losses P_J defined as follows:

$$P_\mathrm{J} = \frac{1}{\sigma} \iiint_\mathrm{V} \mathbf{j}^2 \, d\mathrm{V}, \tag{2.26}$$

with V being the conductive volume of the studied problem, $\mathbf{j}$ the current density, and σ the electric conductivity.

To deduce the self resistance R_{s_i} from Joule losses, each conductor "i" is successively set to a given value I_i, while the others are set to $I_j = 0$ A. The expression of the resistance is straightforward:

$$R_{\mathrm{s}_i} = \frac{P_\mathrm{J}}{{I_i}^2}. \tag{2.27}$$

However, when it comes to the mutual resistance R_{ij}, both currents in the i^{th} and j^{th} turns are set to chosen values I_i and I_j respectively, while the others conductors $I_{\mathrm{k}\neq(i,j)}$ are set to 0 A.

The Joule losses expression is thus:

$$P_\mathrm{J} = R_{\mathrm{s}_i} {I_i}^2 + R_{\mathrm{s}_j} {I_j}^2 + \left(R_{ij} + R_{ji}\right) I_i I_j. \tag{2.28}$$

Since the conductors have the same electrical properties, (2.28) becomes:

$$\begin{aligned} P_\mathrm{J} &= R_{\mathrm{s}_i} {I_i}^2 + R_{\mathrm{s}_j} {I_j}^2 + 2\, R_{ij}\, I_i\, I_j, \\ &= R_{\mathrm{s}_i} {I_i}^2 + R_{\mathrm{s}_j} {I_j}^2 + 2\, R_{ji}\, I_j\, I_i. \end{aligned} \tag{2.29}$$

When using the Joule losses to compute the resistances for one frequency we need n computations to compute the self resistances R_{s_i} and $\binom{n}{2}/2$ computations for the mutual resistances R_{ij}, with $\binom{n}{2}$ being the number of two combinations needed out of a pool of n variables—in our case the turns—, and is defined as follows:

$$\begin{aligned}\binom{n}{2} &= \frac{n!}{2!\,(n-2)!} \\ &= \frac{n\,(n-1)}{2}.\end{aligned} \tag{2.30}$$

2.3.1.2 From the impedance of the turn

The value of the resistances could also be deduced from the self impedance of the turn. The latter is deduced from the computed global quantities: voltage across the turn $\overline{U}_i$ and the current flowing through it [162], [171], [172]. Accordingly, to compute the self resistance of the i^{th} turn R_{s_i}, the current of this turn is set to a chosen value of I_i, while the remaining turns are kept to $I_j = 0\,\text{A}$ and are only submitted to the induced currents.

The self impedance is expressed in (2.31), where its real part is the self resistance of the studied turn:

$$\begin{aligned}\overline{Z}_{s_i} &= \frac{\overline{U}_i}{I_i} \\ &= R_{s_i} + j\,L_{s_i}\,\omega.\end{aligned} \tag{2.31}$$

Concerning the mutual resistances R_{ij}, they are deduced from the quotient of the voltage drop in the j^{th} conductor and the current flowing through the energized i^{th} conductor I_i.

It is expressed as follows, and its real part is the mutual resistance:

$$\begin{aligned}\overline{Z}_{m_{ij}} &= \frac{\overline{U}_j}{I_i} \\ &= R_{ij} + j\,M_{ij}\,\omega.\end{aligned} \tag{2.32}$$

Hence, in order to identify the self and the different mutual resistive behaviours using the impedance when conductor i is excited with a current of a chosen value I_i, one computation is needed. Thus, when using the impedance to determine the resistances for an n-turns winding, we need n computations.

A comparative table of the number of computations needed for the different resistance identification techniques is presented in Tab. 2.2.

TABLE 2.2: Comparison of the number of computations needed for each resistance identification technique when studying an n-turns wind

Resistance identification technique	Number of computations
Using P_{J}	$n + \binom{n}{2}/2$
Using $\overline{Z}_{s_i}$ and $\overline{Z}_{m_{ij}}$	n

Eventually, for whatever identification technique, and for an n-turns winding, we end up with a matrix of the form seen in (2.33), where the diagonal values are the self resistances whereas the off-diagonal values are the different mutual resistances between turns.

$$\mathbf{R} = \begin{pmatrix} R_{s_1} & R_{12} & \cdots & R_{1n} \\ R_{12} & R_{s_2} & \cdots & R_{2n} \\ \vdots & \cdots & \ddots & \vdots \\ R_{1n} & R_{2n} & \cdots & R_{s_n} \end{pmatrix}. \tag{2.33}$$

2.3.2 The self and mutual inductances

The self inductance of the turn models the electromotive force generated by the magnetic flux flowing through it. The mutual inductance however, describes the magnetic interaction between the turns of the winding as depicted in Fig. 2.11. Therefore, a variation in the current of the i^{th} turn leads to the appearance of an induced voltage in the j^{th} turn and vice versa.

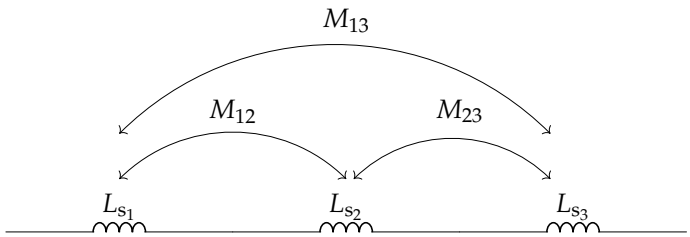

FIGURE 2.11: Illustration of the inductive coupling between turns.

The values of L_{s_i} and M_{ij} could be computed in three ways:

- deduce the inductances from the computed magnetic energy W_{m};
- deduce the inductances from the computed flux ϕ embraced by the turn;
- deduce the inductances from the computed impedances $\overline{Z}_{s_i}$ and $\overline{Z}_{m_{ij}}$ of the turn.

The three inductance identification techniques are elaborated hereinafter.

2.3.2.1 From the magnetic energy

Computing the self inductance of the i^{th} turn from the magnetic energy of the system is performed by setting the studied conductor to a chosen current value I_i and solving the magnetodynamic formulation (2.22) while keeping the remaining turns set to $I_j = 0$.

The stored magnetic energy W_{m} is computed as follows:

$$W_{\text{m}} = \frac{1}{2} \iiint_{\text{V}} \left(\overline{\mathbf{b}} \cdot \overline{\mathbf{h}} \right) d\text{V}, \tag{2.34}$$

where V is the volume of the studied problem, $\mathbf{b}$ is the magnetic induction, $\mathbf{h}$ is the magnetic field and "$\cdot$" denotes the complex scalar product.

The value of the self inductance is then deduced using the following expression:

$$L_{s_i} = \frac{2\,W_m}{{I_i}^2}. \tag{2.35}$$

Concerning the mutual inductance M_{ij} magnetically coupling the i^{th} and j^{th} turns, it is deduced after setting the two considered coupled turns to chosen current values I_i and I_j, respectively, while the remaining turns $I_{k\neq i,j}$ are set to 0 A.

Its expression is the following:

$$\begin{aligned} M_{ij} &= \frac{1}{I_i\,I_j}\left(W_m - \frac{1}{2}\,L_{s_i}\,{I_i}^2 - L_{s_j}\,{I_j}^2\right) \\ &= M_{ji}. \end{aligned} \tag{2.36}$$

When using the magnetic energy to compute the inductances, both self and mutual, and for an n-turns winding, we need $n + \binom{n}{2}/2$ computations.

2.3.2.2 From the magnetic flux density

A solenoid of n turns carrying a current $\overline{I}$, generates a magnetic field in its vicinity, which produces a flux through each loop expressed as follows:

$$\overline{\phi} = \iint_S \left(\overline{\mathbf{b}} \cdot \mathbf{n}\right)\, dS, \tag{2.37}$$

where $\mathbf{n}$ is the outward vector to the boundary of the studied geometry.

The inductance L_{s_i} of this solenoid is linked to the total flux ϕ flowing through it by the following expression:

$$\overline{\phi} = \frac{L_{s_i}\,\overline{I}}{n}. \tag{2.38}$$

By that means, each conductor is set to a chosen value I_i, while the remaining conductors are set to $I_j = 0$ A. The self inductance L_{s_i} is deduced from the flux flowing the through the surface bounded by the studied turn, whereas the mutual coupling with the remaining turns is computed from the flux seen by each corresponding turn.

When using the flux to compute the different inductances for an n-turns winding we need n computations, where we deduce the self and mutuals simultaneously at each computation.

2.3.2.3 From the impedance of the turn

As stated previously (refer to paragraph 2.3.1.2), the quotient of the two global quantities, the current and the voltage, defined for each conductor, yields the impedance. Thus, from (2.31) the self inductance is computed straightforwardly using the following expression

$$L_{s_i} = \frac{\mathrm{Im}\left(\overline{Z}_{s_i}\right)}{\omega}, \tag{2.39}$$

whereas the mutual inductances, also derived from the imaginary part of the mutual impedance, are expressed as

$$M_{ij} = \frac{\mathrm{Im}\left(\overline{Z}_{m_{ij}}\right)}{\omega}. \tag{2.40}$$

When using the impedance to identify the inductances for an n-turns winding, we need n computations.

A comparative table of the number of computations needed for the different inductance identification techniques is presented in Tab. 2.3.

TABLE 2.3: Comparison of the number of computations needed for each inductance identification technique when studying an n-turns winding

Inductance identification technique	Number of computations
Using W_m	$n + \binom{n}{2}/2$
Using ϕ	n
Using $\overline{Z}_{s_i}$ and $\overline{Z}_{m_{ij}}$	n

Eventually, for whatever inductance identification technique, the inductance matrix of the studied n-turns winding is symmetrical and is expressed in (2.41). The diagonal elements of the matrix contain the self inductances, whilst the off-diagonal elements contain the mutual inductances.

$$\mathbf{L} = \begin{pmatrix} L_{s_1} & M_{12} & \cdots & M_{1n} \\ M_{12} & L_{s_2} & \cdots & M_{2n} \\ \vdots & \cdots & \ddots & \vdots \\ M_{1n} & M_{2n} & \cdots & L_{s_n} \end{pmatrix}. \tag{2.41}$$

2.3.3 The dielectric losses parameters

The turns of a winding, either adjacent or not, are electrostatically influencing each other. They also exhibit an electrostatic coupling to the GND. This electrostatic influence is modelled by a capacitive coupling which could be computed in two ways, by solving (2.13) for v:

- deduce the capacitive coupling from the computed electric energy W_e;
- deduce the capacitive coupling from the computed charge $\overline{Q}$.

Both capacitive coupling identification techniques are elaborated hereinafter.

2.3.3.1 From the electric energy

The expression of the electric energy stored in the studied system is:

$$W_{\mathrm{e}} = \frac{1}{2} \iiint_{\mathrm{V}} \left(\overline{\mathbf{d}} \cdot \overline{\mathbf{e}} \right) \, d\mathrm{V}. \tag{2.42}$$

where V is the volume of the studied system, $\mathbf{d}$ is the electric induction and $\mathbf{e}$ is the electric field.

To compute the capacitive coupling from the electric energy, each turn is alternatively set to a chosen voltage value V_i while the others are set to $V_j = 0\,\mathrm{A}$. The value of the self capacitance C_i is deduced and expressed as:

$$C_i = \frac{2\,W_{\mathrm{e}}}{{V_i}^2}. \tag{2.43}$$

Then, the value of the inter-turn capacitance $C_{\mathrm{t}_{ij}}$ between the i^{th} and the j^{th} is computed as

$$\begin{aligned} C_{\mathrm{t}_{ij}} &= \frac{W_{\mathrm{e}} - \frac{1}{2}\,C_i\,{V_i}^2 - \frac{1}{2}\,C_j\,{V_j}^2}{V_i\,V_j} \\ &= C_{\mathrm{t}_{ji}}. \end{aligned} \tag{2.44}$$

In the case of the presence of a conductive magnetic core, the latter is considered the GND and is set to a chosen voltage value, while the n-turns are set to 0 V. Then the values of C_{G_i}, modelling the capacitive coupling of each turn i to the core, are deduced from (2.44) by replacing the subscript "j" by the subscript "G". In its absence, the turns are not kept floating and are coupled to the GND through the remaining spatial charges.

Following the same approach, the computation of the dielectric losses resistances $R_{\mathrm{t}_{ij}}$, can be deduced from the dielectric losses P_ε [173], [174]:

$$P_\varepsilon = \iiint_{\mathrm{V}} \varepsilon_0\,\varepsilon_{\mathrm{r}}''\,\omega\,\mathbf{e}^2\,d\mathrm{V}. \tag{2.45}$$

When using the electrical energy and the dielectric losses to identify the capacitive couplings for an n-turns winding, we need $n + 1 + \binom{n+1}{2}/2$ computations[2].

2.3.3.2 From the charges

The capacitive couplings can also be determined using the global quantity: the charge $\overline{Q}$. Thus, by setting a potential difference between two studied turns to a chosen voltage value $U_{ij}\,(= V_i - V_j)$ as the excitation of the system, the capacitive coupling is straightforwardly deduced[3]:

$$\begin{aligned} C_{\mathrm{t}_{ij}} &= \frac{\mathrm{Re}\left(\overline{Q}\right)}{U_{ij}} \\ &= C_{t_{ji}}, \end{aligned} \tag{2.46}$$

the dielectric losses resistances, on the other hand, are computed as follows:

$$\begin{aligned} R_{\mathrm{t}_{ij}} &= \frac{U_{ij}}{\mathrm{Im}\left(\overline{Q}\right)\,\omega} \\ &= R_{t_{ji}}. \end{aligned} \tag{2.47}$$

[2] In the case of an absence of the magnetic core only $n + \binom{n}{2}/2$ computations are needed.
[3] The same expressions are used for C_{G_i} and R_{G_i}

Therefore, for an n-turns winding, each conductor is alternatively set to a chosen voltage value V_i while the remaining $(n-1)$ turns are set to $V_j = 0\,\mathrm{A}$ (*i.e.* $U_{ij} = V_i$). In the absence of a magnetic core or when it is not conductive, the coupling of the turns to the GND is accounted for in order to avoid floating potentials, through the remaining spatial charges. To elaborate on this, in an electrostatic equilibrium and assuming the turn 1 is set to 1 V while the rest are short circuited (0 V), the charge $\overline{Q}_1$ on the first conductor is:

$$\overline{Q}_1 = \sum_{j=2}^{n} \overline{Q}_j + \overline{Q}_{\mathrm{G}_1}, \tag{2.48}$$

where $\overline{Q}_{\mathrm{G}_1}$ is the remaining spatial charge that serves as a capacitive coupling of the turn to the GND.

When using the electrical charge to identify the capacitive couplings for an n-turns winding, we need n computations.

A comparative table of the number of computations needed for the different capacitance identification techniques is presented in Tab. 2.4.

TABLE 2.4: Comparison of the number of computations needed for each capacitance identification technique when studying an n-turns winding

Capacitance identification technique	Number of computations
Using W_e	$n + 1 + \binom{n+1}{2}/2$
Using $\overline{Q}$	n

The capacitance and the dielectric losses resistance matrices of the studied n-turns winding are symmetrical matrices expressed in (2.49) and (2.50), respectively. The diagonal elements represent the coupling of turns to the GND, whilst the off-diagonal elements represent the inter-turn couplings.

$$\mathbf{C} = \begin{pmatrix} C_{\mathrm{G}_1} & C_{\mathrm{t}_{12}} & \cdots & C_{\mathrm{t}_{1n}} \\ C_{\mathrm{t}_{12}} & C_{\mathrm{G}_2} & \cdots & C_{\mathrm{t}_{2n}} \\ \vdots & \cdots & \ddots & \vdots \\ C_{\mathrm{t}_{1n}} & C_{\mathrm{t}_{2n}} & \cdots & C_{\mathrm{G}_n} \end{pmatrix}, \tag{2.49}$$

$$\mathbf{R}_\varepsilon = \begin{pmatrix} R_{\mathrm{G}_1} & R_{\mathrm{t}_{12}} & \cdots & R_{\mathrm{t}_{1n}} \\ R_{\mathrm{t}_{12}} & R_{\mathrm{G}_2} & \cdots & R_{\mathrm{t}_{2n}} \\ \vdots & \cdots & \ddots & \vdots \\ R_{\mathrm{t}_{1n}} & R_{\mathrm{t}_{2n}} & \cdots & R_{\mathrm{G}_n} \end{pmatrix}. \tag{2.50}$$

After elaborating on the different capacitance identification techniques, we will investigate experimentally the frequency dependent behaviour of the used insulation (PEI as a first layer and PAI as a top one). This is performed hereinafter.

2.3.3.3 Investigation of the frequency behaviour of the capacitive coupling

An experimental investigation has been performed in the LSEE laboratory to study the frequency dependent of the used dielectric materials. A classical wire sample with PEI as the first layer with PAI on top, was further coated with Gallium (Ga) as illustrated in Fig. 2.12, where r_a, r_b and L being the internal radius, the external radius and the length of the sample, respectively.

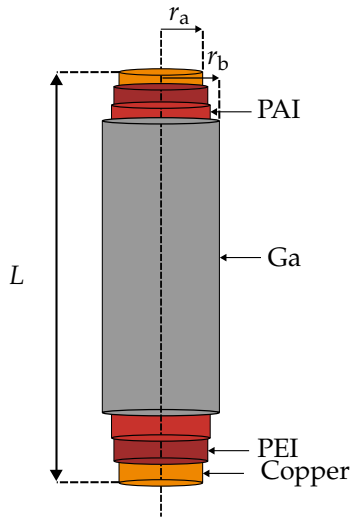

FIGURE 2.12: The measurement setup used to investigate the frequency behaviour of the capacitance with the help of Cristian Franzoi Mazzola.

This was carried out in order to create a cylindrical capacitor. Techniques of the sort, usage of liquid metals to ensure a capacitive coupling, are widely used for flat capacitors [175]. Using a liquid metal as an external electrode fills the potential empty spaces, enabling hence a better characterization of the material. The choice of the Ga is justified by the fact that it is relatively safe to deal with in elemental form and is easily accessible on the market, in comparison to the mercury. Moreover, it has a melting point of 30 °C which is just above room temperature (20 °C - 22 °C). It was melted with warm water and applied with a syringe where it proved a good adhesion to the wire insulation. Next, the impedance measurements were performed using the impedance analyser Agilent 4980A [176].

The measured impedance is of the following expression:

$$\begin{aligned} \overline{Z}_c(f) &= \frac{1}{j\,\overline{C}(f)\,\omega} \\ &= \frac{\ln\left(\frac{r_a}{r_b}\right)}{2\,\pi\,L\,\varepsilon_0\,\bar{\varepsilon}_r(f)\,\omega} \\ &= \left(\frac{1}{R_t} + j\,C_t\,\omega\right)^{-1}. \end{aligned} \tag{2.51}$$

A straightforward identification enables to extract the variations of the real and imaginary parts of $\bar{\varepsilon}_r$ from $\overline{Z}_c(f)$ and are depicted in Fig. (2.13).

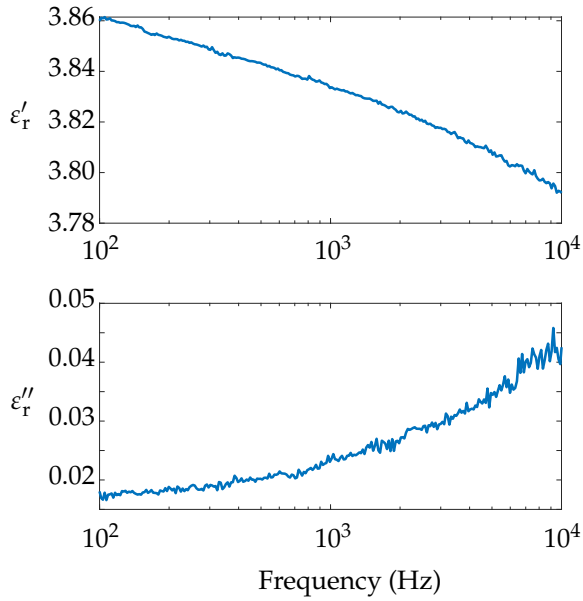

FIGURE 2.13: The deduced frequency behaviour of ε'_r and ε''_r.

The frequency variations of ε'_r and ε''_r were presented up to 10 kHz since the values beyond this frequency start to get impacted by the beginning of a resonance with the different parasitic inductances. This can be seen when changing the logarithm scaling into a semi-logarithmic as presented in Fig. (2.14).

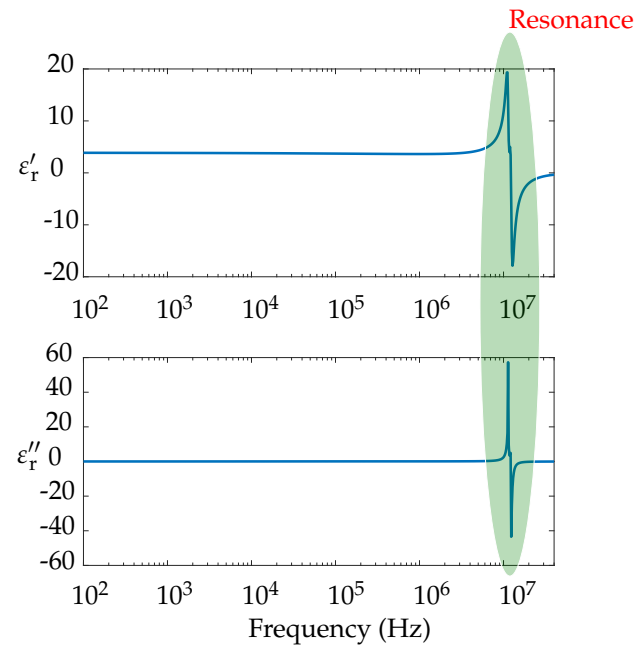

FIGURE 2.14: The resonance of the measured capacitance and the parasitic inductance present in the measurement setup.

Upon zooming on the ranges of interest, we notice the beginning of the resonance in Fig. 2.15 and after the resonance in Fig. 2.16.

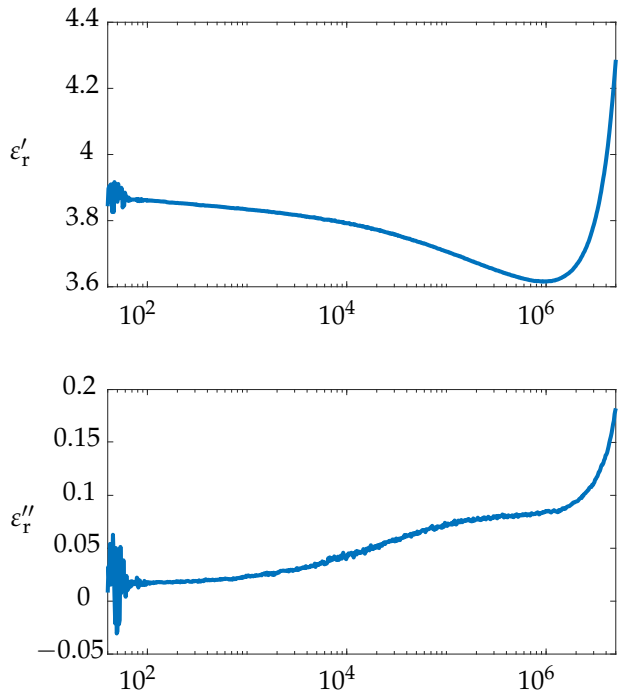

FIGURE 2.15: The low and medium frequency behaviour of the measured complex dielectric permittivity before the resonance happens.

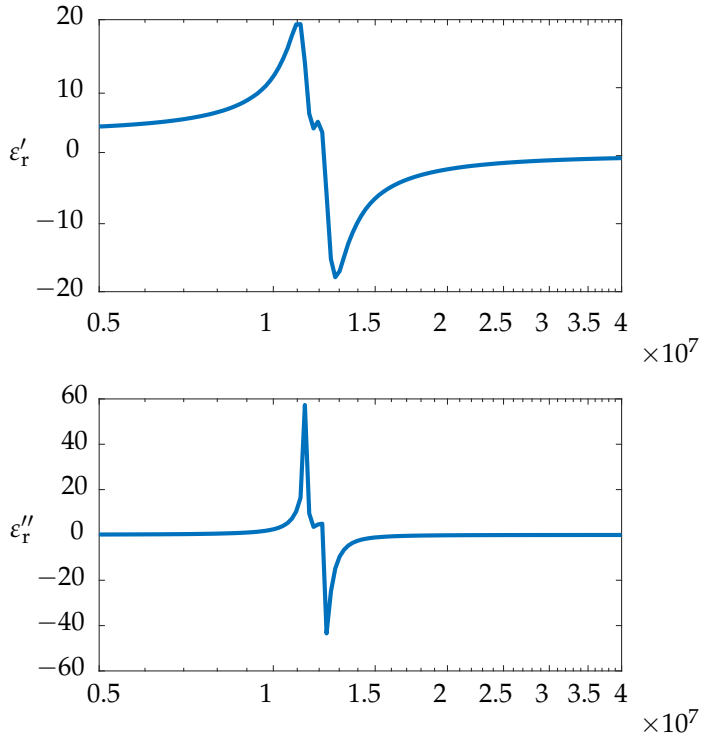

FIGURE 2.16: The high frequency behaviour of the measured complex dielectric permittivity during and after the resonance occurs.

Further studies on the high frequency behaviour of the permittivity have to be carried out by either including the existence of the parasitic inductance in the measured impedance, or proposing a new experimental setup. This is left for the future work. For this research work, we consider the capacitive coupling invariant according to frequency.

It should be emphasized that the computed values of the different parameters are per unit length, hence, a scaling by the appropriate geometrical coefficient is mandatory.

At this stage, we have presented the different identification techniques of the adopted LPM parameters and experimentally investigated the frequency behaviour of the capacitive coupling. The next section discusses and compares the different identification techniques and justifies the choice of one over the other in terms of accuracy and number of computations needed.

2.4 Comparison of the identification techniques

After presenting the different identification techniques for each parameter, a choice has to be made on which one to use in order to launch the computations. This section studies the differences between the identification techniques in terms of the computational time and accuracy of the FEM results. For this, a one layer three turns ($n = 3$) winding sample presented in Fig. 2.17, is used for illustration and comparison.

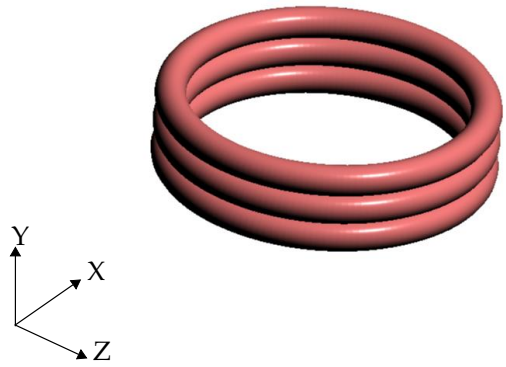

FIGURE 2.17: The 3D geometry of the three turns winding used to compare the different identification techniques.

The geometrical definition of this test case is summarized in Tab. 2.5, where d_c, ℓ_{insul}, e_{it}, σ_{copper} and r_{air} are the conductor diameter, the thickness of the PEI insulation layer (PAI was not considered), the inter-turn spacing, the copper conductivity and the distance between the conductors and the symmetry axis, respectively.

TABLE 2.5: The geometrical and electrical definition of the three turns winding sample.

n	3 turns
n_{ℓ_1}	3 turns
d_c	1.25 mm
σ_{copper}	60 MS
ℓ_{insul}	0.0495 mm
$\bar{\varepsilon}_{PEI}$	$(3.5 - j\,0.5)\ \varepsilon_0$
e_{it}	0.01 mm
r_{air}	23.1501 mm

The chosen geometry enables to reduce of the 3D model (Fig. 2.17) to a 2D one (Fig. 2.18) by accounting for its axisymmetric property during the FEM resolution. The IET is performed in the annular region bounded by R_{int} and R_{ext} radii.

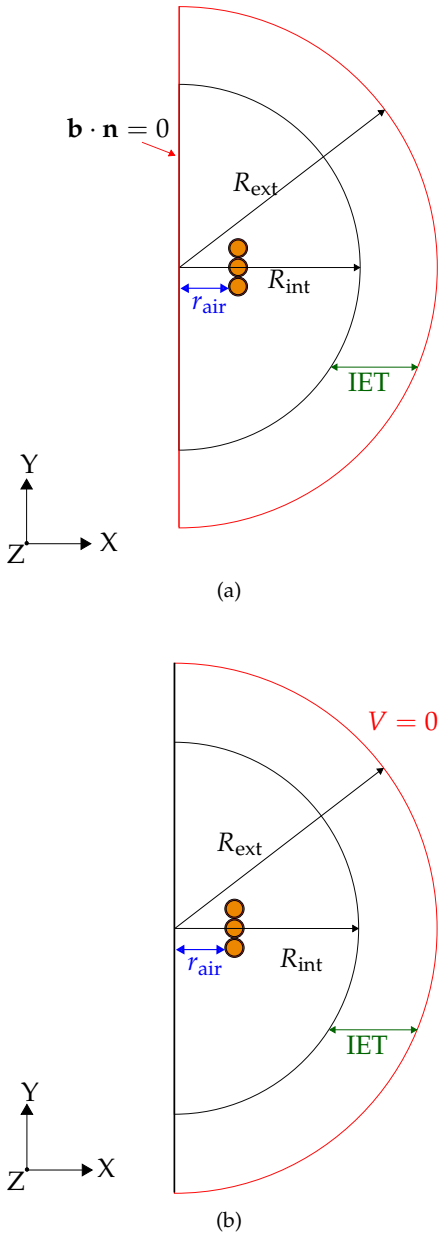

FIGURE 2.18: The studied 2D cross-section geometry of the three turns winding, and the corresponding boundary conditions consisting in (a) supposing a null flux ϕ in magneto-dynamics study at both infinity and the axisymmetric axis (b) a null voltage at infinity in an electrostatic study.

For this work we use Gmsh [177] to generate and mesh the geometries, whereas, the FEM resolution of the context-appropriate formulation is performed in the complex frequency domain using the solver GetDP [178].

With the geometrical definition of the three turns winding sample complete, comes the selection of the identification technique to be used. This is discussed in the coming section.

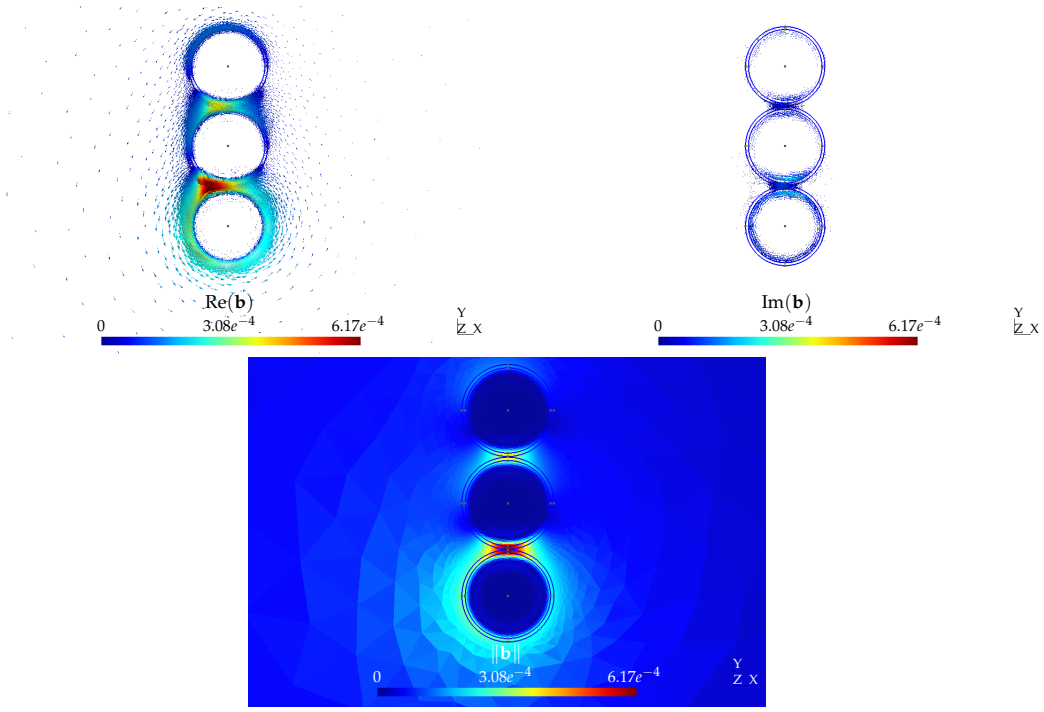

FIGURE 2.19: An example of the magnetic induction distribution when the first turn (*conductor at the bottom*) is set to 1 A at 1 MHz.

2.4.1 The Ohmic losses resistance

The ohmic losses resistance can be computed either from the Joule losses (2.26) or the impedance of the turn (as in (2.31) for R_{s_i} and (2.32) for R_{ij}). This is performed after solving the magneto-dynamic formulation (2.22) for the magnetic vector potential $\mathbf{a}$. An example of the magnetic field distribution when the first conductor is set to 1 A is presented in Fig. 2.19 at 1 MHz.

The resistance identification techniques are compared in Tab. 2.6 when computing the self resistance R_{s_i} together with the values deduced from the analytical expression (1.1) where the proximity effect is not accounted for and ℓ in this case being the length of the turn ($\ell = 2\,\pi\,r_{\text{air}} = 2\,\pi \times 23.1501\,\text{mm}$).

Here, the comparison is performed on the computed resistance of the first turn : $i = 1$[4], the remaining turns are set to 0 A.

[4]The same conclusions were drawn when studying the other turns.

TABLE 2.6: Comparison of the resistance identification techniques.

Frequency (Hz)	R_{s_1} (mΩ) from (1.1)	R_{s_1} (mΩ) from P_J	R_{s_1} (mΩ) from $\overline{Z}_{s_i}$
40	2.033	2.033	2.033
10^3	2.033	2.034	2.034
10^4	2.036	2.179	2.179
10^5	3.700	5.756	5.756
10^6	10.31	21.57	21.57
10^7	31.14	78.99	78.99

As noticed in Tab. 2.6, the resistance deduced from the Joule losses and the resistance deduced from the impedance are exactly the same. We also notice a difference between using the latter techniques and the analytical method where only skin effect is accounted for.

Concerning the mutual resistances, we study R_{12}, the comparative study is presented in Tab. 2.7, where we notice that no matter the chosen identification technique the values are again the same, which is expected. We also notice the extremely small value of R_{12} at low frequencies, where practically no proximity effect takes place.

TABLE 2.7: Comparison of the mutual resistance identification techniques.

Frequency (Hz)	R_{12} (Ω) from P_J	R_{12} (Ω) from $\overline{Z}_{m_{ij}}$
40	$0.75\,10^{-9}$	$0.75\,10^{-9}$
10^3	$4.95\,10^{-8}$	$4.95\,10^{-8}$
10^4	$4.55\,10^{-5}$	$4.55\,10^{-5}$
10^5	$4.37\,10^{-4}$	$4.37\,10^{-4}$
10^6	$9.02\,10^{-4}$	$9.02\,10^{-4}$
10^7	$1.73\,10^{-3}$	$1.73\,10^{-3}$

The comparison of the computed values of both the self R_{s_i} and the mutual R_{ij} resistances serves as a verification that the studied identification methods give indeed the same values. Hence, the choice of the resistance identification technique is solely based in this case on the required number of computations. As highlighted in Tab. 2.2, using the impedance, we only need n-computations (n = 3 for the studied winding sample). Therefore, the resistances are deduced from the impedance in this work.

2.4.2 The self and mutual inductances

The computation of the inductances, both self and mutual, could be done in three ways: they could be deduced from the magnetic energy (2.35), the magnetic flux (2.38), or the characteristic impedance of the turn (2.31) and (2.32). The three aforementioned inductance identification techniques are compared for various frequency samples in this section. The self inductance results are presented in Tab. 2.8, whereas the mutual inductance values are seen in Tab. 2.9.

TABLE 2.8: Comparison of the self inductance identification techniques.

Frequency (Hz)	L_{s_1} (nH) from W_m	L_{s_1} (nH) from $\overline{Z}_{s_i}$	L_{s_1} (nH) from ϕ
40	118.38	118.38	118.40
10^3	118.38	118.38	118.39
10^4	117.60	117.80	117.80
10^5	109.00	109.50	109.50
10^6	102.41	102.50	102.50
10^7	99.38	99.86	99.86

TABLE 2.9: Comparison of the mutual inductance identification techniques.

Frequency (Hz)	M_{12} (nH) from W_m	M_{12} (nH) from $\overline{Z}_{m_{ij}}$	M_{12} (nH) from ϕ
40	88.07	88.08	88.09
10^3	88.07	88.08	88.09
10^4	87.84	87.85	87.85
10^5	85.93	85.95	85.95
10^6	85.57	85.58	85.58
10^7	85.50	85.52	85.52

We can see that the values of the inductances are the same no matter the chosen method. Moreover, the decrease of the values according to the frequency is captured as well, modelling thus the flux penetration.

This comparative study serves as a verification of the aforementioned inductance identification techniques. Since the purpose is to develop a predictive model with the lowest computational complexity possible, the number of computations needed for each method is compared. Using the first method, for an n-turns winding, n computations are needed to compute the self

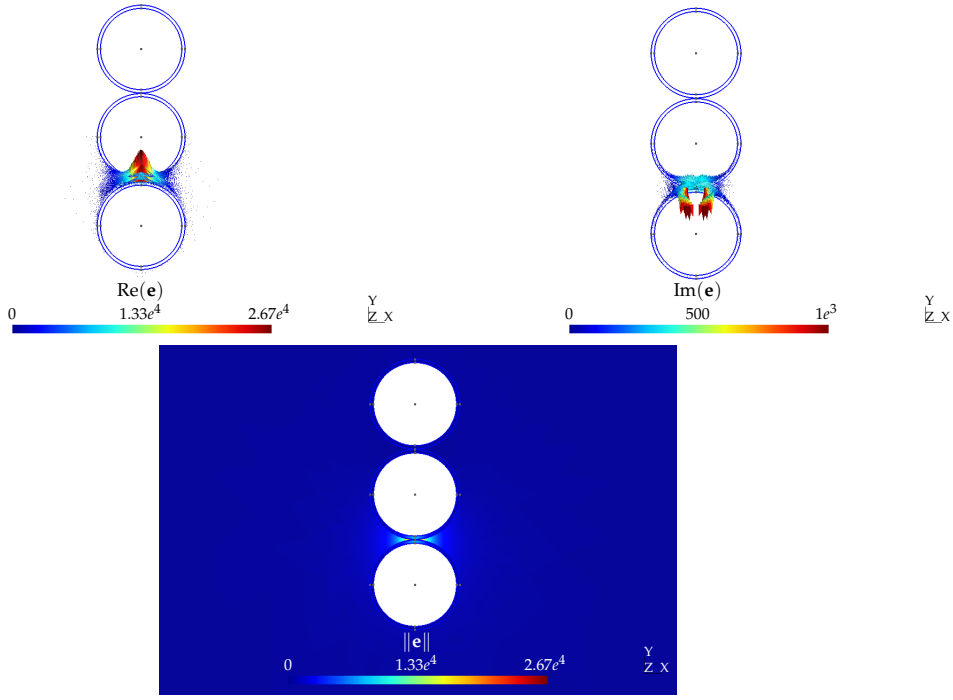

FIGURE 2.20: An example of the electric field distribution when the first turn (*conductor at the bottom*) is set to 1 V at 40 Hz.

inductances and $\binom{n}{2}/2$ computations to deduce the mutual couplings between turns. Nevertheless, using the second and third identification techniques, only n computations are needed to compute both the self and mutual inductances.

For this work, the latter are deduced from the numerically computed impedance of the studied turn (L_{s_i} is deduced from (2.31), whereas M_{ij} is deduced from (2.32)). Hence, for an n-turns winding, we need n computations to deduce simultaneously the resistance and inductances matrices.

2.4.3 The dielectric losses parameters

The capacitive coupling between turns could be deduced from either the electric energy (2.44), or the charge on the conductors (2.46). An example of the electrical field distribution is presented in Fig. 2.20, where the first turn of the three turns winding is set 1 V while the remaining two are short circuited (set to 0 V).

The two capacitive coupling identification techniques have both been extensively studied and validated in the literature [13], [17], [34], [55], [71], [167]. Consequently, the comparative study is performed according to the number of computations needed to fully electrostatically model the winding. Using the first method, and in the case of an n-turns winding, (n+1) computations are needed to compute the values of the self capacitances as expressed in (2.43), and $\binom{n+1}{2}/2$ more computations are needed to eventually deduce the different capacitive couplings between turns. Nevertheless, adopting the second identification technique, only n computations are needed, whether there is a magnetic core or not.

In this work, we use the second capacitive coupling identification technique.

To summarize, for each parameter, the chosen identification technique is seen in Tab.2.10.

TABLE 2.10: The chosen identification technique for each parameter.

Parameter	The chosen identification technique
The self and mutual resistances	From (2.31) and (2.32), respectively
The self and mutual,inductances	From (2.31) and (2.32) respectively
Turn-to-turn and turn-to-GND capacitances	From (2.46)
Turn-to-turn and turn-to-GND resistances	From (2.47)

At this stage, we have proposed a FEM model that allows to compute by inspection the values of the parameters on the frequency range of interest.

In the next section, we will see how to account for this frequency dependency in frequency domain simulations without having to use fitting techniques.

2.5 The proposed elementary cell of the winding

In order to account for the frequency behaviour of the winding, the parameters of the model are computed at different frequency samples within the frequency range of interest. The latter extends from $f_1 = 40\,\text{Hz}$ to $f_\text{m} = 110\,\text{MHz}$ (frequency range of the used impedance analyser, with "m" being the number of frequency samples). Therefore, each parameter is henceforth a vector of values according to frequency. Ergo, after m computations (the value depends on the sampling of the frequency range), (2.33) becomes:

$$\mathbf{R}_n^\text{m} = \begin{pmatrix} R_{s_1}(f_1) & R_{12}(f_1) & \cdots & R_{1n}(f_1) \\ R_{12}(f_1) & R_{s_2}(f_1) & \cdots & R_{2n}(f_1) \\ \vdots & \cdots & \ddots & \vdots \\ R_{1n}(f_1) & R_{2n}(f_1) & \cdots & R_{s_n}(f_1) \end{pmatrix} \begin{matrix} \\ \\ \\ \\ \end{matrix} \begin{pmatrix} R_{s_1}(f_\text{m}) & R_{12}(f_\text{m}) & \cdots & R_{1n}(f_\text{m}) \\ R_{12}(f_\text{m}) & R_{s_2}(f_\text{m}) & \cdots & R_{2n}(f_\text{m}) \\ \vdots & \cdots & \ddots & \vdots \\ R_{1n}(f_\text{m}) & R_{2n}(f_\text{m}) & \cdots & R_{s_n}(f_\text{m}) \end{pmatrix} \quad , \tag{2.52}$$

n (under the first matrix) ; m (along the diagonal)

and (2.41) becomes:

$$\mathbf{L}_n^{\mathrm{m}} = \begin{pmatrix} L_{\mathrm{s}_1}(f_1) & M_{12}(f_1) & \cdots & M_{1n}(f_1) \\ M_{12}(f_1) & L_{\mathrm{s}_2}(f_1) & \cdots & M_{2n}(f_1) \\ \vdots & \cdots & \ddots & \vdots \\ M_{1n}(f_1) & M_{2n}(f_1) & \cdots & L_{\mathrm{s}_n}(f_1) \end{pmatrix} \begin{pmatrix} L_{\mathrm{s}_1}(f_{\mathrm{m}}) & M_{12}(f_{\mathrm{m}}) & \cdots & M_{1n}(f_{\mathrm{m}}) \\ M_{12}(f_{\mathrm{m}}) & L_{\mathrm{s}_2}(f_{\mathrm{m}}) & \cdots & M_{2n}(f_{\mathrm{m}}) \\ \vdots & \cdots & \ddots & \vdots \\ M_{1n}(f_{\mathrm{m}}) & M_{2n}(f_{\mathrm{m}}) & \cdots & L_{\mathrm{s}_n}(f_{\mathrm{m}}) \end{pmatrix}$$

(n: blue arrow; m: red arrow). (2.53)

However, and as stated earlier in paragraph in 2.3.3.3, the capacitance and the dielectric losses matrices are only computed at low frequency (40 Hz for this work), and remain therefore two-dimensional,

$$\mathbf{C} = \begin{pmatrix} C_{\mathrm{G}_1} & C_{\mathrm{t}_{12}} & \cdots & C_{\mathrm{t}_{1n}} \\ C_{\mathrm{t}_{12}} & C_{\mathrm{G}_2} & \cdots & C_{\mathrm{t}_{2n}} \\ \vdots & \cdots & \ddots & \vdots \\ C_{\mathrm{t}_{1n}} & C_{\mathrm{t}_{2n}} & \cdots & C_{\mathrm{G}_n} \end{pmatrix} \quad (n), \tag{2.54}$$

$$\mathbf{R}_\varepsilon = \begin{pmatrix} R_{\mathrm{G}_1} & R_{\mathrm{t}_{12}} & \cdots & R_{\mathrm{t}_{1n}} \\ R_{\mathrm{t}_{12}} & R_{\mathrm{G}_2} & \cdots & R_{\mathrm{t}_{2n}} \\ \vdots & \cdots & \ddots & \vdots \\ R_{\mathrm{t}_{1n}} & R_{\mathrm{t}_{2n}} & \cdots & R_{\mathrm{G}_n} \end{pmatrix} \quad (n). \tag{2.55}$$

Once the values have been computed using FEM, and since the impedance of each turn is deduced numerically and not from measurements, the first though is to build up from the LPM model (refer to Fig. 1.7) by applying the VF algorithm for each turn. Hence, an upgraded circuit per turn similar to the one seen in Fig. 2.21, where the sub-circuit highlighted in red is deduced by applying VF to the self admittance of each turn.

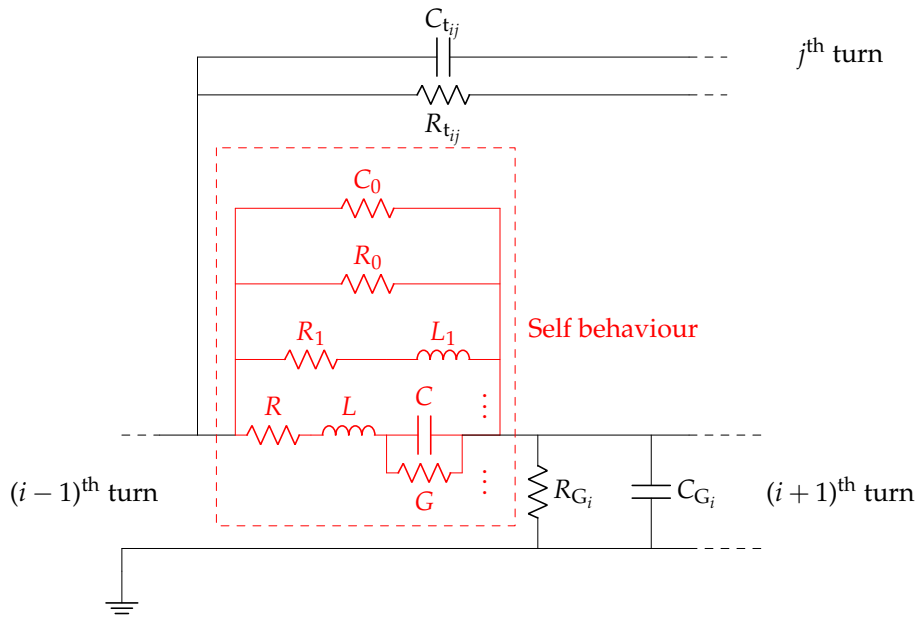

FIGURE 2.21: Upgrading the template model using vector fitting in order to account for the frequency dependent behaviour of the parameters.

Consequently, each turn becomes a combination of branches with constant valued passive components (R_0, C_0, R_1, L_1, R, L, C and G), with each branch duplicated (with different values of course) as many times as the used number of poles for the fitting. This is depicted using the red vertical dots. The real poles used for the fitting are represented with the R_1 in series with L_1 branch, whereas each conjugate pair of complex poles is represented with the R,L, C and G branch.

Nonetheless, generating the VF passive circuit calls for the intervention of the user in order to properly set up the fitting parameters: number of poles, the type spacing (logarithmically spaced poles or linearly spaced poles), the chosen weighting, etc. This makes the methodology no longer automatic, heavily dependent on the winding to be studied, and its precision reliant on the chosen parameters of the fitting. Another inconvenience emerges after generating the VF equivalent circuit for each turn in accounting for the mutual inductive and resistive behaviour between turns. In this case the mutually inductive and resistive couplings are forsaken because the fitted admittance is of the following expression:

$$\overline{Y}_{s_i}(f) = \frac{1}{R_{s_i}(f) + j\, L_{s_i}(f)\, \omega}. \tag{2.56}$$

To find a solution, and starting with the mutual inductive coupling, we need to first of all understand how the frequency-independent behaviour was taken into account in previous work with the used circuit simulator LTspice [179]. In the latter, the frequency-independent mutual inductive coupling between inductors is taken into account using the mutual coupling coefficient k. An example is portrayed in Fig. 2.22, where the inductors L_1 and L_2 are inductively coupled with a factor k whose definition was already viewed in (1.3).

FIGURE 2.22: Accounting for the mutual coupling using LTspice syntax.

This solution cannot be implemented for our case because once the VF equivalent circuit is deduced, the model of each turn is no longer a simple resistance in series with an inductance (as seen in Fig. 2.21) but rather an electrical circuit. The used inductances serve for fitting purposes only and are devoid of physical meaning.

To consider the mutual couplings in this case, it is mandatory to add multiple ($= n - 1$, with n being the number of turns) behavioural voltage sources in series with each turn i, whose expressions are the following:

$$V_{ij} = \sum_{j=1, j\neq i}^{n} M_{ij} \frac{\partial I_j}{\partial t}. \tag{2.57}$$

where $\partial I_j/\partial t$ is automatically converted by LTspice to $j\, I_j\, \omega$ in frequency domain simulations. These behavioural voltage sources link the current of the turn to the mutually induced voltage, consequently modelling the mutual inductive coupling. Therefore, the circuit represented in Fig. 2.22, used for illustration, becomes that seen in Fig. 2.23.

FIGURE 2.23: Accounting for the inductive coupling using behavioural voltage sources.

Applying this on the elementary cell seen in Fig. 2.21, we get the new equivalent turn model presented in Fig 2.24.

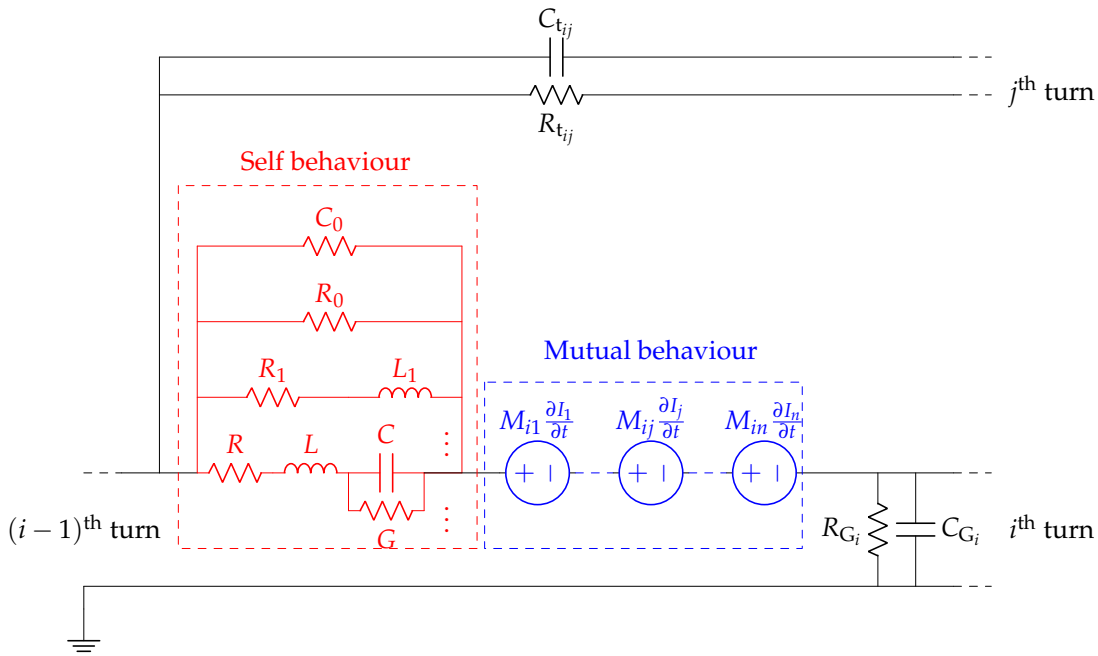

FIGURE 2.24: Upgrading the elementary cell of the winding to account for the mutual inductive coupling.

Using this technique the frequency behaviour of $M_{ij}(f)$ is not taken into account. An alternative solution could be to account for $M_{ij}(f)$ by including it with the self inductive behaviour of each turn as portrayed in Fig. 2.25.

FIGURE 2.25: Accounting for the inductive coupling as another self.

Therefore, when using the VF algorithm the fitted admittance of each turn (2.56) is redefined to become:

$$\begin{cases} \overline{Y}_{s_i}(f) = \dfrac{1}{R_{s_i}(f) + j\, L_{eq_i}(f)\, \omega}, \\ L_{eq_i}(f) = L_{s_i}(f) + \displaystyle\sum_{j=1, j\neq i}^{n} M_{ij}(f). \end{cases} \tag{2.58}$$

However, this hypothesis allows the redefinition of the admittance of each turn by implying that the current flowing through all the turns is the same ($I_1 = I_2 = I_3$ in Fig. 1.9 for instance), which contradicts with the subject of this work.

The same difficulty was encountered when willing to account for the presence of the mutual resistances. Following the same approach performed on the mutual inductances, the resistances R_{ij} could be accounted for using behavioural voltage sources. Hence, the simplified circuit portraying the resistive coupling:

FIGURE 2.26: Accounting for the resistive coupling using behavioural voltage sources.

However, its frequency behaviour is neglected.

Given the difficulties encountered to account for the mutual couplings between the turns (both resistive and inductive), we decided to make use of LTspice look-up tables. This has enabled to relinquish the usage of the VF fitting algorithm altogether, although a very powerful tool, it proved unnecessary for this work. The idea behind the LTspice look-up tables allows for inserting the scatter plots deduced from the computations directly into the netlist without the need of an intermediate step whatsoever. Whenever an interpolation is necessary, the circuit simulator takes care of it. This has allowed using the behavioural voltage sources enabling to model both the self and mutual behaviour of the turn. The proposed model of each turn is presented in Fig. 2.27.

The 0 V voltage source is used so as to permit measuring the current of the turn that is later on used in the computation of the mutual inductive and resistive coupling, henceforth referred to as impedance coupling. It has an internal series resistance of 1 nΩ to avoid ending up with parallel voltage sources.

One might argue that the same current could be measured from a series resistor of 1 nΩ. However, the used circuit simulator assumes that the current flowing through the circuit elements is quasi-static. Ergo, the usage of the 0 V voltage source as a current sensor. The behavioural voltage source B_{s_i} links the current flowing through the turn to its voltage with the self impedance (inverse of (2.56)) and is saved in a table, whereas, the remaining behavioural voltage sources $B_{m_{i1}}$, $B_{m_{ij}}$ and $B_{m_{in}}$ reproduce the electromotive forces modelling the impedance coupling with the remaining turns also saved in tables. Particularly speaking, they link the induced voltages to the currents with the coupling impedances. This way, not only the frequency dependency of the self behaviour is accounted for, but that of the impedance couplings as well.

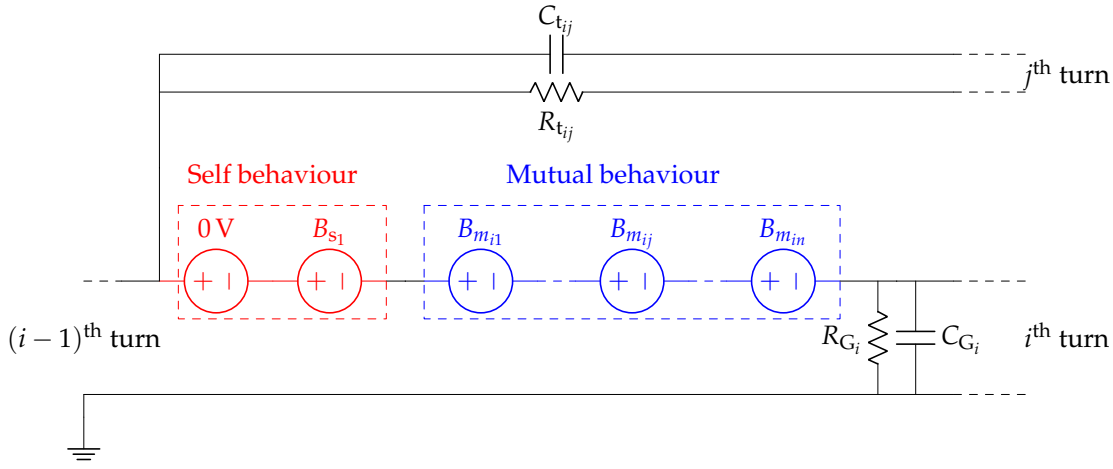

FIGURE 2.27: Upgrading the elementary cell of the winding to account for the frequency dependent behaviour of its parameters both self or mutual.

The tables in which the values according to frequency are stored are of the structure seen in Tab. 2.11. It is a three row matrix, where the first row contains the frequency samples, whilst the second and third rows contain the corresponding module in Ohms and phase $\Phi(f)$ in degrees of the called impedance $\overline{Z}(f)$, respectively.

TABLE 2.11: An **.inc** file example.

$$
\begin{array}{lll}
+(f_1, & Z(f_1), & \Phi(f_1)) \\
+(f_2, & Z(f_2), & \Phi(f_2)) \\
+(f_3, & Z(f_3), & \Phi(f_3)) \\
\vdots & \vdots & \vdots \\
+(f_m, & Z(f_m), & \Phi(f_m))
\end{array}
$$

Again, using the three turns winding for illustration, the model of the winding is upgraded from Fig. 1.10 to Fig. 2.28.

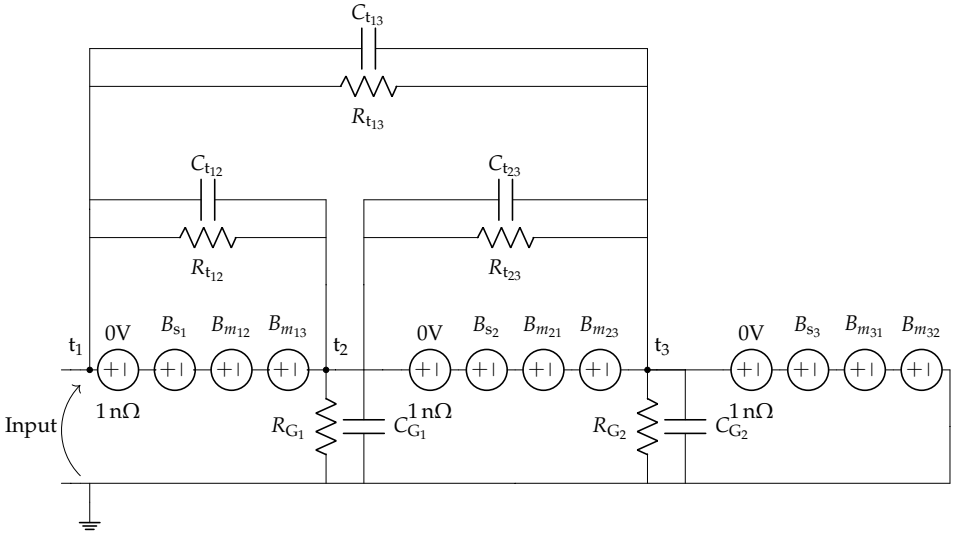

FIGURE 2.28: The proposed model applied on the three turns winding sample.

It is noteworthy that even though the presented winding sample is of only three turns, building the model manually is both time consuming and laborious. An automation of the corresponding netlist generation is therefore a must and we use python for that.

At this stage, we have accounted for the frequency behaviour of the parameters in a frequency domain simulation including the impedance coupling between turns. The proposed elementary cell accounts not only for the frequency behaviour of the self impedance but that of the mutual impedance as well without having to call for the usage of any fitting technique whatsoever. The proposed tool is hence automatic, not needing the intervention of the user to correctly parametrize the fitting procedure.

The flowchart of the proposed tool is seen in Fig. 2.29.

In the next section, we will test the proposed model by comparing the computed frequency response—impedance—of different test case with its corresponding frequency measurement. The robustness of the model is also tested by studying test cases with magnetic materials.

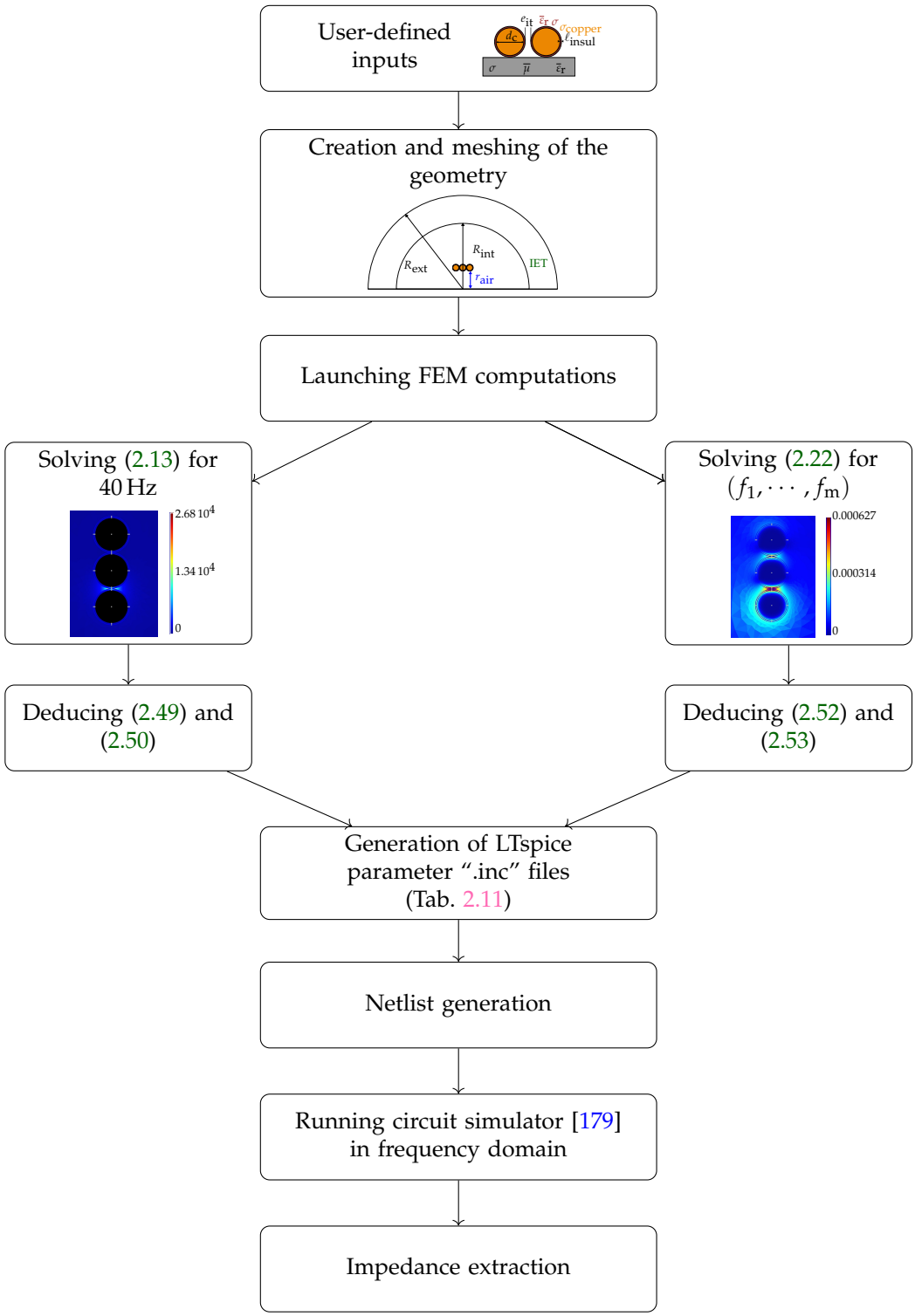

FIGURE 2.29: Flowchart of the proposed frequency domain tool.

2.6 Experimental validation

In this section, the proposed model is put to test by comparing it to experimental measurements performed using the impedance analyser Agilent 4980A [176]. It uses the auto-balancing bridge method, which is based on equating the current flowing through a large resistor and that flowing through the winding. An amplifier is used to balance both currents, from which the impedance of the device under test—the winding—is deduced. This represents the best option for high frequency behaviour investigations. Also, in order to best minimize the introduced uncertainty in the test fixture, a compensation is required and is performed by the user. By performing the compensation measurement, the parasitics are accounted for during the frequency identification of the winding and are subtracted from the measurement.

We have prepared different windings that satisfy the axisymmetric geometrical approximation; a three-layered 21 turns winding, a two-layered 69 turns windings, a two-layered 147 turns winding, a winding inserted in half a magnetic core and a winding with a full magnetic core. They are presented in Fig. 2.30.

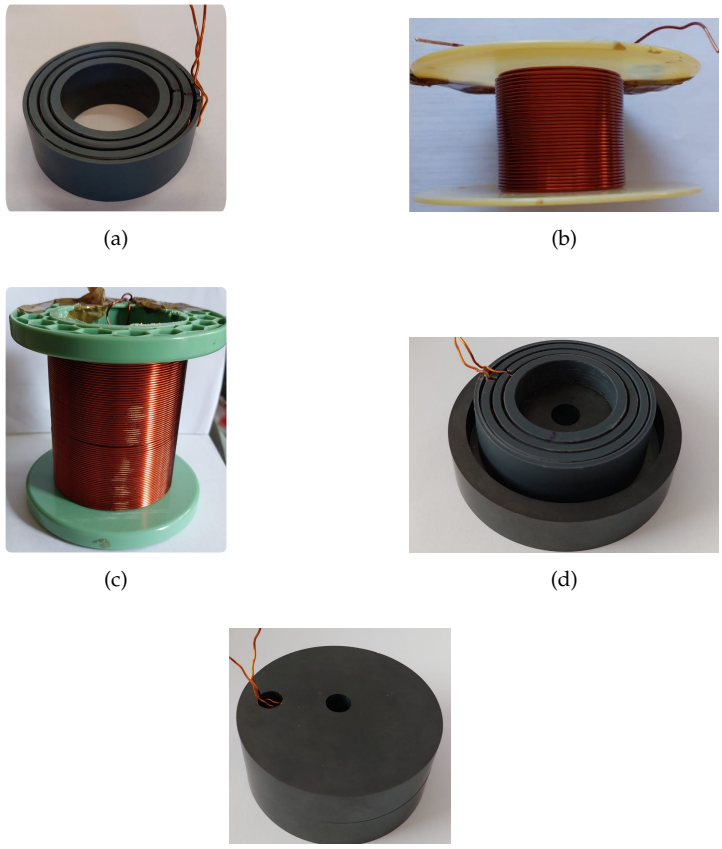

(a) (b) (c) (d) (e)

FIGURE 2.30: The chosen test cases on which the experimental validation is performed: (a) A three-layered 21 turns winding. (b) A two-layered 69 turns winding. (c) A two-layered 147 turns winding. (d) The 21 turns winding inserted in a magnetic core. (e) The 21 turns winding fully emerged in a magnetic core.

2.6.1 The three-layered 21 turns winding

The first case study is the one presented in Fig. 2.30a with its internal structure depicted in Fig. 2.31.

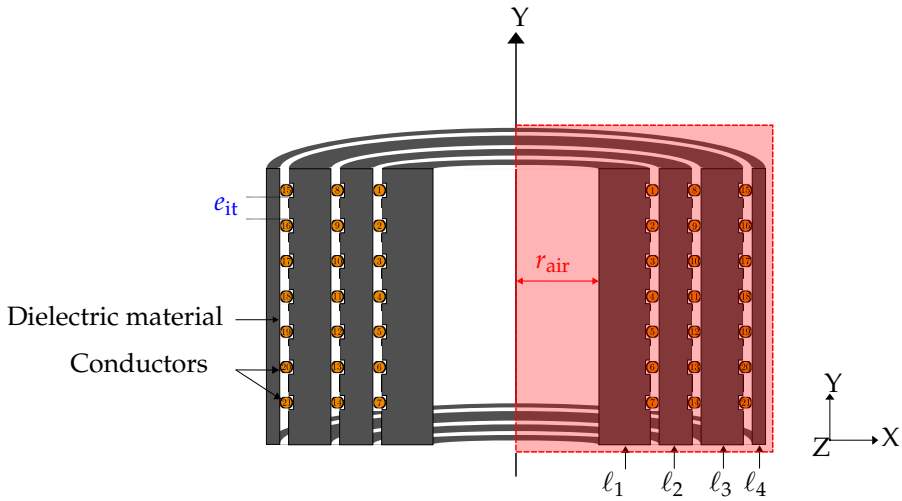

FIGURE 2.31: The internal structure of the 21 turns winding.

For this case study, the wire used in the making of this winding satisfies the American Wire Gauge (AWG) specifications. The geometrical definition of this case study is summarized in Tab. 2.12 for results reproducibility purposes.

TABLE 2.12: The geometrical and electrical definition of the 21 turns winding.

n	21 turns
n_{ℓ_1}	7 turns
n_{ℓ_2}	7 turns
n_{ℓ_3}	7 turns
d_c	0.723 mm
σ_{copper}	60 MS
ℓ_{insul}	0.0235 mm
$\bar{\varepsilon}_{PE}$	$(2.3 - j\,0.5)\ \varepsilon_0$
e_{it}	0.725 µm
r_{air}	14.55 mm
ℓ_1	3 mm
ℓ_2	2 mm
ℓ_3	2.09 mm
ℓ_4	1.1 mm

The conductors of this case study are ideally arranged on different layers, meaning the inter-turn spacing e_{it} is regular. The geometry is axisymmetric, hence only half of its 2D cross-section, framed in red dashed lines in Fig. 2.31, is sufficient to run the computations. It has n_{ℓ_1}, n_{ℓ_2}, n_{ℓ_3} number of conductors in the first, second and third layers, respectively. The dielectric layers have thicknesses of ℓ_1, ℓ_2, ℓ_3 and ℓ_4, respectively. The insulation used is Polyethylene (PE) and has a permittivity $\bar{\varepsilon}_{\text{PE}}$ and a thickness of ℓ_{insul}. The dielectric material on which the conductors are fixed has a relative permittivity of $\bar{\varepsilon}_{\text{PVC}}$. The internal radius of the used dielectric material on which the conductors are set is r_{air}.

The frequency behaviour of the impedance of the 21 turns air winding according to frequency is presented in Fig. 2.32 and compared to the measurement. The low, medium and high frequency behaviours are well predicted, from the resonance and anti-resonance frequencies to the amplitude of the impedance at these frequencies.

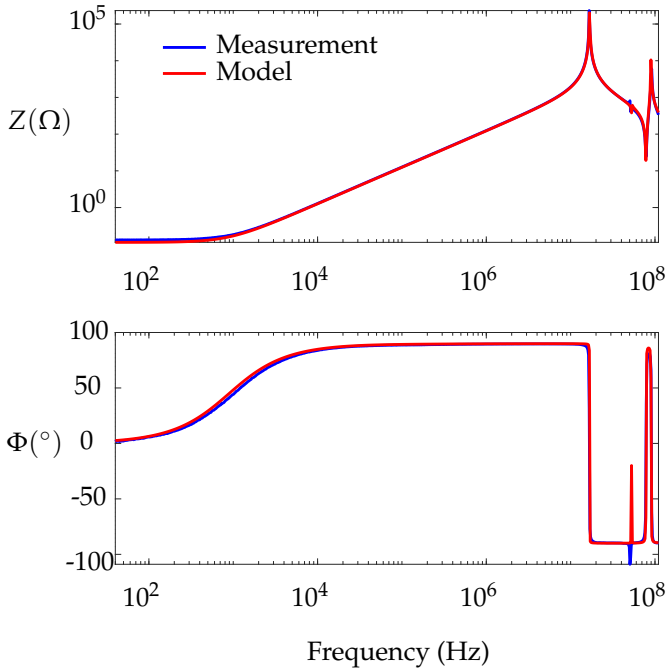

FIGURE 2.32: Comparison of the proposed model and the measurement of the 21 turns winding.

For the study to be complete and in order to highlight the added value of the proposed model, we compare these results with those of the previous work [17]. The comparison is presented in Fig. 2.33. Although the proposed model predicts better, the added value is not really highlighted since the three curves seem to match across the entire frequency range. This is due to the relatively small number of turns of the winding as well as the high value of the inter-turn spacing between turns. This caused the different high frequency resonances to shift to even higher frequencies and not be captured by the impedance analyser, given the frequency range limitation.

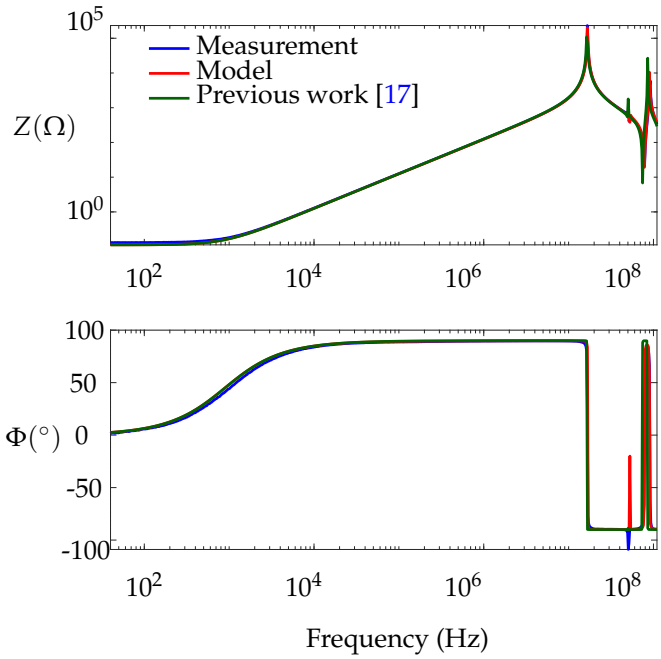

FIGURE 2.33: Comparison of the proposed model with both the measurement of the 21 turns winding and the model of from previous work.

The simulation time of the proposed model is presented in Tab. 2.13, where the FEM computations took 21 min whereas the circuit simulator simulations were completed in 11 s.

TABLE 2.13: The 21 turns winding simulation time.

FEM computations	21 min
LTspice simulation	11 s

Unlike the measurement setup, the simulation allows to go as high as the user wants to: we thus report the results from 100 MHz up to 10 GHz for future reference in Fig. 2.34, where the high frequency resonance and anti-resonances do not match at all.

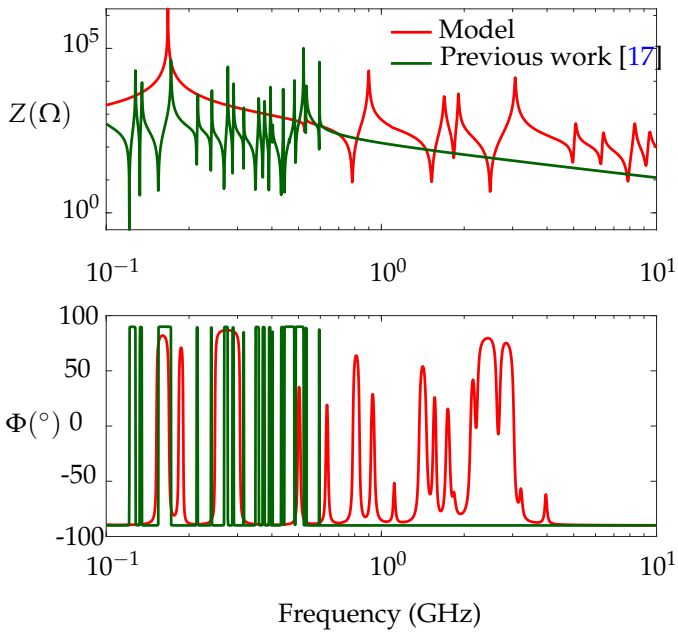

FIGURE 2.34: Investigating the frequency behaviour of the model beyond f_m and comparing it to the output of the previous work.

2.6.2 The two-layered 69 turns winding

The second case study is the $n = 69$ turns winding presented in Fig. 2.30b with its 3D geometrical definition depicted in Fig. 2.35, where h_{int} and h_{ext} refer to the internal and external heights of the PVC, whereas r_{PVC} refers to the outer radius of the PVC.

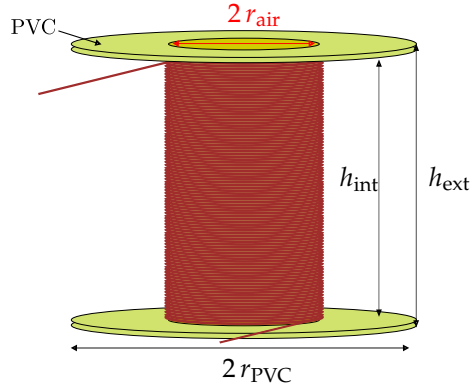

FIGURE 2.35: The 3D geometrical definition of the studied 69 turns winding seen in Fig.2.30b.

This winding has n_{ℓ_1} turns in the first layer and n_{ℓ_2} turns in the second layer. The used wire is PEI-PAI insulated with a copper diameter d_c and an insulation thickness ℓ_{insul}. The geometrical definition of the conductors is presented in Fig. 2.36, where e_{it} is regular.

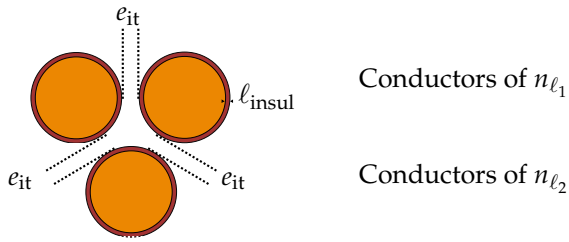

FIGURE 2.36: The geometrical definition of the conductors.

The value of e_{it} is computed as follows:

$$e_{it} = \frac{h_{int} - n_{\ell_1}\left(d_c + \ell_{insul}\right)}{n_{\ell_1} + 1}. \tag{2.59}$$

As a matter of fact, when it comes to the geometrical definition of the conductors, the norm CEI 60317-0-1 specifies for each copper diameter an insulation thickness. However, the EIS is two layered as elaborated in section 1.3.4, and since the PEI layer is thicker that the PAI, we suppose for the current and ensuing case studies, that the conductor is one layered with PEI with a permittivity of $\bar{\varepsilon}_{PEI}$. The permittivity of the PVC on which the conductors are set is $\bar{\varepsilon}_{PVC}$. Also, the conductivity of the copper is set to σ_{copper}. The geometrical and electrical definition of this case study are summarized in Tab.2.14, where e_{PVC} is the thickness of the PVC.

TABLE 2.14: The geometrical and electrical definition of the 69 turns winding.

n	69 turns
n_{ℓ_1}	35 turns
n_{ℓ_2}	34 turns
d_c	1.25 mm
σ_{copper}	60 MS
ℓ_{insul}	0.0495 mm
$\bar{\varepsilon}_{PEI}$	$(3.5 - j\,0.5)\ \varepsilon_0$
$\bar{\varepsilon}_{PVC}$	$4\,\varepsilon_0$
e_{it}	7.91 µm
r_{air}	23.05 mm
r_{PVC}	58.05 mm
e_{PVC}	1.8 mm
h_{ext}	51.55 mm
h_{int}	47.5 mm

The studied 2D cross-section used to run the FEM computations as well as the arrangement of the conductors on the PVC are seen in Fig. 2.37 and Fig. 2.38, respectively.

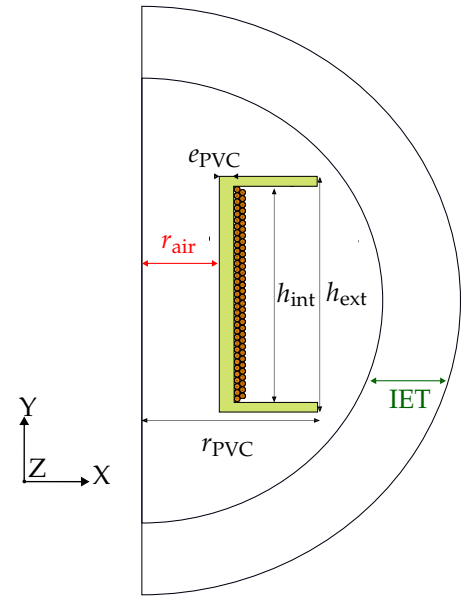

FIGURE 2.37: The studied 2D cross-section of the 69 turns winding.

FIGURE 2.38: The arrangement of the 69 turns on the PVC. *The arrangement from right to left in this figure corresponds to the arrangement from bottom to top in Fig. 2.37.*

This computation time is summarized in Tab. 2.15.

TABLE 2.15: The 69 turns winding simulation time.

FEM computations	2 h 12 min
LTspice simulation	2 min 3 s

The comparison between the simulation and the measurements is presented in Fig. 2.39, where we can see that both the different resonance and anti-resonance frequencies were well predicted.

The relative permittivity of the PAI is in reality higher than that of PEI which justifies why the computed frequencies are over-estimated. An improvement is to be made for a better prediction of the different values of the impedance at these frequencies since they depend on the value of the capacitance, by performing a more throughout investigation of the dielectric properties. Comparing these results with the output of the previous research work [17] is presented in Fig. 2.40, where both low and medium frequency behaviours match, unlike the high frequency behaviour that is completely missed by the model developed in previous works [17]. A zoom is presented in Fig. 2.41 and underlines the importance of accounting for the frequency behaviour of the parameters and accentuates the added value of the proposed model.

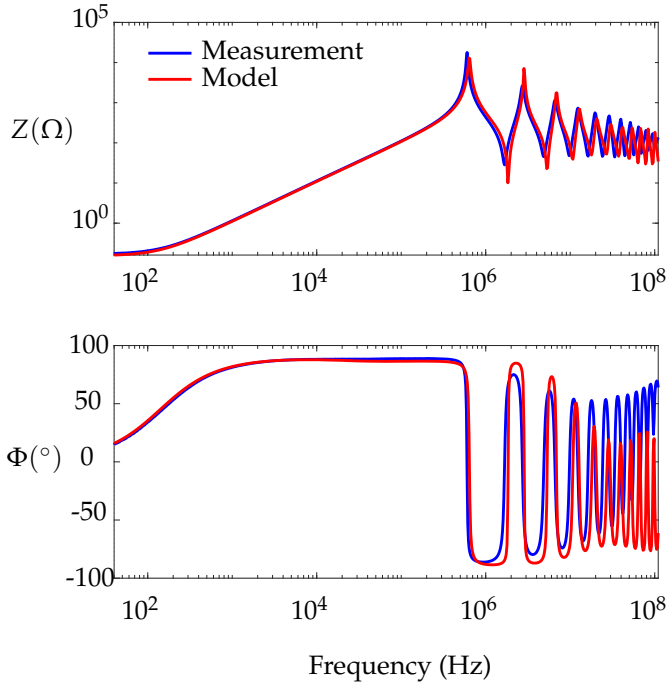

FIGURE 2.39: Comparison of the proposed model and the measurement of the 69 turns winding.

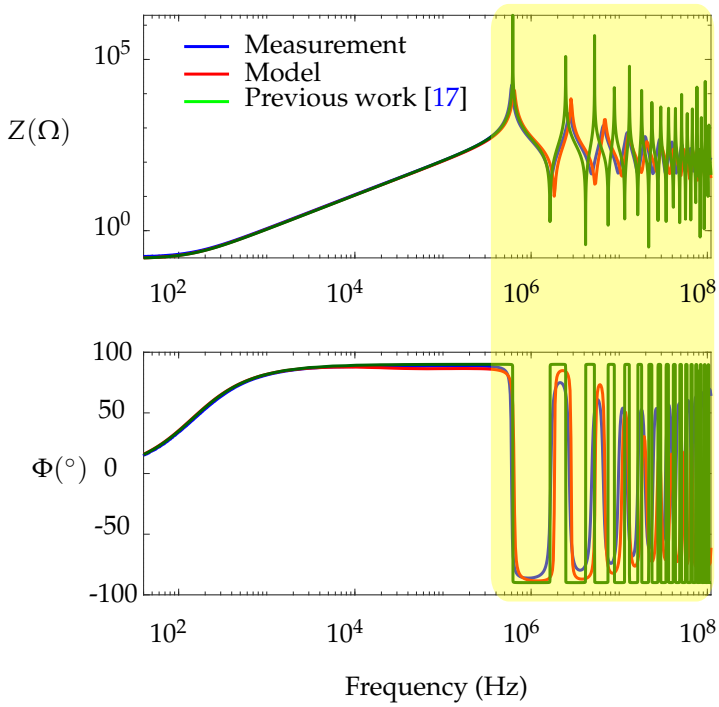

FIGURE 2.40: Comparison of the proposed model, the measurement and the previous work model of the 69 turns winding.

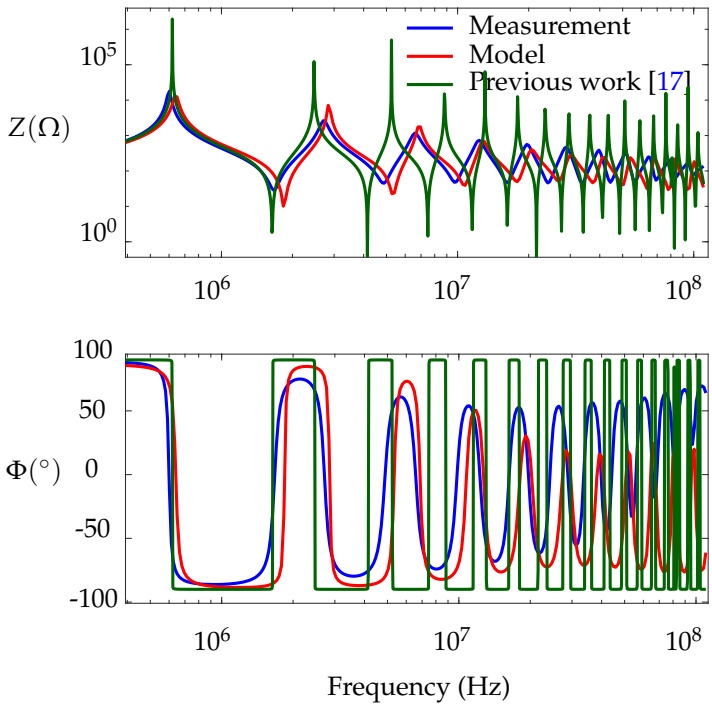

FIGURE 2.41: A zoom on the high frequency behaviour of the 69 turns winding.

2.6.3 The two-layered 147 turns winding

The third case study is the two-layered $n = 147$ turns winding seen in Fig. 2.30c, with its 3D geometry similar to the previous case study seen in Fig. 2.35. The corresponding geometrical and electrical definition of this case are summed up in Tab. 2.16.

TABLE 2.16: The geometrical and electrical definition of the 69 turns winding.

n	147 turns
n_{ℓ_1}	74 turns
n_{ℓ_2}	75 turns
d_c	1.25 mm
σ_{copper}	60 MS
ℓ_{insul}	0.0495 mm
$\bar{\varepsilon}_{PEI}$	$(3.5 - j\,0.5)\ \varepsilon_0$
$\bar{\varepsilon}_{PVC}$	$4\,\varepsilon_0$
e_{it}	15.6 µm
r_{air}	37.1 mm
r_{PVC}	62.1 mm
e_{PVC}	31.4 mm
h_{ext}	12.4 cm
h_{int}	10.1 cm

The 2D cross-section as well as the arrangement of the turns are also similar to the previous case study (refer to Fig. 2.37).

The computational time for this case study is seen in Tab. 2.17, where we see that the FEM computations took 9 h 56 min to complete, whereas the LTspice frequency domain simulation took 1 h and 19 min. This is due to the important number of behavioural voltage sources modelling the impedance coupling that make the system to be solved even larger.

TABLE 2.17: The 147 turns winding simulation time.

FEM computations	9 h 56 min
LTspice simulation	1 h 19 min 41 s

The comparison between the output of the proposed model and the measurement is presented in Fig. 2.42. Across the entire frequency range, the model accurately predicts the behaviour of the winding. From the slope, to the first resonance frequency to the ensuing high resonance and anti-resonance frequencies. The slip noticed is due to the hypothesis made (one layer of PEI insulation on conductors). Moreover, the frequency dependent behaviour of the permittivity was considered constant across the entire frequency range of interest. This justifies the noticed high frequency discrepancy. However, given the results of the permittivity measurements, an investigation of its behaviour for even higher frequencies has to be performed. The comparison with the previous work [17] is presented in Fig. 2.43, where again, the high frequency behaviour is completely missed.

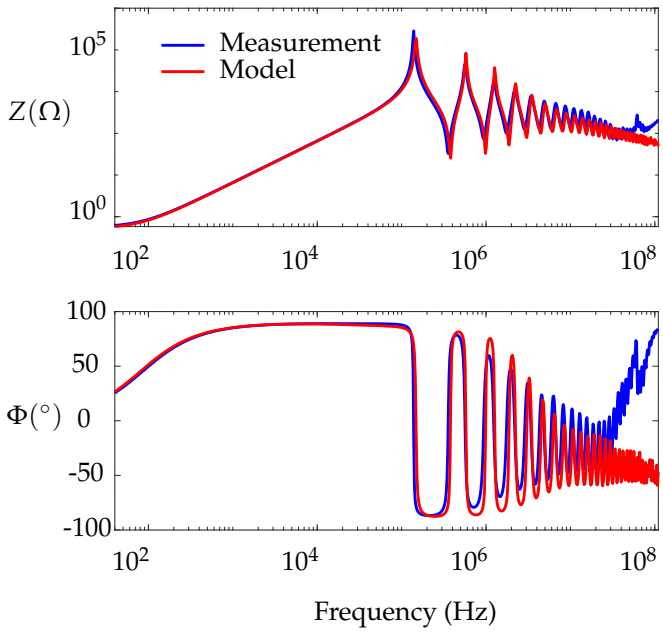

FIGURE 2.42: Comparison of the proposed model and the measurement of the 147 turns winding.

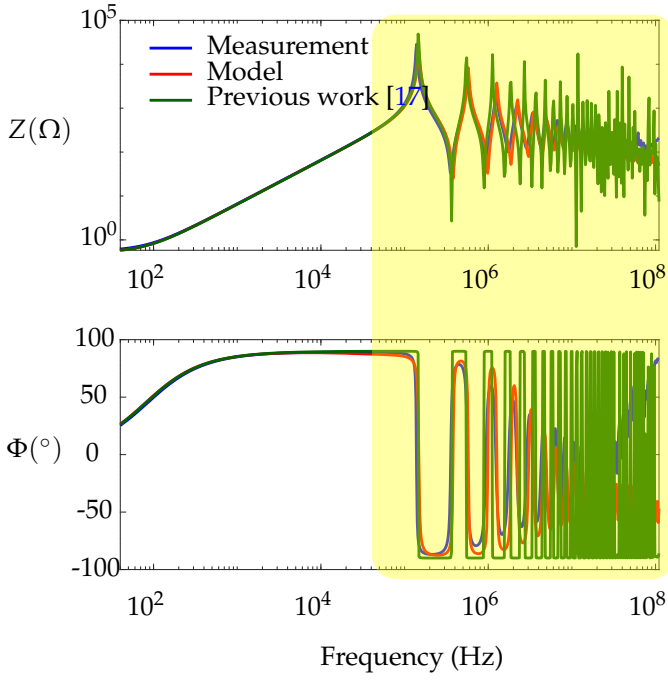

FIGURE 2.43: Comparison of the proposed model, the measurement and the previous work model of the 147 turns winding.

A zoom on the high frequency behaviour is depicted in Fig. 2.44, where not only the frequencies predicted by the model of previous work, but the value of the impedance at these frequencies seems to diverge even further from the measurement as the frequency increases. This highlights the necessity to account for the frequency behaviour of the parameters when the high frequency response of the winding is of interest. Further improvement could be achieved with the inclusion of the frequency behaviour of the capacitive coupling.

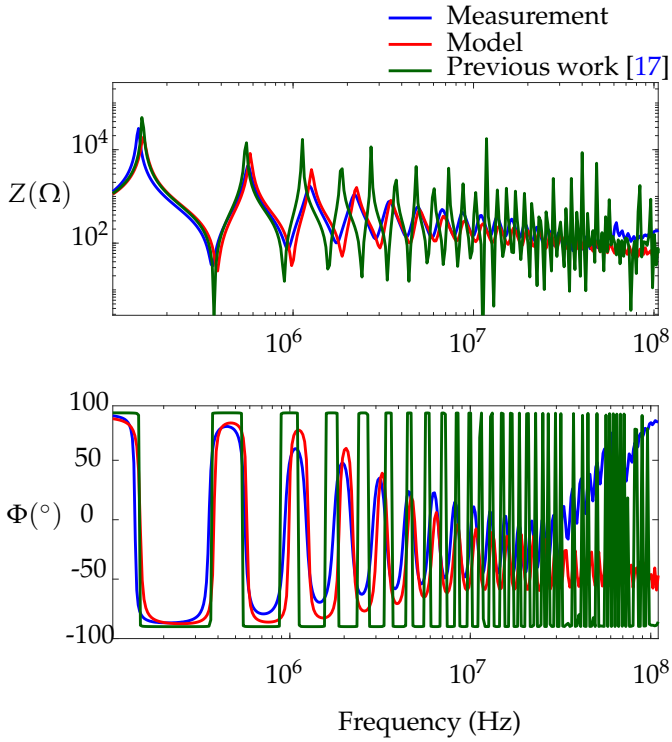

FIGURE 2.44: A zoom on the high frequency behaviour of the 147 turns winding.

2.6.4 A 21 turns winding with half magnetic core

To study the robustness of the model, case studies with a magnetic core have been investigated.

The first case study case with a magnetic material is presented in Fig. 2.30d. The lower half of the 21 turns winding is inserted in a Mn-Zn ferrite magnetic core (reference N22) usually used for EMI filtering. The soft magnetic material is made of iron oxide mixed with Manganese (Mn) and Zinc (Zn) [180], [181] whose properties depend on its polycrystalline structure. Its permittivity as well as its resistivity are determined by its grain and insulating grain boundary. Unlike ferrites grains, the Mn-Zn ferrites display different physical and chemical properties. During the cooling process, a partial re-oxidation of the iron (Fe^{+2}) as well as the segregation of the ferrites' impurities occur on the grain boundaries, thus making the latter significantly insulating. The insulating layers feature a high electrical capacity [182], [183]. Hence, it is not only a high permeability material but also a high permittivity material behaving as a capacitor [182].

A sketch of the internal structure of a polycrystalline material is depicted in Fig. 2.45.

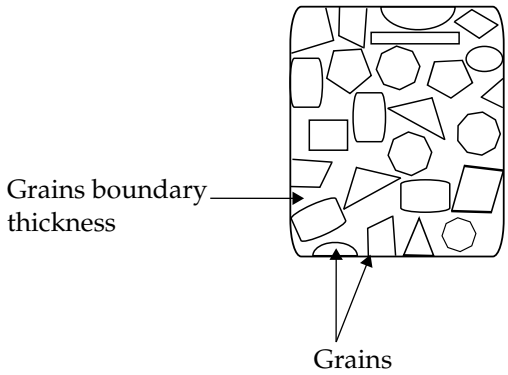

FIGURE 2.45: A sketch of the ideal microstructure of Physical polycrystalline structure with isolated magnetic grains.

The constructor gives no information whatsoever on its dielectric properties. Petrovic' in [182] studied the dielectric behaviour of a Mn-Zn ferrite powder (M-30-HS) which gave us an idea of the order of magnitude of the relative dielectric constant of ferrites. The values of 350 for the real part and 150 for the imaginary part of the permittivity have been chosen to obtain the best fit with the measured impedance.

The internal structure for this first case study with a magnetic core is depicted in Fig. 2.46.

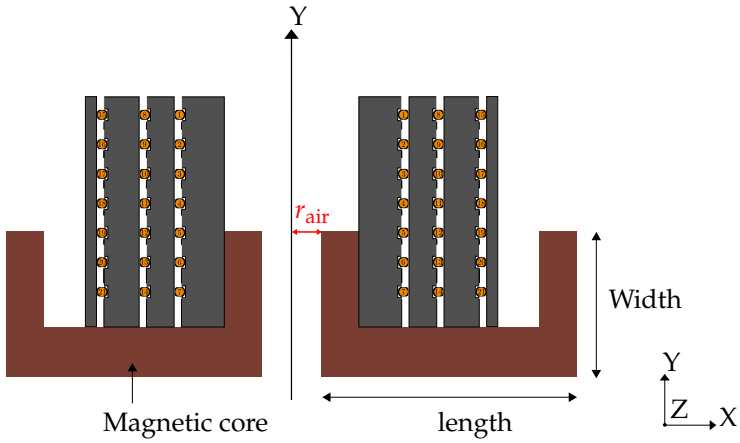

FIGURE 2.46: The 2D cross-section of the first case study with a magnetic core.

The corresponding geometrical definition summarized is in Tab. 2.18.

TABLE 2.18: The geometrical definition of the magnetic material.

Width	14.5 mm
Length	30.75 mm
r_{air}	4.25 mm

In order to account for the magnetic losses, a complex magnetic permeability is used to describe the stored magnetic energy, with its real part, and the magnetic losses, with the imaginary one. According to the data-sheet, the permeability has a value of:

$$\overline{\mu} = 2300\,\mu_0 - j\,3\,\mu_0. \tag{2.60}$$

The latter is the series electrical representation of the magnetic material [9]. Hence, using the complex form of the magnetic permeability, the inductance is complex (similar approach to the capacitance).

To further understand the concept of the complex magnetic permeability, let us take as an example the toroid depicted in Fig. 2.47, where r, R and h are the internal radius, external radius and height of the studied toroid which is of $\overline{\mu}_{r_T}$ complex relative permeability.

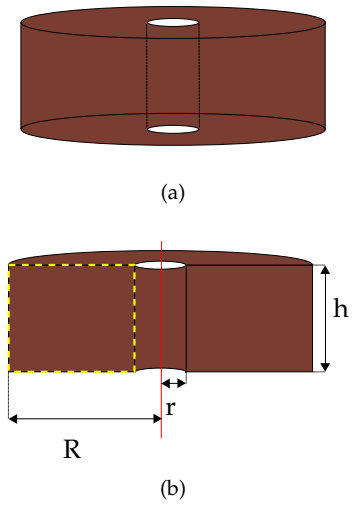

FIGURE 2.47: (a) The toroid used for illustration of the series representation of the complex magnetic permeability. (b) The cross section of the toroid sample.

Let us suppose a one turn winding is wounded on the toroid and excited with a current I. The induced magnetic flux density going through the yellow bounded square surface S_T has the following expression:

$$\overline{b}_T = \frac{\mu_0\,\overline{\mu}_{r_T}\,I}{2\,\pi\,r}. \tag{2.61}$$

From (2.37), the expression of the corresponding inductance L_T is deduced from the flux:

$$\begin{aligned} \overline{\phi}_T &= \overline{L}_T\,I \\ &= \iint_{S_T} \overline{b}_T\,dS \\ &= \iint_{S_T} \frac{\mu_0\,\overline{\mu}_{r_T}\,I}{2\,\pi\,r}\,dx\,dz \\ &= \int_r^R \int_0^h \frac{\mu_0\,\overline{\mu}_{r_T}\,I}{2\,\pi\,r}\,dr\,dz. \end{aligned} \tag{2.62}$$

Hence, deducing the expression of the inductance L_T is straightforward:

$$\begin{aligned} \overline{L}_T &= \mu_0 \, \overline{\mu}_{r_T} \, \frac{h}{2\,\pi} \ln\left(\frac{R}{r}\right), \\ &= \mu_0 \, \left(\mu'_{r_T} + j\,\mu''_{r_T}\right) \, \frac{h}{2\,\pi} \ln\left(\frac{R}{r}\right). \end{aligned} \tag{2.63}$$

Therefore, when computing the self impedance of the turn using (2.31), a real part is added to the Joule losses resistance that accounts for the iron losses given the chosen model of the iron losses. The computational time for this case study is presented in Tab. 2.19.

TABLE 2.19: The 21 turns winding placed in half a magnetic core simulation time.

FEM computations	2 h 12min
LTspice simulation	2 min 3 s

The comparison of the model with the impedance measurement are presented in Fig. 2.48.

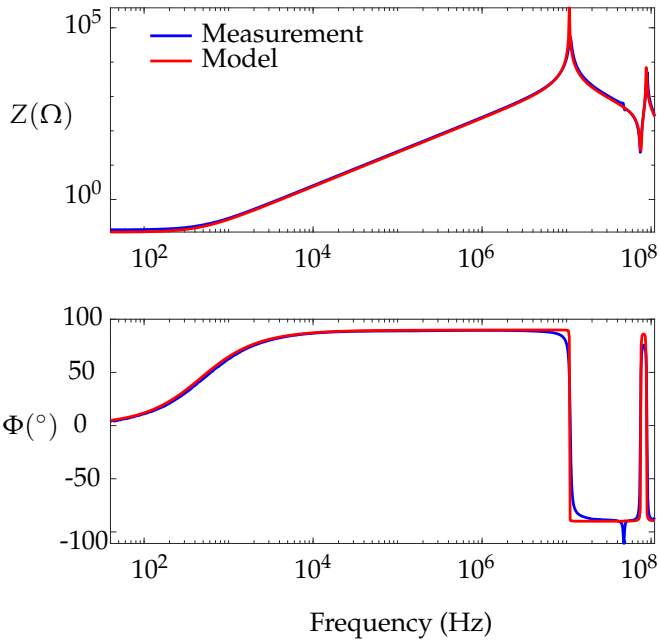

FIGURE 2.48: Comparison of the measurement and the proposed model of the 21 turns on half a magnetic core.

The resonance frequencies are well predicted, however prediction the magnitude of the first resonance frequency could be further improved with the set of exact values describing the dielectric behaviour of the core. These results prove the added value of accounting the frequency

behaviour of the parameters and the reliability of the model even after inserting a magnetic core. The comparison with previous work is depicted in Fig. 2.49.

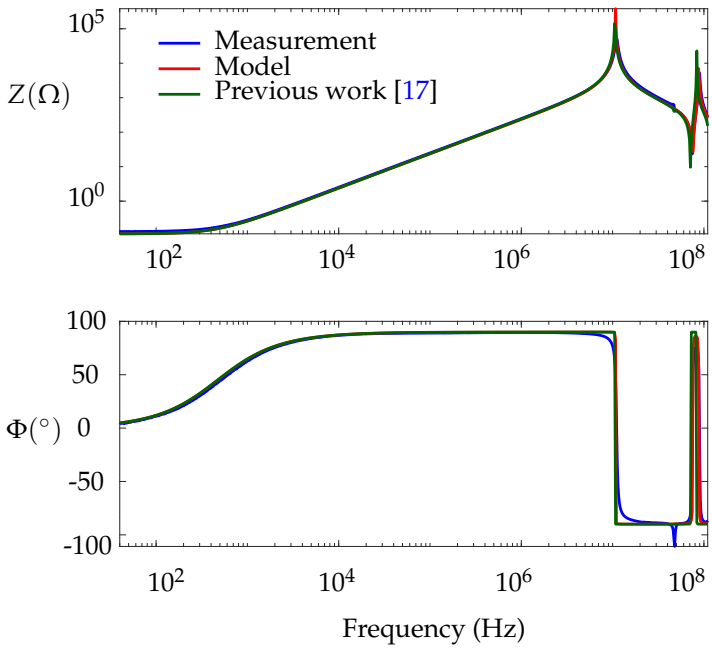

FIGURE 2.49: Comparison of the measurement and the proposed model of the 21 turns on half magnetic core.

2.6.5 A 21 turns winding with a full magnetic core

For the second case study with a magnetic material, the other half of the magnetic material is added, making thus the 21 turns positioned within the magnetic material, the 2D cross-section is seen in Fig. 2.50.

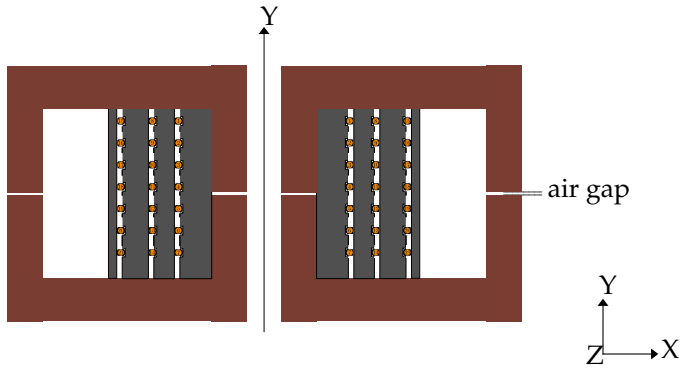

FIGURE 2.50: The 2D cross-section of the second case study with a magnetic core.

An air-gap is measured to be of 20 µm value. The comparison of the model and the measurement is seen in Fig. 2.51, where they match well across the frequency range. A further

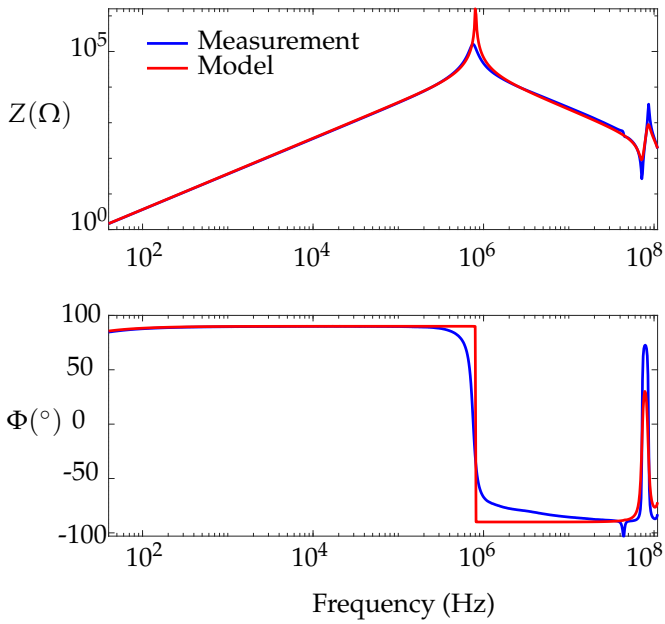

FIGURE 2.51: Comparison of the measurement and the proposed model of the 21 turns placed within a magnetic core.

improvement could be performed once the inserted magnetic material fully dielectrically characterized. The comparison with previous work is presented in Fig. 2.52. Again, the proposed model predicts more accurately than previous work the resonance frequencies. However, given the small number of turns as well as the high value of the inter-turn spacing between turns, its added value is not highlighted for this case study. Still, the robustness of the proposed tool is highlighted.

For this case study, the FEM simulations took 21 min, whereas the LTspice simulation only takes 11 s to complete. This is summarized in Tab. 2.20.

TABLE 2.20: The 21 turns winding placed within a magnetic core simulation time.

FEM computations	2 h 12 min
LTspice simulation	2 min 3 s

At this stage, we have validated the frequency domain model by studying and comparing it to measurements performed on multiple case studies. The robustness of the model was examined and validated on windings with and without magnetic cores.

In the next section, we will study an non-reducible 2D geometry and quantify the geometrical impact on the results.

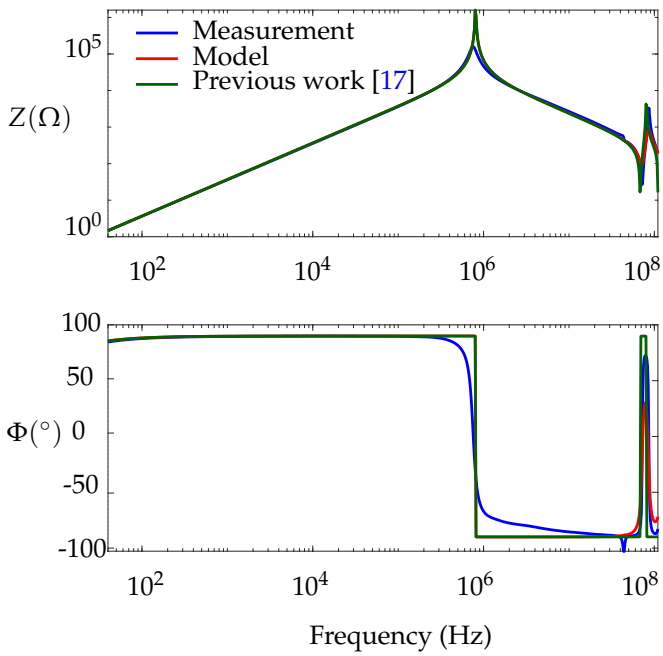

FIGURE 2.52: Comparison of the measurement and the proposed model of the 21 turns placed within a magnetic core with previous work.

2.6.6 A four-layered 126 turns winding

In this section, we study a geometry that neither satisfies the axisymmetric geometrical approximation nor the planar approximation. This is performed in the aim of quantifying the geometrical impact non-2D-reducible geometries have on the results.

Accordingly, two test cases are investigated, the first is an air winding, with no magnetic core, and the second is the same winding inserted on an E-shaped laminated magnetic core. A photo of the two test cases is seen in Fig. 2.53a and Fig. 2.53b, respectively.

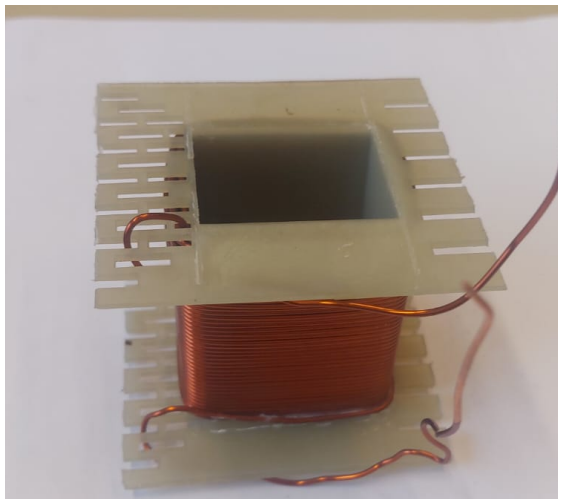

(a)

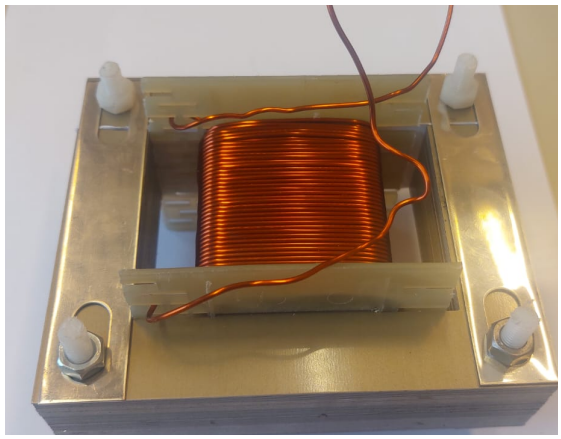

(b)

FIGURE 2.53: Photos of the four layered 126 turns winding (a) with no magnetic core (b) with a laminated magnetic core

2.6.6.1 Winding (coil) without a magnetic material

The first case study here has the 3D geometry presented in Fig. 2.54, where its parameters are summed up in Tab. 2.21.

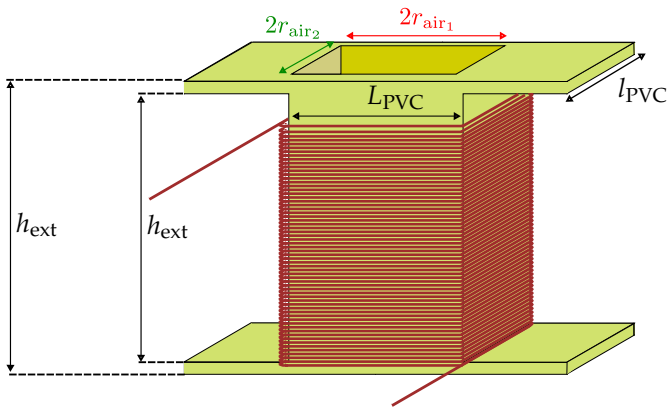

FIGURE 2.54: The corresponding 3D geometrical definition of the studied 126 turns air winding seen in Fig. 2.53a.

TABLE 2.21: The geometrical and electrical definition of the 69 turns winding.

n	126 turns
n_{ℓ_1}	42 turns
n_{ℓ_2}	41 turns
n_{ℓ_3}	42 turns
n_{ℓ_4}	1 turn
d_{c}	1.25 mm
σ_{copper}	60 MS
ℓ_{insul}	0.0495 mm
$\bar{\varepsilon}_{\text{PEI}}$	$(3.5 - j\,0.5)\ \varepsilon_0$
$\bar{\varepsilon}_{\text{PVC}}$	$4\,\varepsilon_0$
e_{it}	8.3 µm
l_{PVC}	41 mm
L_{PVC}	57 mm
h_{ext}	59 cm
h_{int}	57 cm

It is a four-layered ($n = 126$) turns winding set on a PVC, the fours layers contain n_{ℓ_1}, n_{ℓ_2}, n_{ℓ_3} and n_{ℓ_4} turns, respectively. The studied 2D cross-section is depicted in Fig. 2.55.

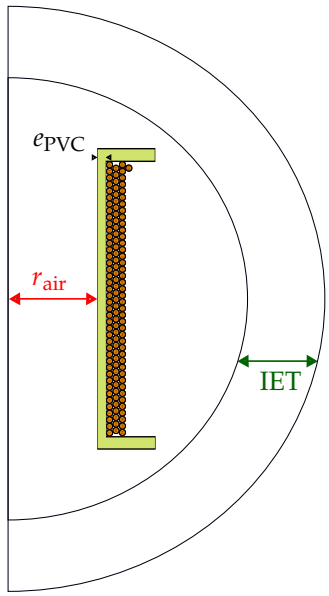

FIGURE 2.55: The studied cross-section of the 3D geometry seen in Fig. 2.54

The corresponding arrangement is seen in Fig. 2.56.

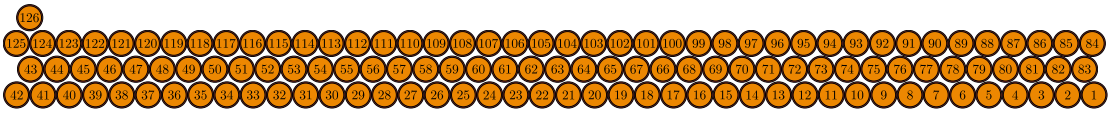

FIGURE 2.56: The arrangement of the 126 turns winding. *The arrangement from right to left in this figure corresponds to the arrangement from bottom to top in Fig. 2.55.*

As noticed, the local coordinate system (X, Y, Z) was not presented in Fig. 2.55. This is because we study this winding in three different geometrical approximations in order to quantify the geometrical impact on the computations. Hence, the value of r_{air} depends on the adopted geometrical approximation. In these cases, the computed electrical parameters are per units (per meter for the first two approximations and per radiant in the last approximation) and ought to be multiplied by the corresponding geometrical coefficient. We call CoefGeoL the geometrical coefficient that corrects the computed inductance and CoefGeoRC that corrects both capacitances and resistance. This is done in means to account for the third dimension. Their values as well as those of are r_{air} summarized in Tab. 2.22 for each approximation.

The comparisons of the computed winding impedances when applying the three aforementioned geometrical approximations and the impedance measurement are seen in Fig. 2.57, 2.58 and 2.59, respectively.

The FEM computations for each of the three cases take 4 h and 3 min to complete, whereas the LTspice frequency domain simulations concluded in 1 h and 34 min. This is summarized in Tab. 2.23.

TABLE 2.22: The values of r_{air} according to the adopted geometrical approximation.

Approx	**1**	**2**	**3**
r_{air}	$L_{\text{PVC}}/2$	$l_{\text{PVC}}/2$	$\sqrt{S_{\text{air}}/\pi}$
CoefGeoL	$2\,l_{\text{PVC}}$	$2\,L_{\text{PVC}}$	$2\,\pi$
CoefGeoRC	$2\,(l_{\text{PVC}} + e_{\text{PVC}} + L_{\text{PVC}})$	$2\,(l_{\text{PVC}} + e_{\text{PVC}} + L_{\text{PVC}})$	$2\,\pi$

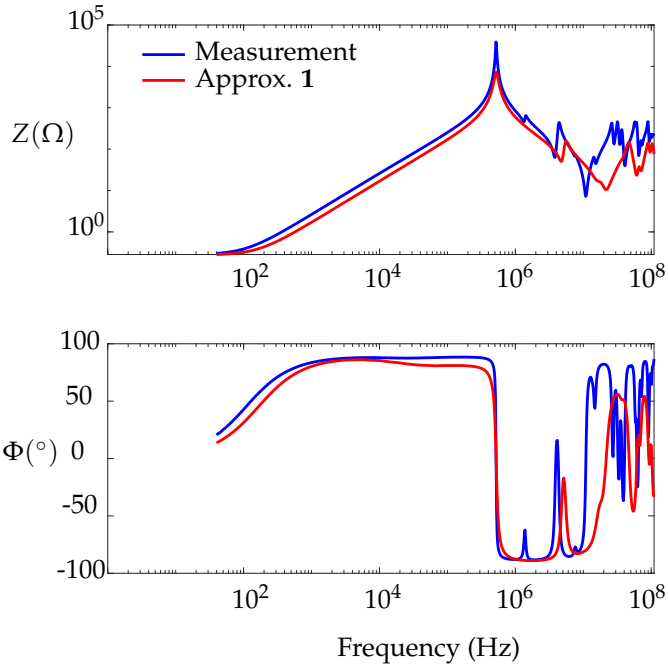

FIGURE 2.57: Measurement VS results of the 2D approximation **1**.

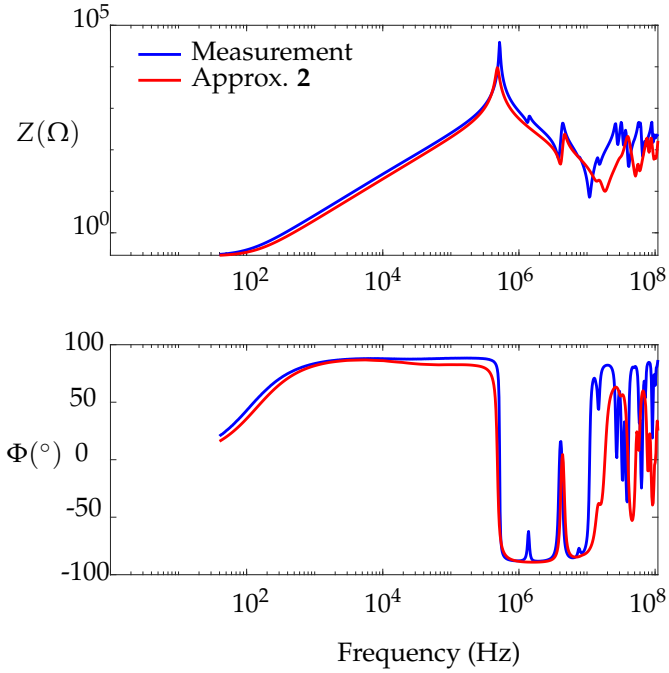

FIGURE 2.58: Measurement VS results of the 2D approximation **2**.

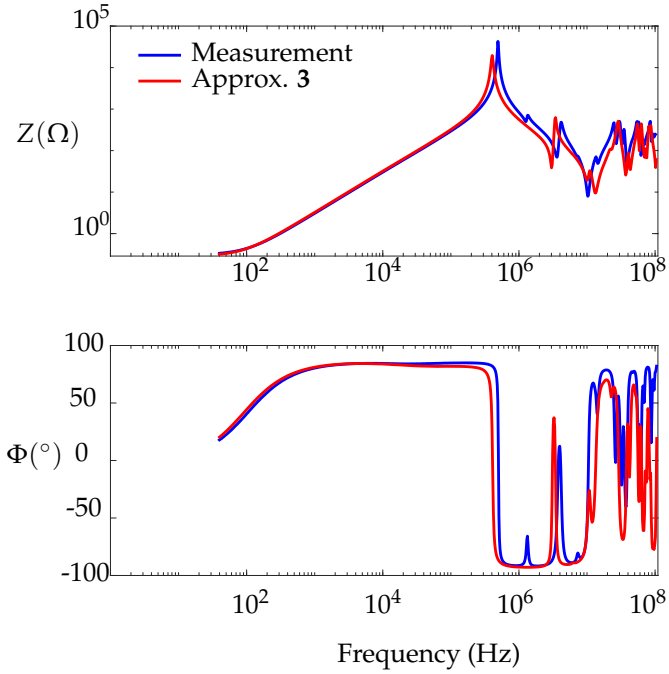

FIGURE 2.59: Measurement VS results of the 2D approximation **3**.

TABLE 2.23: The 21 turns winding placed within a magnetic core simulation time.

FEM computations	4 h 3 min
LTspice simulation	1 h 34 min

Even though the planar geometrical definition is not satisfied for this case study—the test case is not infinitely long across the third dimension—-, the results still give a global idea on the frequency behaviour of the winding, at least up to 1 MHz. In particular, the axisymmetric approximation where the model approximates best the measured behaviour. When applying approximations **1** and **2** the impact of coil heads is forsaken and a part of the inductive behaviour information is lost, justifying thus the difference when comparing the slopes.

The following results highlight the impact of the geometry reduction, when the 3D geometry is neither planar, asymmetric or helicoidal, on the frequency domain results and supports the notion that the proposed method may be effective, provided a 3D geometrical definition is adopted.

2.6.6.2 Winding on a laminated magnetic core

In this section we study the same 126 turns winding, but this time it is placed on an E-shaped laminated magnetic core and is l_{PVC} long in the z dimension.

The 3D geometrical definition is depicted in Fig. 2.60.

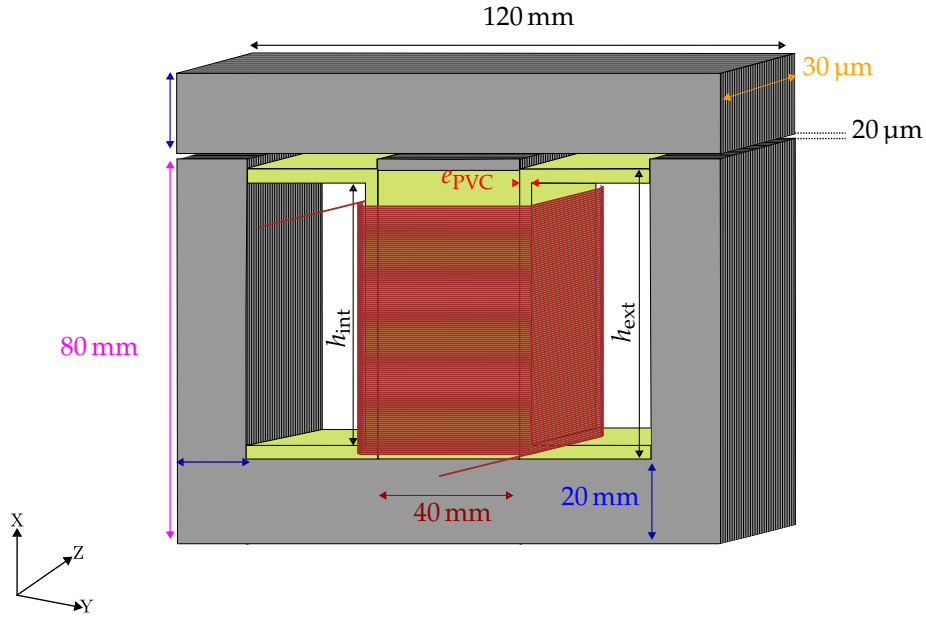

FIGURE 2.60: The 3D geometry of the studied winding on a magnetic core.

The laminations are made of FeSi M400-50A, a type of electrical steel that is designed to be used in electrical equipments. Amongst the key properties behind its broad usage, it showcases low core losses, has a high magnetic permeability and a high resistance to magnetic ageing. The

"FeSi" refers to the main components of the alloy which are iron and silicon, the "M400" on the other hand, makes reference to the magnetic field that can be supported by the material. Finally, the "50A" refers to the lamination thickness in µm.

The laminations are thin layers of non-conductive materials (*i.e.* paper or plastic) sandwiching an even thinner layer sheet of the magnetic material and serve to reduce losses induced by eddy currents. The later create heat and occur when the magnetic material is subject to a changing magnetic field reducing therefore the efficiency of the material. Additionally, they can even contribute to increasing the circulating flux density since they present a path of lower reluctance. For this case study, 60 laminations were stacked together to be fitted inside the PVC that hold still the studied conductors. When it comes to the magnetic behaviour of the M400-50A, it depends on multiple factors including its material composition.

Having no preliminary idea on its magnetic permeability, we run multiple FEM computations on the geometry seen in Fig. 2.61, with various values of relative magnetic permeability μ_r: μ_r = 15000, μ_r = 1000, μ_r = 200, μ_r = 100 and μ_r = 10. We suppose for now that the imaginary part of the complex magnetic permeability is null $\overline{\mu} = \mu_0 \, \mu_r$.

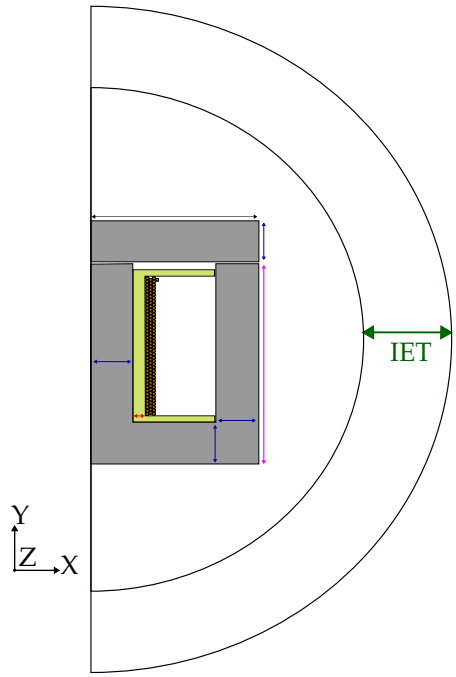

FIGURE 2.61: The studied 2D cross-section of the 126 turns winding on a magnetic core.

The hypotheses made are the following:

- the geometry is infinitely long across the third dimension;
- the magnetic material is non-conductive in the z dimension;
- the magnetic losses are neglected for the time being.

The results of the comparative study are plotted in Fig. 2.62. We notice that for μ_r = 200, the computed inductive behaviour matches the most with the measurements up to 1 kHz.

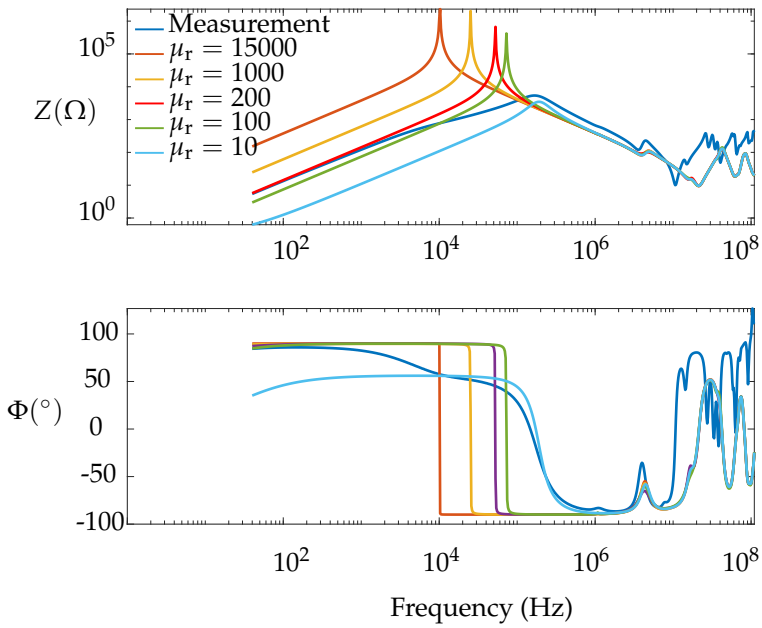

FIGURE 2.62: The computed impedances of the 126 turns winding for multiple relative permeability values compared with the measurement.

We justify the low value of the magnetic permeability by the low excitation imposed by the impedance analyser. Now that we have an idea of the magnetic permeability that enables modelling the measured frequency behaviour of the magnetic core and in order to perform a proper comparative study with the measurements we ought to account for the magnetic losses that occur in the magnetic core. Doing this in finite-element analysis is not self-evident and requires few hypotheses.

We suppose that:

- the magnetic steel is isotropic,
- the magnetic steel is magnetically non-hysteric,
- the magnetic steel has a constant conductivity (still considered null for this test case).

The irreversible behaviour of the magnetic material was studied and expressed by Gyselinck in [184] by linking $\mathbf{h}$ to $\mathbf{b}$ through the following equation:

$$\mathbf{h} = \frac{1}{\mu}\,\mathbf{b} + \frac{1}{12}\,\sigma\, {e_{\text{lam}}}^2\,\frac{\partial \mathbf{b}}{\partial t}, \tag{2.64}$$

where e_{lam} is the thickness of a lamination, which in this case is equal to 50 µm, σ is the conductivity of the laminations which is of 42 MS cm value.

Expressing (2.64) in Fourier domain, we obtain:

$$\begin{aligned} \mathbf{h}(f) &= \frac{1}{\mu}\,\mathbf{b}(f) + \frac{1}{12}\,\sigma\, {e_{\text{lam}}}^2\, j\,\omega\,\mathbf{b}(f) \\ &= \left(\underbrace{\frac{1}{\mu} + j\,\omega\,\frac{1}{12}\,\sigma\, {e_{\text{lam}}}^2}_{\bar{\nu}} \right) \mathbf{b}(f), \end{aligned} \tag{2.65}$$

with $\overline{\nu}$ being the reluctivity.

Running the computations for the following complex permeability:

$$\begin{aligned}\overline{\mu} &= \frac{1}{\overline{\nu}} \\ &= \frac{1}{\frac{1}{200\,\mu_0} + j\,\omega\,\frac{1}{12}\,\sigma\,{e_{\text{lam}}}^2},\end{aligned} \tag{2.66}$$

yields the results seen in Fig. 2.63.

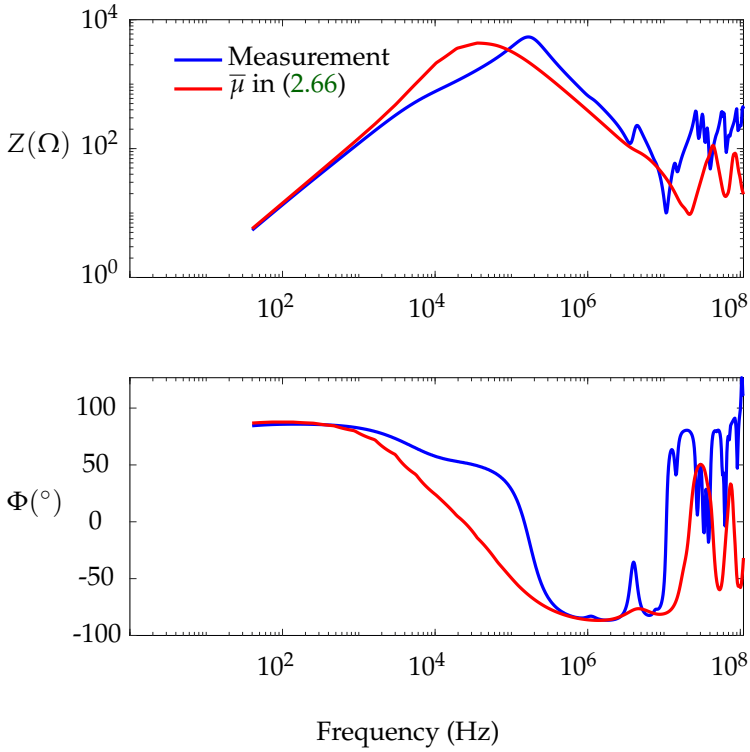

FIGURE 2.63: The results after taking into account the iron losses in the laminations of the 126 turns winding.

Accounting for the iron losses in the laminations allows to match more accurately the non-purely resistive behaviour at low frequencies in comparison to when they are neglected. However, even though a loss of accuracy is noticed the higher the frequency given the simplifying hypotheses made (*i.e.* the considered geometrical hypothesis and the adopted frequency-independent behaviour of the magnetic laminations), the results still give an overall idea of the frequency response. This conclusion provides evidence to bolster the claim that the proposed frequency domain model could be efficacious and implemented as is when properly accounting for the frequency dependent behaviour of the iron losses together with a 3D geometrical definition of the studied winding.

2.7 Conclusion and discussion

In this chapter, the frequency domain elementary cell has been presented: from the choice of the appropriate electromagnetic field model to the convenient choice of the identification technique of each parameter serving as a numerical characterization of the winding, to the adopted methodology to the experimental validation. The frequency dependent behaviour of the used insulation was experimentally investigated, and proved to not vary with frequency for low and medium frequencies. Further work needs to be performed for an accurate high frequency investigation. Moreover, the computational complexity of the model has been reduced by choosing the less computationally expensive identification techniques, unlike in previous research works [17], where the inductances were computed from the energy, hence $\binom{n}{2}/2$ slower than the proposed method in addition to not accounting for the proximity effect. The proposed phenomenological model of the windings accounts for the frequency dependent behaviour of its parameters, without requiring fitting techniques. The proposed solution is thus automatic and need not the intervention of the user. For the experimental validation, five test cases have been studied, modelled and validated. Unlike in [17], the choice of the winding samples on which the validation were performed has been based on reducing the geometrical impact on the results. The studied cases were all axisymmetric and satisfied the geometrical reduction constraints. Comparisons with our implementation of the model proposed by previous work have been performed, where the difference is noticed at high frequencies. The proposed model accurately predicts the high frequency resonances and anti-resonances of the different studied test cases unlike the model from [17].

We pushed the frequency investigation even further by studying a non-2D reducible geometry in order to quantify the geometrical impact on the results. The results gave a global idea of the frequency response of the winding and provides empirical evidence highlighting the fact that the usage of the proposed model as is on a correctly defined geometry (3D geometries for non-2D-reducible ones) could be effective. The same test case was placed on a laminated magnetic core and studied in 2D where the results only matched at low frequencies. This emphasizes on the necessity to account for 3D geometrical definitions for these cases and include the frequency behaviour of the magnetic materials.

As a matter of fact, even though the frequency domain model does not output the voltage distribution of the turns, it still could be used as a diagnostic tool in Frequency Response Analysis (FRA) [185] described by Alvarez in [82] to be amongst the advanced diagnostic tools. The idea behind it consists in detecting the presence of a failure, or the start thereof, based on a performed comparison between the measured frequency response of the operating machine and its initial frequency response, which in our case is accurately predicted by our proposed model. A slight inter-turn spacing change, deformation or breakdown of the insulation will transpire in the frequency response, mainly the resonance frequencies hinting hence at an internal fault.

CHAPTER

3

TIME DOMAIN MODELLING

Contents

3.1 Introduction

After accounting for the different frequency dependencies in the frequency domain in the previous chapter, we will now focus on accounting for them in time domain with the objective being the extraction of the inter-turn voltage distribution. As a matter of fact, given the nature of the proposed frequency domain model, its implementation as-is in time domain is not possible. The different frequency dependent parameters are defined as frequency domain vectors and cannot be directly simulated in a transient analysis. We hence need to implement the appropriate technique to convert the frequency domain model into a time domain one.

Accordingly, and as already discussed in the first chapter (refer to section 1.4), one way of converting the frequency domain description to a time domain is through convolution integrals, which present the inconvenience of not only having an exponential runtime cost but require the solution storage at antecedent time-steps [120], [121]. Another solution that can be implemented is the frequency dependent network equivalent, where the frequency behaviour is emulated through passive electrical circuits. However, incorporating the different mutual couplings between the turns in time domain simulations through behavioural voltage sources lacks robustness. Although it initially showed promise on small circuits, it has been observed that for moderately complex circuits, the occurrence of stability issues becomes more frequent.

A more robust alternative approach is the usage of the time domain Nodal Analysis (NA). NA enables to analyse circuits that are not just simple series or simple parallel circuits under the condition that they have an admittance representation. It is, as its name might have already insinuated, a mathematical method that computes the voltage/current distribution at the nodes (*i.e.* points of connection *e.g.* t_1, t_2 and t_3 in Fig. 2.28), of the circuit relative to a reference node, or ultimately the GND. It produces a set of equations describing the circuit that, depending on its level of complexity, can either be solved by hand or using linear algebra by a computer. When using this technique, a linear behaviour of the network is assumed. Although a powerful tool used to solve electrical circuits, the NA presents some limitations. The most inconvenient and related to this research work is its inability to handle voltage (and current for that matter) dependent sources.

A workaround to the aforementioned NA limitation is the implementation of the Modified Nodal Analysis (MNA) method also known as "loop analysis method" [186]–[189]. It is a common approach adopted by most circuit simulators, SPICE included, when the elements do not have an admittance representation. Using this method, the nodal equations are modified by incorporating the mutual couplings between the different elements of the studied circuit. Firstly, the different circuit loops paths including the mutual coupling are identified. Then, each current loop is defined and linked to the current of the mutual coupling. Next, the nodal equations are written, as in the regular NA, but with the addition of the mutual coupling terms. Following that, the same methods used in NA are applied. The solution in this case yields nodal voltages and currents accounting for the different couplings between the components. Indeed, MNA allows to take into account the different coupling between the turns, still, with the added set of equations the complexity of the system to be solved is increased. Therefore, the idea of using the time domain MNA to solve the previously presented frequency domain circuit in time domain is cast aside. For this, and instead of applying the time domain MNA to deduce each node voltage alone, we study the winding by describing it using the nodal admittance matrix in frequency domain, which is appropriately made use of to deduce a new electrical circuit [190] suitable for a time domain investigation. This allows a straightforward usage of IFFT as well as the VF implementation to calculate the time domain nodal voltages.

This chapter is organised as follows: we start by reminding the definition of the nodal admittance matrix in section 3.2. Then, in section 3.2.1, we explain the adopted method used to

extract its parameters by inspection. Next, and following the same approach as in the previous chapter by conserving the automation of the script, we will present a simple technique to compute the nodal voltages using IFFT in section 3.2.4. The experimental investigation is performed and the results are confronted to those deduced for an equivalent VF implementation in section 3.3, followed by the verification of the computed inter-turn voltages according to the measurements. Finally, a comparison with the computed results when adopting the previous developed model [17] is presented.

3.2 Nodal Admittance Matrix

The proposed frequency model involves a large variety and number of network components as has been presented in the previous chapter. The individual behaviour of each turn was developed and we are now concerned with a more compact representation of these components that will allow for a time domain evaluation of the voltage distribution. For similar large-scale systems, the analysis of the network model is done in the form of a network matrix. The voltage drop can be linked to the current flowing through the network by either the impedance or admittance parameter, *i.e.* the inverse of the impedance matrix. For this work, we will focus on the nodal admittance matrix.

The nodal admittance matrix mathematically links the voltages and the currents of an electrical circuit

$$\left[\overline{\mathbf{I}}\right] = \overline{\mathbf{Y}}\left[\overline{\mathbf{V}}\right], \tag{3.1}$$

where $\left[\overline{\mathbf{V}}\right]$ contains the nodal voltages and $\left[\overline{\mathbf{I}}\right]$ contains the corresponding currents, whereas the n-bus admittance matrix $\overline{\mathbf{Y}}$ is the nodal admittance matrix and writing it requires the aforementioned steps of NA. It is used to study linear circuits with several components (inductors, resistors and capacitors) linked through nodes. It is a square matrix with its dimension equating to the number of nodes n, *e.g.* 69×69 for the $n = 69$ turns winding, and appears as follows:

$$\overline{\mathbf{Y}}_n = \begin{pmatrix} \overline{Y}_{11} & \overline{Y}_{12} & \cdots & \overline{Y}_{1n} \\ \overline{Y}_{12} & \overline{Y}_{23} & \cdots & \overline{Y}_{2n} \\ \vdots & \ddots & \ddots & \\ \overline{Y}_{1n} & \overline{Y}_{2n} & \cdots & \overline{Y}_{nn} \end{pmatrix}, \tag{3.2}$$

where its parameters $\overline{Y}_{ij}$ are the different complex admittances of the circuit components. Each one of its parameters represents the admittance between two nodes in the circuit. The diagonal parameters $\overline{Y}_{ii}$ are the sum of the different admittances $\overline{y}_{ij}$ of the components connecting the j^{th} turn to the i^{th} turn. The off-diagonal entities $\overline{Y}_{ij}$, on the other hand, are the negative of the admittance $\overline{y}_{ij}$ connecting the two turns i and j [190].

The general mathematical expressions of its parameters are summed up in (3.3).

$$\overline{Y}_{ij} = \begin{cases} \sum_{j=1}^{n} \overline{y}_{ij}, \text{ if } i = j \\ -\overline{y}_{ij}, \text{ if } i \neq j. \end{cases} \tag{3.3}$$

To illustrate this, we use the three bus network seen in Fig. 3.1.

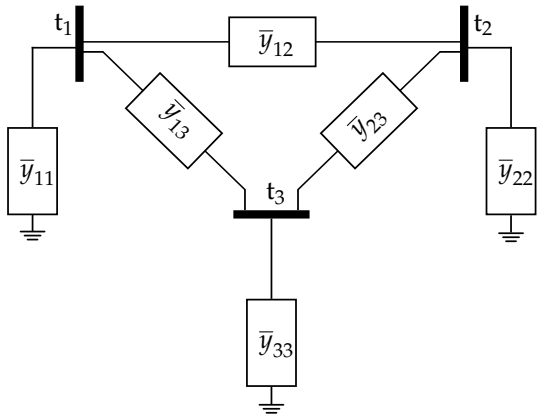

FIGURE 3.1: A three bus network used to illustration the computation of $\overline{Y}_{ij}$ parameters.

Applying (3.3), the nodal admittance matrix of the three bus network writes:

$$\overline{\mathbf{Y}}_3 = \begin{pmatrix} \overline{y}_{11}+\overline{y}_{12}+\overline{y}_{13} & -\overline{y}_{12} & -\overline{y}_{13} \\ -\overline{y}_{12} & \overline{y}_{22}+\overline{y}_{12}+\overline{y}_{23} & -\overline{y}_{23} \\ -\overline{y}_{13} & -\overline{y}_{23} & \overline{y}_{33}+\overline{y}_{13}+\overline{y}_{23} \end{pmatrix}. \tag{3.4}$$

The nodal admittance matrix is typically a symmetric matrix, *i.e.* $\overline{Y}_{ij} = \overline{Y}_{ji}$, but there are cases where it can be asymmetric, like for an instance in the presence of unilateral components in the circuit than allow for the current in one direction only (*i.e.* transistors, amplifier, switch, etc). Anyhow, given the nature of the previously developed frequency model of the winding, the admittance matrix of our winding is symmetrical. Given the context of this research work, and alluding to equations (2.52) and (2.53), the expression (3.2) becomes:

$$\overline{\mathbf{Y}}_n^{\mathrm{m}} = \begin{pmatrix} \overline{Y}_{11}(f_1) & \overline{Y}_{12}(f_1) & \cdots & \overline{Y}_{1n}(f_1) \\ \overline{Y}_{12}(f_1) & \overline{Y}_{22}(f_1) & \cdots & \overline{Y}_{2n}(f_1) \\ \vdots & \ddots & \ddots & \\ \overline{Y}_{1n}(f_1) & \overline{Y}_{2n}(f_1) & \cdots & \overline{Y}_{nn}(f_1) \end{pmatrix} \begin{pmatrix} \overline{Y}_{11}(f_{\mathrm{m}}) & \overline{Y}_{12}(f_{\mathrm{m}}) & \cdots & \overline{Y}_{1n}(f_{\mathrm{m}}) \\ \overline{Y}_{12}(f_{\mathrm{m}}) & \overline{Y}_{22}(f_{\mathrm{m}}) & \cdots & \overline{Y}_{2n}(f_{\mathrm{m}}) \\ \vdots & \ddots & \ddots & \\ \overline{Y}_{1n}(f_{\mathrm{m}}) & \overline{Y}_{2n}(f_{\mathrm{m}}) & \cdots & \overline{Y}_{nn}(f_{\mathrm{m}}) \end{pmatrix}, \tag{3.5}$$

where m, f_1 and f_m refer to the number of frequency samples, the first frequency and the mth frequency, respectively.

The same inconvenience as to how to account for the multiple occurring impedance couplings between the turns arises. To overcome this, we choose to make use of the developed frequency domain model to deduce the admittance matrix by inspection. This is further elaborated in the ensuing section.

3.2.1 Extraction of the nodal admittance matrix

An n-ports admittance matrix describes the behaviour of the device under test seen from its n-ports, in our case turns, as depicted in Fig. 3.2, by linking its voltages $(V_{t_1}, V_{t_2}, \cdots, V_{t_n})$ to the corresponding currents $(I_1, I_2, \cdots, I_n)$.

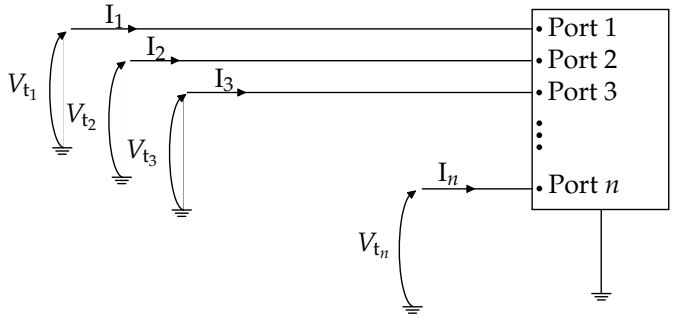

FIGURE 3.2: An n-port network.

In light of our interest in the nodal voltages, it is more interesting to study the system, *i.e.* the winding of electrical machines, as an n-port network, with n being the number of turns. However, given the multiple impedance couplings between turns we have come to the conclusion that using the MNA matrix to take them into account results in very large matrices. As a solution, we make use of the already validated frequency domain model to extract the nodal admittance by inspection. For that we excite the nodes of the winding one at a time in complex frequency domain while short-circuiting the remaining turns. Then, we extract the values of the parameters of the corresponding row of the nodal admittance matrix [191].

For illustration, we use the three turns winding seen in Fig. 2.17, whose nodal admittance matrix writes:

$$\overline{\mathbf{Y}}_3^{\mathrm{m}} = \begin{pmatrix} \overline{Y}_{11}(f_1) & \overline{Y}_{12}(f_1) & \overline{Y}_{13}(f_1) \\ \overline{Y}_{12}(f_1) & \overline{Y}_{22}(f_1) & \overline{Y}_{23}(f_1) \\ \overline{Y}_{13}(f_1) & \overline{Y}_{23}(f_1) & \overline{Y}_{33}(f_1) \end{pmatrix} \cdots \begin{pmatrix} \overline{Y}_{11}(f_m) & \overline{Y}_{12}(f_m) & \overline{Y}_{13}(f_m) \\ \overline{Y}_{12}(f_m) & \overline{Y}_{22}(f_m) & \overline{Y}_{23}(f_m) \\ \overline{Y}_{13}(f_m) & \overline{Y}_{23}(f_m) & \overline{Y}_{33}(f_m) \end{pmatrix} \quad \text{m} \quad , \tag{3.6}$$

and which is hereinafter studied as a 3 ports network.

To compute $\overline{\mathbf{Y}}_3^{\mathrm{m}}$ by inspection, we start by exciting the first turn with a chosen value $\overline{V}_{\mathrm{t}_1}$ while short-circuiting the second and third turns. We run the simulation in frequency domain in the frequency range of interest and extract the values of $\overline{Y}_{11}(f)$, $\overline{Y}_{12}(f)$ and $\overline{Y}_{13}(f)$, whose expressions are the following, respectively:

$$\begin{cases} \overline{Y}_{11}(f) = \dfrac{\bar{\mathrm{I}}_1(f)}{\overline{V}_{\mathrm{t}_1}(f)}, \\ \overline{Y}_{12}(f) = \dfrac{\bar{\mathrm{I}}_2(f)}{\overline{V}_{\mathrm{t}_1}(f)}, \\ \overline{Y}_{13}(f) = \dfrac{\bar{\mathrm{I}}_3(f)}{\overline{V}_{\mathrm{t}_1}(f)}. \end{cases} \tag{3.7}$$

We repeat the same procedure for the second turn: we excite the second turn while short-circuiting the first and the third turns. Then, we extract the values of its parameters the same way the first parameters were computed in (3.7). Similarly, the third row parameters are determined.

This enables the study of the circuit as a whole, where the different couplings (resistive, inductive and capacitive) between turns are accounted for. Using the nodal admittance matrix the inter-turn voltage distribution could be deduced numerically or from the eigenvalues and eigenvectors of as elaborated by Dassios [192]. In this work, and following the footsteps of the previous chapter, we study the possibility of solving the circuit in frequency domain, by computing the spectrum of the different nodal voltages. Then, we compute their IFFT that allow for a time domain representation of the circuit which will allow an eventual computation of the PD occurrence probability. However, we still need to convert the nodal admittance matrix to an electrical circuit linking the different nodes through admittances. This is touched upon in the subsequent section.

3.2.2 The equivalent multi-port circuit

Once the frequency dependent nodal admittance matrix is computed by inspection using the frequency domain model we have developed, the new multi-port circuit describing the studied system can be deduced, where the number of ports equals the number of the winding turns. In this case we will not need to add behavioural voltage sources to account for the impedance couplings between turns. The required information has already been computed by inspection and stacked in the nodal matrix. Again, using the three turns winding sample as an example, its corresponding multi-port π-equivalent once the frequency dependency accounted for is depicted in Fig. 3.3.

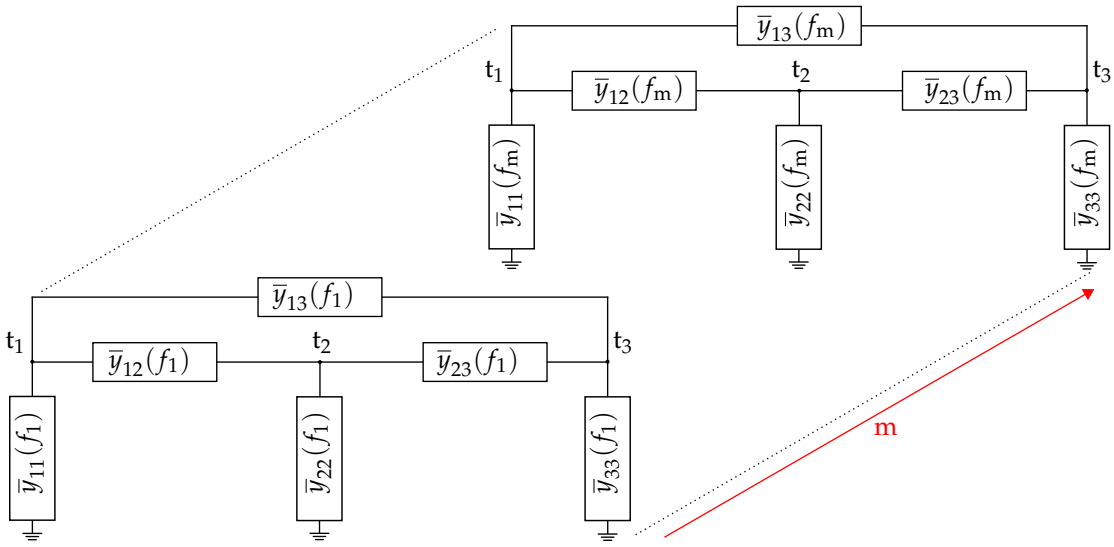

FIGURE 3.3: The equivalent multi-port circuit deduced from the nodal admittance matrix $\overline{\mathbf{Y}}_3^{\mathrm{m}}$ of the three turns winding sample.

The components of the new circuit are easily computed from the nodal admittance matrix. Each node (t_1, t_2 and t_3) is connected to the GND through the admittance $\overline{y}_{ii}$ (where $i = 1, 2, 3$), that is given by the sum of the element of the i^{th} row of the nodal admittance matrix,

$$\overline{y}_{ii}(f) = \sum_{j=1}^{n} \overline{Y}_{ij}(f), \tag{3.8}$$

whereas, for the inter-turn connections $\overline{y}_{\mathrm{ij}}$, they are computed as follows:

$$\overline{y}_{ij}(f) = -\overline{Y}_{ij}(f). \tag{3.9}$$

The computation of $\overline{y}_{ii}$ and $\overline{y}_{ij}$ is summarized in (3.10).

$$\overline{\mathbf{Y}}_3(f_i) = \sum \begin{pmatrix} \overline{Y}_{11}(f_i) & \overline{Y}_{12}(f_i) & \overline{Y}_{13}(f_i) \\ \overline{Y}_{12}(f_i) & \overline{Y}_{22}(f_i) & \overline{Y}_{23}(f_i) \\ \overline{Y}_{13}(f_i) & \overline{Y}_{23}(f_i) & \overline{Y}_{33}(f_i) \end{pmatrix} \begin{matrix} = \overline{y}_{11}(f_i) \\ \\ \\ \end{matrix} \\ \begin{matrix} -\overline{y}_{13}(f_i) & & -\overline{y}_{23}(f_i) \end{matrix} \tag{3.10}$$

Instead of studying the full nodal admittance matrix, we choose to study its reduced version to one node at a time in order to reduce the number of unknowns in the generated complex circuits. This procedure, referred to as node elimination, is touched up in the ensuing section.

3.2.3 The Reduced Nodal Admittance Matrix

When studying the windings of electrical machines turn by turn, we end up with very large systems to be solved. To avoid the latter, the studied system could be reduced to an equivalent

multi-port system allowing access only to the nodes of interest. The eliminated nodes are those at which no current enters or leaves. They can either be eliminated one after the other or in one group. Since we are making use of the frequency dependent model, the nodes that cannot be eliminated are node t_1 and GND. Hence the different input nodes of the remaining turns could be removed without changing the properties of the studied system. The reduced nodal admittance matrix can be achieved by performing node elimination on the extracted nodal admittance matrix. The idea behind it is to transform the studied system into an equivalent and simpler one by removing chosen nodes and the branches that connect them. This can be be performed by either using linear algebra, or properly manipulating the developed frequency domain model.

When using matrix algebra the elements of the extracted nodal admittance matrix are rearranged so that the nodes to be eliminated are placed in the lower rows of the matrix. The generated sub-matrices are later on combined using Kronecker product to eventually create a reduced system. The voltages at the eliminated nodes are therefore expressed according to the remaining variables of the circuit and eventually substituted into the reduced system.

The second method to perform node elimination is by properly manipulating the developed frequency domain model. The idea behind it is to only excite/short circuit the nodes of interest. Taking for instance the three turns winding as an example, the nodes that cannot be eliminated are "t_1" and the GND. Thus, the proposed frequency domain circuit can be reduced to either node "t_2" or node "t_3". Its nodal admittance matrix (3.5) in these two cases becomes:

$$\overline{\mathbf{Y}}_2^{\mathrm{m}} = \begin{pmatrix} \overline{Y}_{11}(f_1) & \overline{Y}_{12}(f_1) \\ \overline{Y}_{12}(f_1) & \overline{Y}_{22}(f_1) \end{pmatrix}_{2} \begin{pmatrix} \overline{Y}_{11}(f_{\mathrm{m}}) & \overline{Y}_{12}(f_{\mathrm{m}}) \\ \overline{Y}_{12}(f_{\mathrm{m}}) & \overline{Y}_{22}(f_{\mathrm{m}}) \end{pmatrix}_{\mathrm{m}}, \tag{3.11}$$

Reducing the three turns winding to only node "t_2" is performed by exciting first "t_1" while short circuiting the turn "t_2" to extract the values defining the first row of the $\overline{\mathbf{Y}}_2^{\mathrm{m}}$, as illustrated in Fig. 3.4 and 3.5, respectively.

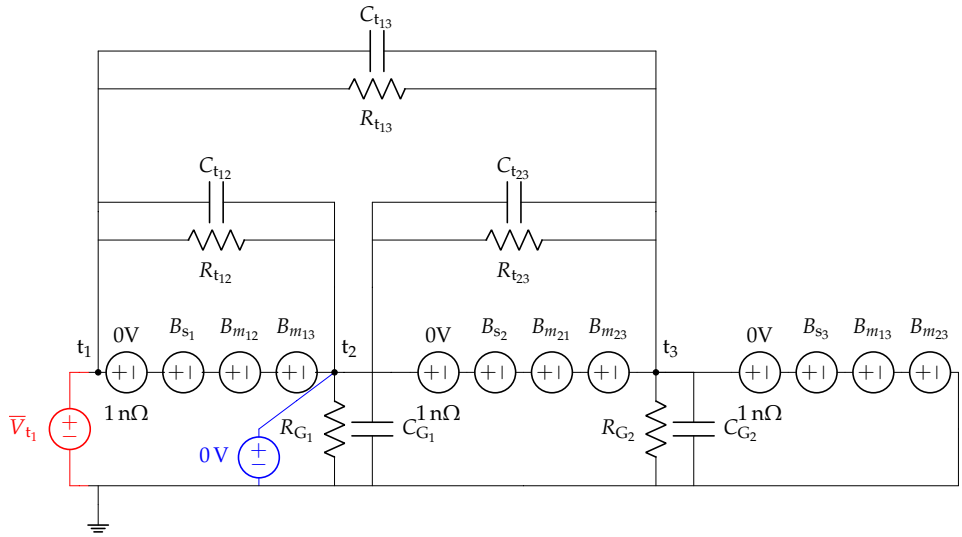

FIGURE 3.4: Exciting the first turn of the three turns winding sample to extract the reduced nodal admittance matrix to turn t_2.

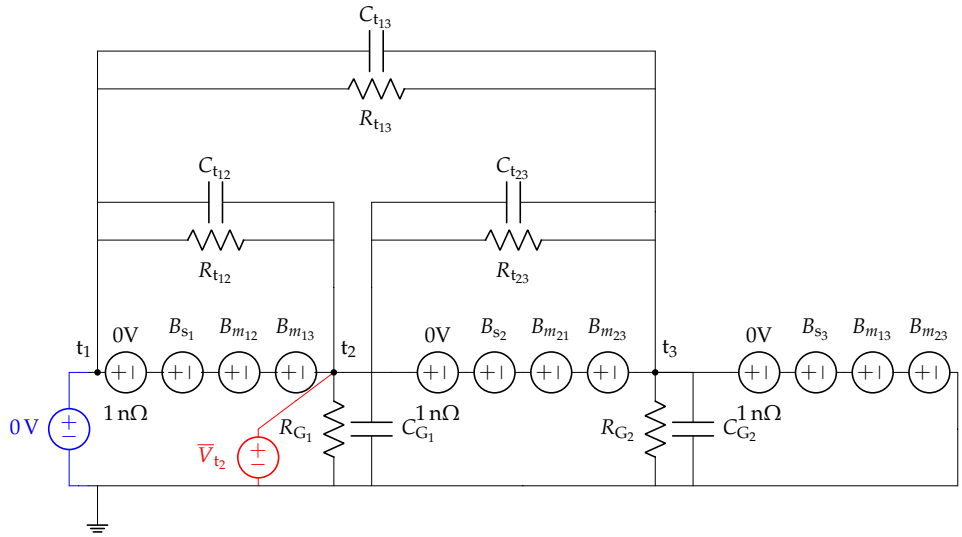

FIGURE 3.5: Exciting the second turn of the three turns winding sample to extract the reduced nodal admittance matrix to turn t_2.

After presenting a technique that allows the deduction by inspection of the reduced nodal matrix from the already developed frequency domain model, we will discuss in the next section the computation of the time domain nodal voltages.

3.2.4 Deduction of the nodal voltages

Up to this point the usage of the developed frequency domain to compute the reduced nodal admittance matrix of the studied winding by inspection has been elaborated on. The computation of the nodal voltages in time domain can be performed in two ways:

1. without having to call for fitting techniques by deducing the equivalent multi-port network from the reduced nodal matrix computed by inspection and applying IFFT, provided that the spectrum $\overline{V}_{t_1}(f)$ is known;
2. applying the VF algorithm [150] on the deduced reduced nodal admittance matrix (3.11), enforce its passivity [151], generate the equivalent multi-port circuit and then run the transient simulation in the used circuit simulator.

Referring to section 3.2.2, the reduced NA can be converted to an equivalent multi-port circuit where the electrical link between the considered nodes (the n nodes of the winding, or just the ones in the reduced nodal matrix) is ensured through the admittances $\overline{y}_{ij}$ deduced from $\overline{Y}_{ij}$. For illustration, the reduced version of the circuit in Fig. 2.28 is presented in Fig. 3.6.

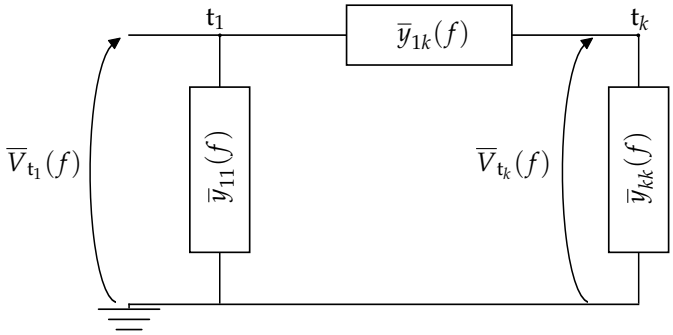

FIGURE 3.6: The IFFT reduced version of the circuit seen in Fig. 2.28 to the k^{th} node.

Subsequently, the computation of the frequency domain spectrum of the k^{th} nodal voltage

$$\overline{V}_{t_k}(f) = \overline{V}_{t_1}(f)\,\frac{\overline{y}_{kk}(f)^{-1}}{\overline{y}_{kk}(f)^{-1} + \overline{y}_{1k}(f)^{-1}}. \tag{3.12}$$

enables the deduction of the k^{th} nodal voltage time domain evolution by applying an IFFT. The second nodal voltage computation technique requires the use of the VF algorithm on the reduced nodal matrix as described in [150], where all its elements are fitted with identical poles, then the passivity enforcement is imposed so as to avoid having unstable transient simulations [151] (refer to section 1.4.3.3). Following this, the frequency dependent network equivalents reproducing the frequency behaviour of $\overline{y}_{11}(f)$, $\overline{y}_{1k}(f)$ and $\overline{y}_{kk}(f)$ are deduced. The reduced circuit when using the second approach is presented in Fig. 3.7.

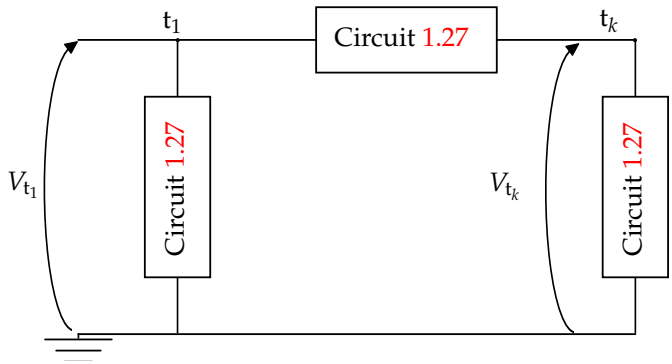

FIGURE 3.7: The reduced version of the circuit seen in Fig. 2.28 to the k^{th} node deduced from vector fitting.

This technique, however, requires the intervention of the user to properly configure the fitting parameters. The two techniques are summarized in the flowchart seen in Fig. 3.8.

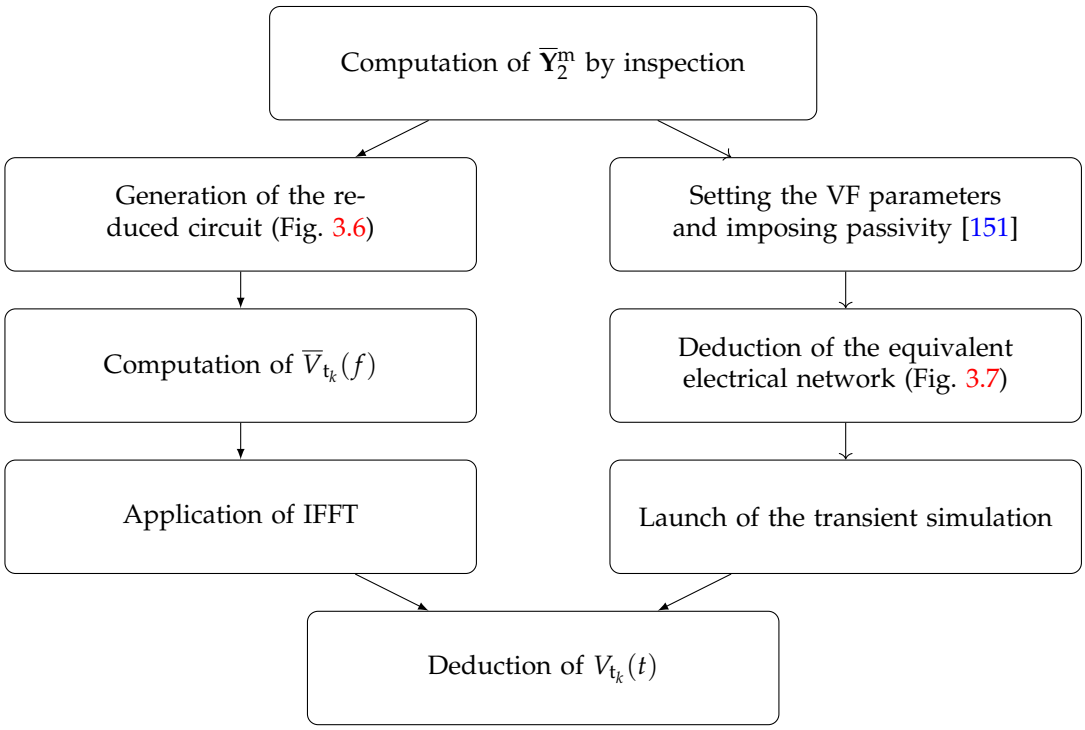

FIGURE 3.8: Flowchart of the two investigated time domain models (the proposed inverse fast Fourier transform model and the previously developed vector fitting model).

The two nodal voltages computation techniques are investigated in the ensuing section by being confronted to the time domain measurements of measured some nodal voltages of a chosen test case.

3.3 Experimental validation

The time domain measurements are performed using the energy conversion system presented in Fig. 1.1, with its internal structure depicted in Fig. 3.9. The used converter is made of only one transistor-diode cell seen in Fig. 1.2. The model of the cable as well as that of the converter were not developed for this research work. Hence, we measure the voltage V_{t_1} imposed on the windings (*e.g.* the first turn nodal voltage), and compute the internal voltages of the considered winding. We perform the time domain investigation on the $n = 69$ turns winding presented in Fig. 2.35.

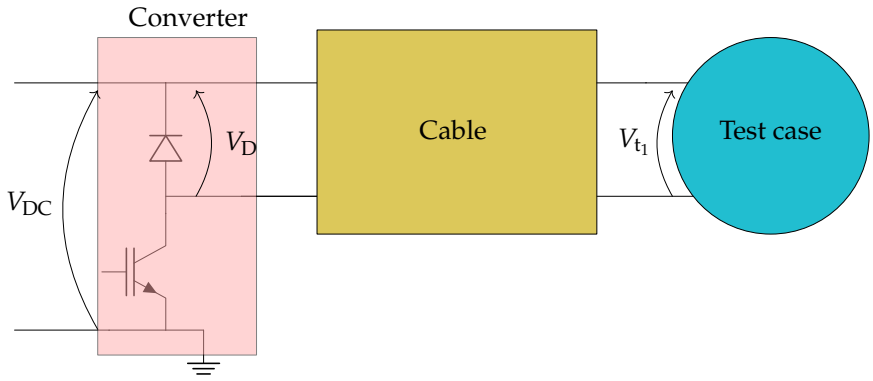

FIGURE 3.9: A time domain measurements setup. *The command of the transistor was developed with the help of Matteo Cicuttin.*

The values of the imposed DC voltage V_{DC}, the duty cycle α, the switching frequency, the rise t_r and the fall t_f times, respectively, are summed up in Tab. 3.1. Due to the small value of the duty cycle, the steady state is reached before the end of the period.

TABLE 3.1: The specifications of the imposed voltage.

V_{DC}	α	f_{sw}	t_r	t_f
25 V	2 %	10 kHz	66.7 ns	25 ns

Since electrical constraints primarily affect the initial turns of the electrical machines windings, and considering that we do not have access to the conductors of the first layer, our time domain experimental investigation has been concentrated on the first turns of the second layer. The investigation was performed on the 37th, 38th and 40th turns of the 69 turns winding which are highlighted in Fig. 3.10.

FIGURE 3.10: The turns of the 69 turns winding on which the time domain experimental investigation is performed are highlighted in blue.

For each one of these turns, the frequency domain model is used to extract the reduced electrical circuit (either the one seen in Fig. 3.6 or in Fig. 3.7) to one node at a time by following the

approaches described in section 3.2.4. The two aforementioned techniques to compute the time domain variation of these nodal voltages are both investigated in the ensuing sections.

3.3.1 The proposed IFFT model to compute the nodal voltages

In this section, we start by experimentally investigating the accuracy of the proposed IFFT model. The comparison between the computed and the measured 37^{th} nodal voltage for the entire period is seen in Fig. 3.11, where satisfactory results are noticed.

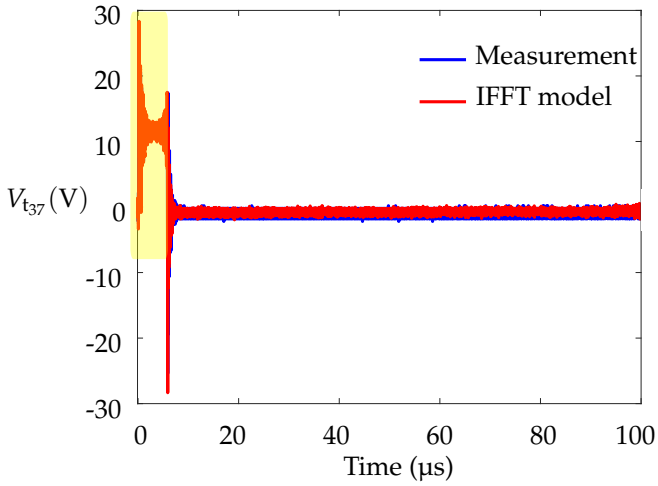

FIGURE 3.11: The comparison between the measured and the IFFT deduced 37^{th} nodal voltage over the whole period.

Zooming over the measured and computed voltage overshoots of the 37^{th}, 38^{th} and 40^{th} nodal voltages are depicted in Fig. 3.12, Fig. 3.13 and Fig. 3.14, respectively.

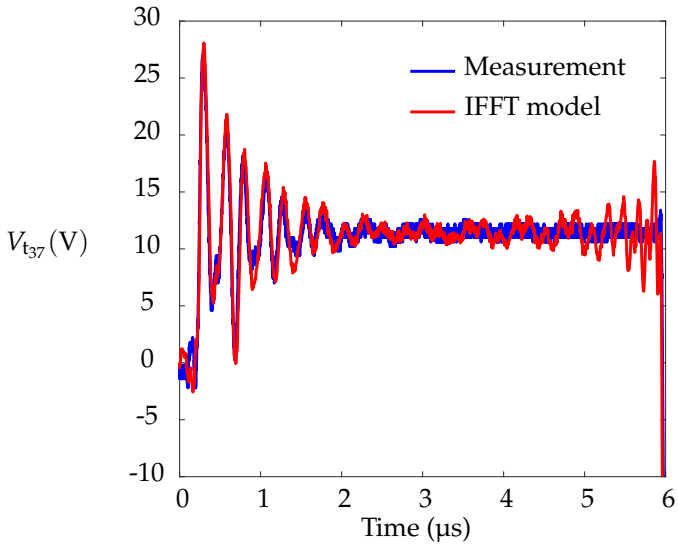

FIGURE 3.12: The comparison between the measured and the IFFT deduced 37^{th} nodal voltage.

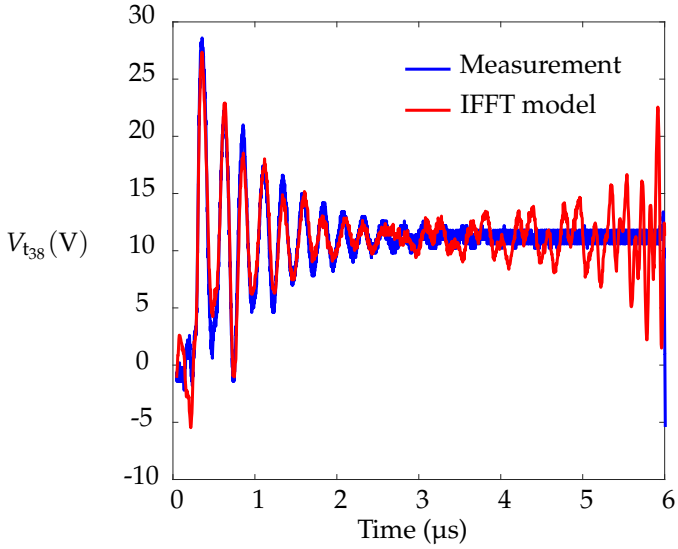

FIGURE 3.13: The comparison between the measured and the IFFT deduced 38th nodal voltage.

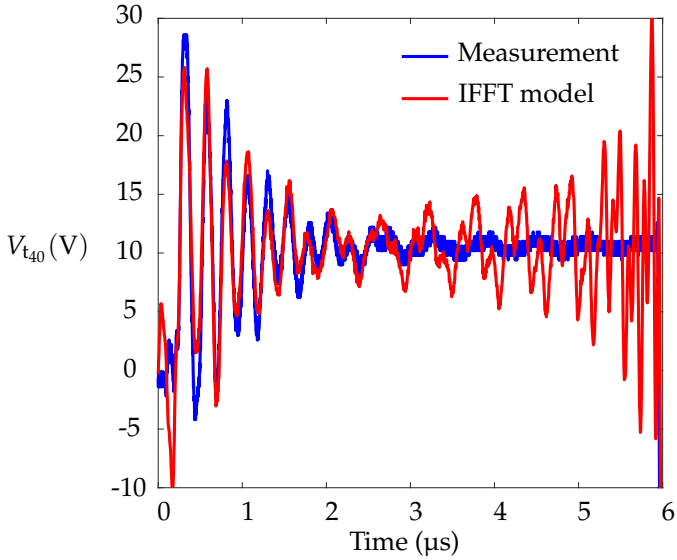

FIGURE 3.14: The comparison between the measured and the IFFT deduced 40th nodal voltage.

As noticed, the overshoots are well predicted with the proposed IFFT model. However, we notice oscillations around the falling front that are not present in the measurements. We have tried various filtering strategies to alleviate this problem without any promising solutions. Interestingly, these oscillations did not appear when applying the proposed IFFT method in the three turns winding test case subject to a voltage of the form seen in Fig. 1.15.

While these the spurious oscillations do not prevent the proposed IFFT method to be used as an input to the different numerical methods to eventually compute the PD occurrence possibility, an improvement is still to be made so as to better match the experimental measurements.

To this end, in the next section, we will apply the VF model on the same turns so as to compare the two techniques.

3.3.2 The vector fitting model to compute the nodal voltages

In this section, we study the results of using the VF algorithm to fit the aforementioned reduced nodal matrices ($\overline{\mathbf{Y}}_2^{\mathrm{m}}$ reduced to the 37^{th}, 38^{th} and 40^{th} nodes, respectively) of the 69 turns winding, from which the reduced electrical circuits are deduced (Fig. 3.7). For this fitting, n_{p}=50 poles linearly and logarithmically spaced inversely weighed are used. A high number of poles was chosen for the fitting, so that both the IFFT and the VF models have approximately the same nodal admittance matrix as an input so as to compare the results of both techniques. An example of the fitting of the parameters of $\overline{\mathbf{Y}}_2^{\mathrm{m}}$ reduced to the 37^{th} turn is depicted in Fig. 3.15.

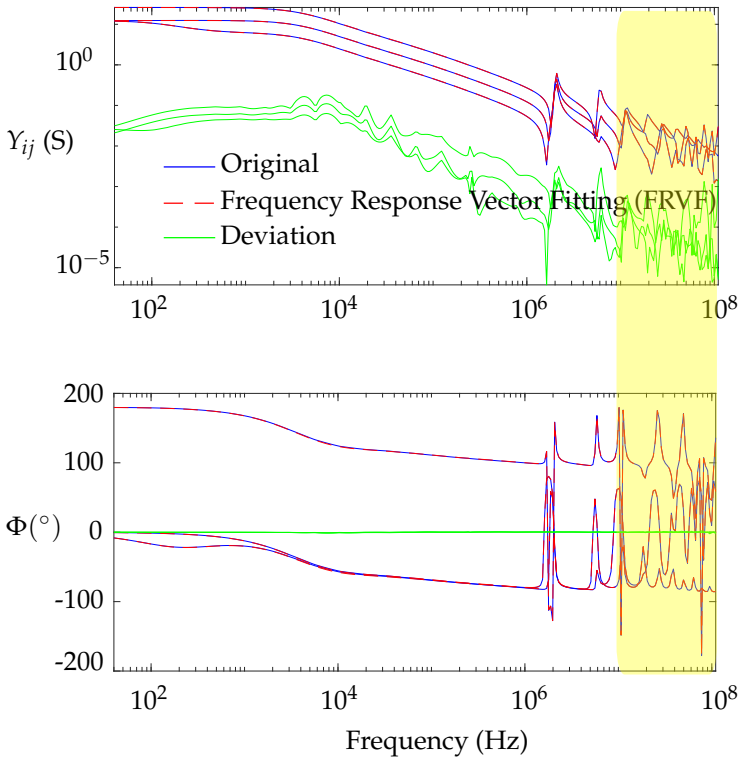

FIGURE 3.15: Applying the VF algorithm [150] to the parameters of $\overline{\mathbf{Y}}$ reduced to the 37^{th} turn ($= \overline{\mathbf{Y}}_2^{\mathrm{m}}$).

A zoom on the high frequency vector fitting is seen in Fig. 3.16.

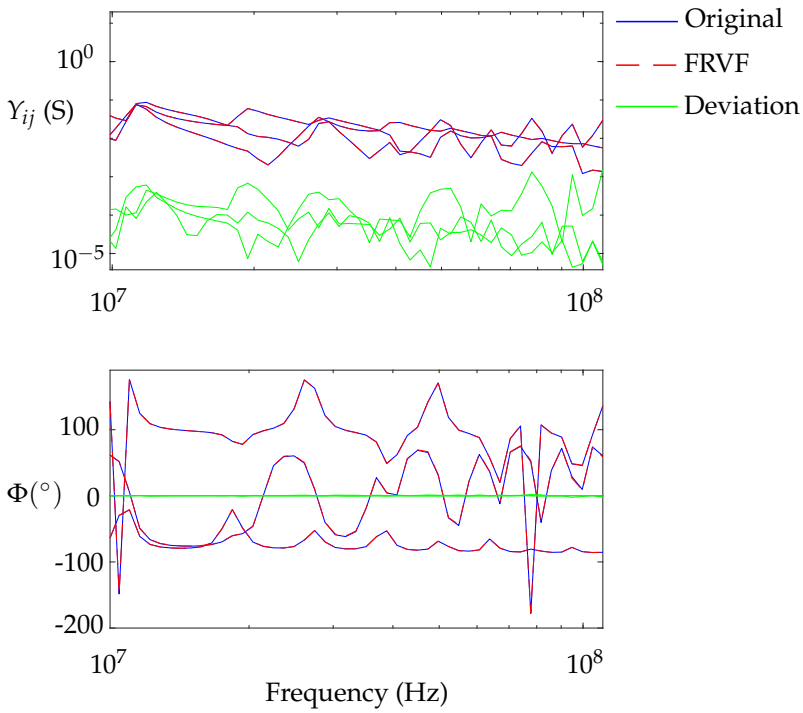

FIGURE 3.16: A zoom on the high frequency vector fitting of Fig. 3.15.

Once the fitting completed and validated, the reduced electrical circuits are generated and are then run in transient simulations of the used circuit simulator LTspice. The experimental comparisons are displayed in Fig. 3.17, Fig. 3.18 and Fig. 3.19.

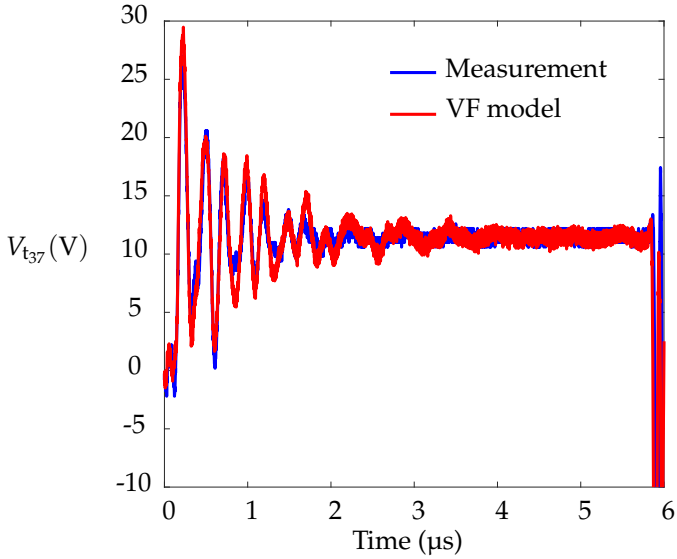

FIGURE 3.17: The comparison between the measured and the vector fitting deduced 37^{th} nodal voltage.

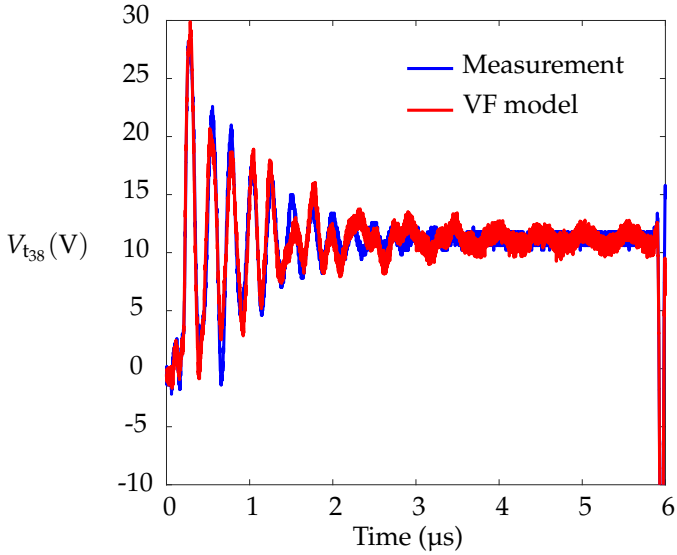

FIGURE 3.18: The comparison between the measured and the vector fitting deduced 38$^{\text{th}}$ nodal voltage.

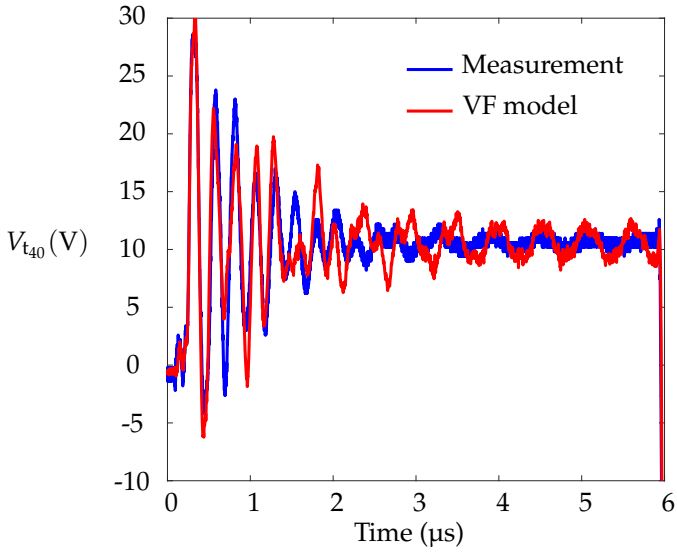

FIGURE 3.19: The comparison between the measured and the vector fitting deduced 40$^{\text{th}}$ nodal voltage.

The mathematical artefacts are less prominent when using the VF algorithm, this is due to the fact that even though the fitting was set up to reproduce the frequency behaviour of interest up to $f_{\text{m}} = 110\,\text{MHz}$, the response of the deduced network equivalent does not "stop" at f_{m}; unlike the proposed IFFT model where the frequency response above f_{m} is ignored by being set to 0. Using an appropriate windowing function could prove useful and is left for future research work.

For each of the experimentally investigated turn (37$^{\text{th}}$, the 38$^{\text{th}}$ and the 40$^{\text{th}}$), the computational expenses of both the extraction of the reduced nodal admittance matrix as explained in section 3.2.3 and the IFFT application in comparison with the VF computation time are summed

up in Tab. 3.2. We notice that the IFFT computation is almost instantaneous. However, for a higher accuracy, the VF model could be applied but is more computationally expensive.

TABLE 3.2: Comparison of the computational time needed when implementing the IFFT method and the vector fitting method.

Extraction of $\overline{\mathbf{Y}}_2^m$	IFFT method	VF method		
4 min 6 s	0.122 sec	VF & Passivity	Generation of 3.7	LTspice simulation
		0.443 s	0.0105 s	4 min 5 s

Similarly to the previous chapter, and for a comparative study to be complete, we investigate the time domain results of the previously proposed LPM model [17] where the frequency behaviour was not accounted for. This is performed on the 37th, the 38th and the 40th turns of the 69 turns winding. The results are presented in Fig. 3.20, Fig. 3.21 and Fig. 3.22, respectively.

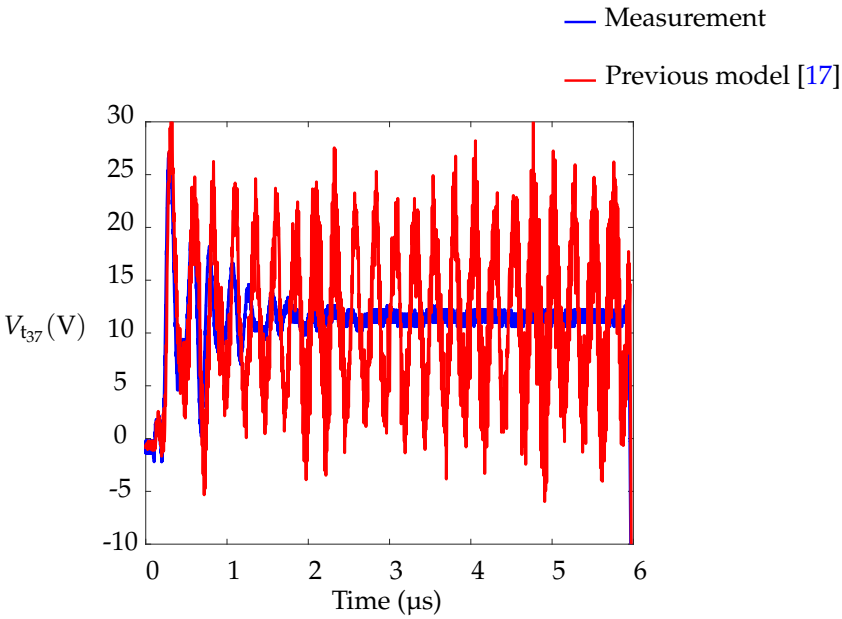

FIGURE 3.20: The comparison between the measured and the computed 37th nodal voltage using the model presented in previous research work [17].

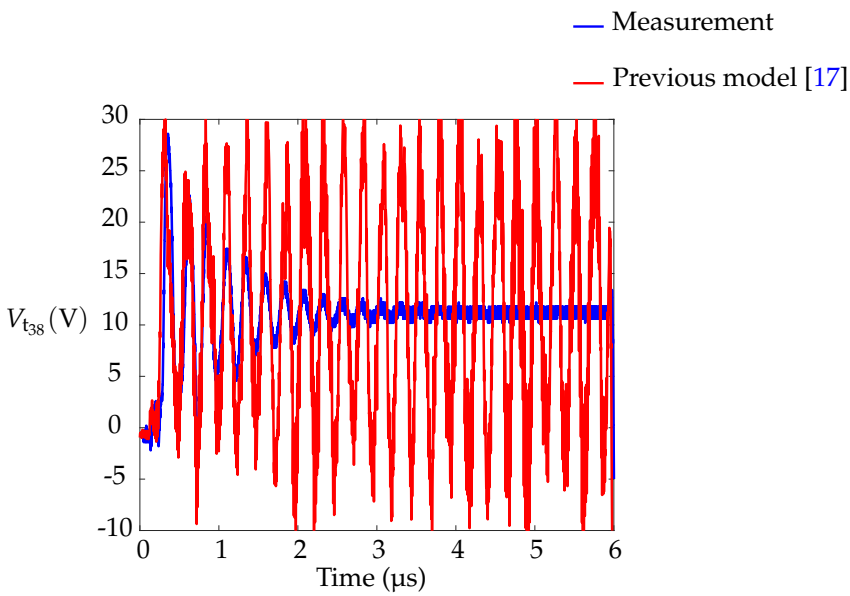

FIGURE 3.21: The comparison between the measured and the computed 38th nodal voltage using the model presented in previous research work [17].

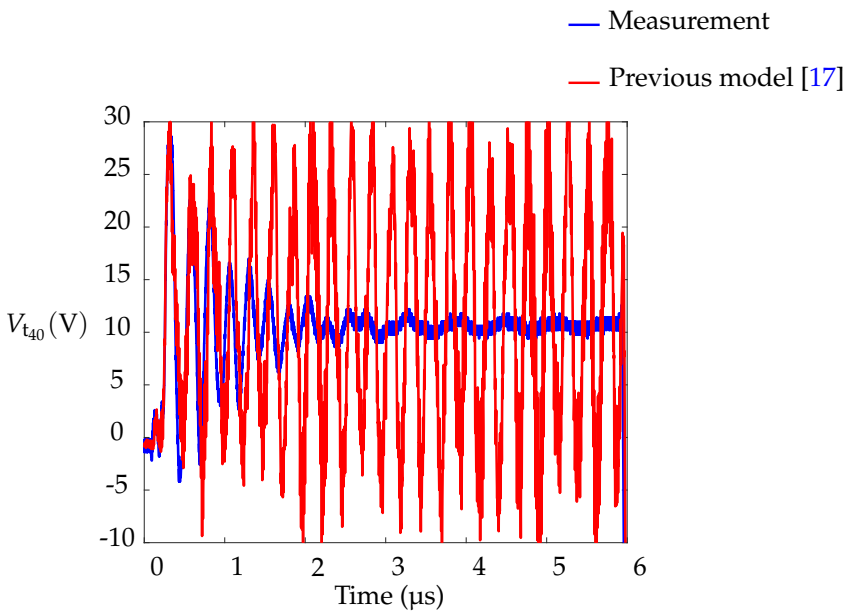

FIGURE 3.22: The comparison between the measured and the computed 40th nodal voltage using the model presented in previous research work [17]

These results are far from being satisfactory and do not allow a prediction of the time domain inter-turn distribution. This highlights the necessity to account for the frequency dependent behaviour of the phenomenological model parameters for a better prediction of the nodal voltages distribution.

With the VF results now in mind, we can utilize the nodal voltages deduced from the VF algorithm to calculate the inter-turn voltages between the investigated turns, including the measured V_{t_1}, to fully verify the proposed approach. The inter-turn voltages $U_{t_1t_{37}} = V_{t_1} - V_{t_{37}}$, $U_{t_1t_{38}} = V_{t_1} - V_{t_{38}}$ and $U_{t_1t_{40}} = V_{t_1} - V_{t_{40}}$ with their corresponding experimental measurements are plotted in Fig. 3.23a, 3.23b and 3.23c respectively.

These results prove the validity of the proposed model and highlight its accuracy in computing the nodal voltages from which the computations of the inter-turn voltages is straightforward.

3.4 Conclusion and discussion

In this chapter we proposed a time domain model of electrical machine windings. We first started by investigating the usage of the fitting techniques on a turn level where only the self behaviour was modelled using an equivalent electrical network, the mutual coupling was accounted for using behavioural voltage sources placed in series. The latter proved impractical for time domain simulations since they caused its divergence because of the called derivative in its expression. We then shifted to modelling the system through its nodal admittance matrix that can be deduced from the previously proposed frequency domain model without having to call for mathematical tools to compute it, that can, for large systems, be laborious when willing to account for the mutual couplings. We presented a method to deduce it by inspection when willing to study the winding as an n port network, or reduced to the chosen number of turns of interest. We chose for this work, to experimentally validate the time domain model by reducing the matrix to one node at a time before studying the full matrix. We noticed the emergence of mathematical artefacts which are a direct consequence the Fourier series truncation. These spurious oscillations do not occur when using the corresponding VF electrical network, since its frequency behaviour is not truncated even though the fitting is performed up to 110 MHz.

the choice between the proposed IFFT model and the previously developed VF model will rely on the required accuracy by the user as well as the computational complexity. Accuracy-wise, the VF proved to be more precise when compared to the IFFT model, however it is roughly two times slower, which is heavily dependent on the selected number of poles: the lesser the poles, the smaller the equivalent circuit is and the faster the time domain simulation—the required trial-error time to set up a good fitting was not accounted for—than the IFFT model, it also requires to properly set up the fitting parameters by the user. Unlike the brute-force IFFT model that is fully automatic.

The usage of the VF results allowed a good prediction of the inter-turn voltages which was the ultimate objective of this research work. The results of this technique can be used as an input to the different numerical efforts performed to correctly configure the PD predictors. In terms of the computational time, the usage of the proposed IFFT model can be more interesting once the spurious oscillations reduced. Their study is left for future work.

The comparison with the model proposed by the previous research work [17] have been performed where the results were clearly not satisfactory. This highlights the importance to account for the different frequency dependencies for a better prediction of the inter-turn voltages.

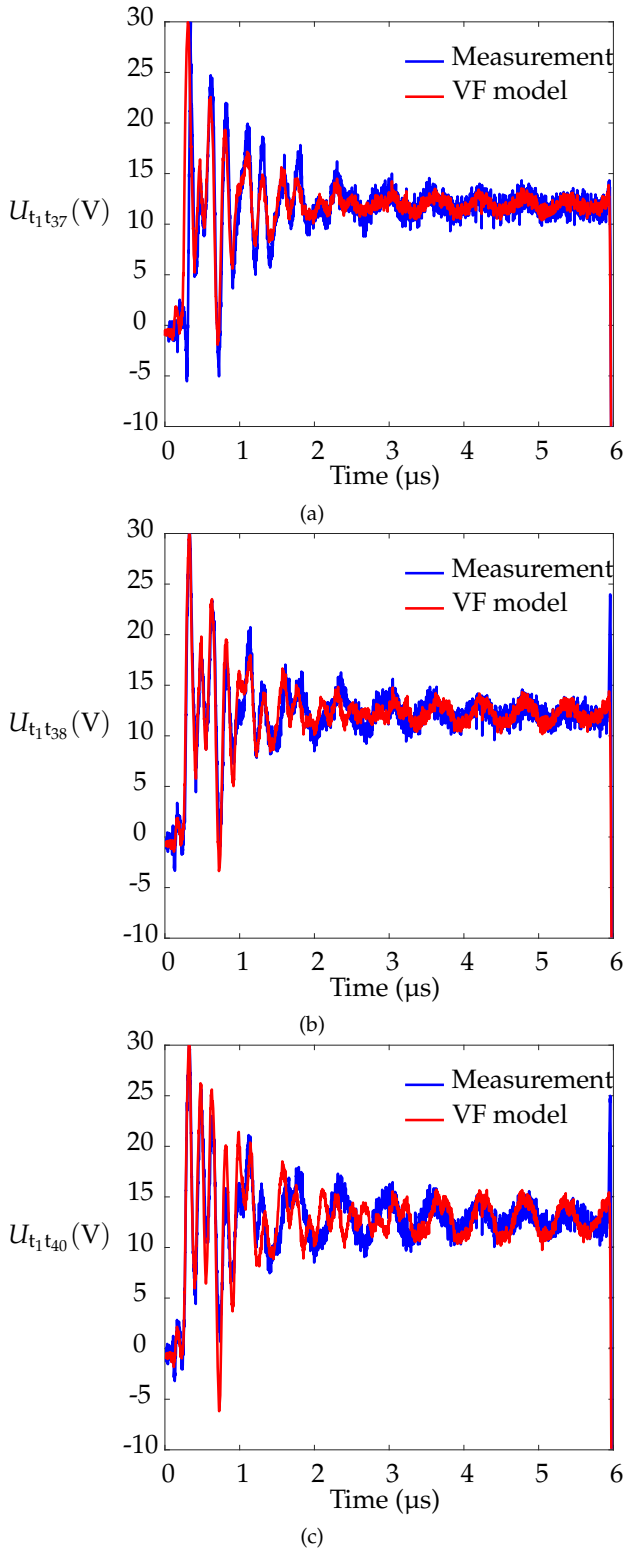

FIGURE 3.23: Comparison between the measurement and the vector fitting computation of (a) $U_{t_1t_{37}}$, (b) $U_{t_1t_{38}}$ and (c) $U_{t_1t_{40}}$.

GENERAL CONCLUSION AND PERSPECTIVES

Summary of the main contributions

This thesis commenced with a state-of-the-art review, where the different electrical windings models were compared. The interest we have in these models stems from our desire to develop a predictive model that allow the computation of the voltage distribution within the electrical machines windings. We particularly focused on the previously proposed phenomenological LPM [17] that we used as a basis model, with the objective being to account for the frequency-dependent behaviour of its parameters. This is necessary for a good voltage distribution prediction to be achieved given the harmonically rich input voltage. The different frequency dependencies of its parameters were reviewed, including that of the capacitive coupling, generally neglected in similar studies. Followed by this, the different methods proposing to include the different frequency dependencies suggested in the literature were elaborated on and compared.

In the second chapter, the electromagnetic field modelling was presented and the used formulations, depending on the computed parameter, were introduced. Then, the different parameter identification techniques were presented, verified, and compared based on the required number of computations. Those with the lowest computational complexity were chosen and implemented to identify the elements of the basis LPM over the frequency range of interest. The frequency-dependent behaviour of the used insulation was experimentally investigated and the choice of neglecting it justified. Subsequently, a novel method that accounts for the different frequency dependencies of the adopted model, including the different mutual couplings between the turns, without having to call for fitting techniques in the frequency domain was presented. The methodology is thus automatic and does not necessitate the intervention of the user to properly parametrize its fitting. The robustness of the model was tested by being applied to multiple test cases with and without a magnetic core. The accuracy of the proposed method was experimentally validated on these test cases and yielded a good agreement on the

entire frequency range of interest. A comparison with the results of the previously proposed LPM [17] was performed and the added value of this research work highlighted.

In the third chapter, we proposed to study the electrical machine windings as an n-ports network described by its reduced nodal admittance matrix. The latter was computed by inspection from the proposed frequency domain model by only exciting the node of interest. This has allowed to account for the different impedance couplings between the turns without having to call for behavioural voltage sources; which unlike in the frequency domain modelling; proved impractical for time domain modelling. The reduced nodal admittance matrix is used to deduce the equivalent multi-port electrical circuit allowing therefore a straightforward access to the spectrum of the node of interest, provided that the input voltage of the winding is known. Subsequently, an application of an IFFT gives the time domain variation of the nodal voltage of interest. Although automatic and computationally cheap, this method is subject to spurious oscillations due to the truncation of the frequency behaviour. These oscillations were significantly reduced when implementing the equivalent VF solution, which on the other hand proved to be two times slower and needs the intervention of the user to correctly set up the fitting parameters.

While our proposed methodology has been validated on windings of increasing complexity, it has not yet been applied on realistic electrical machine windings, which can exhibit additional specific features: three phases excitations, conductors in parallel, conductors with non-round cross sections, ... We do not foresee any major difficulties in including these specificities in the proposed workflow. Placing the conductors in series or in parallel and changing the number of phases can be performed as-is with the current frequency domain. In the time domain, when computing by inspection the nodal admittance matrix, the conductors placed in parallel will be merged into one equivalent conductor as they are subject to the same voltage difference. Hence, in case of an n turns winding with, for instance, 2 turns in parallel, the nodal admittance matrix will be of size $(n-1) \times (n-1)$ for a given frequency.

The studied and proposed techniques allow for an accurate enough computation of the inter-turn voltages and can be implemented as an input to the numerous numerical efforts set to predict the PD probability occurrences that give an idea on the potential whereabouts of PD. Once the latter located, precautionary steps can be taken to avert their onset. Nevertheless, some improvements could still be made. This is discussed in the ensuing section.

Perspectives

In light of the findings and contributions presented in this study, it is crucial to explore the future prospects and potential implications that emerge from this research. As a first step, if necessary, a thorough frequency behaviour investigation of the capacitive coupling behaviour beyond 10 kHz could be performed. Thus, a new setup that minimizes the impact of the different present parasitics has to be developed for a full—or at least for the frequency range of interest—dielectric characterization. This ought be performed for both the PEI and PAI layers separately to allow the inclusion of the frequency behaviour in the model no matter their respective thicknesses. Then, an appropriate model that allows the inclusion of the frequency-dependent behaviour of the iron losses has to be added to the frequency domain model. For this, we propose the usage of the frequency-dependent series representation of the complex magnetic permeability as a starting point. Accordingly, an implementation of a Debye model could prove interesting on the frequency range of interest when using soft magnetic materials. Afterwards, the study of the various LTspice alternatives to account for the different mutual couplings between turns modelled using behavioural voltage sources in this work is deemed necessary. This could be performed by examining the various circuit alternatives suggested

by LTspice, which could potentially diminish the computational complexity of the frequency domain simulation.

Once the aforementioned frequency dependencies have been accounted for, it will be more appropriate to generalize the frequency domain model to account for the different complex geometries non-reducible to 2D, by either using 3D slices linked with the appropriate virtual connections that allow to correctly account for the edge and boundary effects, as stated in section 2.1, or by proposing a set of geometrical coefficients that will enable the correction of the 2D computed values to 3D ones.

As far as the time domain is concerned, and given the way it is deduced in this research work, whatever improvement in the frequency domain will directly increase the accuracy of the time domain voltage distributions. Anyhow, due the nature of the proposed brute-force IFFT model, and given not only its low time complexity but also its automation when compared to the equivalent implementation of the VF, a proposition of a suitable windowing to smooth out the high frequency truncation is a must. With these spurious oscillations mitigated—or at least reduced—, the study of the whole system, not only reduced to one node, could be performed. It is worth mentioning that although the VF allows more precise results, inconveniences were faced when willing to fit the whole nodal admittance matrix. This point could also be further studied.

Both the frequency domain and time domain perspectives are illustrated in Flowchart 3.24. The colour choice specifies the urgency of the perspective. The green cells present the work already performed during this thesis. From the automation of the frequency model to the extraction by inspection of the nodal admittance matrix, whether full or reduced, to the time domain implementation. Although the frequency domain model still needs few improvements like for instance the inclusion of the iron losses model, the reduction of the emerging IFFT spurious oscillations takes on a heightened sense of importance and is highlighted in red. In case these oscillations prove hard to reduce, a study of VF the full nodal admittance matrix, highlighted in pink, could be performed. This will enable the implementation of the time domain model for the whole circuit instead of looping on the number of turns. Once the time domain mathematical artefacts controlled, the frequency domain model could then be improved by including not only the iron losses model, using an equivalent complex non-linear law, but the study of randomly would windings as well. This is highlighted in blue.

With these perspectives, especially the time domain ones, accounted for, the deduction of the inter-turn voltages for the whole system could be performed once, instead of looping over the winding turns as proposed here.

Additionally and finally, considering the long-term perspectives, it is important to assess the potential far-reaching impacts and future advancements that may stem from this research. One main point seems interesting to investigate and is the inclusion of the frequency-dependent behaviour of the input cable. This could either be performed by including the measured frequency-dependent behaviour of the cable in the frequency domain model, from which the nodal admittance matrix will be computed and an extra cable node will be added, or modelled as a black-box using the VF algorithm.

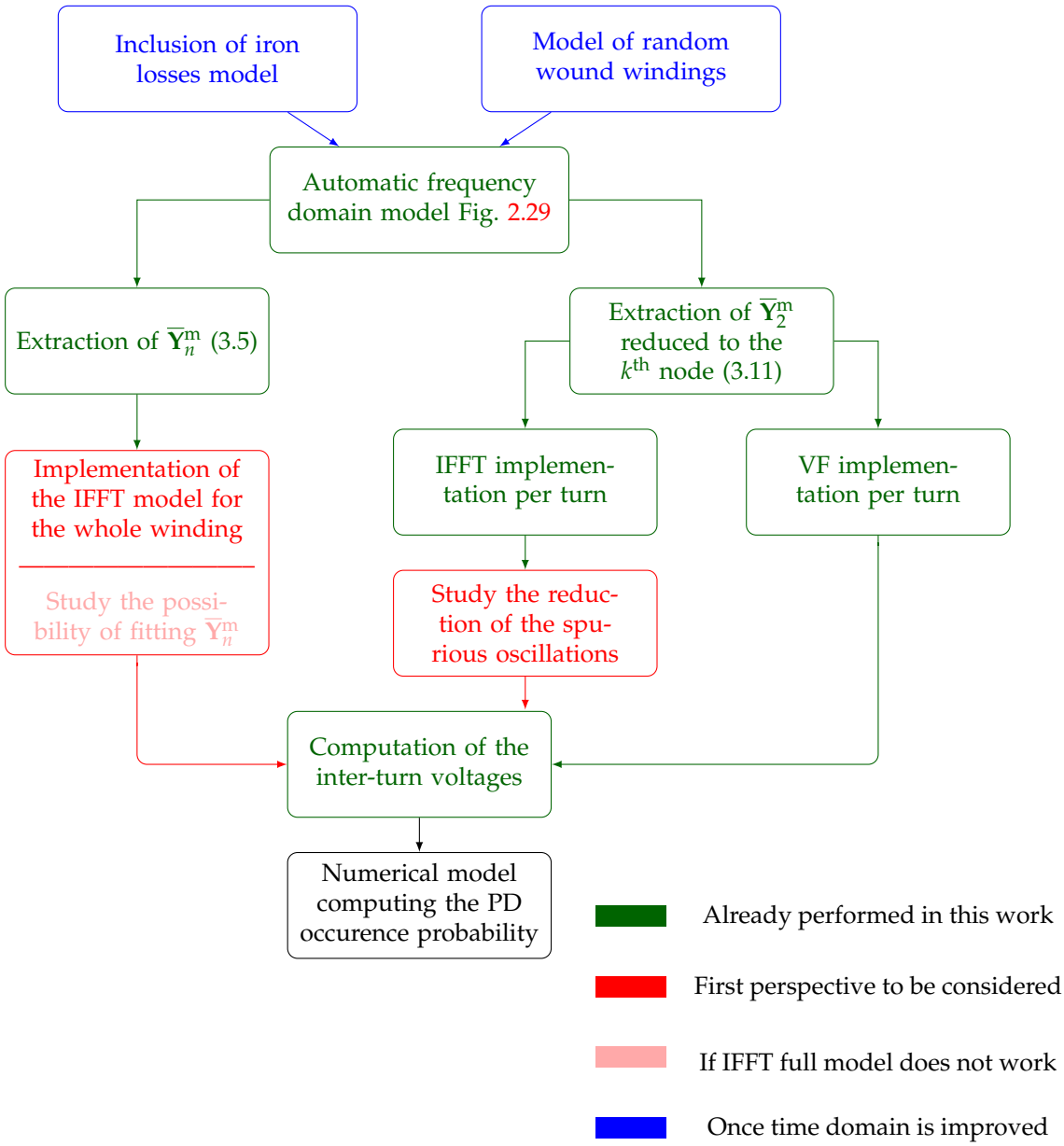

FIGURE 3.24: Flowchart illustrating the work performed in this thesis (highlighted in green), the perspectives for the frequency domain model (highlighted in blue) and the perspectives for the time domain model (highlighted in red).

BIBLIOGRAPHY

[1] European Commision, *Communication from the Commision to the European Parliament, the Council, the European Economic and Social Committee and the Committee of the Regions. Towards a Thriving Data-Driven Economy. 2014*, 2017.

[2] J. Barkenbus, "Our electric automotive future: CO2 savings through a disruptive technology," *Policy and Society*, vol. 27, no. 4, pp. 399–410, 2009, ISSN: 1449-4035. DOI: 10.1016/j.polsoc.2009.01.005. [Online]. Available: https://academic.oup.com/policyandsociety/article/27/4/399/6420838.

[3] C. Berggren and T. Magnusson, "Reducing automotive emissions—The potentials of combustion engine technologies and the power of policy," *Energy Policy*, vol. 41, pp. 636–643, 2012, ISSN: 03014215. DOI: 10.1016/j.enpol.2011.11.025. [Online]. Available: http://dx.doi.org/10.1016/j.enpol.2011.11.025https://linkinghub.elsevier.com/retrieve/pii/S0301421511009025.

[4] J. E. Ruiz-Sarrió, "High-frequency modelling of rotating electrical machines," Ph.D. dissertation, Technical University of Cluj-Napoca, Romania, 2022.

[5] B. Bilgin, P. Magne, P. Malysz, *et al.*, "Making the Case for Electrified Transportation," *IEEE Transactions on Transportation Electrification*, vol. 1, no. 1, pp. 4–17, 2015, ISSN: 2332-7782. DOI: 10.1109/TTE.2015.2437338. [Online]. Available: http://ieeexplore.ieee.org/document/7112507/.

[6] Y. A. Alamoudi, A. Ferrah, R. Panduranga, A. Althobaiti, and F. Mulolani, "State-of-the Art Electrical Machines for Modern Electric Vehicles," in *2019 Advances in Science and Engineering Technology International Conferences (ASET)*, IEEE, 2019, pp. 1–8, ISBN: 978-1-5386-8271-5. DOI: 10.1109/ICASET.2019.8714343. [Online]. Available: https://ieeexplore.ieee.org/document/8714343/.

[7] L. Lusuardi, A. Rumi, A. Cavallini, D. Barater, and S. Nuzzo, "Partial Discharge Phenomena in Electrical Machines for the More Electrical Aircraft. Part II: Impact of Reduced Pressures and Wide Bandgap Devices," *IEEE Access*, vol. 9, pp. 27 485–27 495, 2021, ISSN: 2169-3536. DOI: 10.1109/ACCESS.2021.3058089. [Online]. Available: https://ieeexplore.ieee.org/document/9350624/.

[8] J. Benzaquen, F. Fateh, M. B. Shadmand, and B. Mirafzal, "Performance Comparison of Active Rectifier Control Schemes in More Electric Aircraft Applications," *IEEE Transactions on Transportation Electrification*, vol. 5, no. 4, pp. 1470–1479, 2019, ISSN: 2332-7782. DOI: 10.1109/TTE.2019.2940847. [Online]. Available: https://ieeexplore.ieee.org/document/8832233/.

[9] B. Zaidi, A. Videt, and N. Idir, "Optimization method of CM inductor volume taking into account the magnetic core saturation issues," *IEEE Transactions on Power Electronics*, vol. 34, no. 5, pp. 4279–4291, 2018.

[10] F. Zare, D. Kumar, M. Lungeanu, and A. Andreas, "Electromagnetic interference issues of power, electronics systems with wide band gap, semiconductor devices," in *2015 IEEE Energy Conversion Congress and Exposition (ECCE)*, IEEE, 2015, pp. 5946–5951, ISBN: 978-1-4673-7151-3. DOI: 10.1109/ECCE.2015.7310494. [Online]. Available: http://ieeexplore.ieee.org/document/7310494/.

[11] F. Salomez, A. Videt, and N. Idir, "Modeling and Minimization of the Parasitic Capacitances of Single-Layer Toroidal Inductors," *IEEE Transactions on Power Electronics*, vol. 37, no. 10, pp. 12 426–12 436, 2022, ISSN: 0885-8993. DOI: 10.1109/TPEL.2022.3177642. [Online]. Available: https://ieeexplore.ieee.org/document/9780542/.

[12] A. Videt, "Variateur de vitesse à impact électromagnétique réduit: Onduleur multiniveaux et nouvelles stratégies de modulation," Ph.D. dissertation, 2008.

[13] J. E. Ruiz-Sarrió, F. Chauvicourt, J. Gyselinck, and C. Martis, "High-Frequency Modelling of Electrical Machine Windings Using Numerical Methods," in *2021 IEEE International Electric Machines & Drives Conference (IEMDC)*, IEEE, 2021, pp. 1–7, ISBN: 978-1-6654-0510-2. DOI: 10.1109/IEMDC47953.2021.9449561. [Online]. Available: https://ieeexplore.ieee.org/document/9449561/.

[14] V. Madonna, P. Giangrande, W. Zhao, *et al.*, "Reliability vs. Performances of Electrical Machines: Partial Discharges Issue," in *2019 IEEE Workshop on Electrical Machines Design, Control and Diagnosis (WEMDCD)*, vol. 1, IEEE, 2019, pp. 77–82, ISBN: 978-1-5386-8107-7. DOI: 10.1109/WEMDCD.2019.8887809. [Online]. Available: https://ieeexplore.ieee.org/document/8887809/.

[15] V. Madonna, P. Giangrande, W. Zhao, H. Zhang, C. Gerada, and M. Galea, "On the Design of Partial Discharge-Free Low Voltage Electrical Machines," in *2019 IEEE International Electric Machines & Drives Conference (IEMDC)*, IEEE, 2019, pp. 1837–1842, ISBN: 978-1-5386-9350-6. DOI: 10.1109/IEMDC.2019.8785413. [Online]. Available: https://ieeexplore.ieee.org/document/8785413/.

[16] P. Giangrande, V. Madonna, S. Nuzzo, and M. Galea, "Moving Toward a Reliability-Oriented Design Approach of Low-Voltage Electrical Machines by Including Insulation Thermal Aging Considerations," *IEEE Transactions on Transportation Electrification*, vol. 6, no. 1, pp. 16–27, 2020, ISSN: 2332-7782. DOI: 10.1109/TTE.2020.2971191. [Online]. Available: https://ieeexplore.ieee.org/document/8978960/.

[17] M. Toudji, G. Parent, S. Duchesne, and P. Dular, "Determination of winding lumped parameter equivalent circuit by means of finite element method," *IEEE Transactions on Magnetics*, vol. 53, no. 6, pp. 1–4, 2017.

[18] J. dos S. Cruz et al, "Partial Discharges Monitoring for Electric Machines Diagnosis: A Review," *Energies*, vol. 15, no. 21, p. 7966, 2022, ISSN: 1996-1073. DOI: 10.3390/en15217966.

[19] V. Madonna, P. Giangrande, W. Zhao, *et al.*, "Reliability vs. Performances of Electrical Machines: Partial Discharges Issue," in *2019 IEEE Workshop on Electrical Machines Design, Control and Diagnosis (WEMDCD)*, vol. 1, IEEE, 2019, pp. 77–82, ISBN: 978-1-5386-8107-7. DOI: 10.1109/WEMDCD.2019.8887809. [Online]. Available: https://ieeexplore.ieee.org/document/8887809/.

[20] B. Vaseghi, "Contribution à l'étude des machines électriques en présence de défaut entrespires," Ph.D. dissertation, 2009.

[21] V. Madonna, P. Giangrande, W. Zhao, H. Zhang, C. Gerada, and M. Galea, "Electrical Machines for the More Electric Aircraft: Partial Discharges Investigation," *IEEE Transactions on Industry Applications*, vol. 57, no. 2, pp. 1389–1398, 2021, ISSN: 0093-9994. DOI: 10.1109/TIA.2020.3046434. [Online]. Available: https://ieeexplore.ieee.org/document/9302643/.

[22] F. Wu, P. Zheng, and T. M. Jahns, "Analytical Modeling of Interturn Short Circuit for Multiphase Fault-Tolerant PM Machines With Fractional Slot Concentrated Windings," *IEEE Transactions on Industry Applications*, vol. 53, no. 3, pp. 1994–2006, 2017, ISSN: 0093-9994. DOI: 10.1109/TIA.2017.2665626. [Online]. Available: https://ieeexplore.ieee.org/document/7845684/.

[23] W. Thomson and M. Fenger, "Current signature analysis to detect induction motor faults," *IEEE Industry Applications Magazine*, vol. 7, no. 4, pp. 26–34, 2001, ISSN: 10772618. DOI: 10.1109/2943.930988. [Online]. Available: http://ieeexplore.ieee.org/document/930988/.

[24] N. Hayakawa and H. Okubo, "Partial discharge characteristics of inverter-fed motor coil samples under ac and surge voltage conditions," *IEEE Electrical Insulation Magazine*, vol. 21, no. 1, pp. 5–10, 2005, ISSN: 0883-7554. DOI: 10.1109/MEI.2005.1389265. [Online]. Available: http://ieeexplore.ieee.org/document/1389265/.

[25] S. Duchesne, G. Parent, J. Moenecley, and D. Roger, "Prediction of PDIV in motor coils using finite element method," in *2016 IEEE International Conference on Dielectrics (ICD)*, vol. 2, IEEE, 2016, pp. 638–641, ISBN: 978-1-5090-2804-7. DOI: 10.1109/ICD.2016.7547696. [Online]. Available: http://ieeexplore.ieee.org/document/7547696/.

[26] L. Benmamas, P. Teste, G. Krebs, E. Odic, F. Vangraefschepe, and T. Hamiti, "Contribution to partial discharge analysis in inverter-fed motor windings for automotive application," *2017 IEEE Electrical Insulation Conference, EIC 2017*, no. June, pp. 348–351, 2017. DOI: 10.1109/EIC.2017.8004701.

[27] G. Galli, H. Hamrita, C. Jammes, *et al.*, "Paschen's law in extreme pressure and temperature conditions," *IEEE Transactions on Plasma Science*, vol. 47, no. 3, pp. 1641–1647, 2019. DOI: 10.1109/TPS.2019.2896352.

[28] T. Mathurin, S. Duchesne, and G. Parent, "Assessment of Finite Element Simulation Methodologies for the Use of Paschen's Law in the Prediction of Partial Discharge Risk in Electrical Windings," *IEEE Access*, vol. 8, pp. 144 557–144 564, 2020, ISSN: 2169-3536. DOI: 10.1109/ACCESS.2020.3013337. [Online]. Available: https://ieeexplore.ieee.org/document/9153750/.

[29] F. Kreuger, E. Gulski, and A. Krivda, "Classification of partial discharges," *IEEE Transactions on Electrical Insulation*, vol. 28, no. 6, pp. 917–931, 1993, ISSN: 00189367. DOI: 10.1109/14.249365. [Online]. Available: http://ieeexplore.ieee.org/document/249365/.

[30] A. Krivda, "Automated recognition of partial discharges," *IEEE Transactions on Dielectrics and Electrical Insulation*, vol. 2, no. 5, pp. 796–821, 1995, ISSN: 10709878. DOI: 10.1109/94.469976. [Online]. Available: http://ieeexplore.ieee.org/document/469976/.

[31] L. Lusuardi, A. Cavallini, M. G. de la Calle, J. M. Martinez-Tarifa, and G. Robles, "Insulation design of low voltage electrical motors fed by PWM inverters," *IEEE Electrical Insulation Magazine*, vol. 35, no. 3, pp. 7–15, 2019, ISSN: 0883-7554. DOI: 10.1109/MEI.2019.8689431. [Online]. Available: https://ieeexplore.ieee.org/document/8689431/.

[32] H. Schefer, L. Fauth, T. H. Kopp, R. Mallwitz, J. Friebe, and M. Kurrat, "Discussion on electric power supply systems for all electric aircraft," *IEEE access*, vol. 8, pp. 84 188–84 216, 2020.

[33] M. A. Lieberman and A. J. Lichtenberg, *Principles of plasma discharges and materials processing*. John Wiley & Sons, 2005. DOI: 10.1002/0471724254.

[34] V. Mihaila, S. Duchesne, and D. Roger, "A simulation method to predict the turn-to-turn voltage spikes in a PWM fed motor winding," *IEEE Transactions on Dielectrics and Electrical Insulation*, vol. 18, no. 5, pp. 1609–1615, 2011.

[35] A. Yoon, J. Xiao, D. Lohan, F. Arastu, and K. Haran, "High-Frequency Electric Machines for Boundary Layer Ingestion Fan Propulsor," *IEEE Transactions on Energy Conversion*, vol. 34, no. 4, pp. 2189–2197, 2019, ISSN: 0885-8969. DOI: 10.1109/TEC.2019.2942775. [Online]. Available: https://ieeexplore.ieee.org/document/8845621/.

[36] Y. Wang, X. Yi, Y. Wang, *et al.*, "Partial Discharge Investigation of Form-Wound Electric Machine Winding for Electric Aircraft Propulsion," *IEEE Transactions on Transportation Electrification*, vol. 7, no. 1, pp. 78–90, 2021, ISSN: 2332-7782. DOI: 10.1109/TTE.2020.2992052. [Online]. Available: https://ieeexplore.ieee.org/document/9085348/.

[37] B. Mirafzal, G. L. Skibinski, and R. M. Tallam, "Determination of Parameters in the Universal Induction Motor Model," *IEEE Transactions on Industry Applications*, vol. 45, no. 1, pp. 142–151, 2009, ISSN: 0093-9994.

[38] J. Millan, P. Godignon, X. Perpina, A. Perez-Tomas, and J. Rebollo, "A Survey of Wide Bandgap Power Semiconductor Devices," *IEEE Transactions on Power Electronics*, vol. 29, no. 5, pp. 2155–2163, 2014, ISSN: 0885-8993. DOI: 10.1109/TPEL.2013.2268900. [Online]. Available: http://ieeexplore.ieee.org/document/6532359/.

[39] J. B. Varley, B. Shen, and M. Higashiwaki, "Wide bandgap semiconductor materials and devices," *Journal of Applied Physics*, vol. 131, no. 23, p. 230 401, 2022, ISSN: 0021-8979. DOI: 10.1063/5.0100601. [Online]. Available: https://aip.scitation.org/doi/10.1063/5.0100601.

[40] A. Burk, M. O'Loughlin, R. Siergiej, *et al.*, "SiC and GaN wide bandgap semiconductor materials and devices," *Solid-State Electronics*, vol. 43, no. 8, pp. 1459–1464, 1999, ISSN: 00381101. DOI: 10.1016/S0038-1101(99)00089-1. [Online]. Available: https://linkinghub.elsevier.com/retrieve/pii/S0038110199000891.

[41] J. G. Kassakian and T. M. Jahns, "Evolving and Emerging Applications of Power Electronics in Systems," *IEEE Journal of Emerging and Selected Topics in Power Electronics*, vol. 1, no. 2, pp. 47–58, 2013, ISSN: 2168-6777. DOI: 10.1109/JESTPE.2013.2271111. [Online]. Available: http://ieeexplore.ieee.org/document/6547655/.

[42] M. Barnes, *Practical variable speed drives and power electronics*. Newnes, 2003.

[43] Mandeep Kaur, Shikha Kakar, Danvir Mandal, "Electromagnetic Interference," *Sen'i Gakkaishi*, vol. 44, no. 9, P334–P335, 1988, ISSN: 0037-9875. DOI: 10.2115/fiber.44.9_P334. [Online]. Available: http://www.jstage.jst.go.jp/article/fiber1944/44/9/44{_}9{_}P334/{_}article.

[44] J. Rodriguez, J. Pontt, C. Silva, *et al.*, "Resonances and overvoltages in a medium-voltage fan motor drive with long cables in an underground mine," *IEEE Transactions on Industry Applications*, vol. 42, no. 3, pp. 856–863, 2006, ISSN: 0093-9994. DOI: 10.1109/TIA.2006.872936. [Online]. Available: http://ieeexplore.ieee.org/document/1634692/.

[45] E. Persson, "Transient effects in application of PWM inverters to induction motors," *IEEE Transactions on Industry Applications*, vol. 28, no. 5, pp. 1095–1101, 1992, ISSN: 00939994. DOI: 10.1109/28.158834. [Online]. Available: http://ieeexplore.ieee.org/document/158834/.

[46] A. Moreira, T. Lipo, G. Venkataramanan, and S. Bernet, "High-frequency modeling for cable and induction motor overvoltage studies in long cable drives," *IEEE Transactions on Industry Applications*, vol. 38, no. 5, pp. 1297–1306, 2002, ISSN: 0093-9994.

[47] M. Berth, M. Kung, and E. Limbeek, "Switching overvoltages in motor circuits," *IEEE Transactions on Industry Applications*, vol. 37, no. 6, pp. 1582–1589, 2001, ISSN: 00939994.

DOI: 10.1109/28.968164. [Online]. Available: http://ieeexplore.ieee.org/document/968164/.

[48] Y. Wu, K. Choksi, M. ul Hassan, and F. Luo, "An Extendable and Accurate High- Frequency Modelling of Three-phase Cable for Prediction of Reflected Wave Phenomenon," in *2022 IEEE Applied Power Electronics Conference and Exposition (APEC)*, IEEE, 2022, pp. 944–950, ISBN: 978-1-6654-0688-8. DOI: 10.1109/APEC43599.2022.9773493. [Online]. Available: https://ieeexplore.ieee.org/document/9773493/.

[49] G. Skibinski, R Kerkman, D Leggate, J Pankau, and D Schlegel, "Reflected wave modeling techniques for PWM AC motor drives," in *APEC '98 Thirteenth Annual Applied Power Electronics Conference and Exposition*, vol. 2, IEEE, 1998, pp. 1021–1029, ISBN: 0-7803-4340-9. DOI: 10.1109/APEC.1998.654023. [Online]. Available: http://ieeexplore.ieee.org/document/654023/.

[50] D. Potoradi, C. Hofmeier, R. Nuscheler, and W. Hutter, "Transient overvoltages caused by switching of high voltage asynchronous machines and their distribution in stator windings," in *International Conference on Electrical Machines, ICEM 94*, 1994.

[51] W. Yin, "Failure mechanism of winding insulations in inverter-fed motors," *IEEE Electrical Insulation Magazine*, vol. 13, no. 6, pp. 18–23, 1997, ISSN: 0883-7554. DOI: 10.1109/57.637150. [Online]. Available: http://ieeexplore.ieee.org/document/637150/.

[52] E. W. Greenfield, "Transient Behavior of Short and Long Cables," *IEEE Power Engineering Review*, vol. PER-4, no. 11, pp. 27–28, 1984, ISSN: 0272-1724. DOI: 10.1109/MPER.1984.5526505. [Online]. Available: http://ieeexplore.ieee.org/document/5526505/.

[53] M. Kaufhold, "Failure mechanism of the interturn insulation of low voltage electric machines fed by pulse controlled inverters," in *Proceedings of 1995 Conference on Electrical Insulation and Dielectric Phenomena*, IEEE, 1995, pp. 254–257, ISBN: 0-7803-2931-7. DOI: 10.1109/CEIDP.1995.483711.

[54] A. Krivda, "Automated recognition of partial discharges," *IEEE Transactions on Dielectrics and Electrical Insulation*, vol. 2, no. 5, pp. 796–821, 1995, ISSN: 10709878. DOI: 10.1109/94.469976. [Online]. Available: http://ieeexplore.ieee.org/document/469976/.

[55] V. Mihaila, "Nouvelle conception des bobinages statoriques des machines à courant alternatif pour réduire les effets négatifs des dv/dt," Ph.D. dissertation, Université d'Artois, 2011.

[56] D. F. Kavanagh, D. A. Howey, and M. D. McCulloch, "An applied laboratory characterisation approach for electric machine insulation," in *2013 9th IEEE International Symposium on Diagnostics for Electric Machines, Power Electronics and Drives (SDEMPED)*, IEEE, 2013, pp. 391–395, ISBN: 978-1-4799-0025-1. DOI: 10.1109/DEMPED.2013.6645745. [Online]. Available: http://ieeexplore.ieee.org/document/6645745/.

[57] Y. Wang, X. Yi, Y. Wang, *et al.*, "Partial Discharge Investigation of Form-Wound Electric Machine Winding for Electric Aircraft Propulsion," *IEEE Transactions on Transportation Electrification*, vol. 7, no. 1, pp. 78–90, 2021, ISSN: 2332-7782. DOI: 10.1109/TTE.2020.2992052. [Online]. Available: https://ieeexplore.ieee.org/document/9085348/.

[58] R. Dyczij-Edlinger, G. Peng, and J.-F. Lee, "Efficient finite element solvers for the Maxwell equations in the frequency domain," *Computer Methods in Applied Mechanics and Engineering*, vol. 169, no. 3-4, pp. 297–309, 1999, ISSN: 00457825. DOI: 10.1016/S0045-7825(98)00159-5. [Online]. Available: https://linkinghub.elsevier.com/retrieve/pii/S0045782598001595.

[59] J. Zhu and D. Jiao, "Eliminating the Low-Frequency Breakdown Problem in 3-D Full-Wave Finite-Element-Based Analysis of Integrated Circuits," *IEEE Transactions on Microwave Theory and Techniques*, vol. 58, no. 10, pp. 2633–2645, 2010, ISSN: 0018-9480. DOI: 10.1109/TMTT.2010.2065930. [Online]. Available: http://ieeexplore.ieee.org/document/5575379/.

[60] R. Hiptmair, F. Kramer, and J. Ostrowski, "A Robust Maxwell Formulation for All Frequencies," *IEEE Transactions on Magnetics*, vol. 44, no. 6, pp. 682–685, 2008, ISSN: 0018-9464. DOI: 10.1109/TMAG.2007.915991. [Online]. Available: http://ieeexplore.ieee.org/document/4526888/.

[61] M. Eller, S. Reitzinger, S. Schöps, and S. Zaglmayr, "A Symmetric Low-Frequency Stable Broadband Maxwell Formulation for Industrial Applications," *SIAM Journal on Scientific Computing*, vol. 39, no. 4, B703–B731, 2017, ISSN: 1064-8275. DOI: 10.1137/16M1077817. [Online]. Available: https://epubs.siam.org/doi/10.1137/16M1077817.

[62] L. Montier, T. Henneron, S. Clénet, and B. Goursaud, "Transient simulation of an electrical rotating machine achieved through model order reduction," *Advanced Modeling and Simulation in Engineering Sciences*, vol. 3, no. 1, p. 10, 2016, ISSN: 2213-7467.

[63] S. A. Saied, K. Abbaszadeh, and M. Fadaie, "Reduced Order Model of Developed Magnetic Equivalent Circuit in Electrical Machine Modeling," *IEEE Transactions on Magnetics*, vol. 46, no. 7, pp. 2649–2655, 2010, ISSN: 0018-9464.

[64] C. Bals and D. Gerling, "Reduced order model of the induction machine derived from finite-element-analysis," in *2016 XXII International Conference on Electrical Machines (ICEM)*, IEEE, 2016, pp. 2038–2044, ISBN: 978-1-5090-2538-1.

[65] H. De Gersem and K. Hameyer, "Electrodynamic finite element model coupled to a magnetic equivalent circuit," *The European Physical Journal Applied Physics*, vol. 12, no. 2, pp. 105–108, 2000, ISSN: 1286-0042. DOI: 10.1051/epjap:2000176. [Online]. Available: http://www.epjap.org/10.1051/epjap:2000176.

[66] H. De Gersem, K. Hameyer, and T. Weiland, "Field–circuit coupled models in electromagnetic simulation," *Journal of Computational and Applied Mathematics*, vol. 168, no. 1-2, pp. 125–133, 2004, ISSN: 03770427. DOI: 10.1016/j.cam.2003.05.008. [Online]. Available: http://dx.doi.org/10.1016/j.cam.2003.05.008https://linkinghub.elsevier.com/retrieve/pii/S0377042703009701.

[67] P. Dular, F. Henrotte, and W. Legros, "A general and natural method to define circuit relations associated with magnetic vector potential formulations," *IEEE Transactions on Magnetics*, vol. 35, no. 3, pp. 1630–1633, 1999, ISSN: 00189464. DOI: 10.1109/20.767310. [Online]. Available: http://ieeexplore.ieee.org/document/767310/.

[68] R. Sabariego, P. Dular, and J. Gyselinck, "Time-Domain Homogenization of Windings in 3-D Finite Element Models," *IEEE Transactions on Magnetics*, vol. 44, no. 6, pp. 1302–1305, 2008, ISSN: 0018-9464. DOI: 10.1109/TMAG.2007.915908. [Online]. Available: http://ieeexplore.ieee.org/document/4526988/.

[69] K. Hameyer and R. Belmans, *Numerical modelling and design of electrical machines and devices*. WIT press, 1999, vol. 1.

[70] J. Smajic, T. Steinmetz, M. Ruegg, *et al.*, "Simulation and Measurement of Lightning-Impulse Voltage Distributions Over Transformer Windings," *IEEE Transactions on Magnetics*, vol. 50, no. 2, pp. 553–556, 2014, ISSN: 0018-9464. DOI: 10.1109/TMAG.2013.2283061. [Online]. Available: http://ieeexplore.ieee.org/document/6749231/.

[71] F. Perisse, P. Werynski, and D. Roger, "A New Method for AC Machine Turn Insulation Diagnostic Based on High Frequency Resonances," *IEEE Transactions on Dielectrics and Electrical Insulation*, vol. 14, no. 5, pp. 1308–1315, 2007, ISSN: 1070-9878.

[72] J. Gyselinck, R. V. Sabariego, and P. Dular, "Time-Domain Homogenization of Windings in 2-D Finite Element Models," *IEEE Transactions on Magnetics*, vol. 43, no. 4, pp. 1297–1300, 2007, ISSN: 0018-9464. DOI: 10.1109/TMAG.2007.892408. [Online]. Available: http://ieeexplore.ieee.org/document/4137727/.

[73] A. Kameari, H. Ebrahimi, K. Sugahara, Y. Shindo, and T. Matsuo, "Cauer Ladder Network Representation of Eddy-Current Fields for Model Order Reduction Using Finite-Element Method," *IEEE Transactions on Magnetics*, vol. 54, no. 3, pp. 1–4, 2018, ISSN:

0018-9464. DOI: 10.1109/TMAG.2017.2743224. [Online]. Available: https://ieeexplore.ieee.org/document/8015180/.

[74] K. Niyomsatian, J. Gyselinck, and R. V. Sabariego, "Time-domain homogenization of multiturn windings based on RL Cauer ladder networks," *International Journal of Numerical Modelling: Electronic Networks, Devices and Fields*, vol. 33, no. 5, pp. 1–11, 2020, ISSN: 0894-3370. DOI: 10.1002/jnm.2649.

[75] P. Russer, "Applied Computational Electromagnetics," *Applied Computational Electromagnetics*, no. May, 2000.

[76] P. Johns and R. Beurle, "Numerical solution of 2-dimensional scattering problems using a transmission-line matrix," *Proceedings of the Institution of Electrical Engineers*, vol. 118, no. 9, p. 1203, 1971, ISSN: 00203270.

[77] T. Q. Van Hoang, "Maillage cartesian non-confrome pour la méthode TLM. Application à la conception de rectennas compactes," Ph.D. dissertation, Université Nice Sophia Antipolis, 2012.

[78] J. Guardado, J. Flores, V Venegas, J. Naredo, and F. Uribe, "A machine winding model for switching transient studies using network synthesis," *IEEE Transactions on energy conversion*, vol. 20, no. 2, pp. 322–328, 2005, ISSN: 0885-8969.

[79] S. Islam and G. Ledwich, "An equivalent circuit for calculation of interturn voltage distribution of stator windings in the presence of slot discharges," in *Proceedings of 5th International Conference on Properties and Applications of Dielectric Materials*, IEEE, vol. 1, 1997, pp. 507–510.

[80] G. Suresh, H. Toliyat, D. Rendusara, and P. Enjeti, "Predicting the transient effects of PWM voltage waveform on the stator windings of random wound induction motors," *IEEE Transactions on Power Electronics*, vol. 14, no. 1, pp. 23–30, 1999, ISSN: 0885-8993.

[81] O Moreau, G. Santos, and Y Guillot, "Computation of very fast transient overvoltages inside transformers resulting from switchings in power plants," in *Proc. of Int. Conf. on Power Syst. Trans.*, Montreal, QC, Canada, Jun. 2005.

[82] D. L. Alvarez, J. A. Rosero, and E. E. Mombello, "Circuit model of transformers windings using vector fitting, for frequency response analysis (FRA)," in *2013 Workshop on Power Electronics and Power Quality Applications (PEPQA)*, IEEE, 2013, pp. 1–6, ISBN: 978-1-4799-1007-6. DOI: 10.1109/PEPQA.2013.6614961. [Online]. Available: http://ieeexplore.ieee.org/document/6614961/.

[83] E. Dick and C. Erven, "Transformer Diagnostic Testing by Frequency Response Analysis," *IEEE Transactions on Power Apparatus and Systems*, vol. PAS-97, no. 6, pp. 2144–2153, 1978, ISSN: 0018-9510.

[84] L. Wang, C. Ngai-Man Ho, F. Canales, and J. Jatskevich, "High-Frequency Modeling of the Long-Cable-Fed Induction Motor Drive System Using TLM Approach for Predicting Overvoltage Transients," *IEEE Transactions on Power Electronics*, vol. 25, no. 10, pp. 2653–2664, 2010, ISSN: 0885-8993.

[85] I. Metwally, "Simulation of the impulse response of electrical machines," *IEEE Transactions on Energy Conversion*, vol. 14, no. 4, pp. 861–867, 1999, ISSN: 08858969. DOI: 10.1109/60.815000. [Online]. Available: http://ieeexplore.ieee.org/document/815000/.

[86] B. Gustavsen, "Wide Band Modeling of Power Transformers," *IEEE Transactions on Power Delivery*, vol. 19, no. 1, pp. 414–422, 2004, ISSN: 08858977.

[87] Z. Zhao, Y. Chen, Y. Yu, M. Han, C. Tang, and C. Yao, "Equivalent broadband electrical circuit of synchronous machine winding for frequency response analysis based on gray box model," *IEEE Transactions on Energy Conversion*, vol. 36, no. 4, pp. 3512–3521, 2021.

[88] Q. Wang, H. Sun, Y. Zheng, Z. An, and H. Peng, "Fast modeling of the motor broadband equivalent circuit model," *Chongqing Daxue Xuebao(Ziran Kexue Ban)*, vol. 35, no. 12, pp. 34–39, 2012.

[89] N. Idir, Y. Weens, M. Moreau, and J. J. Franchaud, "High-Frequency Behavior Models of AC Motors," *IEEE Transactions on Magnetics*, vol. 45, no. 1, pp. 133–138, 2009, ISSN: 0018-9464. DOI: 10.1109/TMAG.2008.2006006. [Online]. Available: http://ieeexplore.ieee.org/document/4773617/.

[90] B. Mirafzal, G. L. Skibinski, R. M. Tallam, D. W. Schlegel, and R. A. Lukaszewski, "Universal Induction Motor Model With Low-to-High Frequency-Response Characteristics," *IEEE Transactions on Industry Applications*, vol. 43, no. 5, pp. 1233–1246, 2007, ISSN: 0093-9994.

[91] I. Power and E. Society, "IEEE Standard Test Procedure for Polyphase Induction Motors Generators Sponsored by the Electric Machinery Committee," Tech. Rep., 1991, pp. 112–1991. DOI: 10.1109/IEEESTD.2018.8291810.

[92] N. B. Chagas and T. B. Marchesan, "Analytical Calculation of Static Capacitance for High-Frequency Inductors and Transformers," *IEEE Transactions on Power Electronics*, vol. 34, no. 2, pp. 1672–1682, 2019, ISSN: 0885-8993. DOI: 10.1109/TPEL.2018.2829716. [Online]. Available: https://ieeexplore.ieee.org/document/8345653/.

[93] B. S. Oyegoke *et al.*, *Transient voltage distribution in stator winding of electrical machine fed from a frequency converter*. Helsinki University of Technology, 2000.

[94] D. Shi, D. J. Tylavsky, K. M. Koellner, N. Logic, and D. E. Wheeler, "Transmission line parameter identification using PMU measurements," *European Transactions on Electrical Power*, vol. 21, no. 4, pp. 1574–1588, 2011, ISSN: 1430144X.

[95] R. E. Wilson, G. A. Zevenbergen, D. L. Mah, and A. J. Murphy, "Calculation of transmission line parameters from synchronized measurements," *Electric Machines and Power Systems*, vol. 27, no. 12, pp. 1269–1278, 1999, ISSN: 0731356X.

[96] L. Gubbala, A. von Jouanne, P. Enjeti, C. Singh, and H. Toliyat, "Voltage distribution in the windings of an AC motor subjected to high dV/dt PWM voltages," in *Proceedings of PESC '95 - Power Electronics Specialist Conference*, vol. 1, IEEE, 1995, pp. 579–585, ISBN: 0-7803-2730-6.

[97] H. De Gersem, O. Henze, T. Weiland, and A. Binder, "Simulation of wave propagation effects in machine windings," *COMPEL - The international journal for computation and mathematics in electrical and electronic engineering*, vol. 29, no. 1, pp. 23–38, 2010, ISSN: 0332-1649.

[98] N. S. Gokhale, *Practical finite element analysis*. Finite to infinite, 2008.

[99] F. M. Kahnert, "Numerical methods in electromagnetic scattering theory," *Journal of Quantitative Spectroscopy and Radiative Transfer*, vol. 79, pp. 775–824, 2003.

[100] E. Haber and U. M. Ascher, "Fast finite volume simulation of 3D electromagnetic problems with highly discontinuous coefficients," *SIAM Journal on Scientific Computing*, vol. 22, no. 6, pp. 1943–1961, 2001.

[101] T. H. Hubing, "Survey of numerical electromagnetic modeling techniques," *Department of Electrical Engineering, University of Missouri-Rolla, USA*, 1991.

[102] W. H. Schilders and E. J. W. ter Maten, *Numerical Methods in Electromagnetics: Special Volume*. Elsevier, 2005.

[103] P. Meyer and Y. Perriard, "Skin and proximity effects for coreless transformers," in *2011 International Conference on Electrical Machines and Systems*, vol. 1, IEEE, 2011, pp. 1–5, ISBN: 978-1-4577-1044-5. DOI: 10.1109/ICEMS.2011.6073351. [Online]. Available: http://ieeexplore.ieee.org/document/6073351/.

[104] Y. Tang, "Analysis of steep-fronted voltage distribution and turn insulation failure in inverter-fed form-wound AC motor," *IEEE Transactions on Industry Applications*, vol. 34, no. 5, pp. 1088–1096, 1998, ISSN: 00939994. DOI: 10.1109/28.720449. [Online]. Available: http://ieeexplore.ieee.org/document/720449/.

[105] S. Mei, C. Amin, and Y. I. Ismail, "Efficient model order reduction including skin effect," in *Proceedings of the 40th conference on Design automation - DAC '03*, New York, New York, USA: ACM Press, 2003, pp. 232–237, ISBN: 1581136889.

[106] B. Mirafzal, G. L. Skibinski, and R. M. Tallam, "Determination of Parameters in the Universal Induction Motor Model," *IEEE Transactions on Industry Applications*, vol. 45, no. 1, pp. 142–151, 2009, ISSN: 0093-9994.

[107] M. Popov, L. van der Sluis, R. P. P. Smeets, and J. Lopez Roldan, "Analysis of Very Fast Transients in Layer-Type Transformer Windings," *IEEE Transactions on Power Delivery*, vol. 22, no. 1, pp. 238–247, 2007, ISSN: 0885-8977.

[108] O. Bottauscio, M. Chiampi, A. Manzin, and M. Zucca, "Additional Losses in Induction Machines Under Synchronous No-Load Conditions," *IEEE Transactions on Magnetics*, vol. 40, no. 5, pp. 3254–3261, 2004, ISSN: 0018-9464.

[109] C. Graham Jr, "Physical origin of losses in conducting ferromagnetic materials," *Journal of Applied Physics*, vol. 53, no. 11, pp. 8276–8280, 1982.

[110] A. Krings and J. Soulard, "Overview and comparison of iron loss models for electrical machines," *Journal of Electrical Engineering*, vol. 10, no. 3, pp. 8–8, 2010.

[111] Y. Weens, "Modélisation des câbles d'énergie soumis aux contraintes générées par les convertisseurs électroniques de puissance," Ph.D. dissertation, Université de Lille, 2006.

[112] A. Toureille, *Mesures Electriques Des Meteriaux Dielectriques Solides*. Ed. Techniques Ingénieur, 2009.

[113] S. Diaham, M. L. Locatelli, T. Lebey, and S. Dinculescu, "Dielectric and thermal properties of Polyamide-imide (PAI) films," in *2009 IEEE Conference on Electrical Insulation and Dielectric Phenomena*, IEEE, 2009, pp. 482–485, ISBN: 978-1-4244-4557-8.

[114] S. Orlowska, "Conception et prédiction des caractéristiques diélectriques des matériaux composites à deux et trois phases par la modélisation et la validation expérimentale," Ph.D. dissertation, Ecole Centrale de Lyon, 2003.

[115] Y. Feldman, A. Puzenko, and Y. Ryabov, "Dielectric Relaxation Phenomena in Complex Materials," in *Advances in Chemical Physics, Fractals, Diffusion and Relaxation in Disordered Complex Systems*, October 2017, vol. 133, 2006, pp. 1–125, ISBN: 9780471790266.

[116] J. I. Lauritzen, "Analysis of Dielectric Loss in Two Urea Addition Compounds : The Hindered Single Axis Polar Rotator," *The Journal of Chemical Physics*, vol. 28, no. 1, pp. 118–131, 1958, ISSN: 0021-9606.

[117] G. G. Raju, *Dielectrics in electric fields: Tables, Atoms, and Molecules*. CRC press, 2017.

[118] F. Loubeau, "Analyse des phénomènes de vieillissement des matériaux d'isolation électrique de machines de traction électrique," Ph.D. dissertation, Université Grenoble Alpes (ComUE), 2016.

[119] M. Celik, L. Pileggi, L. Pileggi, and A. Odabasioglu, *IC interconnect analysis*. Springer Science & Business Media, 2002.

[120] M. Sarto, A. Scarlatti, and C. Holloway, "On the use of fitting models for the of problems with frequency-dependent parameters," in *2001 IEEE EMC International Symposium. Symposium Record. International Symposium on Electromagnetic Compatibility (Cat. No.01CH37161)*, vol. 1, IEEE, 2001, pp. 588–593, ISBN: 0-7803-6569-0.

[121] A. Semlyen and A. Dabuleanu, "Fast and accurate switching transient calculations on transmission lines with ground return using recursive convolutions," *IEEE Transactions on Power Apparatus and Systems*, vol. 94, no. 2, pp. 561–571, 1975, ISSN: 0018-9510.

[122] J. Smajic, M. Bucher, T. Franz, B. Cranganu-Cretu, A. Shoory, and J. Tepper, "Modeling of Frequency Dependent Parameters in Time Domain High Frequency Transformer Simulations," *Procedia Engineering*, vol. 202, pp. 251–263, 2017, ISSN: 18777058.

[123] M. K. Bucher, T. Franz, M. Jaritz, J. Smajic, and J. Tepper, "Frequency-Dependent Resistances and Inductances in Time-Domain Transient Simulations of Power Transformers," *IEEE Transactions on Magnetics*, vol. 55, no. 9, pp. 1–5, 2019, ISSN: 0018-9464.

[124] B. Kordi, J. LoVetri, and G. Bridges, "Finite-Difference Analysis of Dispersive Transmission Lines Within a Circuit Simulator," *IEEE Transactions on Power Delivery*, vol. 21, no. 1, pp. 234–242, 2006, ISSN: 0885-8977.

[125] H. De Gersem, O. Henze, T. Weiland, and A. Binder, "Simulation of wave propagation effects in machine windings," *COMPEL - The international journal for computation and mathematics in electrical and electronic engineering*, vol. 29, no. 1, pp. 23–38, 2010, ISSN: 0332-1649. DOI: 10.1108/03321641011007948. [Online]. Available: https://www.emerald.com/insight/content/doi/10.1108/03321641011007948/full/html.

[126] M. E. Potter, M. Okoniewski, and M. A. Stuchly, "Low Frequency Finite Difference Time Domain (FDTD) for Modeling of Induced Fields in Humans Close to Line Sources," *Journal of Computational Physics*, vol. 162, no. 1, pp. 82–103, 2000, ISSN: 00219991. DOI: 10.1006/jcph.2000.6523. [Online]. Available: https://linkinghub.elsevier.com/retrieve/pii/S0021999100965239.

[127] R. Neumayer, A. Stelzer, F. Haslinger, and R. Weigel, "On the synthesis of equivalent-circuit models for multiports characterized by frequency-dependent parameters," *IEEE Transactions on Microwave Theory and Techniques*, vol. 50, no. 12, pp. 2789–2796, 2002, ISSN: 0018-9480.

[128] A. Schellmanns, J. Keradec, and J. Schanen, "Electrical equivalent circuit for frequency dependant impedance: minimum lumped elements for a given precision [SMPS transformer]," in *Conference Record of the 2000 IEEE Industry Applications Conference. Thirty-Fifth IAS Annual Meeting and World Conference on Industrial Applications of Electrical Energy (Cat. No.00CH37129)*, vol. 5, IEEE, 2000, pp. 3105–3110, ISBN: 0-7803-6401-5.

[129] A. Dounavis, Xin Li, M. Nakhla, and R. Achar, "Passive closed-form transmission-line model for general-purpose circuit simulators," *IEEE Transactions on Microwave Theory and Techniques*, vol. 47, no. 12, pp. 2450–2459, 1999, ISSN: 00189480.

[130] J. Marti, "Accurate Modelling of Frequency-Dependent Transmission Lines in Electromagnetic Transient Simulations," *IEEE Transactions on Power Apparatus and Systems*, vol. PAS-101, no. 1, pp. 147–157, 1982, ISSN: 0018-9510. DOI: 10.1109/TPAS.1982.317332. [Online]. Available: http://ieeexplore.ieee.org/document/4111151/.

[131] M. Sarto, A. Scarlatti, and C. Holloway, "On the use of fitting models for the time-domain analysis of problems with frequency-dependent parameters," in *2001 IEEE EMC International Symposium. Symposium Record. International Symposium on Electromagnetic Compatibility (Cat. No.01CH37161)*, vol. 1, IEEE, 2001, pp. 588–593, ISBN: 0-7803-6569-0. DOI: 10.1109/ISEMC.2001.950710. [Online]. Available: http://ieeexplore.ieee.org/document/950710/.

[132] B. Gustavsen and A. Semlyen, "Rational approximation of frequency domain responses by vector fitting," *IEEE Transactions on Power Delivery*, vol. 14, no. 3, pp. 1052–1061, 1999, ISSN: 08858977.

[133] G. Antonini, "Spice equivalent circuits of frequency-domain responses," *IEEE Transactions on Electromagnetic Compatibility*, vol. 45, no. 3, pp. 502–512, 2003, ISSN: 0018-9375. DOI: 10.1109/TEMC.2003.815528. [Online]. Available: http://ieeexplore.ieee.org/document/1223619/.

[134] Y. Weens, N. Idir, R. Bausiere, and J. Franchaud, "Modeling and simulation of unshielded and shielded energy cables in frequency and time domains," *IEEE Transactions on Magnetics*, vol. 42, no. 7, pp. 1876–1882, 2006, ISSN: 0018-9464.

[135] M. Chaves, J. Oliveira, J. Resende, and A. Lopes, "Time domain cable modeling with frequency dependent parameters," *IPST Proceedings*, pp. 275–279, 1997.

[136] H. De Paula, D. A. de Andrade, M. L. R. Chaves, J. L. Domingos, and M. A. A. de Freitas, "Methodology for Cable Modeling and Simulation for High-Frequency Phenomena Studies in PWM Motor Drives," *IEEE Transactions on Power Electronics*, vol. 23, no. 2, pp. 744–752, 2008, ISSN: 0885-8993.

[137] A Kunakom, J Hiley, and K. Smith, "Frequency dependent time domain models for calculating switching transients in PWM drives," in *PowerCon 2000. 2000 International Conference on Power System Technology. Proceedings (Cat. No. 00EX409)*, IEEE, vol. 1, 2000, pp. 205–210.

[138] B. Revol, J. Roudet, J.-L. Schanen, and P. Loizelet, "EMI Study of Three-Phase Inverter-Fed Motor Drives," *IEEE Transactions on Industry Applications*, vol. 47, no. 1, pp. 223–231, 2011, ISSN: 0093-9994.

[139] O. Magdun, S. Blatt, and A. Binder, "Calculation of stator winding parameters to predict the voltage distributions in inverter fed AC machines," in *2013 9th IEEE International Symposium on Diagnostics for Electric Machines, Power Electronics and Drives (SDEMPED)*, IEEE, 2013, pp. 447–453, ISBN: 978-1-4799-0025-1.

[140] T. Ming, S. Jianyang, G. Jianzhao, L. Hongjie, Z. Wei, and L. Deliang, "Time-Domain Modeling and Simulation of Partial Discharge on Medium-Voltage Cables by Vector Fitting Method," *IEEE Transactions on Magnetics*, vol. 50, no. 2, pp. 993–996, 2014, ISSN: 0018-9464.

[141] S. Kim and D. Neikirk, "Compact equivalent circuit model for the skin effect," in *1996 IEEE MTT-S International Microwave Symposium Digest*, vol. 3, IEEE, 1996, pp. 1815–1818, ISBN: 0-7803-3246-6.

[142] Chu-Sun Yen, Z. Fazarinc, and R. Wheeler, "Time-domain skin-effect model for transient analysis of lossy transmission lines," *Proceedings of the IEEE*, vol. 70, no. 7, pp. 750–757, 1982, ISSN: 0018-9219.

[143] Shizhong Mei and Y. Ismail, "Modeling skin and proximity effects with reduced realizable RL circuits," *IEEE Transactions on Very Large Scale Integration (VLSI) Systems*, vol. 12, no. 4, pp. 437–447, 2004, ISSN: 1063-8210.

[144] M. D'Amore and M. Sarto, "Time-domain analysis of field-excited transmission line systems by using model-based parameter estimation," in *Proceedings of IEEE Symposium on Electromagnetic Compatibility*, IEEE, pp. 258–263, ISBN: 0-7803-1398-4.

[145] M. D'Amore and M. Sarto, "Transient formulation of lossy ground return parameters for time-domain transmission line analysis," in *Proceedings of Symposium on Electromagnetic Compatibility*, IEEE, 1996, pp. 213–218, ISBN: 0-7803-3207-5.

[146] W. Beyene, "Improving time-domain measurements with a network analyzer using a robust rational interpolation technique," *IEEE Transactions on Microwave Theory and Techniques*, vol. 49, no. 3, pp. 500–508, 2001, ISSN: 00189480.

[147] A. Scarlatti and C. Holloway, "An equivalent transmission-line model containing dispersion for high-speed digital lines-with an FDTD implementation," *IEEE Transactions on Electromagnetic Compatibility*, vol. 43, no. 4, pp. 504–514, 2001, ISSN: 0018-9375. DOI: 10.1109/15.974629. [Online]. Available: https://ieeexplore.ieee.org/document/974629/.

[148] C. Holloway, P. McKenna, and R. Johnk, "The effects of gaps in ferrite tiles on both absorber and chamber performance," in *1999 IEEE International Symposium on Electromagnetic Compatability. Symposium Record (Cat. No.99CH36261)*, vol. 1, IEEE, 1999, pp. 239–244, ISBN: 0-7803-5057-X. DOI: 10.1109/ISEMC.1999.812902. [Online]. Available: http://ieeexplore.ieee.org/document/812902/.

[149] W. Hendrickx and T. Dhaene, "A Discussion of "Rational Approximation of Frequency Domain Responses by Vector Fitting"," *IEEE Transactions on Power Systems*, vol. 21, no. 1, pp. 441–443, 2006, ISSN: 0885-8950.

[150] B. Gustavsen, "Computer code for rational approximation of frequency dependent admittance matrices," *IEEE Transactions on Power Delivery*, vol. 17, no. 4, pp. 1093–1098, 2002, ISSN: 0885-8977.

[151] B. Gustavsen and A. Semlyen, "Enforcing passivity for admittance matrices approximated by rational functions," *IEEE Transactions on Power Systems*, vol. 16, no. 1, pp. 97–104, 2001, ISSN: 08858950.

[152] S. Pasha, M. Celik, A. Cangellaris, and J. Prince, "Passive SPICE-compatible models of dispersive interconnects," in *1999 Proceedings. 49th Electronic Components and Technology Conference (Cat. No.99CH36299)*, IEEE, 1999, pp. 493–499, ISBN: 0-7803-5231-9.

[153] R. Chen, J. van Wyk, S. Wang, and W. Odendaal, "Planar electromagnetic integration technologies for integrated EMI filters," in *38th IAS Annual Meeting on Conference Record of the Industry Applications Conference, 2003.*, vol. 3, IEEE, 2003, pp. 1582–1588, ISBN: 0-7803-7883-0. DOI: 10.1109/IAS.2003.1257767. [Online]. Available: http://ieeexplore.ieee.org/document/1257767/.

[154] I. Lope, C. Carretero, J. Acero, R. Alonso, and J. M. Burdio, "AC Power Losses Model for Planar Windings With Rectangular Cross-Sectional Conductors," *IEEE Transactions on Power Electronics*, vol. 29, no. 1, pp. 23–28, 2014, ISSN: 0885-8993. DOI: 10.1109/TPEL.2013.2256928. [Online]. Available: https://ieeexplore.ieee.org/document/6508936/.

[155] P. L. D. Crevecoeur and D. Guillaume, "Optimization and inverse problems in electromagnetism," *COMPEL: The International Journal for Computation and Mathematics in Electrical and Electronic Engineering*, vol. 33, no. 3, 2014, ISSN: 0332-1649. DOI: 10.1108/COMPEL-10-2013-0333. [Online]. Available: https://www.emerald.com/insight/content/doi/10.1108/COMPEL-10-2013-0333/full/html.

[156] G. Meunier, D. Shen, and J.-L. Coulomb, "Modelisation of 2D and axisymmetric magnetodynamic domain by the finite elements method," *IEEE Transactions on Magnetics*, vol. 24, no. 1, pp. 166–169, 1988, ISSN: 00189464. DOI: 10.1109/20.43882. [Online]. Available: http://ieeexplore.ieee.org/document/43882/.

[157] C. A. Valdivieso, G. Meunier, B. Ramdane, J. Gyselinck, C. Guerin, and R. V. Sabariego, "Time-Domain Homogenization of Foil Windings in 2-D Axisymmetric Finite-Element Models," *IEEE Transactions on Power Delivery*, vol. 36, no. 3, pp. 1264–1269, 2021, ISSN: 0885-8977. DOI: 10.1109/TPWRD.2020.3005225. [Online]. Available: https://ieeexplore.ieee.org/document/9127108/.

[158] A. Konrad, M. Chari, and Z. Csendes, "New finite element techniques for skin effect problems," *IEEE Transactions on Magnetics*, vol. 18, no. 2, pp. 450–455, 1982, ISSN: 0018-9464. DOI: 10.1109/TMAG.1982.1061859. [Online]. Available: http://ieeexplore.ieee.org/document/1061859/.

[159] G. Chitarin, M. Guarnieri, and A. Stella, "Transient behaviour of thick-walled axisymmetric windings: a lumped parameters approach," *IEEE Transactions on Magnetics*, vol. 24, no. 1, pp. 205–208, 1988, ISSN: 00189464. DOI: 10.1109/20.43890. [Online]. Available: http://ieeexplore.ieee.org/document/43890/.

[160] R. A. Waldron, "A helicoidal coordinate system and its applications in electromagnetic theory," *The Quarterly Journal of Mechanics and Applied Mathematics*, vol. 11, no. 4, pp. 438–461, 1958, ISSN: 0033-5614. DOI: 10.1093/qjmam/11.4.438. [Online]. Available: https://academic.oup.com/qjmam/article-lookup/doi/10.1093/qjmam/11.4.438.

[161] K. Hazim, G. Parent, S. Duchesne, A. Nicolet, and C. Geuzaine, "2D electrostatic modeling of twisted pairs," *COMPEL-The international journal for computation and mathematics in electrical and electronic engineering*, vol. 41, no. 1, pp. 48–63, 2022.

[162] C. Geuzaine, "High order Hybrid finite element schemes for Maxwell's equations taking thin structures and global quantities into account," Ph.D. dissertation, 2001.

[163] P. Dular, "Modélisation du champ magnétique et des courants induits dans des systèmes tridimensionnels non linéaires," Ph.D. dissertation, 1994.

[164] E. Freeman and D. Lowther, "An open boundary technique for axisymmetric and three dimensional magnetic and electric field problems," *IEEE Transactions on Magnetics*, vol. 25,

no. 5, pp. 4135–4137, 1989, ISSN: 00189464. DOI: 10.1109/20.42546. [Online]. Available: http://ieeexplore.ieee.org/document/42546/.

[165] J. Imhoff, G. Meunier, X. Brunotte, and J. Sabonnadiere, "An original solution for unbounded electromagnetic 2D- and 3D-problems throughout the finite element method," *IEEE Transactions on Magnetics*, vol. 26, no. 5, pp. 1659–1661, 1990, ISSN: 00189464. DOI: 10.1109/20.104482. [Online]. Available: http://ieeexplore.ieee.org/document/104482/.

[166] F. Henrotte, B. Meys, H. Hedia, P. Dular, and W. Legros, "Finite element modelling with transformation techniques," *IEEE Transactions on Magnetics*, vol. 35, no. 3, pp. 1434–1437, 1999, ISSN: 00189464. DOI: 10.1109/20.767235.

[167] Z. De Greve, O. Deblecker, and J. Lobry, "Numerical Modeling of Capacitive Effects in HF Multiwinding Transformers—Part I: A Rigorous Formalism Based on the Electrostatic Equations," *IEEE Transactions on Magnetics*, vol. 49, no. 5, pp. 2017–2020, 2013, ISSN: 0018-9464. DOI: 10.1109/TMAG.2013.2243421. [Online]. Available: http://ieeexplore.ieee.org/document/6514689/.

[168] J. Spreen, "Electrical terminal representation of conductor loss in transformers," *IEEE Transactions on Power Electronics*, vol. 5, no. 4, pp. 424–429, 1990, ISSN: 0885-8993. DOI: 10.1109/63.60685.

[169] R. S. Hoyt and S. P. Mead, "Mutual Impedances of Parallel Wires," *Bell System Technical Journal*, vol. 14, no. 3, pp. 509–533, 1935, ISSN: 00058580. DOI: 10.1002/j.1538-7305.1935.tb00696.x. [Online]. Available: https://ieeexplore.ieee.org/document/6772839.

[170] K. Niyomsatian, J. J. C. Gyselinck, and R. V. Sabariego, "Experimental Extraction of Winding Resistance in Litz-Wire Transformers—Influence of Winding Mutual Resistance," *IEEE Transactions on Power Electronics*, vol. 34, no. 7, pp. 6736–6746, 2019, ISSN: 0885-8993. DOI: 10.1109/TPEL.2018.2876310.

[171] P. Dular and W. Legros, "Coupling of local and global quantities in various finite element formulations and its application to electrostatics, magnetostatics and magnetodynamics," *IEEE Transactions on Magnetics*, vol. 34, no. 5 PART 1, pp. 3074–3077, 1998, ISSN: 00189464. DOI: 10.1109/20.717719.

[172] A. W. Cirino, H. de Paula, R. C. Mesquita, and E. Saraiva, "Cable parameter variation due to skin and proximity effects: Determination by means of Finite Element Analysis," in *2009 35th Annual Conference of IEEE Industrial Electronics*, IEEE, 2009, pp. 4073–4079, ISBN: 978-1-4244-4648-3. DOI: 10.1109/IECON.2009.5415128. [Online]. Available: http://ieeexplore.ieee.org/document/5415128/.

[173] T. Guillod, R. Faerber, D. Rothmund, F. Krismer, C. M. Franck, and J. W. Kolar, "Dielectric losses in dry-type insulation of medium-voltage power electronic converters," *IEEE Journal of Emerging and Selected Topics in Power Electronics*, vol. 8, no. 3, pp. 2716–2732, 2020, ISSN: 2168-6777. DOI: 10.1109/JESTPE.2019.2914997. [Online]. Available: https://ieeexplore.ieee.org/document/8706953/.

[174] Z. Nadolny, "Determination of dielectric losses in a power transformer," *Energies*, vol. 15, no. 3, p. 993, 2022.

[175] O. Hoseini Izadi and D. Pommerenke, "Measurement of Dielectric Constant and Cross-Sectional Variations of a Wire," *IEEE Transactions on Instrumentation and Measurement*, vol. 67, no. 6, pp. 1409–1416, 2018, ISSN: 0018-9456. DOI: 10.1109/TIM.2018.2792878. [Online]. Available: https://ieeexplore.ieee.org/document/8281085/.

[176] Agilent Technologies, *Agilent 4294a precision impedance analyzer operation manual*, 2003.

[177] C. Geuzaine and J.-F. Remacle, "Gmsh: A 3-D finite element mesh generator with built-in pre- and post-processing facilities," *Int. J. Numer. Methods Eng.*, vol. 79, no. 11, pp. 1309–1331, May 2009, doi10.1002/nme.2579.

[178] P. Dular, C. Geuzaine, F. Henrotte, and W. Legros, "A general environment for the treatment of discrete problems and its application to the finite element method," *IEEE transactions on magnetics*, vol. 34, no. 5, Sep. 1998, doi:10.1109/20.717799.

[179] M Engelhardt, "LTspice manual," *Accessed: Jul*, vol. 25, p. 2018, 2011.

[180] P. Thakur, D. Chahar, S. Taneja, N. Bhalla, and A. Thakur, "A review on MnZn ferrites: Synthesis, characterization and applications," *Ceramics International*, vol. 46, no. 10, pp. 15 740–15 763, 2020, ISSN: 02728842. DOI: 10.1016/j.ceramint.2020.03.287.

[181] S. Coulibaly, D. Malec, V. Bley, D. Mary, B. Schlegel, *et al.*, "New use of mn-zn ferrite material in power electronics integrated lc filters," *Engineering*, vol. 9, no. 12, p. 993, 2017.

[182] D. Petrović, M. Lazić, O. AleksiĆ, M. V. NikoliĆ, V. Ibrahimovć, and M. PAJNIć, "Mn-Zn ferrite line EMI suppressor for power switching noise in the impulse/high current bias regime," *Turkish Journal Of Electrical Engineering & Computer Sciences*, vol. 26, no. 5, pp. 2426–2436, 2018, ISSN: 13000632. DOI: 10.3906/elk-1710-52. [Online]. Available: https://journals.tubitak.gov.tr/elektrik/vol26/iss5/22.

[183] M. Drofenik, A. Žnidaršič, and I. Zajc, "Highly resistive grain boundaries in doped mnzn ferrites for high frequency power supplies," *Journal of Applied Physics*, vol. 82, no. 1, pp. 333–340, 1997.

[184] J. Gyselinck, L. Vandevelde, J. Melkebeek, P. Dular, F. Henrotte, and W. Legros, "Calculation of eddy currents and associated losses in electrical steel laminations," *IEEE Transactions on Magnetics*, vol. 35, no. 3, pp. 1191–1194, 1999, ISSN: 00189464. DOI: 10.1109/20.767162. [Online]. Available: http://ieeexplore.ieee.org/document/767162/.

[185] S. Ryder, "Diagnosing transformer faults using frequency response analysis," *IEEE Electrical Insulation Magazine*, vol. 19, no. 2, pp. 16–22, 2003, ISSN: 0883-7554. DOI: 10.1109/MEI.2003.1192032. [Online]. Available: http://ieeexplore.ieee.org/document/1192032/.

[186] C.-W. Ho, A. Ruehli, and P. Brennan, "The modified nodal approach to network analysis," *IEEE Transactions on Circuits and Systems*, vol. 22, no. 6, pp. 504–509, 1975, ISSN: 0098-4094. DOI: 10.1109/TCS.1975.1084079. [Online]. Available: http://ieeexplore.ieee.org/document/1084079/.

[187] L. Wedepohl and L Jackson, "Modified nodal analysis: An essential addition to electrical circuit theory and analysis," *Engineering Science & Education Journal*, vol. 11, no. 3, pp. 84–92, 2002.

[188] A. Naikodi and D. Mistry, "Modified nodal analysis; a comprehensive technique for drive modelling and simulation," in *TENCON 2003. Conference on Convergent Technologies for Asia-Pacific Region*, IEEE, vol. 1, 2003, pp. 255–258.

[189] Z. Zhao, L. Luo, Y. Li, J. Zhang, D. He, and P. Shao, "The mathematical model of the new converter transformer based on modified node method," in *2008 International Conference on Electrical Machines and Systems*, IEEE, 2008, pp. 4379–4383.

[190] N. Deo, *Graph theory with applications to engineering and computer science*. Courier Dover Publications, 2017.

[191] B. Gustavsen and A. Semlyen, "Application of vector fitting to state equation representation of transformers for simulation of electromagnetic transients," *IEEE Transactions on Power Delivery*, vol. 13, no. 3, pp. 834–839, 1998, ISSN: 08858977. DOI: 10.1109/61.686981.

[192] I. Dassios, A. Keane, and P. Cuffe, "Calculating Nodal Voltages Using the Admittance Matrix Spectrum of an Electrical Network," *Mathematics*, vol. 7, no. 1, p. 106, 2019, ISSN: 2227-7390. DOI: 10.3390/math7010106. [Online]. Available: https://www.mdpi.com/2227-7390/7/1/106.